

Thesis presented to the Instituto Tecnológico de Aeronáutica, in partial fulfillment of the requirements for the degree of Doctor of Science in the Program of Aeronautics and Mechanical Engineering, of the Materials and Manufacturing Processes Area.

Ronnie Rodrigo Rego

**RESIDUAL STRESS INTERACTION IN-BETWEEN
PROCESSES OF THE GEAR MANUFACTURING CHAIN**

Thesis approved in its final version the signatories below:



Prof. Dr. Jefferson de Oliveira Gomes
Advisor

Prof. Dr.-Ing. Dr.-Ing. E.h. Dr. h.c. Dr. h.c. Fritz Klocke
Co-advisor

Prof. Dr. Luiz Carlos Sandoval Góes
Prorector of Graduate Studies and Research

**Campo Montenegro
São José dos Campos, SP – Brazil
2016**

Cataloging-in-Publication Data
Documentation and Information Division

Rego, Ronnie Rodrigo	Residual stress interaction in-between processes of the gear manufacturing chain / Ronnie Rodrigo
Rego.	
São José dos Campos, 2016.	
196f.	
	Thesis of Doctor of Science – Program of Aeronautics and Mechanical Engineering, Materials and Manufacturing Processes Area – Instituto Tecnológico de Aeronáutica, 2016. Advisor: Prof. Dr. Jefferson de Oliveira Gomes
	1. Residual stress. 2. Gear. 3. Manufacturing chain. I. Instituto Tecnológico de Aeronáutica. II. Residual stress interaction in-between processes of the gear manufacturing chain

BIBLIOGRAPHIC REFERENCE

REGO, R. R. **Residual stress interaction in-between processes of gear manufacturing chain**. 2016. 196f. Thesis of Doctor of Science in Materials and Manufacturing Processes – Instituto Tecnológico de Aeronáutica, São José dos Campos.

CESSION OF RIGHTS

AUTHOR NAME: Ronnie Rodrigo Rego

PUBLICATION TITLE: Residual Stress Interaction In-between Processes of the Gear Manufacturing Chain

PUBLICATION KIND/YEAR: Thesis / 2016

It is granted to Instituto Tecnológico de Aeronáutica permission to reproduce copies of this thesis to only loan or sell copies for academic and scientific purposes. The author reserves other publication rights and no part of this thesis can be reproduced without his authorization.

Ronnie Rodrigo Rego

Praça Marechal-do-Ar Eduardo Gomes, 50 – Vila das Acácias
CEP: 12228-900, São José dos Campos - SP

RESIDUAL STRESS INTERACTION IN-BETWEEN PROCESSES OF THE GEAR MANUFACTURING CHAIN

Ronnie Rodrigo Rego

Thesis Committee Composition:

Prof. Dr.	Gilmar Patrocínio Thim	Chairperson	- ITA
Prof. Dr.	Jefferson de Oliveira Gomes	Advisor	- ITA
Dr.-Ing. Dipl.-Wirt.-Ing.	Christoph Löpenhaus	Representative of the Co-advisor	- RWTH Aachen
Prof. Dr.	Maria Margareth da Silva		- ITA
Prof. Dr.	Walter Lindolfo Weingaertner		- UFSC
Dr.	Edson Costa Santos		- SENAI

ITA

Acknowledgements

Motivation, respect, comprehension and even a contribution for the title of this thesis. Among several other reasons, I could not start this session without expressing my gratefulness to my beloved wife Mariana. She led a wide group, without whom this thesis could not be written, and to whom I would like to thank:

To my parents, brothers and family, who immediately supported my decision of returning to the Academy and conducting the doctoral studies.

To my advisor Prof. Jefferson Gomes, who played an inspiration role for me to keep following the end of this journey. Also from ITA, I am highly indebted to Prof. Anderson Borille, Janete Guska and all the CCM colleagues who enabled this project. I am especially grateful to André Maia, Lucas Robatto, Enivaldo Amaral, Gustavo Ascensão, André Oliveira, Patrícia Teixeira and Rafael Hiroshi. Together with the members of the Gear Innovation Group, they supported with dedication and belief the steps of the thesis.

To my co-advisor Prof. Fritz Klocke, who jointly with Prof. Christian Brecher and Markus Brumm received me with open arms at WZL. In Aachen, I was still granted to receive the guidance of Christoph Löpenhaus and Peter Knecht. The high-level discussions we had were still complemented by André Teixeira and by my office colleagues Philip Konowalczyk and Dieter Renkens, whose countdown for the thesis' delivery will not be forgotten. I could also not forget the extensive help of Sergej Oberdörfer, Egon Winkler, Johanna Figgenger and all the other WZL colleagues.

From WZL, I would like still to dedicate a special thanks to Bernd Krüger. His knowledge and constant interest on participating of this project represented a highly valuable upgrade to the exposed outcomes. I hope we will keep a long-term cooperation.

To the partners CIP gears, SENAI and OSK-Kiefer, here respectively represented by Arthur Facciolla, Alexsandro Rabelo and Oliver Nagels, whose large efforts were employed even under the risk of not achieving the expected results.

Finally to the sponsored support from CAPES, DAAD, CCM and the WZL Gear Research Circle, which enabled the successful completion of this entire doctorate.

"Vai, Corinthians!"

Bando de loucos

Resumo

A cadeia de fabricação de engrenagens é caracterizada por numerosas origens de tensões residuais. A fim de respeitar seu princípio de equilíbrio, uma redistribuição das tensões é necessária na progressão de processos. Contudo, o estado-da-arte revela uma preocupação excessiva com a investigação individualizada de processos. Reduzida acurácia de modelos preditivos, dificuldade de controle da produção e projeto não-otimizado são consequências diretamente decorrentes. A hipótese aqui destacada é de que a intensidade e a heterogeneidade induzidas por processos anteriores são significativas à integridade superficial após o subsequente processo. O objetivo é, portanto, a identificação dos fatores do estado de tensão residual desenvolvidos ao longo da cadeia com relevante influência à integridade superficial final da engrenagem. Uma investigação experimental envolveu as interações entre usinagem e tratamento térmico, assim como entre jateamento de granalhas e retífica. O estudo propõe uma abordagem original de estrutura convergente. Enquanto toda alteração é executada no primeiro processo analisado, o segundo é rigorosamente invariável. As engrenagens retificadas são ainda submetidas a ensaio de fadiga de contato, de modo a apurar a relevância da interação à vida útil do componente. Os resultados provam que o processo anterior pode exercer notável influência à integridade final. Um modelo de mola é a tradução simplificada para o fenômeno, em um conceito de energia potencial em auto-equilíbrio. Do processo anterior, o fator definido como primordial foi denominado como a área instável de tensões residuais. Este promove uma alteração proporcional à superfície resultante do próximo processo. As alterações se reproduzem na forma de distorção ou de variação do próprio estado de tensões residuais, em um mecanismo intimamente conectado ao modo de perturbação do equilíbrio que o processo representa. O efeito deve ser interpretado sob o prisma de seu domínio de atuação. Micro tensões residuais refletem inomogeneidades macroestruturais e padrões de rugosidade entre processos sequenciais. Tal correlação se viabiliza pelo novo método de avaliação do estado de heterogeneidade, por meio do parâmetro “*Gauss* integral breadth”. A interação se mostrou finalmente presente no comportamento em fadiga. Modo de falha e vida útil estão diretamente relacionados à região de intensa influência da interação de processos. Da compreensão dos efeitos de interação se deriva o inédito conceito de “Design for Residual Stress (DRS)”. A cadeia de fabricação pode ser planejada para o estado ótimo de tensões residuais, que potencializa um incremento na capacidade de carga da engrenagem.

Abstract

Several sources of residual stresses characterize the entire gear manufacturing chain. In-between processes, their redistribution has to be the condition to satisfy the equilibrium principle. Nevertheless, the state-of-the-art reveals an excessive concern on optimizing the processes individually. As direct consequences, the accuracy of the prediction models is lowered, the control on the production dispersion is jeopardized and the product design is not optimized. The hypothesis herein stated is that the residual stress intensity and heterogeneity induced by previous processes are significant to the surface integrity of a subsequent process. Consequently, the objective is the identification of the residual stress factors induced along the gear manufacturing chain with relevant influence on the final surface integrity. An experimental investigation was conducted on the interaction between soft machining and heat treatment, and between shot peening and grinding. This study originally proposed to structure the investigation into a convergent approach. Whereas every parameter modification is to be done at the first process, the second process is kept the same. The ground gears were submitted to contact fatigue tests, to identify the relevance of the interaction effects to the part lifetime. The results proved that the previous process can exert a noteworthy influence on the final integrity state. The interaction is understood by a model of springs, into a self-equilibrated potential energy concept. The primary factor from the previous process is the hereafter named unstable area of residual stresses (UARS). It proportionally drives the modifications induced to the surface after the next process. They happen either as distortion or as change in the stress state itself, depending on the equilibrium disturbance mode that the manufacturing process represents. The effect follows the domain size under analysis. Residual microstresses carry and reflect microstructural inhomogeneity and roughness patterns between neighboring processes. The correlation was enabled due to a novel assessment method of the residual stress heterogeneity state, through the *Gauss* integral breadth parameter. The interaction showed also to be present to the gear fatigue behavior. Both the failure mode and the lifetime correspond to the region where the interaction effects were mostly observed. The comprehension of the residual stress interaction effects derives the newly introduced concept of Design for Residual Stress (DRS). The manufacturing chain can be designed with the purpose of providing an optimal residual stress state, with a consequent potential for enhancing the gear load carrying capacity.

List of Figures

Figure 1.1 – The large variability on residual stresses as a product of the intermediate manufacturing processes (HAUK, 1997; BHADHESIA, 2002).	25
Figure 1.2 – Sequential structure of the thesis' chapters.	28
Figure 2.1 – Vehicle manual transmission with its interfaces and the torque flow when the 1st speed is engaged.	29
Figure 2.2 – Longitudinal dynamics analysis and the projection of the torque restriction over the 1st speed regime (REGO, 2011).	30
Figure 2.3 – Wind Power Scenario: Increasing power along the years; Gears appearing as an important player on the downtime metrics; and fatigue failure modes as one of the most frequent failure modes (RIBRANT, 2006; OYAGUE, 2009; WIKRENT, 2008; SHEND; MCDADE; ERRICHELO, 2011).	31
Figure 2.4 – Gear fatigue failure modes: bending and contact stresses (LECHNER; NAUNHEIMER, 1999; DING; RIEGER, 2003; BELSAK; FLASKER, 2006).	33
Figure 2.5 – Example of a gear manufacturing chain (KLOCKE; BRINKSMEIER; WEINERT, 2005; KLOCKE; BRECHER; BRUMM, 2014).	35
Figure 2.6 – Teeth cutting processes: gear hobbing and gear shaping principles (NIKOLAOS; ARISTOMENIS, 2012, KLOCKE; BRECHER; BRUMM, 2014).	36
Figure 2.7 – Induction hardening methods; Case hardening features: carbon content profile, typical gas carburized and nitrided surface structures (AGMA, 2004, DAVIS, 2005; GROSCH, 2014).	38
Figure 2.8 – Schemes and pictures of gear finishing processes (HARADA, MORI, MAKI, 2003; KLOCKE; BRINKSMEIER; WEINERT, 2005; KARPUSCHEWSKI; KNOCH; HIPKE, 2008; BRECHER; LÖPENHAUS; REGO, 2015).	40

Figure 2.9 – Relationship between the crack propagation, the residual stress profile and the fatigue performance (MITSUBAYASHI; MIYATA; AIHARA, 1994).	43
Figure 2.10 – Effect of the residual stress profile on the damage morphology (BATISTA et al., 2000; LV; LEI; SUN, 2015).	44
Figure 2.11 – Relationship between phenomena of the residual stress origins (INOUE, 2014).	46
Figure 2.12 – Explanation model to describe the mechanically originated residual stresses (WANG; GONG, 2002).	47
Figure 2.13 – Thermal load originated residual stresses (EBERT, 1978).	48
Figure 2.14 – Structural residual stresses: (a) phase transformation mechanisms; (b) iron phases' volume variation with the temperature; (c) residual stress profile variation along the grinding temperature (BHADESHIA, 2002; MALKIN; GUO, 2007).	49
Figure 2.15 – (a) Coupling effect for the residual stress profile of grinding; (b) Coupling conceptual model for machining (JACOBUS; DEVOR; KAPOOR, 2000; SHAH, 2011).	50
Figure 2.16 – Example of a gear manufacturing chain with the respective residual stress phenomena to each individual process.	52
Figure 2.17 – (a) Macro RS composed by the contribution of each phase; (b) Scheme of all levels of residual stresses (HAUK; NIKOLIN, 1988; WITHERS; BHADESHIA; 2001; SPIEB et al.; 2009).	53
Figure 2.18 – The equilibrium principle reflected into different domains (PERLOVICH; ISAENKOVA; FESENKO, 2010; ZHAN; JIANG; JI, 2013).	55
Figure 2.19 – A literature survey based on the key words of this study.	58
Figure 3.1 – The basis for the hypothesis, the objective of the study and how to approach it.	62
Figure 4.1 – The residual stress interaction analyzed through two case studies covering different stages of the gear manufacturing chain.	66

Figure 4.2 – Experimental flowchart. The structure with different parameters at the first process and the same second process characterizes the convergent approach.	67
Figure 4.3 – Blocks and gears as respective specimens for the case studies 1 and 2.	68
Figure 4.4 – Proposed method for selecting samples to be submitted to the residual stress measurement.	72
Figure 4.5 – Production of the machined samples: <i>Hermle C600 U</i> equipped with <i>Kistler</i> dynamometer thermocouples and assisted with a thermal camera; (b) Instrumentation detail; (c) Specimen's face to be machined.	75
Figure 4.6 – Heat treatment process: furnace concept, dimensions and the batch arrangement of the specimens.	76
Figure 4.7 – The shot peening parameters were defined to induce different residual stress distributions along the depth and across the surface.	79
Figure 4.8 – Procedures adopted to select ground samples with the same process loads.	82
Figure 4.9 – Residual stress measurement: Calculation method and procedures applied.	84
Figure 4.10 – Techniques and procedures used for topography and dimensional analyses.	87
Figure 4.11 – Methods for the material investigation.	89
Figure 4.12 – Gear fatigue test: power recirculating test rig and the visual inspection procedures of the tested pinion.	92
Figure 4.13 – Procedures for the damage morphology analysis during and after the test completion.	93
Figure 5.1 – The residual stress intensity features explored and the results achieved for the input of the interaction analysis.	95
Figure 5.2 – Results of the mechanical loads assessed for each roughing group.	96
Figure 5.3 – Methods approached to investigate the thermal loads induced during the roughing process.	98

Figure 5.4 – Metallographic comparison exposes the different microstructure observed on the outer layer of the specimens of the group BRL.....	100
Figure 5.5 – Macro residual stress measurements of the machined specimens.	101
Figure 5.6 – Relationship between the depth of cut and the cutting nose radius as the influence for the opposite residual stress states observed between roughing and finishing specimens.	102
Figure 5.7 - The different residual macrostress states induced after machining do not create meaningful differences after the heat treatment.	104
Figure 5.8 – The distortion shape is an effect of the processes' interaction: the case of machining compressive stresses, for the finishing specimens.....	106
Figure 5.9 – The distortion shape is an effect of the processes' interaction: the case of machining tensile stresses, for the roughing specimens.	107
Figure 5.10 – The intensity of the distortion after the heat treatment follows the same trend than the unstable area of residual stress from the machining process.	109
Figure 5.11 – Residual stress measurements on the peened samples on both axial and tangential directions.....	111
Figure 5.12 – Steel phase approach for the residual stress state of the peened samples: retained austenite fraction and the axial stress measurements on both phases.....	112
Figure 5.13 – Different depth profile features achieved with the residual macrostress profiles of the peened pinions.....	113
Figure 5.14 – Criteria to define the stock removal of 30 μm	115
Figure 5.15 – The measured grinding force and the method for selecting the flanks for the surface integrity analysis.	118
Figure 5.16 – Phase residual stresses and retained austenite fraction after the grinding process.	119

Figure 5.17 – The residual macrostress differs between the groups treated with different peening conditions and the same grinding process.	120
Figure 5.18 – The remaining area as the meaningful residual stress profile feature to influence the interaction between shot peening and grinding.	121
Figure 5.19 – Springs model to describe the residual stress behavior: model of Heyn (1914) and the proposed adaptation of equivalent layers (ELM).	123
Figure 5.20 – The unstable area of residual stress (UARS) as the driving factor to the residual stress interaction. The larger is the UARS, the larger will be the surface equilibrium disturbance.	124
Figure 5.21 – The release of the stored potential energy converts the disturbance in distortion and/or internal stress change.	125
Figure 5.22 – The large variability of macro RS is also influenced by its heterogeneity state.	128
Figure 5.23 – Main steps composing the developed method and its application routine.	133
Figure 5.24 – Topography analysis of the gears produced with different shot peening configurations.	134
Figure 5.25 – Residual macrostress maps, the variation bar chart and a scatterplot indicate that the heterogeneity state increase from group GDT to group G1P.	135
Figure 5.26 – The <i>Gauss</i> integral breadth matches the previous analyses and the order of the RS heterogeneity state, indicating a more reliable result than the FWHM.	137
Figure 5.27 – Metallographic and SEM analyses revealed no microcracks; the microhardness results do not match with the micro RS analysis; Results support the study's hypothesis. ...	138
Figure 5.28 – The fatigue results of ground discs conflict with the expected behavior of the residual macrostresses. A potential explanation is given with the RS heterogeneity, by means of the <i>Gauss</i> integral breadth.	141

Figure 5.29 – The <i>Gauss</i> integral breadth along the depth for the groups after milling.	143
Figure 5.30 – Results and literature converging to the influence of the depth of cut on the heterogeneity state of residual stresses.	144
Figure 5.31 – The <i>Gauss</i> integral breadth along the depth after the heat treatment process..	145
Figure 5.32 – The microhardness after the heat treatment and the microstructure before it reveal the reason for the different microstresses of the hardened samples.	146
Figure 5.33 – The <i>Gauss</i> integral breadth along the depth for the groups after shot peening.	148
Figure 5.34 – The <i>Gauss</i> integral breadth along the depth for the groups after grinding.	149
Figure 5.35 – The residual microstress of the peened surface influences the roughness after the grinding process.....	151
Figure 5.36 – Mean lifetime results of the different manufacturing chains.	155
Figure 5.37 – Statistical approach to the fatigue results through the <i>Weibull</i> distribution method.	156
Figure 5.38 – Damage evolution along the fatigue test.	158
Figure 5.39 – The damage morphology found at this investigation is similar to the one from peened surfaces referred in the literature.....	160
Figure 5.40 – The crack is subsurface-originated, propagates outwards the surface and when the opposite extremity finally collapses, the material is removed.....	161
Figure 5.41 – The depth of the crack initiation is 10 μm in average.....	163
Figure 5.42 – A correlation is observed between the part lifetime and the residual stress intensity at the depth of the cracks' initiation.	164
Figure 5.43 – The cracks' initiation depth is possibly influenced by the transition behavior of the residual stress along the depth.	166

Figure 5.44 – The high intensity of residual macrostresses induced on the gears minimized the role of their microstresses to the fatigue performance.	167
--	-----

List of Tables

Table 2.1 – Manufacturing processes and the corresponding residual stress phenomena (LU, 2002).	46
Table 4.1 – Process parameters for the groups representing the finishing machining condition.	72
Table 4.2 – Process parameters for the groups representing the roughing machining condition.	75
Table 4.3 – Parameters for each phase of the heat treatment process.	77
Table 4.4 – Shot peening parameters defined for inducing different intensity and heterogeneity levels of residual stress.	81
Table 5.1 – Samples classification according to the tooth span measured after the pre-grinding.....	118

List of Acronyms

AGMA	American Gear Manufacturers Association
AIAG	Automotive Industry Action Group
ASM	American Society for Metals
ASTM	American Society for Testing and Materials
CAPES	<i>Coordenação de Aperfeiçoamento de Pessoal de Nível Superior</i>
CIP	<i>Companhia Industrial de Peças</i>
cBN	Cubic Boron Nitride
CCM	<i>Centro de Competência em Manufatura</i>
CIRS	Cumulative Integral of the Residual Stress profile
CMM	Coordinate Measuring Machine
DAAD	<i>Deutscher Akademischer Austausch Dienst</i>
DfM	Design for Manufacturing
DfX	Design for eXcellence
DRS	Design for Residual Stress
DIMT	Deformation Induced Martensitic Transformation
DIN	<i>Deutsches Institut für Normung</i>
ELM	Equivalent Layers Model
FLM	Fused Layer Modeling
FVA	<i>Forschungsvereinigung Antriebstechnik</i>
FWHM	Full Width at Half Maximum
FZG	<i>Forschungsstelle für Zahnräder und Getriebebau</i>
HSC	High Speed Cutting
IPS	Invariant-Plane Strain

ISI	<i>Instituto SENAI de Inovação</i>
ISO	International Organization for Standardization
ITA	<i>Instituto Tecnológico de Aeronáutica</i>
LPA	Line Profile Analysis
MRE	Margin of Random Error
NL	Neutral Line
NREL	National Renewable Energy Laboratory
RA	Retained Austenite
RS	Residual Stress
RWTH	<i>Rheinisch-Westfälische Technische Hochschule</i>
SAE	Society of Automotive Engineers
SEM	Scanning Electron Microscopy
SENAI	<i>Serviço Nacional de Aprendizagem Industrial</i>
SURF	Surface
UARS	Unstable Area of Residual Stress
WZL	<i>Werkzeugmaschinenlabor</i>
XRD	X-Ray Diffraction

List of Symbols

a_e	radial depth of cut
a_p	axial depth of cut
b	fatigue strength constant
c	volume fraction of a material phase
C_b	lead crowning
d	diameter
$f(x)$	desired diffraction profile, after effects deconvolution
f_a	axial feed
F	failure probability in %
F_{EQ}	equivalent cutting force
F_X	cutting force, in the direction of the radial depth of cut
F_Y	cutting force, in the feed direction
F_Z	cutting force, in the direction of the axial depth of cut
F_{TRAC}	tractive force
$g(x)$	instrumental calibration profile of the diffracted intensity
$h(x)$	measured profile of the diffracted intensity
HB	<i>Brinell</i> hardness
HV	<i>Vickers</i> hardness
Het.	heterogeneity
Int.	intensity
i	lifetime ranking
I	diffracted intensity

I_{MAX}	maximum diffracted intensity
k	stiffness
K_{Ic}	critical intensity factor of the crack propagation mode I
LC_{50}	number of cycles to a failure probability of 50%
L_{CA}	tip relief
Mfg.	manufacturing
m_N	normal module
n	sample size
N_f	number of cycles up to the failure
Ref	reference
RS_{MAX}	maximum intensity of the residual stress depth profile
S_a	arithmetic mean surface roughness, areal parameter
S_k	core roughness height of the <i>Abbott-Firestone</i> curve, areal parameter
t	time
t_H	thickness
t_C	case depth
T_{INPUT}	input torque
T_{OUTPUT}	output torque
U	potential energy
V	material volume
V_{NEG}	negative volume of the geometric distortion
V_{POS}	positive volume of the geometric distortion
V_{TOT}	total volume of the geometric distortion
V_{TOT}^{HT}	total volume of the heat treated surface

V_{TOT}^{MAC}	total volume of the machined surface
WK	tooth span
x	length
z	gear teeth number
	normal direction to the surface (depth)
Z_{DIST}	depth of the initial disturbance of residual stresses
Z_{STAB}	depth of the end of the unstable area of residual stresses
Z_{STOCK}	depth of the stock removal
α	ferritic phase
α_N	normal pressure angle
β	helix angle
	Integral breadth
β_C^f	<i>Cauchy</i> integral breadth of the desired profile
β_C^g	<i>Cauchy</i> integral breadth of the instrumental calibration profile
β_C^h	<i>Cauchy</i> integral breadth of the measured profile
β_G^f	<i>Gauss</i> integral breadth of the desired profile
β_G^g	<i>Gauss</i> integral breadth of the instrumental calibration profile
β_G^h	<i>Gauss</i> integral breadth of the measured profile
γ	austenitic phase
δ	displacement (distortion)
ΔV_{TOT}	volumetric variation between the analyzed manufacturing processes
$\Delta \varepsilon$	strain variation

$\Delta\sigma_{RS}$	residual stress variation
ε	strain
ε^p	mechanical plastic strain
ε^T	thermal strain
Φ	XRD azimuthal direction
Ψ	grain lattice orientation
σ	standard deviation
	stress
σ_{MAX}	maximum stress
σ_{MIN}	minimum stress
σ_N	normal stress
σ_a	fatigue stress amplitude
$\sigma_{RS,surf}$	residual stress at the surface
σ^I	residual stress type I
σ^{II}	residual stress type II
σ^{III}	residual stress type III
$\bar{\sigma}$	mean stress
\mathbb{L}	centerline
$2w$	full Width at Half Maximum
2θ	diffracted beam angle
$2\theta_f$	initial diffracted angle for the line profile analysis
$2\theta_i$	initial diffracted angle for the line profile analysis

Symbols to describe the samples

BFH	block, finishing setup, high mechanical load expected
BFL	block, finishing setup, low mechanical load expected
BRH	block, roughing setup, high mechanical load expected
BRM1	block, roughing setup, medium mechanical load expected, condition 1
BRM1	block, roughing setup, medium mechanical load expected, condition 2
BRL	block, roughing setup, low mechanical load expected
G1P	gear, media diameter of 1.0 mm, partial coverage level
G6T	gear, media diameter of 0.6 mm, total coverage level
GDT	gear, media diameter of 0.6 mm and 0.3 mm (Dual), total coverage level
G3T	gear, media diameter of 0.3 mm, total coverage level
G3P	gear, media diameter of 0.3 mm, partial coverage level

Contents

1	INTRODUCTION	25
2	LITERATURE REVIEW	30
2.1	On the Connections of Gears to Residual Stresses	30
2.1.1	Gear Failures: The Industrial Scenario	30
2.1.2	Fatigue Failures Modes	33
2.1.3	The Manufacturing Chain.....	35
2.2	Residual Stresses.....	42
2.2.1	Relationship with the Fatigue Strength	43
2.2.2	Origins	46
2.2.3	Classification	53
2.2.4	The Equilibrium Principle	55
2.3	The State-of-the-Art on the Residual Stress Interaction	57
2.4	Summary	61
3	OBJECTIVE AND APPROACH.....	62
4	MATERIALS AND METHODS.....	65
4.1	Overall Experimental Scope	67
4.1.1	Design of the Specimens	69
4.2	Manufacturing of the Specimens.....	71
4.2.1	Soft Machining	71
4.2.2	Heat Treatment	76
4.2.3	Shot Peening	78
4.2.4	Grinding.....	81
4.3	Surface Integrity Assessment	84
4.3.1	Residual Stress Measurement.....	84
4.3.2	Topography and Dimensional Analysis	87
4.3.3	Material Investigation.....	89
4.3.4	Fatigue Tests.....	92
5	RESULTS AND DISCUSSIONS.....	96
5.1	The Role of the Residual Stress Intensity on the Processes' Interaction.....	96
5.1.1	Inducing Different Stress States through the Soft Machining.....	97

5.1.2	The Interaction between Soft Machining and Heat Treatment.....	105
5.1.3	Inducing Different Stress States through the Shot Peening.....	111
5.1.4	The Interaction between Shot Peening and Grinding.....	115
5.1.5	A Physical Model to the Residual Macrostress Interaction.....	123
5.1.6	Summary.....	127
5.2	Residual Stress Heterogeneity: Assessment and its Influence.....	128
5.2.1	Local Residual Stress Deviations	128
5.2.2	The Proposal of a Feasible Assessment Method	131
5.2.3	Method Validation.....	134
5.2.4	The Interaction between Soft Machining and Heat Treatment.....	143
5.2.5	The Interaction between Shot Peening and Grinding.....	148
5.2.6	Summary.....	153
5.3	The Interaction's Relevance to the Fatigue Behavior	154
5.3.1	Contact Fatigue Performance of the Different Manufacturing Chains.....	155
5.3.2	Damage Morphology Analysis.....	158
5.3.3	The Overall Phenomenological Interpretation	165
6	CONCLUSIONS AND OUTLOOK	170
7	BIBLIOGRAPHY.....	175
	APPENDIX A – TERMINOLOGY	190
A.1	Gear Nomenclature for Macro and Micro-Geometry.....	190
	APPENDIX B – SPECIMENS GEOMETRY.....	191
B.1	Blocks for Sample Groups BFH and BFL.....	191
B.2	Blocks for Sample Groups BRH, BRM1, BRM2 and BRL	192
B.3	Gears: FZG-C_{mod} Pinion	193
	ATTACHMENT C – SPECIMENS MATERIAL.....	194
C.1	Blocks, SAE 8620.....	194
C.2	Gears, DIN 16MnCr5	195
	ATTACHMENT D – TESTING SPECIFICATION.....	196
D.1	Testing Oil Specification (<i>Shell Spirax ASX 75W90</i>).....	196

1 Introduction

One hundred years have passed since Prof. Heyn[†] provided the definition for a phenomenon at that time he named as “internal strain”. The lucidity of his words transcended the description of this mechanical property. The words embedded a forecast in which this property would claim the attention of everyone involved with cold-worked metals manufacturing (HEYN, 1914).

Nowadays defined as “residual stress”, its strong relationship with the fatigue strength was the key for the well-succeeded prognosis. The superposing effect to the actuating stresses characterizes the residual stress as a decisive factor to confer either a detrimental or a beneficial contribution upon a component’s lifetime (ALMEN; BLACK, 1963; LÖHE; LANG; VÖHRINGER, 2002).

Gears appear as one of the most featured recipients of the residual stress product. On the one hand, its operational kinematics enables the onset of distinct fatigue mechanisms into different regions of the component (ALBAN, 2002). On the other hand, they are applied to industrial segments facing a progressive demand of higher power density, such as the automotive and the wind energy industries.

The combination of the described scenarios deserved the investment of countless researches on this topic along the past decades. Every hitherto existing process for manufacturing metallic gears has already been investigated under the perspective of residual stresses. Motivated by the need of enhancing the gear durability attribute, the researches’ purpose is usually to optimize certain process parameters in order to induce an appropriate compressive residual stress layer to the surface.

However, the challenge is not restricted to the feasibility of increasing the intensity of the compressive stresses. The high variability observed during the production control is a daily fact faced by the industry. The statement can be quantified by the scatterplot chart of the Figure 1.1, created with production data of an automotive gear. The same design, manufacturing processes and inspection procedure were not sufficient to hinder 50% of variation over the residual stress mean value.

[†] Prof. Emil Heyn was the director of the Royal Prussian Institute for Testing Materials when, in 1914, he delivered a lecture describing the residual stress phenomenon to the Institute of Metals in London.

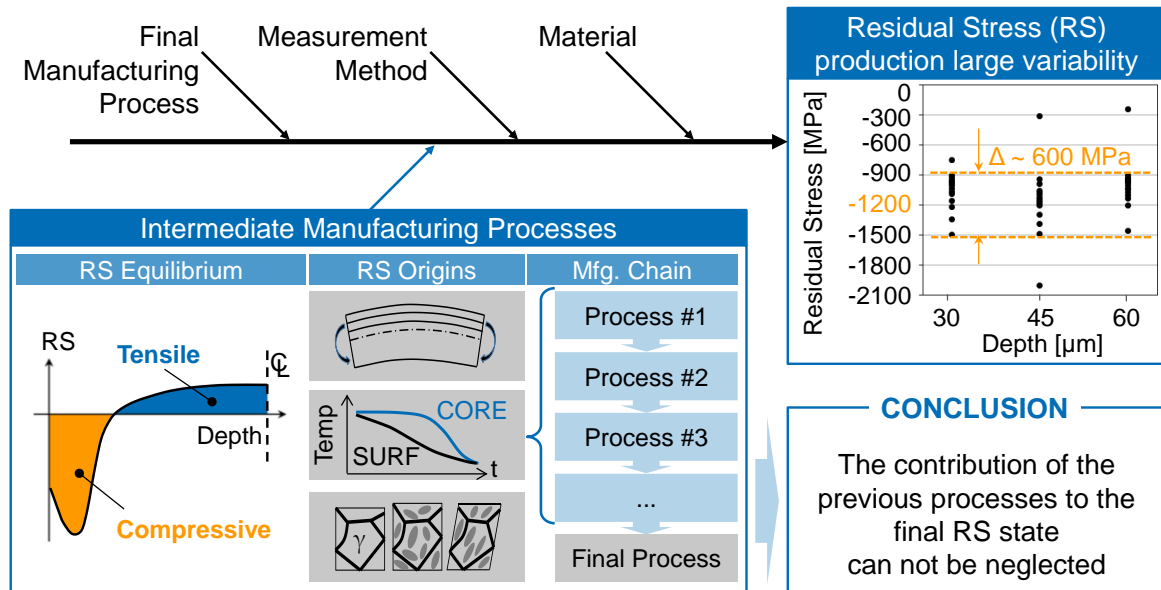


Figure 1.1 – The large variability on residual stresses as a product of the intermediate manufacturing processes (HAUK, 1997; BHADHESIA, 2002).

An irregular material microstructure and the measurement equipment's intrinsic errors can contribute to such a poor repeatability level (LU, 2002; LAW; LUZIN, 2011). Likewise the influence of the final manufacturing process is of incontestable importance. However, this study puts the spotlight on the intermediate processes of the gear manufacturing chain.

Each process of the manufacturing chain modifies the workpiece leaving a trace registered in the form of residual stresses. Mechanical, thermal and structural effects arise and combine themselves into a complex strain arrangement. Still, they are supposed to fulfill the requirements of the most basic residual stress' condition: the equilibrium principle (bottom panel of the Figure 1.1). If each of the manufacturing processes becomes a source of disturbances, and if the variability control is a definitive challenge, how could it be possible to neglect the contribution of these earlier stages to the final residual stress state?

Although a negative answer seems to be quite trivial, this is not the reflection from the Scientific's publications database. Only a few researches aimed at analyzing residual stress as a processes sequence. The great majority approaches an individual process as if no influence would come from the previous ones. One century has passed since the lecture of Prof. Heyn, and society demands a more holistic approach. The importance of understanding the interaction in-between processes is expressed by the assumptions of the "Industry 4.0" concept. It states that the collaboration and interaction among machines is the key factor to the next manufacturing revolution (SCHUH et al., 2014). The phenomenological

understanding of the interaction is the previous necessary step to implement this collaborative production.

The direct consequences of the lack of knowledge on the role of the processes' interaction to the final residual stress state are represented by:

- A limited accuracy of the calculation models for predicting the residual stress state induced by one specific process.
- An additional reason to increase the dispersion of the residual stress intensity, controlled at the end of the production.
- An obstacle to define the optimal residual stress state for a specific application.
- Restricted comprehension of the residual stress influence on the fatigue behavior.

Even the few publications approaching the residual stress along the manufacturing chain do not provide conclusions to satisfy the presented gap (BARSOUM; BARSOUM, 2009; KLEIN; EIFLER, 2010; BRINKSMEIER et al., 2011; NAVAS et al., 2011). The most imprecise assumption made is not to isolate the final process face to the possible distinct incomes from the previous processes. Moreover, several of them do not perform the investigation covering the depth range of the surface contact phenomena. Finally, interactions between early and late stages of the chain are not compared.

The main goal is derived from the previously drawn conclusion and from the just introduced problem statements. The objective of this study is the identification of the relevant residual stress factors from previous manufacturing processes to the final integrity state. The factors broaden the approach to both intensity and heterogeneity levels. They represent different features of the residual stress state, either defined by characterizing a depth distribution or by defining the leading domain size of the stresses' deviations. The integrity state covers further surface aspects than residual stresses, such as geometric deviations, material structure and fatigue strength.

Accomplishing the goals means revealing to society the prime aspects of a residual stress state that drive the surface properties of an upcoming process. This signifies understanding the weighted contribution of individual steps of the production to the final gear integrity state. This attainment is complemented by the additional contribution of establishing a prioritization of processes to be analyzed. Two case studies, one positioned at an early and one at a late production stage, may reveal from how far the interaction's effect comes. The

outcomes may drive the focus of future researches to the stages of the manufacturing chain whose interaction effect is mostly sensitive to the final integrity state.

The demand for a feasible method of assessing the residual stress heterogeneity also offers this study an opportunity to provide an original scientific contribution. The lack of uniformity addresses the exposed control challenge and it is increasingly being referred to as a process limitation and a topic to be further examined (KARABELCHTCHIKOVA; RIVERO, 2005; ZHAN; JIANG; JI, 2013; TOUALBI et al., 2015).

The expectation in an economic context goes toward mapping the evolution of residual stresses along the gear manufacturing chain. A global comprehension of the variability sources would enable the implementation of corrective actions to intermediate stages of the production. A lower amount of workpieces would be produced outside the specified residual stress range, driving the scrap ratio to be reduced. As an indirect result, both the manufacturing chain and the product may be redesigned to accommodate a new knowledge for a current gap accounted into higher safety factors.

A notice should also be given to the proposed experimental scope. Contrasting the state-of-the-art, it was conceived as a convergent structure. Gears produced by inducing different residual stress states at a previous process are later submitted to a same final manufacturing operation. It provides an effective isolation of the last process effects and the appropriate identification of the relevance from early production stages.

The development for this approach was conducted at the Competence Center in Manufacturing (*Centro de Competência em Manufatura*, CCM-ITA). It was empowered by the partnership with the Laboratory for Machine Tools and Production Engineering (*Werkzeugmaschinenlabor*, WZL) of the RWTH Aachen University (*Rheinisch-Westfälische Technische Hochschule*) in Germany.

The herein presented thesis starts with a literature review, essentially composed by a topic on gears and one on residual stresses. Concepts of the gear fatigue behavior and the gear manufacturing chain are followed by the residual stress fundamentals that are relevant to the approached problem statement. They provide the necessary information to the description of the state-of-the-art with regard to the evolution of residual stresses along the manufacturing chain.

The document only states the objective after the reader is fully informed about the existing open points from the state-of-the-art. Together with the secondary goals, the objective is presented as an action to bridge the disclosed gap. In order to organize the

approach to the stated hypothesis, three research questions are announced to cover the entire thesis' development content.

The experimental and analytical procedures to achieve the objective are described in a chapter of materials and methods. On the quest of one answer, two case studies were planned. Their execution is explained by means of the experiments to manufacture the samples and to characterize and test their induced surface integrity.

The results and discussions about the findings are displayed in three topics, according to the sequence of the research questions. The role of the intensity and of the heterogeneity state of residual stresses is demonstrated with the support of the further surface properties collected. The relevance of the residual stress interaction to the fatigue behavior of gears reinforces the relevance of the achievement and the linkage to the motivation, closing the chapter.

The objective is finally recalled to verify to which extension the hypothesis could be proved and the research questions answered. The drawn conclusions do not only summarize the present investigation. They embed the answers for the different questions to a general and fundamental perspective. Moreover, this final chapter presents a forecast to the suggested continuation scenarios that embrace this cause. The mentioned steps form the main structure of the thesis, as depicted in the Figure 1.2.

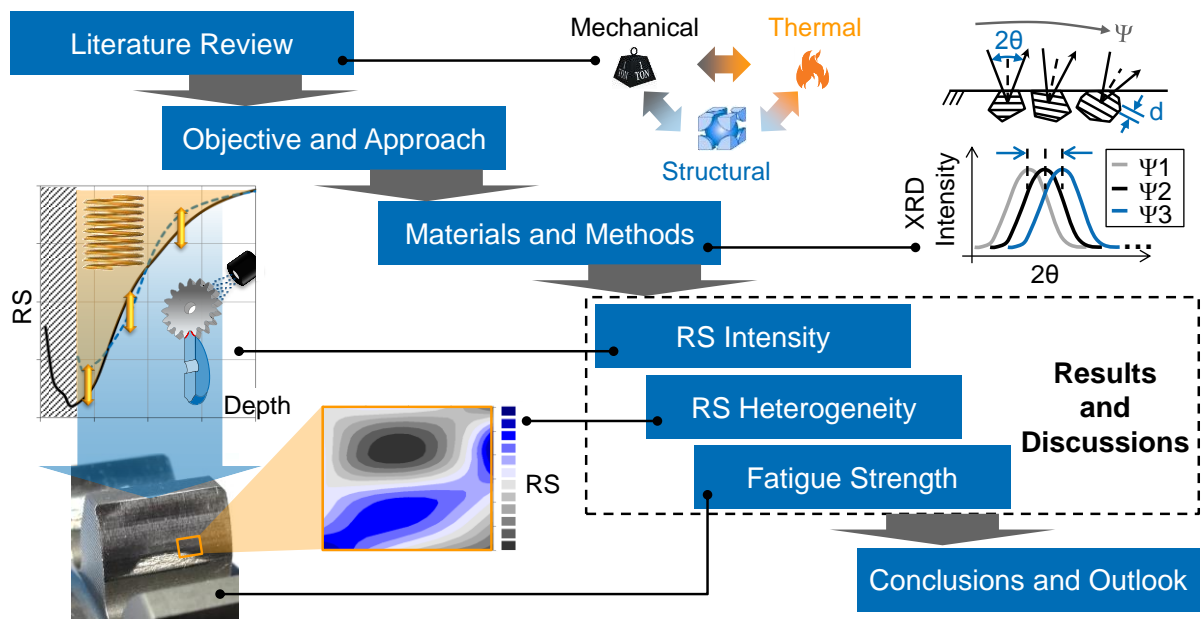


Figure 1.2 – Sequential structure of the thesis' chapters.

2 Literature Review

2.1 On the Connections of Gears to Residual Stresses

Prior to the review of residual stresses, an overall picture of its connections to the context of gears is given. The relevance and description of gear fatigue failure modes, which are associated to the final gear residual stress state, compose the motivation for this study. The gear manufacturing introduction prepares the discussion about the possible different origins to the creation of such stress state.

2.1.1 Gear Failures: The Industrial Scenario

Many of the newest technologies developed for internal combustion engines aims at increasing the delivered torque and power. The purpose is to quickly implement solutions that provide an enhanced vehicle longitudinal dynamics performance. Frequently, these advances crash with the torque capacity limitation of its interface system: the transmission (Figure 2.1).

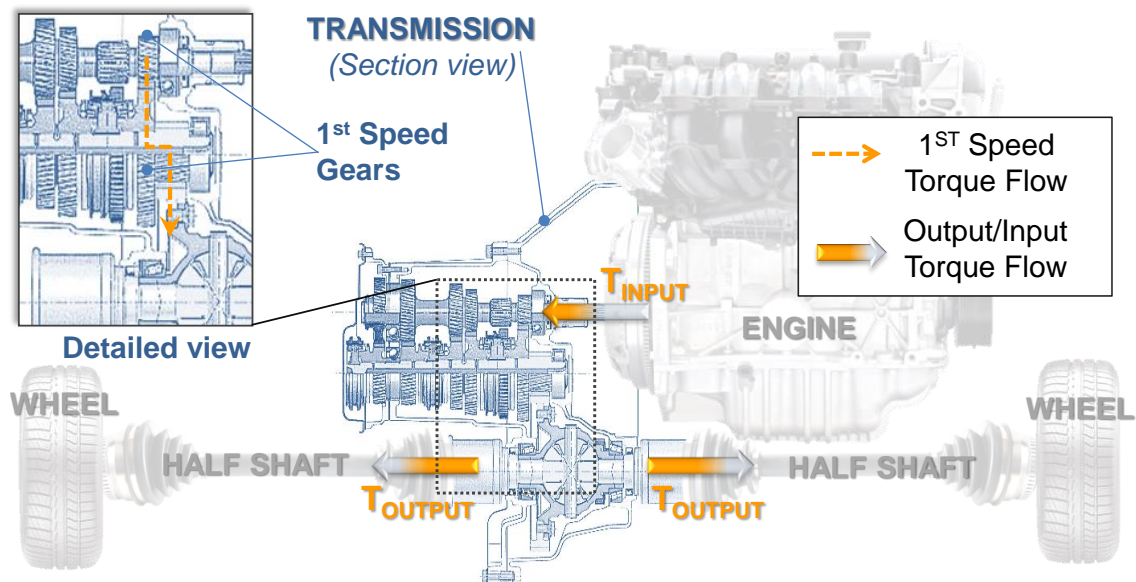


Figure 2.1 – Vehicle manual transmission with its interfaces and the torque flow when the 1st speed is engaged.

For the vehicles equipped with manual transmissions, the restriction is generally defined by the first speed gear lifetime. The high transmission ratios submit them to the highest contact and bending stresses. The most frequent failure mode in the transmission systems of passenger vehicles is the fatigue failure due to the contact stresses. (ALBAN, 2002; ASI, 2006). This limitation is reflected into two usual engineering alternatives. The first one is modifying the gear design through increasing the dimensions that can improve its strength. Alternatively, the engine output torque is truncated by electronic injection module control calibration. In this case, the engine potential is underused and the vehicle longitudinal dynamics performance is jeopardized. The study performed by Rego (2011) provides a quantified example of this torque truncation impact. The chart of Figure 2.2 displays the vehicle tractive force calculated for the regime when the vehicle is moving in the first speed. According to the study, the projected dashed line, representing the truncated torque, can reduce in up to 9% the ramp gradient capacity or up to 0.4 s the 0-100 km/h acceleration time.



Figure 2.2 – Longitudinal dynamics analysis and the projection of the torque restriction over the 1st speed regime (REGO, 2011).

These gear lifetime issues are spread in most part of the machinery industry. This problem has received increasing attention at another relevant industrial sector, the wind power. Similarly to the automotive industry, the importance of this topic is following the increasing power capacity of the wind turbines along the years. According to a North American database (Figure 2.3), the average power of the turbine grew from 50 kW in the 80's to about 8 MW in the year of 2015 (WIKRENT, 2008). Recent studies have demonstrated that gearboxes are the main responsible for wind turbine premature failures. As showed by Ribrant (2006), worse than failures quantity is the impact on the turbine downtime

when gears maintenance is required. Among wind farms of US, Germany, Sweden and Finland, between 2000 and 2004, gears can represent up to 33% on total wind turbine downtime (Figure 2.3).

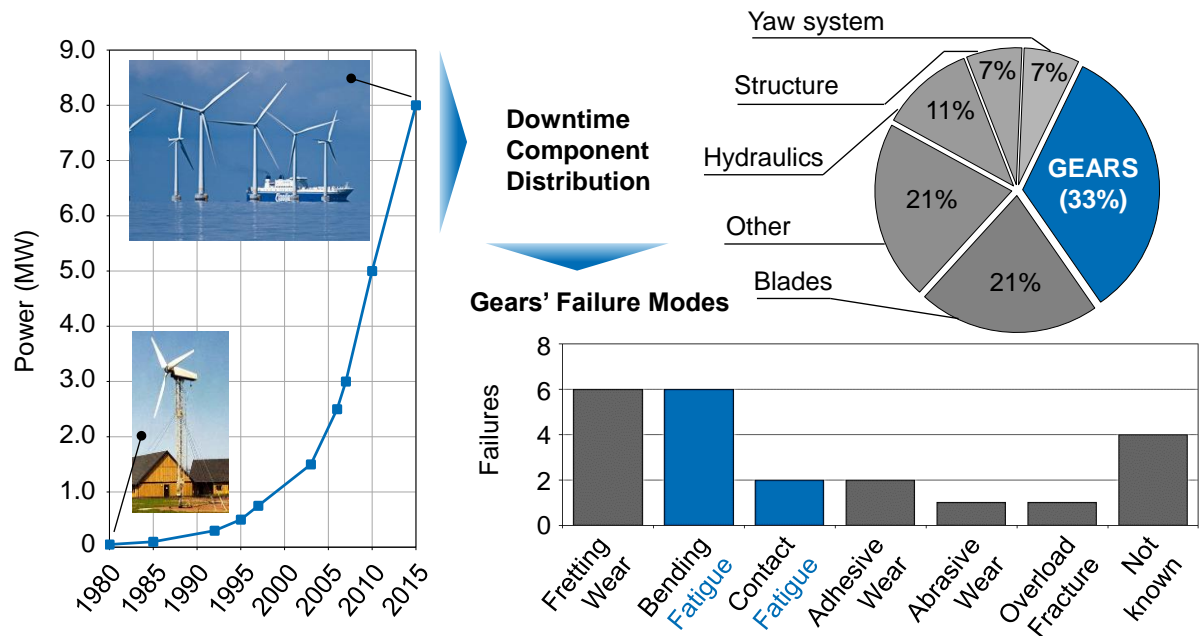


Figure 2.3 – Wind Power Scenario: Increasing power along the years; Gears appearing as an important player on the downtime metrics; and fatigue failure modes as one of the most frequent failure modes (RIBRANT, 2006; OYAGUE, 2009; WIKRENT, 2008; SHEND; MCDADE; ERRICHELO, 2011).

The matter is already considered a challenge. It is widespread, affects most original equipment manufacturers and is not majorly caused by the quality of the manufacturing practice. The published NREL (National Renewable Energy Laboratory, from the USA) technical report went further on the problem definition and mapped the most usual failure modes of a gearbox (Figure 2.3). Top gear failure modes are fretting wear and fatigue, being the last responsible for 36% of the gear failure modes registered. In contrast with the problems that gear manufacturers have faced with for the past 110 years of the automobile age, wind turbines operate with low speed and high torque (MUSIAL; BUTTERFIELD; MCNIFF, 2007; WIKRENT, 2008; OYAGUE, 2009; SHENG; MCDADE; ERRICHELO, 2011, LINK et al., 2011).

2.1.2 Fatigue Failures Modes

Gear failure modes are particular types of failure presenting specific identification. The fractured surface may or not may present an exclusive mode to fail, once crack can have been nucleated in one failure mode, propagated under a second mode and finally fracture due to a third mode. Representing more than 50% of total gear failure occurrences, bending fatigue, contact fatigue and adhesive wear are the most common types of gear failure modes (ALBAN, 2002). This statement reinforces how representative both exposed industrial scenarios are.

Any material submitted to a high amplitude vibration with stresses much lower than the ultimate strength is a candidate to fail by fatigue. A repeated load characterizes a cyclic stress state, in which material is locally hardened. Dislocations move and concentrate for this region, from which a crack nucleates and grows until it reaches the critical size for fracture. This concept is the principle for both main gear fatigue failure modes: bending and contact (ALBAN, 2002; ASHBY; SHERCLIFF; CEBON, 2007).

Tooth bending fatigue is considered the most classic gear failure mode. The failure origin is at the root radius surface of the loaded side. In the most common scenario, the origin is in the tooth width center, where the normal load is expected to be. The crack slowly propagates toward a point under the opposite root radius, finally proceeding outward to the surface of the non-loaded side (Figure 2.4). After the first tooth breaks out due to the fatigue mechanism, the next one will also normally fail by fatigue. But with an abnormal loading and improper gear mesh, fatigue will occur quicker (WULPI, 2000; ALBAN, 2002). For a better comprehension, the appendix “A.1 Gear Nomenclature for Macro and Micro-Geometry” provides a visual aid to the specific nomenclature of gears.

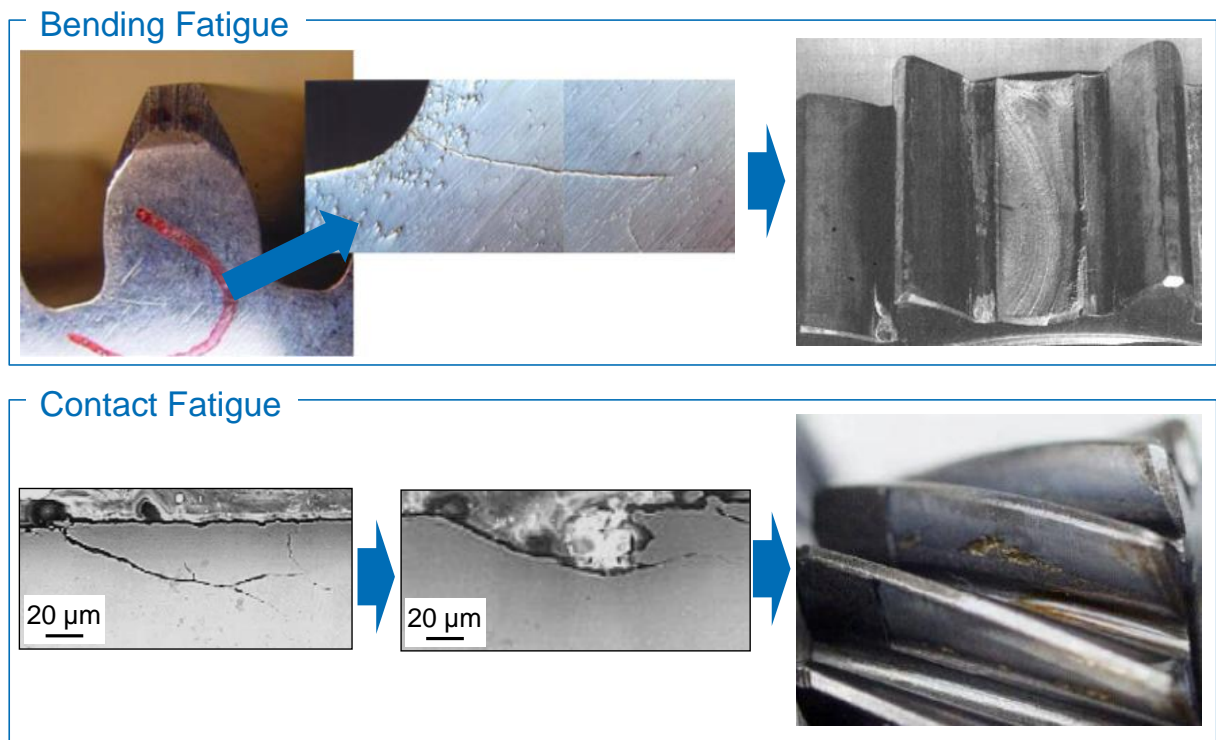


Figure 2.4 – Gear fatigue failure modes: bending and contact stresses (LECHNER; NAUNHEIMER, 1999; DING; RIEGER, 2003; BELSAK; FLASKER, 2006).

Contact fatigue failures are determined by the removal of small metal portions from the surface (Figure 2.4). For gears, they are identified as micropittings, pittings, microspallings or spallings, under a controversial terminology from the state-of-the-art. Therefore, the herein description will be simply separated as surface and subsurface-originated failures. A first approach to understand the difference between them appears over the dimensions of the fractured region. A surface-originated damage is shallower, usually not overcoming the depth of 10 μm . Subsurface failures can overcome a depth of 200 μm , with a proportional relationship to the contact pressure applied (ALBAN, 1993; ANTOINE; BESSON, 2002; DING; RIEGER, 2003; ASLANTAŞ; TASGERIREN, 2004; ABERŠEK; FLAŠKER, 2004).

A more detailed analysis shows that the difference between both goes beyond. The understanding of the gear kinematics (rolling and sliding characterization) and its stress behavior (rolling and sliding forces) enables the creation of a more detailed identification criterion. The cracks of surface-originated damages propagate to the core in a direction of between 20° and 40° with the surface. They are composed by a combination of rolling and sliding forces, thus inducing the damage occurrence on the dedendum. The failure is mostly

dependent on surface stress concentrators, such as scratches and uncontrolled roughness (WULPI, 2000; DING; RIEGER, 2003; FADJIGA; GLODEŽ; KRAMAR, 2007, OLVER et al., 2004; ZAFOŠNIK et al., 2007).

On the other hand, subsurface-originated damages cracks are mostly like to initiate in the region of maximum equivalent stresses due to the *Hertzian* pressure. The crack grows firstly parallel to the surface, driven by the shear propagation mode. It is followed by a direction change that moves the crack towards the surface under the opening propagation mode. The failure is favored by a smooth surface and the presence of non-metallic inclusions. The fractured region is concentrated around the pitch diameter or in the dedendum (DING; RIEGER, 2003; WULPI, 2000; FADJIGA; GLODEŽ; KRAMAR, 2007, OLVER et al., 2004; ZAFOŠNIK et al., 2007; SADEGHI et al., 2009; LÖPENHAUS, 2015).

Independent on the particular features, all mentioned fatigue failure modes follow the same fracture principle: the cracks initiate and propagate exclusively under a tensile stress state (ANDERSON, 2005). Over this statement lays the special connection to residual stresses, as well as it figures as a boundary condition to design and select a specific gear manufacturing chain. A descriptive approach of some manufacturing processes follows inside the next topic.

2.1.3 The Manufacturing Chain

A conventional gear manufacturing chain is composed by a sequence of processes starting from a forged blank up to the finished gear. Different process' alternatives are applied depending on the product specifications, application, resources availability or any other facility restriction. The processes composing this chain can be classified regarding their concepts and purposes in three groups:

- Teeth cutting: milling, shaping, hobbing, shaving, broaching, skiving;
- Heat treatment: carburizing, nitriding, carbonitriding; induction hardening
- Finishing: grinding, honing, shot peening, lapping, superfinishing.

Despite all the possible alternatives, the Figure 2.5 suitably represents a picture of the usual processes composing the gear manufacturing chain.

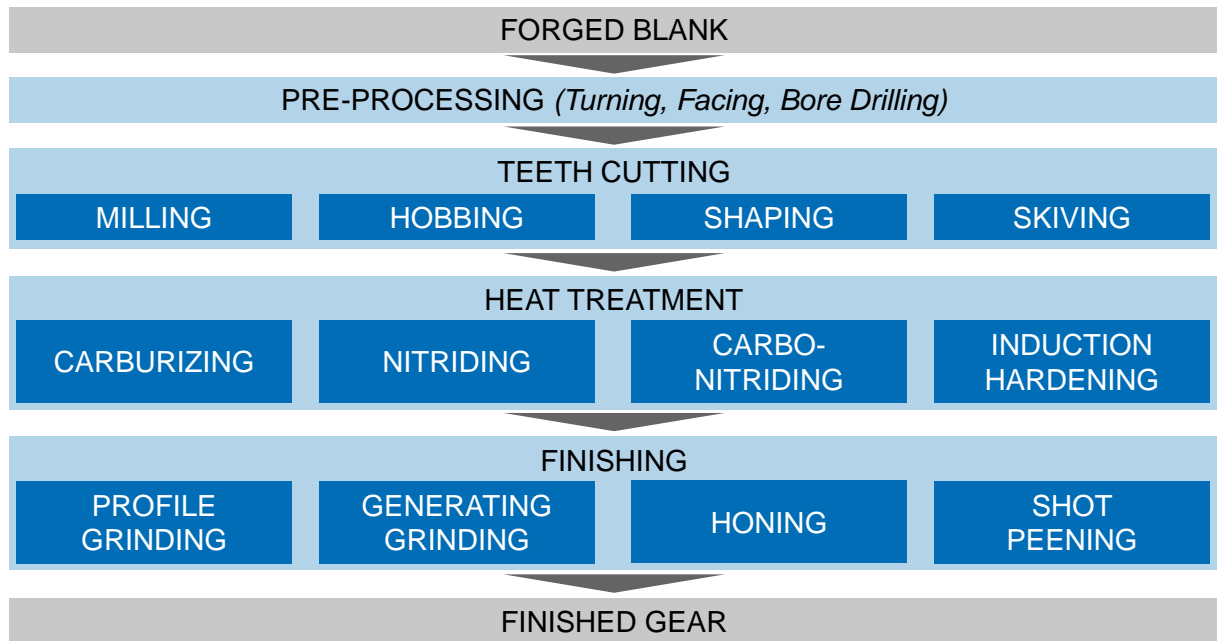


Figure 2.5 – Example of a gear manufacturing chain (KLOCKE; BRINKSMEIER; WEINERT, 2005; KLOCKE; BRECHER; BRUMM, 2014).

The milling is the former developed process to cut a tooth, but also a current topic by means of the researches applying it with 5-axis machining centers. A cutter with the shape of the tooth is positioned in the direction of the tooth helix angle, if it exists. The usual practice is to cut one tooth space at a time. After the gap is cut, the blank is rotated to the position of the next tooth. Gear milling is generally selected for small-lot production, gears demanding coarse finishing or with special tooth forms (DAVIS, 2005).

Most suitable to mass production gears, the hobbing is a generating process in which the gear involute is progressively generated by a series of cuts. The tool, named “hob”, is a fluted worm with form-relieved teeth. Three relative movements compose the kinematics of gear hobbing, as represented by the numbers in the Figure 2.6. They are the hob rotary movement (1), the axial feed of the hobber (2) and the gear rotation (3). For each revolution of the hobber, the gear advances one tooth (DAVIS, 2005; NIKOLAOS; ARISTOMENIS, 2012).

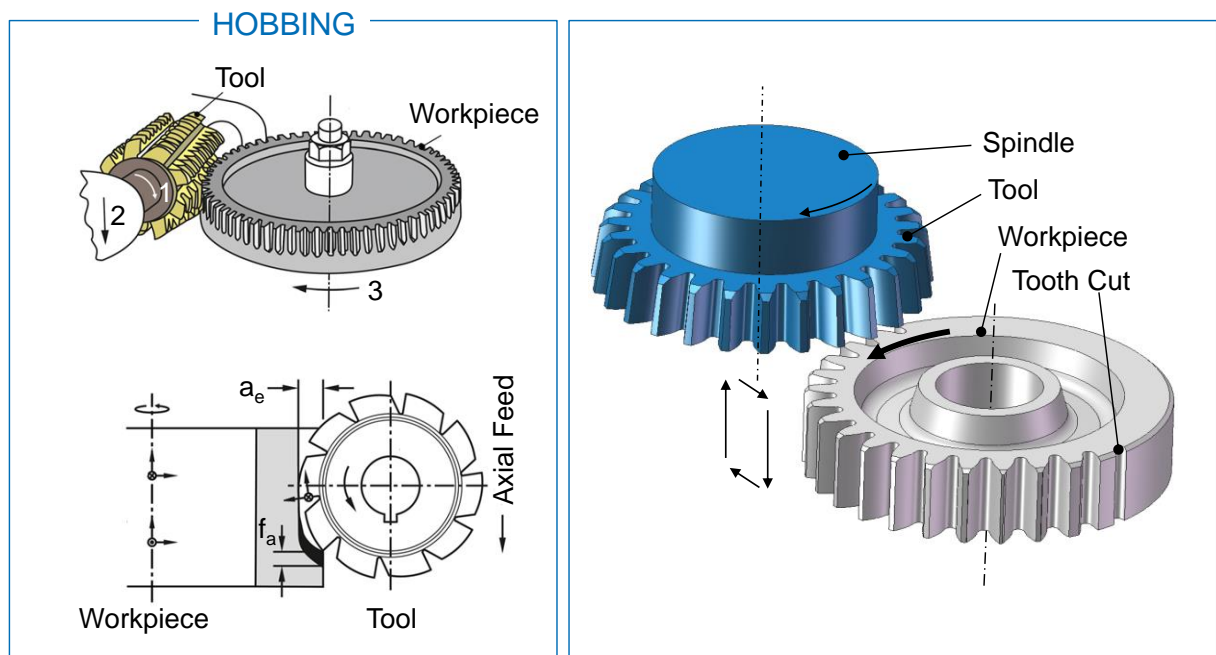


Figure 2.6 – Teeth cutting processes: gear hobbing and gear shaping principles (NIKOLAOS; ARISTOMENIS, 2012, KLOCKE; BRECHER; BRUMM, 2014).

Considered the most versatile gear cutting process, shaping is a generating process based on a spindle that moves in axial strokes as it rotates (Figure 2.6). The gear is mounted on a second spindle and the process principle is of two gears rolling in mesh. The tool is gradually fed to full cutting depth by reducing the center distance between the cutter and the gear. After the full depth is cut, a generating feed motion is engaged, finishing the cut in one revolution of the workpiece (ENDOY, 1990; DAVIS, 2005).

Even the teeth cutting may be conducted in two steps, a roughing and a finishing process. Gear hobbing and shaping are both roughing processes, and the geometric surface quality they produce may not be acceptable for every application. This rough surface cannot always be improved after the heat treatment. Shaving appears in this context as a finishing process of the soft machining, removing small amounts of metal from the teeth flank. For high precision applications, shaving cannot avoid hard finishing processes but it can correct small errors in tooth spacing, helix angle, tooth profile and concentricity. The process can be compared to two gears rotating in tight mesh, with cutter and gear at crossed axes. The tooth thickness is reduced by moving the center of the work gear closer to the cutter. The tool is basically a helical gear in which the helix angle is different from the gear to be cut. It is designed with vertical serration, which enables taking fine cuts from gear teeth (DAVIS, 2005; ENDOY, 1990).

Gears can be manufactured with as many different materials as the application's requirements allow. Among all, the steel alloys can provide outstanding characteristics of high strength per unit volume within low cost restrictions. However, the severe conditions in which gears of the heavy-machinery industry are applied demands improved mechanical properties. The heat treatment process is applied to create a material structure that increase wear resistance, fatigue life and impact resistance. These five most frequent processes are through hardening, induction hardening, carburizing, nitriding and carbonitriding (ENDOY, 1990; RAKHIT, 2000; FUNATANI, 2002, DAVIS, 2005).

The first above mentioned process refers to a method that does not produce a case. Through hardened gears are heated to a required temperature and cooled in the furnace or quenched in air, gas or liquid. This treatment is applicable to workpiece after or before cutting processes. In ascending order of hardness it can be performed by three methods: annealing, normalizing, and quenching and tempering (AGMA, 2004; DAVIS, 2005).

Localized heating is the treatment solution when gear teeth require high hardness, but size or configuration does not lend itself to carburizing and quenching the entire part. This is the concept of Induction Hardening. An encircling coil or tooth by tooth inductor is used and the process is ended with quenching and tempering. A rapid heating is generated by electromagnetic induction when a high-frequency current is passed through a coil surrounding a gear. The depth of the heated area is inversely proportional to the frequency, in function of the electrical phenomenon "skin effect". With regarding to the application condition, different methods can be performed, as shown on Figure 2.7 (AGMA, 2004; DAVIS, 2005).

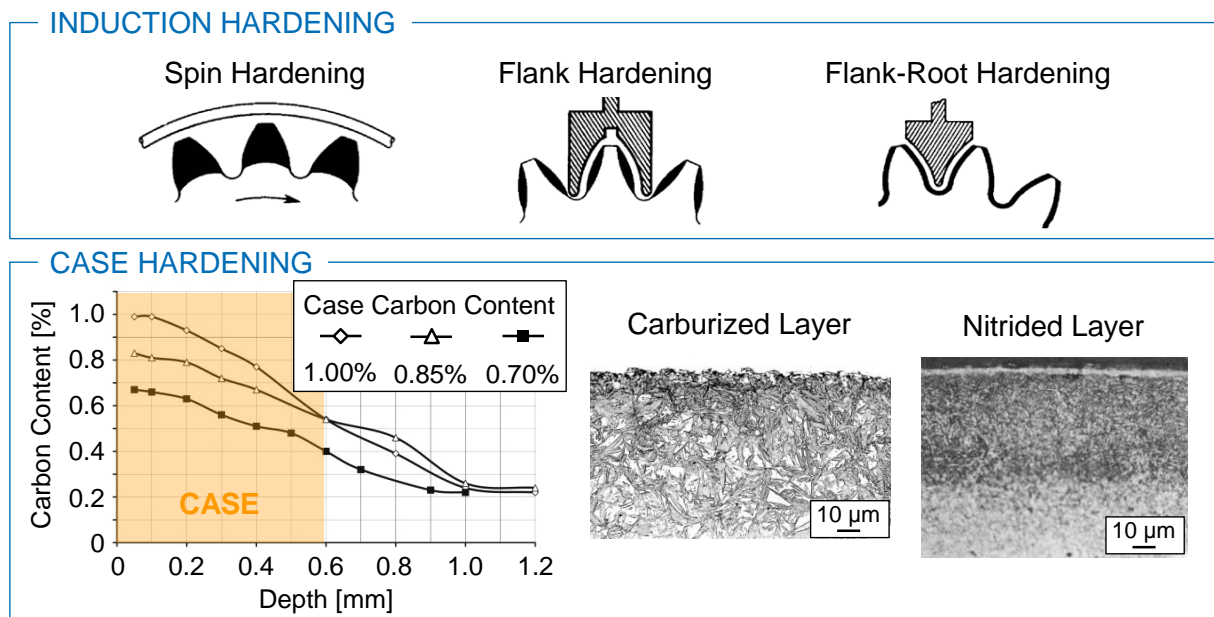


Figure 2.7 – Induction hardening methods; Case hardening features: carbon content profile, typical gas carburized and nitrided surface structures (AGMA, 2004, DAVIS, 2005; GROSCH, 2014).

The latest three heat treatment processes are chemically supported and with the objective of promoting surface enrichment. They are so called “case hardening” processes, and the carburizing is the most usual one. In carburizing, austenitized ferrous metal is brought into a contact with an environment rich of carbon. The difference between the environment and the steel carbon content creates a potential to cause absorption of carbon at the surface. By diffusion, it creates a carbon concentration gradient between the surface and interior of the metal (chart of Figure 2.7). The process can be adjusted in regard of temperature, time and the composition of the carburizing gas in order to induce the desired depth of penetration. The primary objective of carburizing and hardening gears is to secure a hard case and a relatively soft but tough core. This process is generally performed between 870°C and 1010°C. The case depth, defined on a hardness metric basis, can vary over a broad range, up to 8.25mm (RAKHIT, 2000; DAVIS, 2005).

The carbonitriding is a modified form of gas carburizing, rather than a form of nitriding. In the carbon atmosphere, ammonia is introduced in order to add nitrogen to the carburized case. The nitrogen diffuses into the steel simultaneously with carbon and it has an effect similar to carbon on the martensitic structure. The process is conducted with lower temperatures, between 700°C and 900°C. A shallower case, lower than 0.75 mm, can be

produced since nitrogen inhibits the diffusion of carbon. In addition, nitrogen enhances hardenability and enables further hardness increase (RAKHIT, 2000; DAVIS, 2005).

Differently from the other case hardening treatments, the nitriding introduces nitrogen into the surface while it is in the ferritic condition. This means that this process generally takes place in much lower temperatures, in the range of 500 to 575 °C. This concept makes nitriding the selected treatment when there are high concerns with the gear distortion effects. Shallow cases are resultant, being not deeper than 0.65 mm. One of its limitations is the extremely high and brittle surface hardness known as the “white layer”, caused by high thermal gradients on a very localized area (Figure 2.7) (RAKHIT, 2000; DAVIS, 2005).

The structure transformation, the hardness increase, and the change on the residual stress state are not the only outcomes of the heat treatment process. Together, as a non-desired effect, part of the temperature gradients created by the thermal cycles is converted into geometric deformation. Non-accepted distortion levels to the gear functions frequently require finishing manufacturing processes to adjust the flank and root profiles.

The objective of the finishing processes is to create teeth surface modifications that can provide running noise reduction and load capacity improvement. In practice, they are designed to reduce roughness and pitch errors, to promote microgeometry modifications as crowning and tip relief and also to induce a more compressive residual stress state (KARPUSCHEWSKI; KNOCHE; HIPKE, 2008).

As the most usual finishing process, grinding shapes the surface by sequential passes with a rotating abrasive wheel. The tool is a wheel typically built with abrasive materials like corundum (Al_2O_3) or cBN (Cubic Boron Nitride). Usually, it removes from a few micrometers up to several hundredths of millimeters of metal. The gear grinding processes can be classified as generating grinding and profile/form grinding. (DAVIS, 2005; KARPUSCHEWSKI; KNOCHE; HIPKE, 2008).

The form or profile grinding process consists of applying the wheel through a tooth space designed with the shape of the left side of one tooth and the right side of the next tooth (Figure 2.8, left). The workpiece is perpendicularly positioned to the grinding wheel. When the process of this gap is completed, the workpiece is indexed to the next position. The wheel can be projected for grinding one gap as well as multiple gaps at one time (DAVIS, 2005).

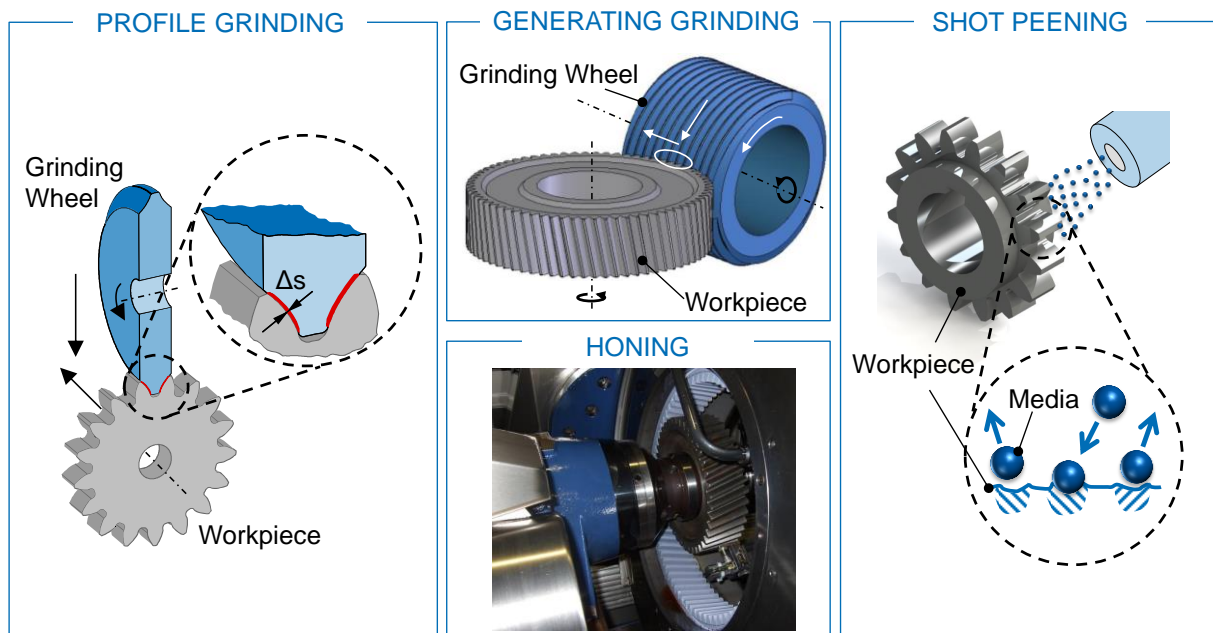


Figure 2.8 – Schemes and pictures of gear finishing processes (HARADA, MORI, MAKI, 2003; KLOCKE; BRINKSMEIER; WEINERT, 2005; KARPUSCHEWSKI; KNOCHE; HIPKE, 2008; BRECHER; LÖPENHAUS; REGO, 2015).

The generating grinding is defined by the movement of the cutting grain in a direction tangent to the involute profile. There are four methods of generating grinding, distinguished by the type of wheel used: straight, cup-shaped, dish-shaped, and rack-tooth worm wheels. The continuous generating method (Figure 2.8, top) has the similar principle of a gear hobbing, and a grinding worm with an undefined cutting edge is used. Stroke movement, feed movement and shift movement are necessary as well (DAVIS, 2005; KLOCKE; BRINKSMEIER; WEINERT, 2005; KARPUSCHEWSKI; KNOCHE; HIPKE, 2008).

Gear Honing is an abrading process that uses bonded abrasive stone tool to remove stock from metallic and nonmetallic surfaces. The difference between honing and grinding processes are basically the tool and the kinematics. The tool is a gear shaped body that removes material from the tooth flanks under crossing rotational axes (Figure 2.8, bottom). Due to these low cutting speeds, high process forces per time unit are necessary to reach a high material removal. The result is lower temperatures at the contact zone and lowered risks of a thermal damage (DAVIS, 2005; KARPUSCHEWSKI; KNOCHE; HIPKE, 2008).

With a different main purpose from the described finishing processes, the goal of shot peening is to induce a compressive residual stress layer in the material to increase the fatigue life. The compressive layer is induced by plastic deformation, which is the result of the mechanical impact of small round hard particles, or simply “media”. The peening media is

accelerated to a high speed with a kinetic energy that is raised by machine propulsion (Figure 2.8, right). The shot peening machine can be classified depending on the system that propels the media. These are pneumatic, centrifugal and vapor blast machines. The resulting residual stress profile is deeply influenced by the processing and machine parameters. Among them, it is included the shot speed and incident angle, the exposure time, the coverage level and the shape, hardness and size of the media (ALMEN; BLACK, 1963; KOSTILNIK, 1994; SAE, 2001).

Each one of the described processes interacts through particular physical phenomena with the gear surface, inducing specific residual stress states into it. As a consequence, the definition of the manufacturing chain directly impact the running behavior of the gear. This functional influence and the manufacturing origins of the residual stresses, such as their classifications and the basic principle of equilibrium are covered along the next topic.

2.2 Residual Stresses

Residual stresses are defined as stresses that are kept applied even when the material is no more submitted to external forces. The first clear definition of this phenomenon was provided by Prof Heyn in his 1914 lecture for the Institute of Metals in London. At that time, residual stresses were still referred to “internal strains”:

The phenomena with which I am about to deal come under the heading of “internal strains”. If portions of a solid or of a number of solids forming together one rigid mass are hindered from assuming the natural length, which they would assume in the absence of any load or hindrance, this solid or number of solids is said to be under strain. The strained condition may be brought about (1) by forces acting on the solid from outside (external forces); but strains may also exist in the solid (2) without any observable action from outside, or after the external action has ceased. These latter strains I define as “internal strains”; the solid is, so to say, “self-strained”. (HEYN, 1914, p. 3).

Residual stresses are originated from heterogeneous dimensional variations resultant of also non-homogeneous deformation. The stress state of a component submitted to external forces is defined by the combination of residual and actuating stresses. With this concept, the residual stress creates direct impacts to several mechanical properties, as the fatigue strength (ALMEN; BLACK, 1963; WITHERS; BHADHESIA, 2001; LU, 2002).

2.2.1 Relationship with the Fatigue Strength

The stress state of a component submitted to external forces is defined by the combination of residual and applied stresses. As an initial and rough comprehension model to the crack nucleation and propagation, the residual stress can be considered as a static and mean value to be summed to the actuating cyclic stress. Therefore, the more compressive the residual stresses are, the lower is the resultant stress state. The residual stress ends by playing a key function in order to increase a component's lifetime (WITHERS; BADHESIA, 2001; LU, 2002; MURAKAMI, 2002; LÖHE; LANG; VÖHRINGER, 2002).

This so-called superposing principle is the basis for different approaches to quantify the influence of residual stresses on the fatigue lifetime. One of them is the adaptation of the Haigh diagram to introduce the residual stress intensity. By considering the effects of mean stress in the fatigue life, also the residual stresses are treated as local and mean effect (LÖHE; LANG; VÖHRINGER, 2002; PREVÉY; JAYARAMAN, 2005). As a second example, Genel (2005) proposed a method based on the *Basquin* relation to estimate the bending fatigue limit smooth case hardened cylindrical specimens subjected to bending fatigue loads. The model considers that the residual stress profile finds maximum value in the surface with a linear behavior up to core, being quantitatively represented by Equation (2.1). With using the a relationship between case depth and fatigue limit, a simple analytical method for estimation of bending fatigue limit on the bases of the effective case depth, core hardness and the residual stress was proposed.

$$\sigma_a = \left(\frac{d}{d - 2t_c} \right) \left(4.25 HB + 225 - \frac{2dt}{(d - 2t)^2} \sigma_{RS,surf} \right) (2N_f)^b \quad (2.1)$$

Where:

σ_a : Fatigue stress amplitude

d: Component diameter

t_c : Case depth

HB – *Brinell* hardness

$\sigma_{RS,surf}$ - Surface residual stress

b: Fatigue strength exponent, from S-n curve

N_f : Number of cycles to failure

The residual stress' influence on the fatigue behavior is extended to the analysis of the entire stress profile. The most important profile characteristics are the stress peak, by means of its intensity and depth, and the depth where the stresses alter from compression to tension, or vice-versa. As an overall role, the fatigue limit is improved by increasing the peak intensity and the total compressive depth. However, the depth profile relationship with the fatigue behavior is dependent on the failure mode. It is over the depth of the residual stress peak where the crack has the lowest propagation rate, as shown in the Figure 2.9(a). In the same study from Mitsubayashi, Miyata and Aihara (1994), it was demonstrated the sensitivity of the tooth contact fatigue performance to different features of the residual stress profile, Figure 2.9(b). The largest distance between the *Wöhler* curves, identified in the top chart of the panel's right side, shows that the highest influence from the residual stress to the analyzed failure mode was characterized by the peak intensity.

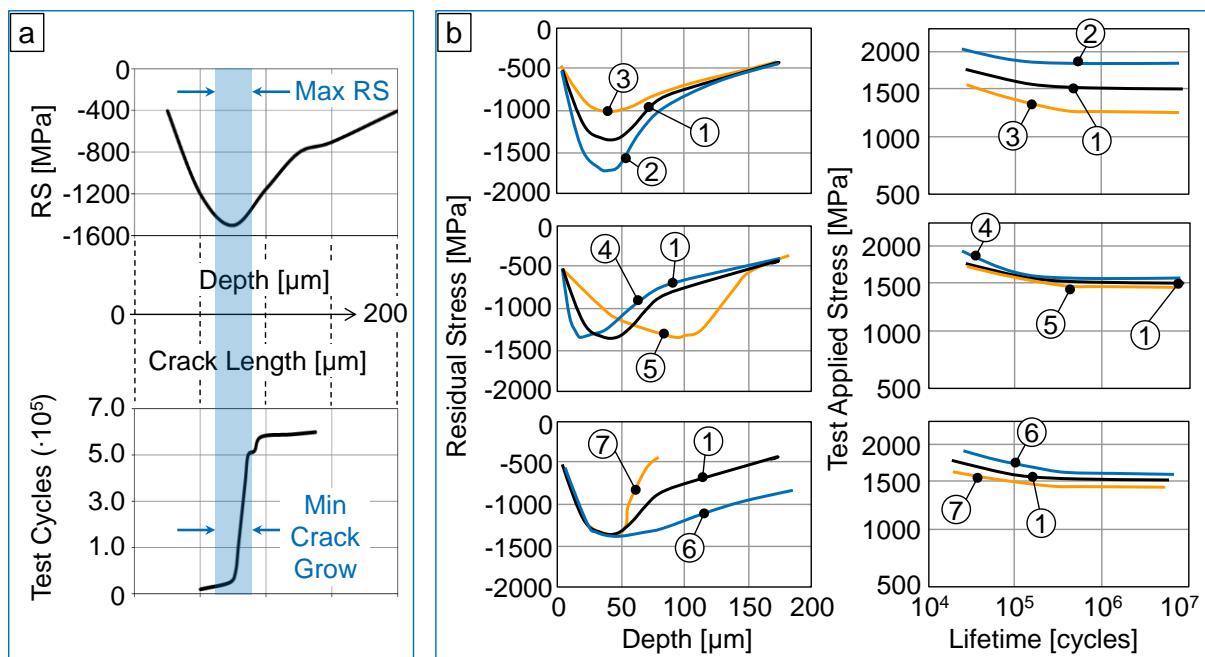


Figure 2.9 – Relationship between the crack propagation, the residual stress profile and the fatigue performance (MITSUBAYASHI; MIYATA; AIHARA, 1994).

This concept highlights the importance of a detailed understanding on the failure mode to be approached. It means that the damage morphology may also be changed by the introduction of different depth profiles of residual stresses. This concept can be clearer demonstrated with the comparative studies from Batista et al. (2000) and Lv, Lei and Sun (2015). Both conducted gear flank investigations on parts with and without the submission to

the shot peening process. The unpeened surfaces showed larger and deeper damages, combining the pitting and the spalling mechanisms (Figure 2.10, left). On the other hand, the introduction of the peening is followed by the appearance of shallower damages (Figure 2.10, right). The layers right underneath the surface showed to be more resistant to the crack initiation and propagation. This is a direct result of the shot peening profile, which has as typical effect on the introduction of maximal compressive residual stress values into the subsurface (KRITZLER; WÜBBENHORST, 2002):

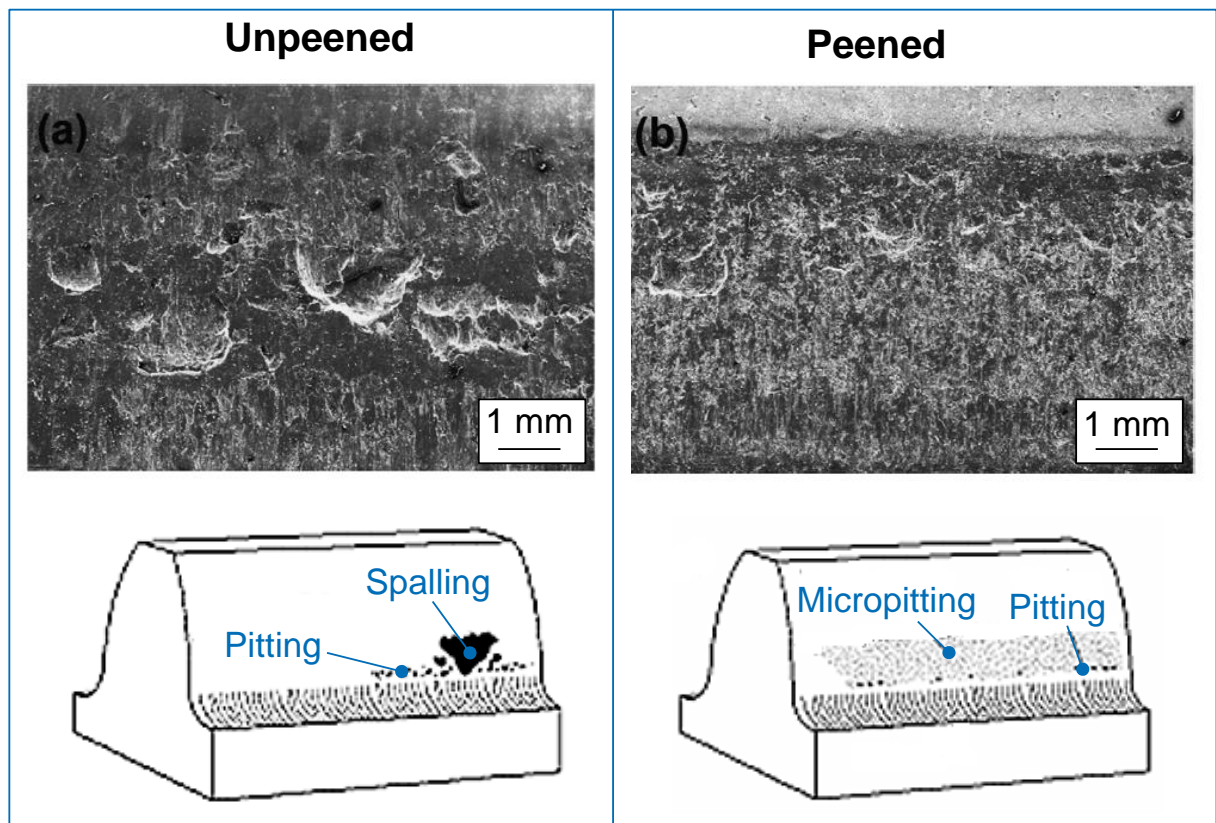


Figure 2.10 – Effect of the residual stress profile on the damage morphology (BATISTA et al., 2000; LV; LEI; SUN, 2015).

The peened gears behavior delivers a glance at how the residual stress state of different manufacturing processes can influence on the fatigue strength of a gear. Based on the distinct origins of residual stresses to be discussed now, it will be possible to observe the described gear manufacturing processes under the perspective of the variability of phenomena taking place along this chain.

2.2.2 Origins

The induction of residual stresses is classified as mechanical, thermal and structural phenomena. The phenomenon that occurs is directly linked to the manufacturing process, and more than one can take place simultaneously. The most usual manufacturing processes and their related phenomena are shown on Table 2.1 (LU, 2002). These three basic phenomena are strongly interrelated (Figure 2.11) and are approached along this topic.

Table 2.1 – Manufacturing processes and the corresponding residual stress phenomena (LU, 2002).

PROCESS	Phenomenon		
	Mechanical	Thermal	Structural
Casting	-	Temperature gradient during cooling	Phase transformation
Forging, Shot Peening, Extruding, Cold Rolling	Heterogeneous plastic deformation between core and surface	-	Dependant on material
Turning, Milling, Grinding, Drilling	Plastic deformation during chip removal	Temperature gradient from machining heating	Phase transformation, depending on process maximum temperature
Quenching	-	Temperature gradient	Volume change due to phase transformation
Carburizing, Nitriding	-	Thermal incompatibility	New chemical composition and volume change
Welding	Contraction	Temperature gradient	Structural modification

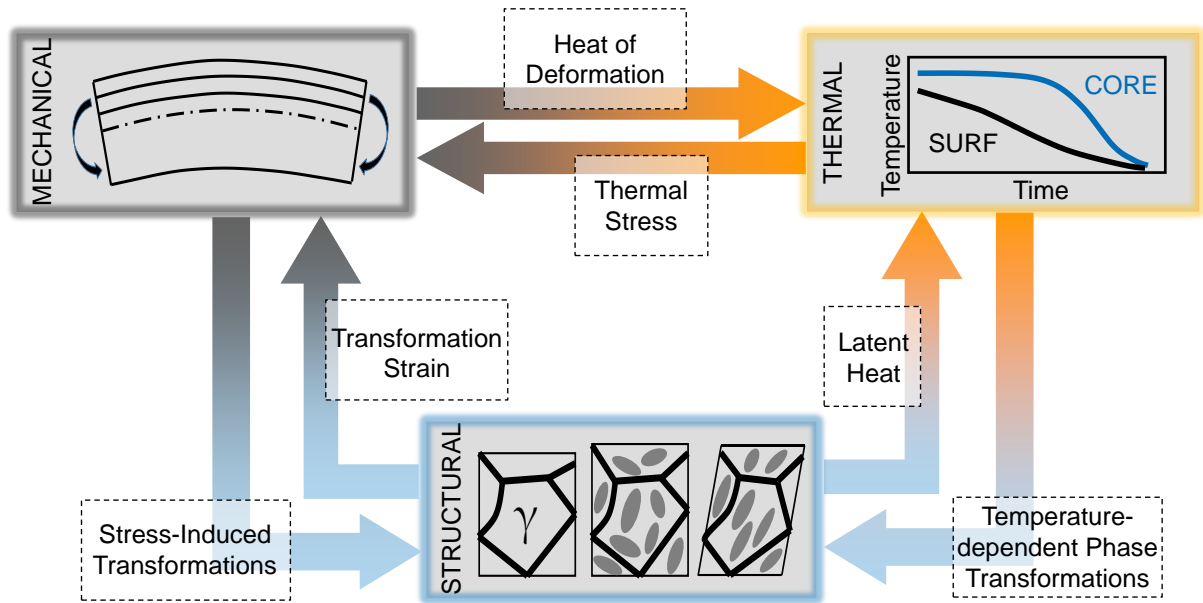


Figure 2.11 – Relationship between phenomena of the residual stress origins (INOUE, 2014).

The basic condition for the existence of residual stresses from mechanical origin is that part of the material undergoes plastic regime. When a metal is being plastically deformed, different strain levels are experienced in different locations at the same time. The generated deformation incompatibility induces internal stresses that, after the external load removal, are converted in residual stresses. This deformation heterogeneity can be resultant from distinct but coexistent material phases with strength difference. Additionally, different actual strains may not be equally accommodated in along a component volume due to its geometry (WANG; GONG, 2002).

The analysis of the plastic bending of a sheet-metal enables a clearer understanding of the residual stress generation from inhomogeneous plastic straining. In the example shown in the Figure 2.12(a), a bent sheet is supposed to be composed by several longitudinal layers. While external forces are applied, the stress reaches a maximum tensile state at upper surface. The bottom surface is represented by the maximum compressive layer, and between both, a neutral layer is located, without stresses. By achieving the plastic condition, these layers extend or compress proportionally to the stress intensity that exceeded yield limit. Naturally, this excess finds maximum values at the extreme layers. The Figure 2.12(b) represents the actuating stresses of each numbered layer in the solid line passing from the points 0 to 5.

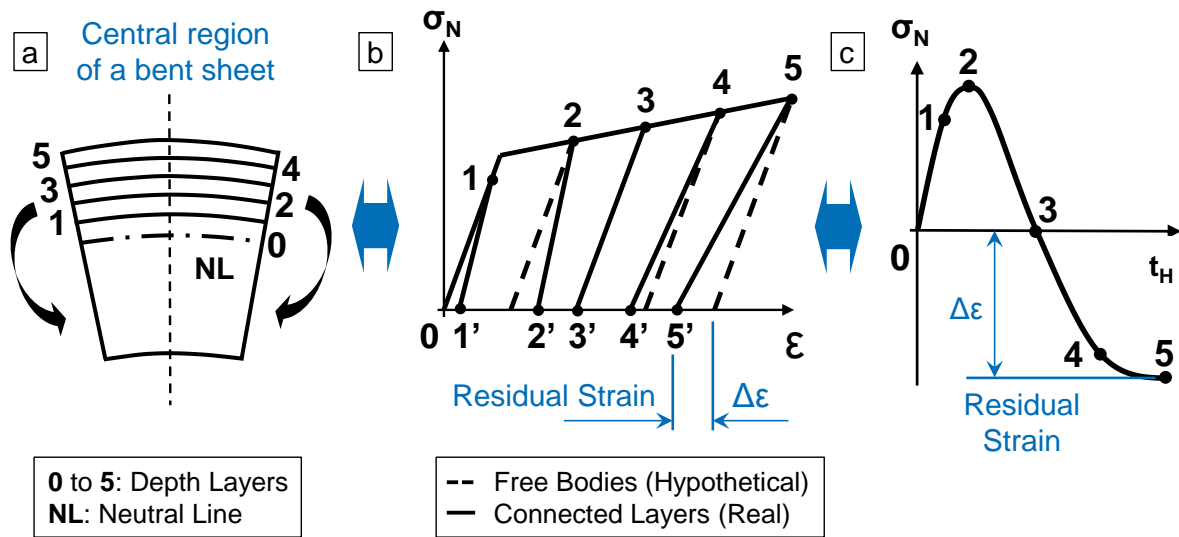


Figure 2.12 – Explanation model to describe the mechanically originated residual stresses (WANG; GONG, 2002).

With the release of the external mechanical load, the beam would spring back toward its original profile. This unloading, supposing no existing connections between layers would be represented in dashed lines in Figure 2.12(b). However, the layers interaction generates a residual stress state which guides the layers to different positions. In the comparison between the layers 4 and 5, the last one is submitted to higher actuating deformations. The layer 4 has thus lower displacement and, during unloading, it resists to the plastic extension of the layer 5. This last layer develops a compressive residual stress state, quantitatively proportional to $\Delta\epsilon$. The residual stress analysis of the layer 4 is now dependent on both the layers 3 and 5. While the layer 5 is promoting extension, the layer 3 is acting in resistance to the extension. The result for the layer 4 is still a compressive residual stress, but less intense than the stress of the layer 5. Considering the basic residual stress condition of equilibrium, at a certain layer, the promotion and resistance to extension become balanced. The result is a reversal point, with zero stresses, as shown by the layer 3 in Figure 2.12(c). From this point on, layers as represented by 1 and 2 are potentially submitted to tensile residual stress states (WANG; GONG, 2002).

The temperature gradient existing on a body submitted to heat exchange is the most common example in which the thermal load originates residual stresses. More specifically considering the cooling down of a material, its conductivity property plays an important role on differentiating the cooling curves of its surface and core. The temperature decrease of the bulky cylinder of Figure 2.13 can illustrate this phenomenon.

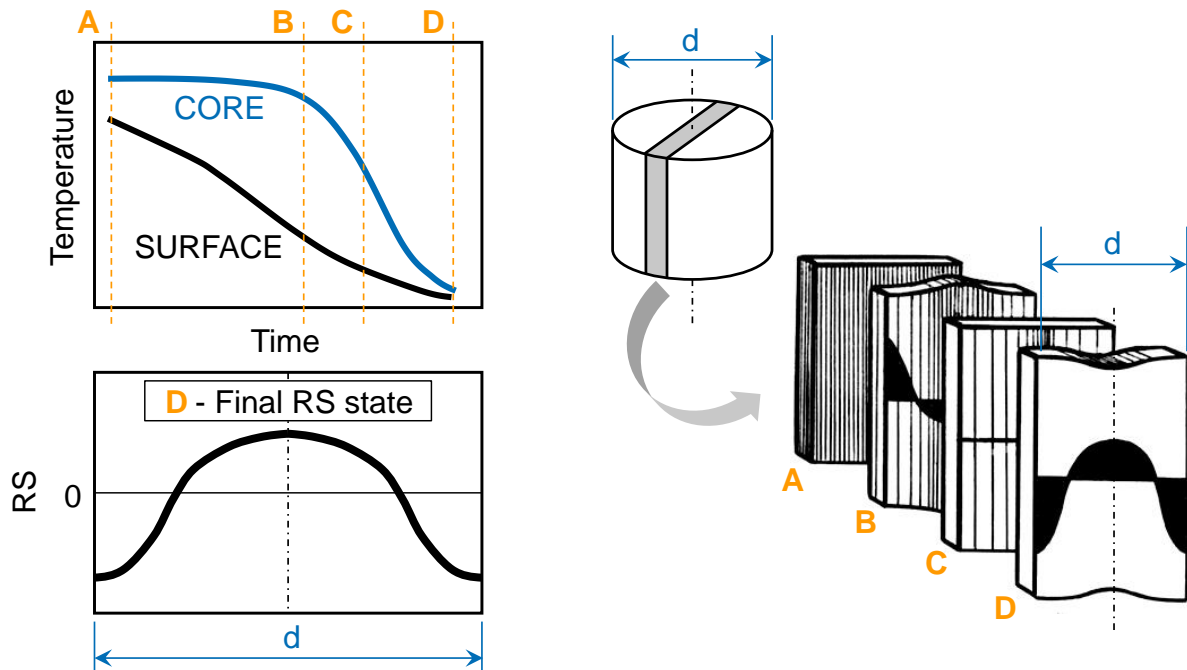


Figure 2.13 – Thermal load originated residual stresses (EBERT, 1978).

The example of Figure 2.13 is considering the temperature evolution of a center thin layer of the cylinder. From the initial time “A” up to the cooling end “D”, both the center and the core temperature reduction curves are analyzed in the upper left corner. The residual stress state of this layer at each time is represented and labeled in the lower right side of the picture.

In the first moment, the surface’s cooling rate is much larger than that of the center. With a higher temperature and a relatively larger area, the center portion does not permit the surface to contract as much as it would as a free body. The result is a surface tensile residual stress state, as shown on the layer B. Considering the equilibrium condition, the cylinder’s center is under compression (EBERT, 1978).

With the time evolution, the warmer core cools down and undergoes its normal contraction. From a certain point, the rate relationship inverts and the cooling is quicker in the core. Now the outer shell acts as a restraint to allow the center to contract. The core becomes longer than it should be if it were a free body, and, consequently, it is submitted to a tensile stress state. Reactively, the outer shell is under compression, as depicted by the layer “D”. Therefore, a body submitted to cooling down, without phase transformation, presents a compressive residual stress state at the surface (EBERT, 1978).

Depending on the manufacturing process and on its parameters, the heat exchanged with the workpiece can increase its temperature to a level that promotes structural changes.

The resultant material phase transformation mostly represents a radical modification over the residual stress profile. The residual stresses induced in phase transformations are resultant from the differences of physical properties between each phase. The temperature variation is the activation for the transformation, which can promote reconstructive and displacive shape changes, as illustrated by Figure 2.14(a) (BHADESHIA, 2002; NARAZAKI, 2002; SHAH, 2011).

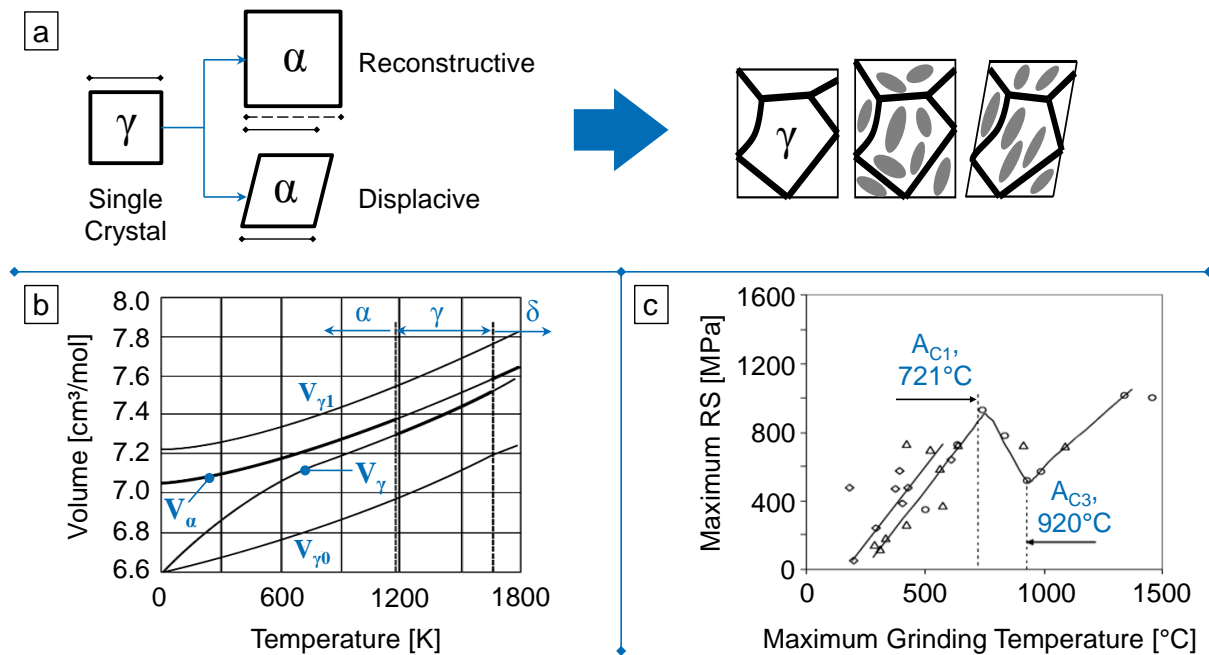


Figure 2.14 – Structural residual stresses: (a) phase transformation mechanisms; (b) iron phases' volume variation with the temperature; (c) residual stress profile variation along the grinding temperature (BHADESHIA, 2002; MALKIN; GUO, 2007).

A reconstructive transformation is defined by a structural change achieved by a flow of matter, without meaningful strains. It is considered that it involves only a volume change together with diffusional mass flow. For each phase, this structure's volume increases proportionally to the material temperature, as shown on the iron phases' chart of volume by temperature, Figure 2.14(b). The occurrence of a phase transformation represents a sudden change on the lattice parameters and thus on the physical properties as density. In order to accommodate the shape changes resultant from volume variation, residual stresses are developed. This is particularly shown on the research of Malkin and Guo (2007), in which the grinding process is evaluated up to very high temperatures. In the chart of Figure 2.14(c), the residual stress profile along temperature presents a high variation between 721°C and 920°C.

These are exactly the temperature values of the ferrite to austenite transformation (BHADESHIA, 2002).

Although all the transformations cause modifications in shape, not all of them are consisted only of volume change. As also displayed on Figure 2.14(a), some transformations convert the physical changes also in deformation of the parent structure, and they are called displacive transformations. This shape change is a combination of shear on the invariant plane and a dilatation normal to that plane. Classified as invariant-plane strain (IPS), it promotes the formation of thin-plate shape phases, minimizing its strain energy. Displacive transformations are characteristic of bainitic and martensitic phases, which grows in the form of plates. In such displacive transformations, the resulting shear strain can be as larger as ten or twenty times the dilatational strain, originated by the volume change (BHADESHIA, 2002).

The three phenomena were so far described in an individual and separated scenario. In manufacturing processes such as machining or grinding, the mechanical and the thermal loads occur simultaneously. This coupling, named as thermo-mechanical model, can completely modify the residual stress state on the manufactured component, and must be explored. As example, the study from Shah (2011) shows the simulation of grinding process and its residual stress profiles from purely thermal, purely mechanical and thermo-mechanical loads, Figure 2.15(a).

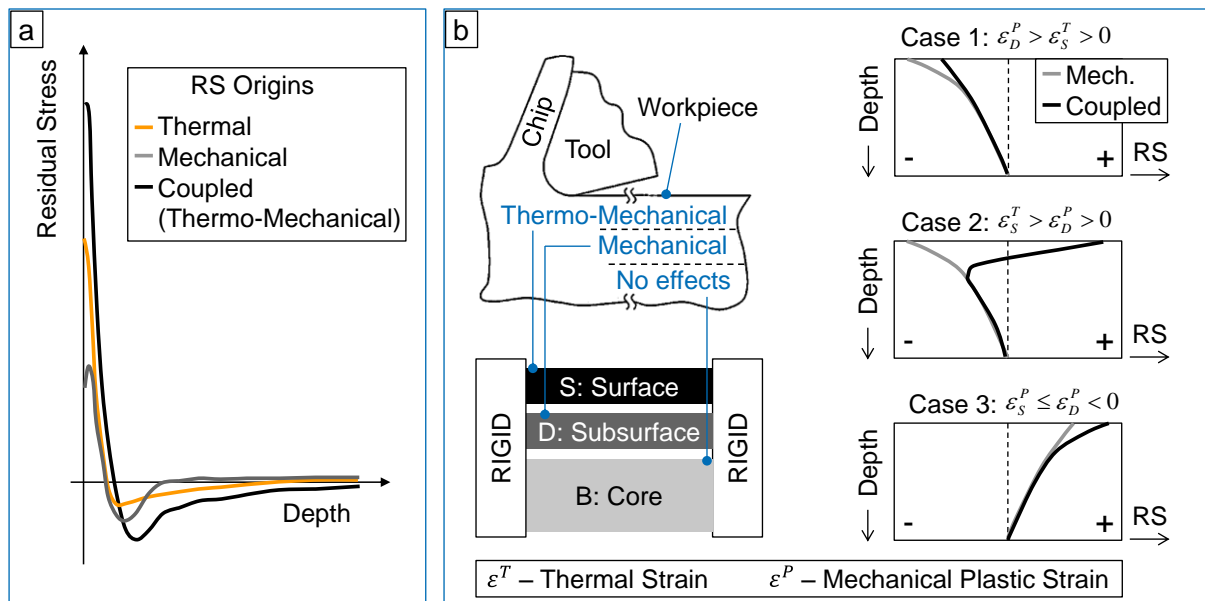


Figure 2.15 – (a) Coupling effect for the residual stress profile of grinding; (b) Coupling conceptual model for machining (JACOBUS; DEVOR; KAPOOR, 2000; SHAH, 2011).

The thermo-mechanical phenomena can be understood by the model of Figure 2.15(b), proposed by Jacobus, Devor and Kapoor (2000). The analysis of the authors is applied to the machining process but the model fits to any process simultaneously submitted to mechanical and thermal loads, when the surface and the near surface regions do not highly differ on thickness. For this rationale, the workpiece is divided in three distinct layers: “S”, “D” and “B”. The first layer “S” considers the surface and near surface region, in which both loads present meaningful intensities. In a deeper position of the workpiece, the layer “D” represents the subsurface region, where residual stresses are purely of a mechanical origin. The model assumes that the thickness of layers “S” and “D” are equivalent. Finally, the substrate is represented by layer “B”, where the residual stress intensity can be considered negligible. It is important to remark that the model considers rigid supports fixed to the ends of all layers. With a rigid support and other constraining translation, the deformation compatibility is assured and the elastic constraint is imposed on each layer by the neighboring layers.

Considering the assumptions above, the concepts of deformation compatibility, the constitutive relationships and the residual stress equilibrium are used to discuss the occurrence of three different cases. By assuming that the thermal strain is always positive ($\varepsilon_s^T > 0$) and that the absolute value of plastic strain at the surface is never lower than at the one at the subsurface ($|\varepsilon_s^P| \geq |\varepsilon_D^P|$), three nontrivial cases inducing residual stresses are explored by Jacobus, Devor and Kapoor (2000):

1. Thermal strain at the surface is lower than the mechanical plastic strain at the subsurface, and both are of positive magnitude ($\varepsilon_D^P > \varepsilon_s^T > 0$).
2. With rising temperature, thermal strain overcomes the mechanical plastic strain at the subsurface ($\varepsilon_s^T > \varepsilon_D^P > 0$).
3. The plastic strain at the subsurface is negative ($\varepsilon_s^P \leq \varepsilon_D^P < 0$).

The most important observation coming from Figure 2.15(b) is that a simple change in the balance between the different loads can definitely alter the residual stress state. This perspective can be converted in a more sensitive situation, when also structural originated residual stresses are included. Depending on the manufacturing process and on its parameters, the heat exchanged with the workpiece can increase its temperature to a level that promotes structural changes. The resultant material phase transformation mostly represents a radical modification over the residual stress profile (SHAH, 2011). This full combination of phenomena is defined by Inoue (2014) as a “Metallo-Thermo-Mechanical” coupling.

The discussed residual stress origins can now be compared to the gear manufacturing processes previously introduced. This combination is observed on a gear manufacturing chain example, depicted in the Figure 2.16. This figure shows the different phenomena occurring along each one of the process of the chain. Most part of the processes presents coupled effects, which highlights the sensitivity of the residual stress state to the evolutionary character.

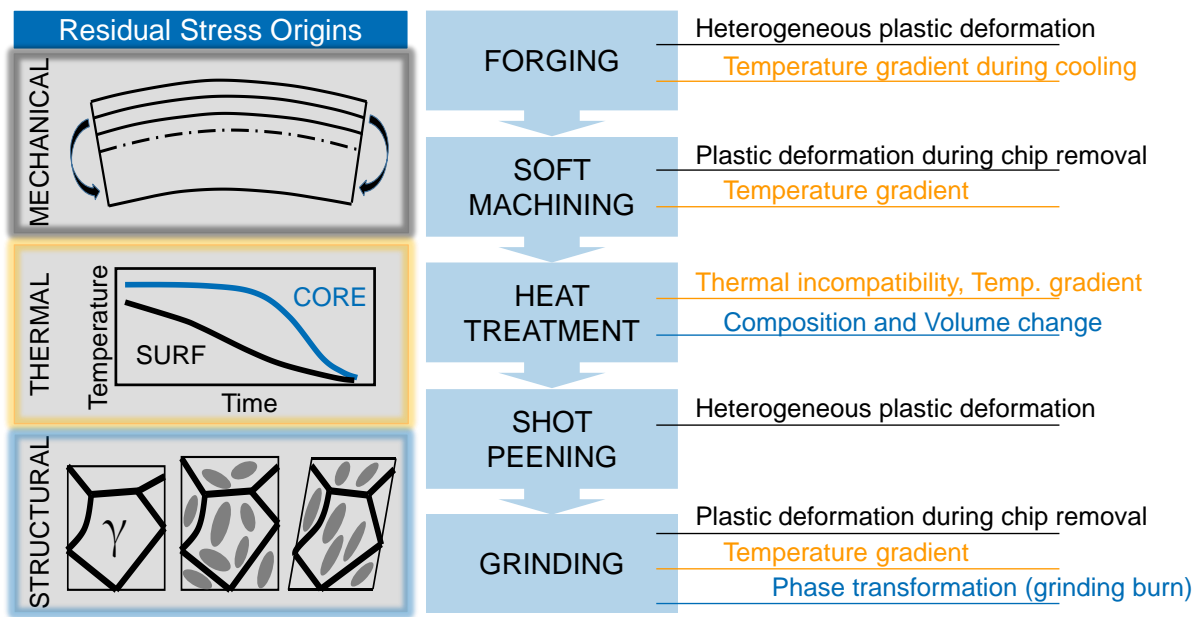


Figure 2.16 – Example of a gear manufacturing chain with the respective residual stress phenomena to each individual process.

2.2.3 Classification

The residual stress state is classified from macro to microstresses in three levels, depending on the domain size of analysis. The definition was formerly proposed by Macherauch, Wohlfahrt and Wolfstiegl (1973), being later complemented by Hauk and Nikolin (1988) and Behnken (1997). The residual stress of type I is known as macro residual stress. It is defined as the average value for the residual stresses which are position-dependent. The average is determined by a volume with several grains, even from different material phases. This volume is usually represented by the amount of material within the measurement limits, as shown with the Equation (2.2). Therefore, the measurement setup must be defined in such a way to represent a macroscopic behavior of the investigated surface.

$$\sigma^I = \frac{1}{V} \int_V \sigma(x) dV \quad (2.2)$$

Where:

σ^I : Macro RS (Type I)

V: Material volume analyzed

This definition still includes crystallites of different material phases. Therefore, even the macrostresses are broken down into type I residual stresses for each one of the phases. The overall macrostresses are thus composed by the macrostress in each of the phases, weighted by the volume fraction of the respective phases. The definition is stated by Equation (2.3) and illustrated in the Figure 2.17(a) (HAUK; NIKOLIN, 1988; SPIEB et al., 2009).

$$\sigma^I = \sum_{phase=1}^n c^{phase} * \sigma^{phase} \quad (2.3)$$

Where:

c: Volume fraction

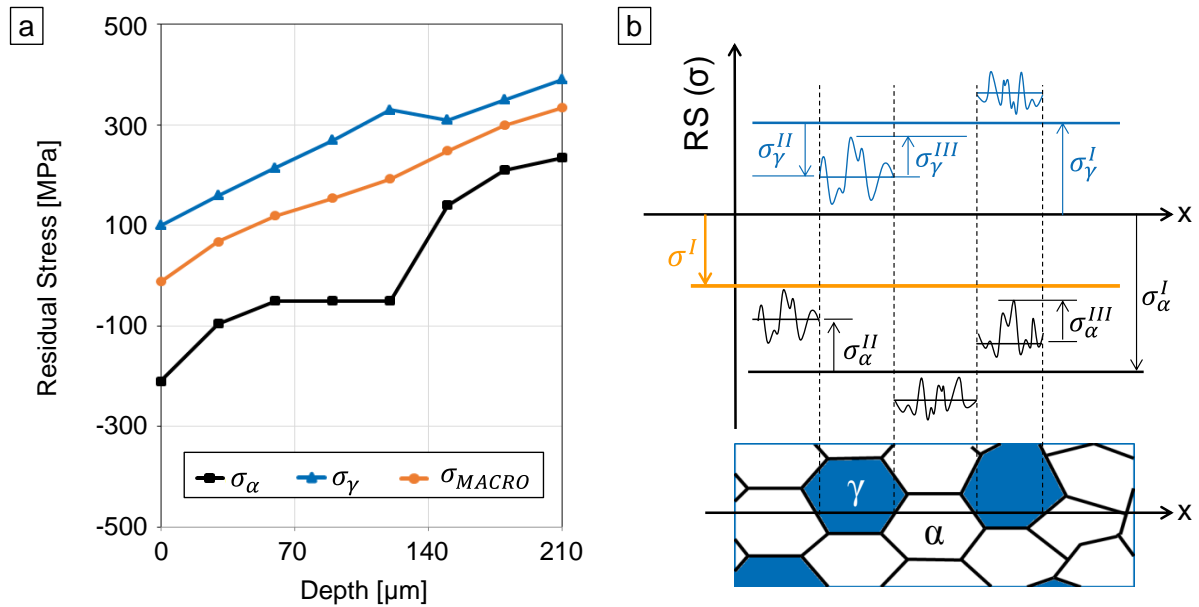


Figure 2.17 – (a) Macro RS composed by the contribution of each phase; (b) Scheme of all levels of residual stresses (HAUK; NIKOLIN, 1988; WITHERS; BHADESHIA; 2001; SPIEB et al., 2009).

From the macro level, the subsequent stress types II and III are defined as micro residual stresses. The residual stress of type II are assessed in between the grains and as an average of the stresses inside the grains. This local volume is used into the same concept from the Equation (2.2) to establish the value of type II stresses, Equation (2.4) (HAUK; NIKOLIN, 1988; WITHERS; BHADSHIA; 2001; SPIEB et al.; 2009).

$$\sigma^{II} = \frac{1}{V_{LOCAL}} \int (\sigma(x) - \sigma^I) dV \quad (2.4)$$

Where:

σ^{II} : Intergranular level micro RS (Type II)

Finally, the referred stresses inside the grains are the type III micro residual stresses. In a domain size of the atomic level, they are influenced by the coherency at interfaces and dislocation stress fields. The corresponding mathematical description, Equation (2.5), is simply defined as the complementary value of the other stress' types described (HAUK; NIKOLIN, 1988; WITHERS; BHADSHIA; 2001; SPIEB et al.; 2009).

$$\sigma^{III} = \sigma(x) - \sigma^I - \sigma^{II} \quad (2.5)$$

Where:

σ^{III} : Atomic level micro RS (Type III)

2.2.4 The Equilibrium Principle

The conceptual definition of residual stresses is stated over the absence of external forces applied to a component. After the induction of residual stresses, the component is a stable and static system. This lack of external forces and internal movements is the basis for the most fundamental condition of residual stresses: the equilibrium principle (BEHNKEN, 1997; LU, 2002).

The practical outcome of the principle is the mandatory distribution of stresses along a certain volume. For a workpiece with a homogeneously stressed surface, the equilibrium is reflected along the depth. Up to the part's centerline, all the compressive stresses must be balanced by a tensile bulk of the same intensity, Figure 2.18(a) (BEHNKEN, 1997; LU,

2002). Bringing the Equation (2.2) to a profile approach, the integral of the derived areas below the profile along the depth must be nil, Equation (2.6).

$$\int_0^{CL} \sigma^I(z) dz = 0 \quad (2.6)$$

Where:

z: depth

CL: centerline

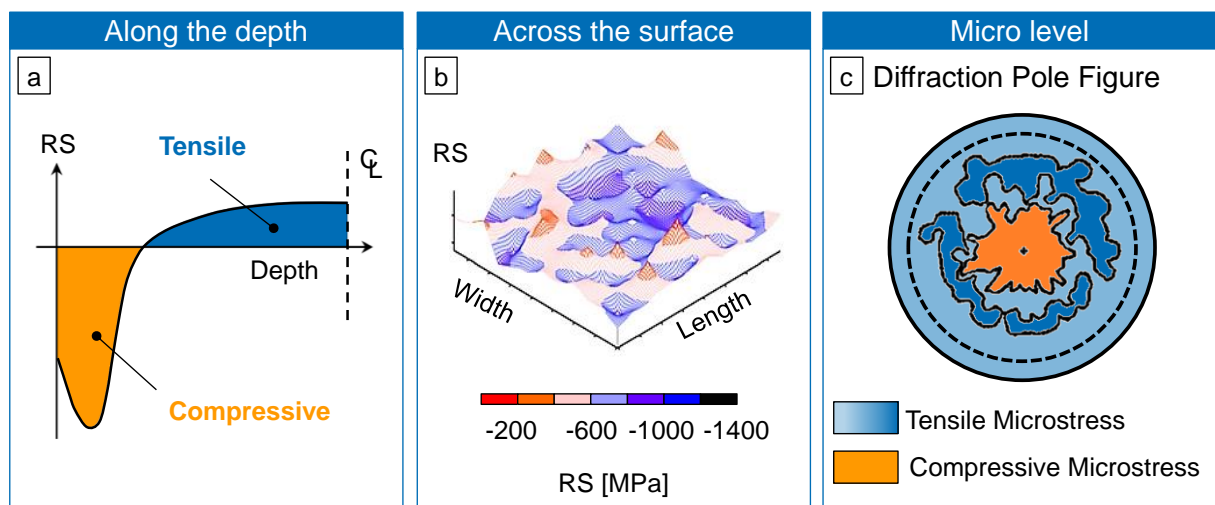


Figure 2.18 – The equilibrium principle reflected into different domains (PERLOVICH; ISAENKOVA; FESENKO, 2010; ZHAN; JIANG; JI, 2013).

The localized characteristic of the loads from most of the manufacturing processes goes beyond the assumption of surface homogeneity. The contact volume between tool and workpiece or cooling temperature heterogeneities do not allow the equilibrium to take place solely along the depth. This concept is depicted by the shot peening simulation of residual stresses performed by Zhan, Jiang and Ji (2013), Figure 2.18(b). The highly compressive zones are balanced by less compressive points across the surface. The equilibrium with positive regions is found along the depth, but differently for each surface position.

The principle must also take into consideration the domain's size. The non-uniform dislocations' density or uneven dispersion of precipitates requires a microstructural approach. The residual microstresses created in the interior or in the vicinities of the grains must be redistributed within this same short domain. This is shown with the pole figure for microstrain analysis from Perlovich, Isaenkova and Fesenko (2010), Figure 2.18(c). This pole figure is the

representation of microstrain on different surface directions of a polar coordinate system for a single crystal. As a result, the picture shows that a central portion of compressive residual microstresses is equilibrated by tensile microstresses over its surroundings.

Therefore, the equilibrium condition must be taken as the most important principle for understanding the disturbances of the residual stress state created by different manufacturing processes, for distinct volumes, directions and domain's size. This statement is the basis for the literature research that defines the state-of-the-art on the residual stress interaction in between processes of the gear manufacturing chain.

2.3 The State-of-the-Art on the Residual Stress Interaction

Extensive studies were developed for determining and improving the residual stress state through specific gear manufacturing processes. The articles from Hua et al. (2005), Capello (2005), Tang et al. (2009), Navas, Gonzalo and Bengoetxea (2012) and Zhang, Ding and Li (2012) are examples of studies of the residual stress profile induced by cutting processes. Parameters like feed, depth of cut, cutting speed, tool nose radius and tool flank wear are analyzed in different levels. Hypotheses for the different residual stress origins were explored to explain the observed behaviors.

Conclusions about the influence of the heat treatment processes on the residual stress profile can be found in the published studies of Réti (2002), Song et al. (2007), Husson et al. (2012) and Lingamaik and Chen (2012). Considering the thermal and structural stress origins, these researches analyze different heating and cooling time and their mean temperature. Additionally, distinct treatment cycles were analyzed, with the approach of quenching, tempering, annealing and stress relieving, individually or combined to the case hardening process, such as the gas carburizing. The hypotheses for the observed results were generally made over metallographic investigations regarding the phases compositions found.

The studies over the finishing processes are the most frequently published. The different gear grinding processes are explored by Brinksmeier et al. (1982), Chen, Rowe and McCormack (2000), Brinksmeier and Giwerzew (2005) and Bell (2009). Similarly to the machining processes, the parameters analyzed include depth of cut, cutting speed, material removal rate and feed rate. There is, furthermore, a high concern with the grinding wheel material, for which Al_2O_3 and cBN (Cubic Boron Nitride) are examples of an investigation

focus. The high differences observed in thermal conductivity directly impact the process temperature and can define the occurrence of structural originated residual stresses.

The high compressive stresses induced by shot peening encouraged a high amount of publications around the topic. Kritzler and Wübbenhorst (2002), Mitsubayashi, Miyata and Aihara (1994) and Rego, Gomes and Barros (2013) apply different approaches, but all with the fatigue strength increase as motivation. The process investigation includes parameters as shot speed, shot angulation, exposure time and media material, hardness, frame and size. Especially depending on the failure mode under analysis, these parameters are changed to set the combination of intensity and depth of stresses that is appropriated to the failure mechanism. It is important to highlight that the residual stress heterogeneity is an increasing concern pointed out on conclusions and outlook of the shot peening investigations.

Other gear finishing processes receive emphasis on the task of inducing a compressive residual stress state. Gear honing, gear lapping and hard turning processes were investigated by Amini, Rósen and Westberg (1998), Matsumoto, Hashimoto and Lahoti (1999), Tönshoff, Friemuth and Marzenell (2000) and Karpuchewski, Knoche and Hipke (2008). These processes are frequently analyzed as a comparison with the grinding or shot peening processes.

It is at this point that the content of the topic 2.2.4 has to be recalled. The residual stress state is a system that must be under equilibrium in case no external forces are applied. Therefore, every occasion in which a gear is submitted to a manufacturing process, the equilibrium condition is disturbed. This concept emphasizes the importance of the residual stress states induced by preliminary stages of the manufacturing chain on the final stress state.

Still, it was verified that only few published researches aimed at analyzing the residual stress evolution in the entire gear manufacturing chain. Between different databases consulted, Figure 2.19 shows the result of a survey performed at the *ScienceDirect* base. The survey was executed through the fields of keywords, title and abstract inputting the keywords of this study: “residual stress”, “gear”, “manufacturing chain” and “interaction. Among other variants, “manufacturing chain” was represented by “manufacturing process”, and “interaction” by “evolution”. Even the results of the complete combinations do not precisely represent the picture of the state-of-the-art. The word “evolution” usually refers to dynamic changes during external load application. The word “interaction” is used with the generic meaning of “relationship” with other properties, but not the interrelation between two residual stress states. Therefore, the results, summed to the holistic context herein presented, characterize a substantial opportunity for a research development.

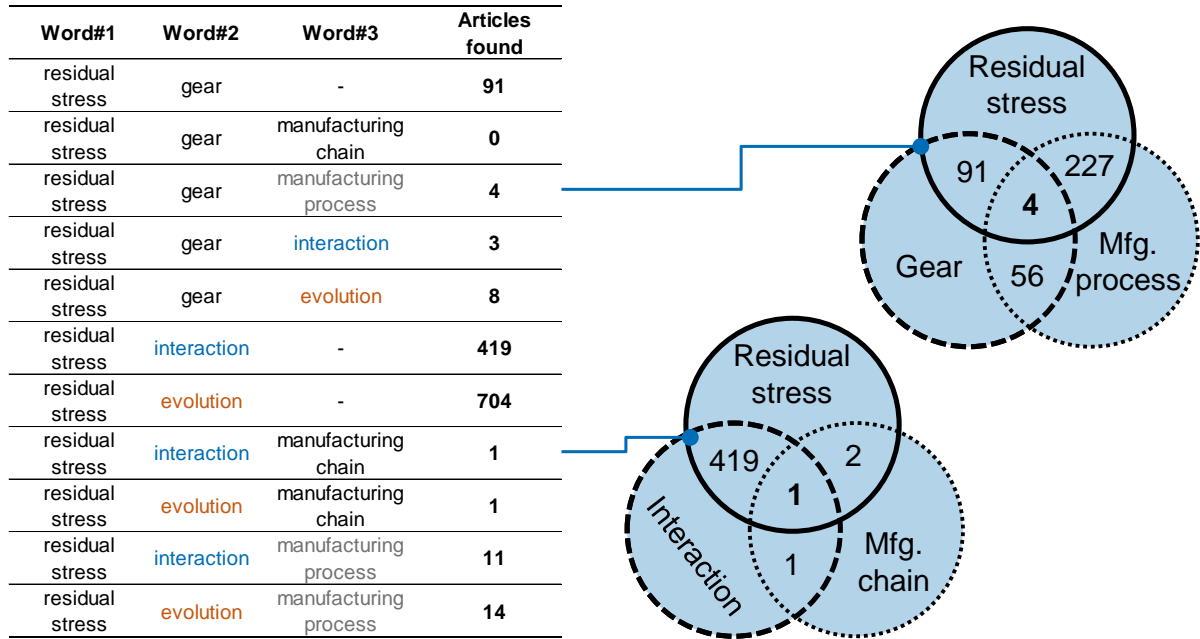


Figure 2.19 – A literature survey based on the key words of this study.

The publications with the closest approaches to what is being proposed, from different publishers' databases are now discussed. Starting with the study of Brinksmeier et al. (2011), the gear chain starting from steel making up to heat treatment was analyzed. But the residual stress was not the property measured along the chain. It was approached as a justification to the observations of geometry distortion. Additionally, the specific processes of gear tooth cutting are not covered.

Funatani (2002) performed a wide review of the residual stresses generated in gear manufacture. It includes the influence of steel grade and the structural phases formed, the analysis of different thermal and thermo-chemical treatments, and the finishing processes were covered. It is thus considered an important reference for gear residual stress investigations. However, all this content was approached in an individual analysis of each process or material property. None evolutionary aspect is shown regarding a workpiece's residual stress state between distinct manufacturing processes.

The research published by Navas et al. (2011) focus on the evolution of the stress state. Although being very detailed, it does not cover the processes after the heat treatment. Additionally, the analysis has focus on core properties, showing residual stress measurements up to 45 mm far from the surface, but in steps of 1 mm. For the failure modes previously described, a detailed analysis close to the surface would be necessary.

Another observation is that some articles, such as Barsoum and Barsoum (2009), Epp et al. (2011) and Navas et al. (2011) use not to consider the influence from processes prior to heat treatment. They assume that plastic deformation after phase transformation erases the stress history. Although being a founded argument, it is not shown exactly what it is meant with “erase”. It is not clear if two samples with extreme different stress profiles would, after the heat treatment, present the same stresses or closer states than they originally were.

Out of the gear context, but still on case hardened steel parts, Afazov (2013) analyzed the stress induced in gas turbine components from casting to heat treatment. The study, however, was all over numerical simulations, not comparing results to measured values.

Only three publications were found with an investigation scope to create different residual stress states with preliminary processes. The research presented by Klein and Eifler (2010) is herein included. From normalizing up to grinding, five processes are considered in the chain. However, residual stress is characterized only by one surface value, and not by a profile. Furthermore, the previous processes are not arranged into a straight structure to isolate the effect of the intermediate steps. Finally, the heat treatment is quenching, without the chemical consideration of carburizing, and the component is even not a gear.

A second study, from Karabelchtchikova and Rivero (2005) has as objective to identify the individual contribution of the heat treatment and the grinding process on the final stress state, when they are respectively applied as a sequence in the manufacturing chain. The experimental verification is however performed only with the final part. Based on a symmetrical design of experiments, the authors draw the conclusion of contribution by performing an analysis of variance. This approach does not allow one to verify how the equilibrium condition is disturbed, and to follow the evolution of mechanical and microstructural properties along the chain. Therefore, the statistical conclusion may not provide physical explanations to the mechanisms of the residual stress interaction.

Lastly, the article from Kovac (1994) was the research that comes closer to the demand of the problem here exposed. The study considered the evolution of a residual stress profile during the manufacturing of a bevel gear. The processes of milling, carburizing, quenching and annealing were approached. On the other hand, it did not analyze the finishing processes and the residual stress measurements were performed in each 200 μm . But what mostly does not meet the herein presented expectations is the not different stress behaviors induced by the previous processes. Without a statistical approach, the investigation of the influence of earlier stages on the final stress state is not possible.

2.4 Summary

Gear fatigue failure modes are widespread in industry segments such as the automotive and the wind energy. Independent on the mechanisms of the specific failure modes, fatigue cracks always start and propagate under a tensile stress state. It is in this context that the introduction of a compressive residual stress layer is desired. It partially offsets the actuating tensile stresses, increasing the part durability.

The induction of the residual stress state is directly dependent on the workpiece's manufacturing chain. Starting from the blank, a conventional sequence of processes to produce a gear can be classified into three groups: tooth cutting, heat treatment and finishing. Each process represents for the part a different combination of applied loads, and therefore different phenomena to induce residual stresses. Heterogeneous plastic deformation, temperature gradient and phase transformation are respective examples for mechanical, thermal and structural origins of residual stresses. Most part of the processes involves simultaneously more than one of the origins, and a simple change on this loads' balance can definitely alter the stress state. This is reflected into distinct structural levels. A typical analysis in the volume of several grains is the definition for residual macrostresses. Towards the direction of residual microstresses, the stress' domain passes through the different phases, the grain boundaries and inside the crystals. For all the levels of residual stresses, one basic condition must always be respected: the equilibrium principle. As a stable and static system, compressive and tensile stresses must be fully balanced.

Residual stress investigations on individual gear manufacturing processes are largely published in scientific and industrial databases. The objective is usually to find an optimal process setup for meeting the requirement of a compressive residual stress state. The same profusion is not seen for an approach of the entire manufacturing chain, even under the combination perspective of different residual stress origins and their need to be equilibrated. The few researches on the topic apply approaches diverging from the initially introduced problem. They were either based on measurements not compatible to a gear fatigue mechanism, or structured with a manufacturing plan that was not able to identify the contribution of a single process on the final residual stress state. This presented context characterizes a substantial opportunity for a doctoral research development.

3 Objective and Approach

The challenge of controlling the final residual stress state of a gear demonstrates to be as complex as the definition of an optimal compressive surface layer, as presented in the introduction chapter. From the literature review, it was possible to observe the several different phenomena that may originate residual stresses along the manufacturing chain. This observation fits to the control challenge comprehension, when considering that residual stresses must be constantly kept under the equilibrium condition. Therefore, the outcome herein stated is that the contribution of the previous processes to the final residual stress state cannot be neglected. Under the perspective of the further reviewed features of the residual stress state, the hypothesis of this study is drawn: due to the stresses' redistribution to satisfy the equilibrium condition, the residual stress intensity and heterogeneity induced by previous processes are significant to the surface integrity of a next process.

Consequently, the objective is the knowledge of the residual stress factors induced along the gear manufacturing chain with relevant influence on the final surface integrity. The residual stress factors are understood as the magnitudes and their deviations both along the depth and across the surface. They are defined along the thesis simply as the intensity and the heterogeneity of the residual stress state. The final surface integrity comprises, in addition to residual stresses, the microhardness profile, the material structure, the topography and the geometric distortion, being finally complemented by the fatigue behavior characteristics. The summarized basis of the hypothesis, the subsequent objective and the approach are depicted in the Figure 3.1.

The focus on the residual stress factors and on the integrity features can be derived to establish three questions that will guide the conduction this research:

1. Which features from the previous residual stress intensity profile are significant to the final integrity state?
2. What is the role of the residual stress heterogeneity to the processes' interaction?
3. How relevant is the residual stress interaction to the gear fatigue behavior?

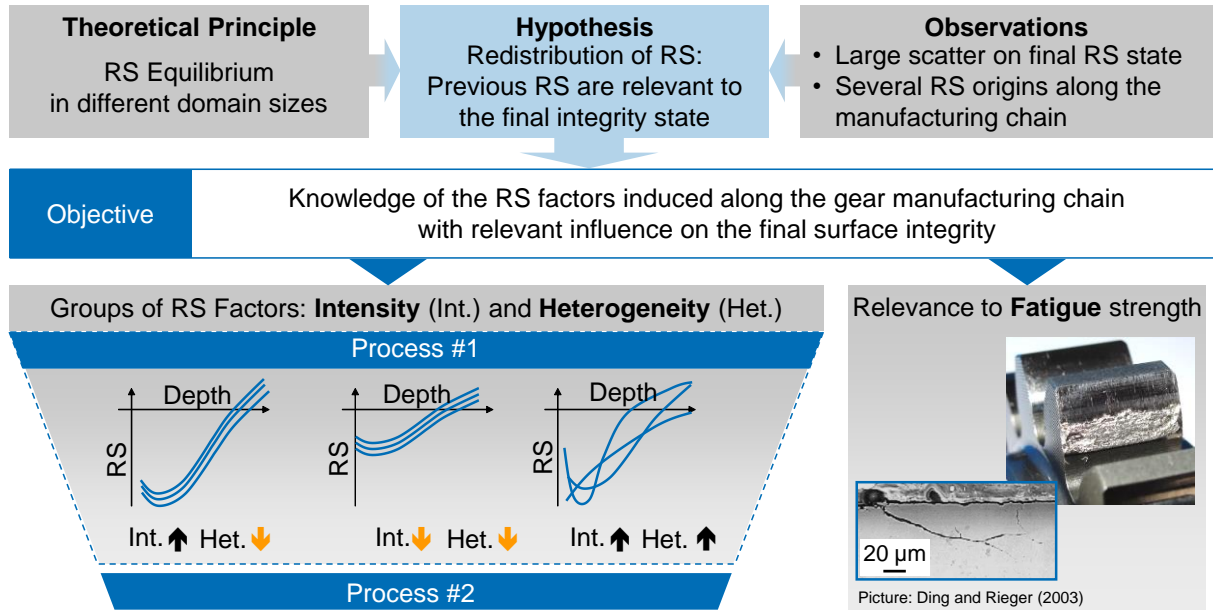


Figure 3.1 – The basis for the hypothesis, the objective of the study and how to approach it.

The first question has a focus on the depth profile features, here classified as intensity factors. Among them appear the maximum value of residual stress, the magnitude at the surface, the depth of the maximum intensity and the depth of transition from compressive to tensile state, or vice-versa. The expectation is to find out which features, from a previous chain's stage, mainly drive the stress state after a next step. Different residual stress profiles from a first process will be the input for the analysis. Complementary surface and material properties will be assessed to support a phenomenological explanation to the interaction model.

A similar approach is applied to the relevance of the heterogeneity state of residual stresses. The investigation related to the second question is addressed to verify whether the distribution of stresses is carried on to a later integrity state. The analysis will be based on the proposed relationship with the residual microstress intensity. Therefore, physical explanations will be supported by microstructural properties to be examined. The outcome should define the stress domain size that influences a further stage of the manufacturing chain.

The influence of the residual stress interaction on the fatigue strength is the content for the third question. Gears produced out of different manufacturing chains are submitted to contact fatigue tests. The examination is not restricted to the distinct performances out of the running procedure. The study goes towards the fatigue behavior direction, considering the initiation and propagation characteristics of the cracks. These may finally enable a connection to the residuals stress factors of intensity and heterogeneity.

The experimental approach to manufacture the specimens is also to be emphasized. The literature review showed that only a few studies follow the evolution of residual stresses along the manufacturing chain. Even for these cases, the evolution is approached into a divergent method. When parameters of a manufacturing process were changed for comparative purposes, they were applied at the final stage of the chain. The earlier stages were kept constant, not enabling the proper identification of their influence on the final residual stress state.

This study proposes to conduct the investigation into a convergent experimental method. For the example of a two-process interaction, the concept defines that every parameter modification is to be done at the first process. The second process must be kept the same, in order to isolate its contribution to the final integrity state. Distinct behaviors after the second process can be thus related to the first one. This approach is illustrated with the different residual stress profiles of Figure 3.1, arranged as a funnel to highlight the convergence from the top to the bottom, within the process chain's scheme. How the convergent concept is applied to the case studies of this research is the content of the next chapter.

4 Materials and Methods

The complexity of an entire gear manufacturing chain makes possible several interaction analyses. This thesis proposes a method to analyze the effects of the residual stress interaction, which would be equally applied to any combination of processes. The method development is investigated through two case studies, each of them approaching different stages of the manufacturing chain.

The selection of the processes for each case study is connected to how the open points observed in the literature review match the study's objective. It basically follows two criteria:

1. The distance of the interaction to the final point of the chain
2. The origins of residual stresses at the approached processes

To the first criterion, one combination of processes was taken from an early stage of the chain. A second one is positioned right at the end of the production. The heat treatment of gears, placed between the soft machining and the finishing processes, can be seen as the separation point between early and late stages. The reason is not only its intermediate position in the sequence of processes, but also its impact to the material structure. The high temperature conducts the steel to a phase transformation, and the associated plastic deformation may significantly alter the residual stress state. However, as reviewed in the state-of-the-art, it is not known how opposite residual stress states coming from previous processes can influence the result after the heat treatment. Phenomena created at the beginning of the chain, and of sensitive impact to the material integrity, like the secondary hardening and banded structures, are examples of additional reasons to justify the research at this early stage (USTINOVSHCHIKOV, 1984; NAVAS et al. 2011; SAHA et al., 2014). Moreover, a comparison between results from different stages of the chain allows identifying where to prioritize the efforts of further interaction analyses in the future. Based on this argumentation, the first case study was established to investigate the interaction effects between the soft machining and the heat treatment processes.

The first criterion was yet decisive in order to define the grinding as the second process of the second case study. The grinding provides an enhancement on the surface quality, supporting the compliance with requirements such as noise behavior and durability. It is usually the last process of the manufacturing chain, and therefore selected as the final

process of the second case study. The shot peening was the selected previous process to the interaction analysis with the grinding. The definition was guided by the thesis' objective and addressed by the second mentioned criterion. As stated by the objective, it is desired to identify the factors from the residual stress state that drives the interaction effects. Additionally to the opposite behaviors to be explored through the machining process, the contrast should also isolate the distribution features of residual stresses. Along the depth, it includes stress intensities of the same nature (tension/compression), and at different depth levels. Along the surface, the uniformity of the stress state. In this context, the process should be of a more reliable predictability, and thus with fewer origins of residual stresses. The shot peening appears as a suitable solution. It always induce surface compressive stresses, and its configuration allows the variation of the mentioned factors. In the case of gears produced out of low-alloy carbon steels, it is reasonable to assign the mechanical phenomena as the fundamental origins of residual stresses. The residual stress prediction models do not require computing thermal loads and phase transformations aspects. Finally, the mechanical deformation concepts can be more simply and reliably managed to generate the requested different residual stress factors.

The Figure 4.1 highlights the two case studies to be experimented along this study. It recalls the content of the Figure 2.16, to show the sequence of processes of the chain, and to display the residual stress origins of the selected processes, as part of the selection criteria. It is also depicted in the Figure 4.1 that each case study was planned to be performed at the different institutes herein involved. The experiments from the "Case Study 1" were executed in Brazil, at CCM-ITA and at the Institute SENAI of Innovation on Manufacturing Systems, in Jonville. The experiments of the second case study were performed at WZL-RWTH. An immediate consequence relies on the specimen design. Considering the existing manufacturing and testing facilities of both institutes, the specimens of the case studies 1 and 2 are respectively blocks and gears.

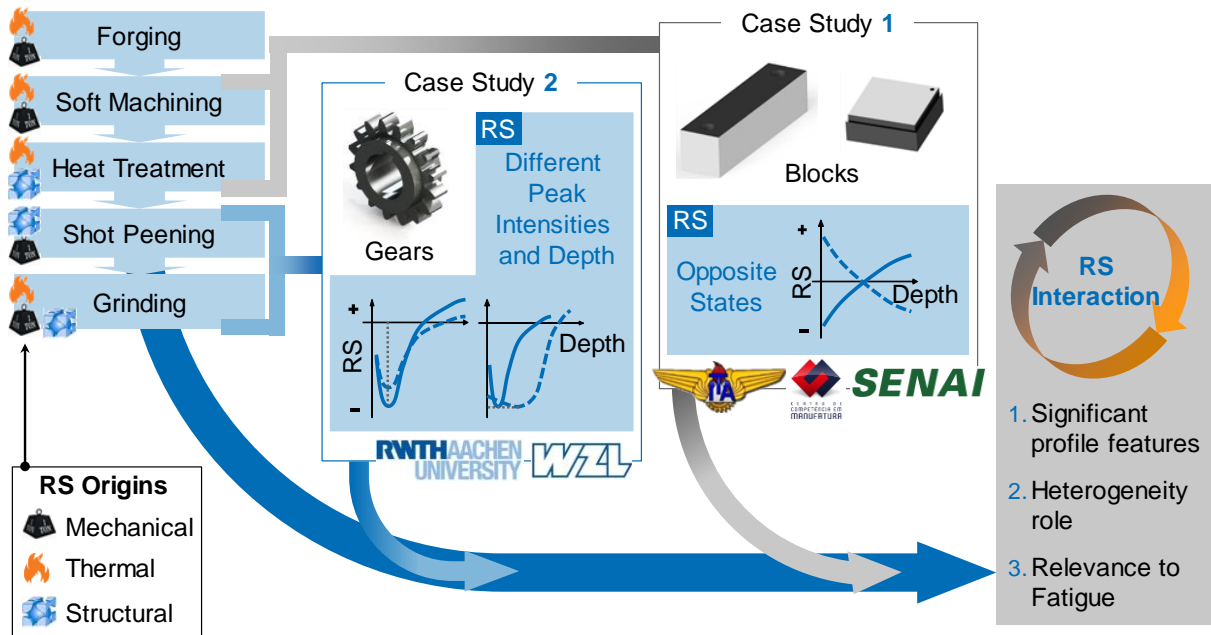


Figure 4.1 – The residual stress interaction analyzed through two case studies covering different stages of the gear manufacturing chain.

4.1 Overall Experimental Scope

Different institutes and specimens are involved in the experimental scope. However, they compose case studies to develop the same method herein proposed. For this reason, their experimental structure must be similar. As it is shown in the Figure 4.2, the surface integrity assessment methods are applied after each of the processes approached by the two case studies. Besides the residual stress assessment, they include topography and dimensional analysis, and the investigation of material properties. It is again important to emphasize the convergent experimental characteristic of this project, as introduced by the Figure 3.1. The first process must be configured to induce different residual stress states. The specimens are then submitted to a second process, which must be carefully planned to be equally applied to all of the samples. That allows identifying the influence of the previous processes to the final integrity state. The case studies are not only distinct by the manufacturing processes. Additionally, the interaction analysis between shot peening and grinding will be concluded with performing contact fatigue tests. With gear specimens, and produced up to the end of the chain, the specific gear functionalities can be examined. The outcomes define the relevance of the interaction effect, which is the content of the third research question previously presented.

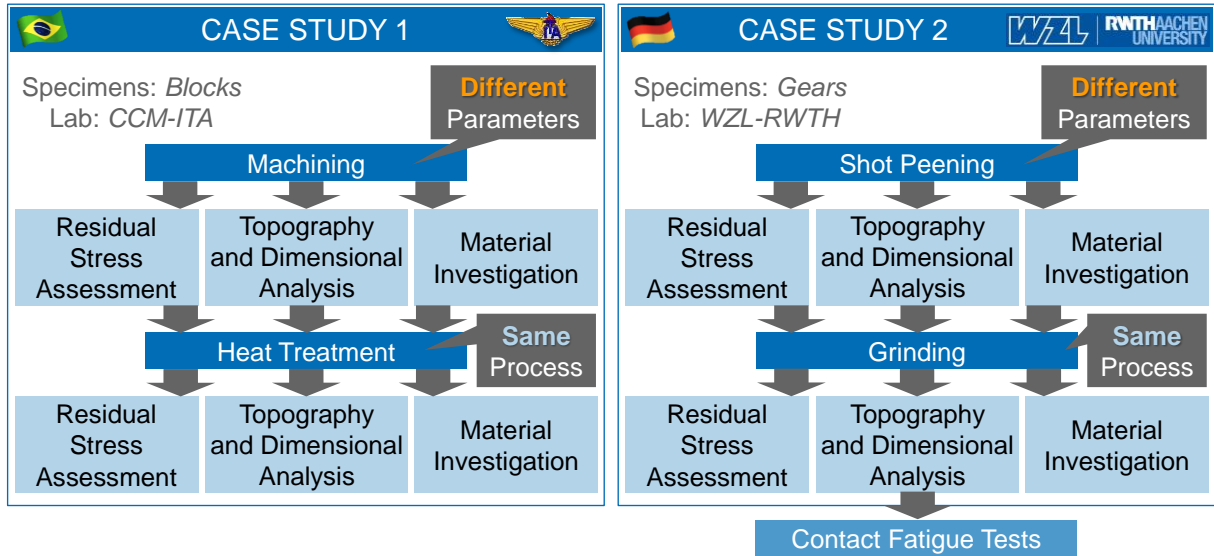


Figure 4.2 – Experimental flowchart. The structure with different parameters at the first process and the same second process characterizes the convergent approach.

The concern on being able to state similar or different results is converted in a statistical approach. This is particularly conducted through a sample size analysis, as shown by the Equation (4.1). The procedure basically correlates the sample size to the margin of random error (MRE), which is the confidence interval to be adopted (JOHNSON; BHATTACHARYYA; 2010). It is calculated using the standard deviation collected from a preliminary population with a higher amount of replications than expected. This concept allows one to define whether the outcome is the MRE or the sample size. As an overall role, the MRE was defined in such a way the amount of experiments could be calculated. For the experiments in which the sample size was limited, it was possible at least to define a reliable MRE. The procedure was performed for all the experimented data, and always considering a confidence level of at least 95%.

$$n = \left(z^* \cdot \frac{\sigma}{MRE} \right)^2 \quad (4.1)$$

Where:

n: Sample size

z*: Confidence level index

σ : Standard deviation

MRE: Margin of Random Error

4.1.1 Design of the Specimens

The blocks of the first case study were produced with two different designs, following the investigation evolution. The initial design is configured by dimensions of 50x50x20 [mm]. The samples produced with these dimensions are identified with the codes BFH and BFL. The investigated region is the squared area with edges of 50 mm. With the experiments' progress, the need of measuring force and temperature during the cutting was identified. As outcome, the specimens' design was updated to address the geometric requirements of the temperature and force sensors. With dimensions of 125x30x30 [mm], these samples are labelled with the codes BRH, BRM1, BRM2 and BRL. The examined region is one of the faces of 125x30 [mm]. The geometry of both models is depicted in the Figure 4.3. The details of each model are available in the appendices “B.1 Blocks for Sample Groups BFH and BFL” and “B.2 Blocks for Sample Groups BRH, BRM1, BRM2 and BRL”.

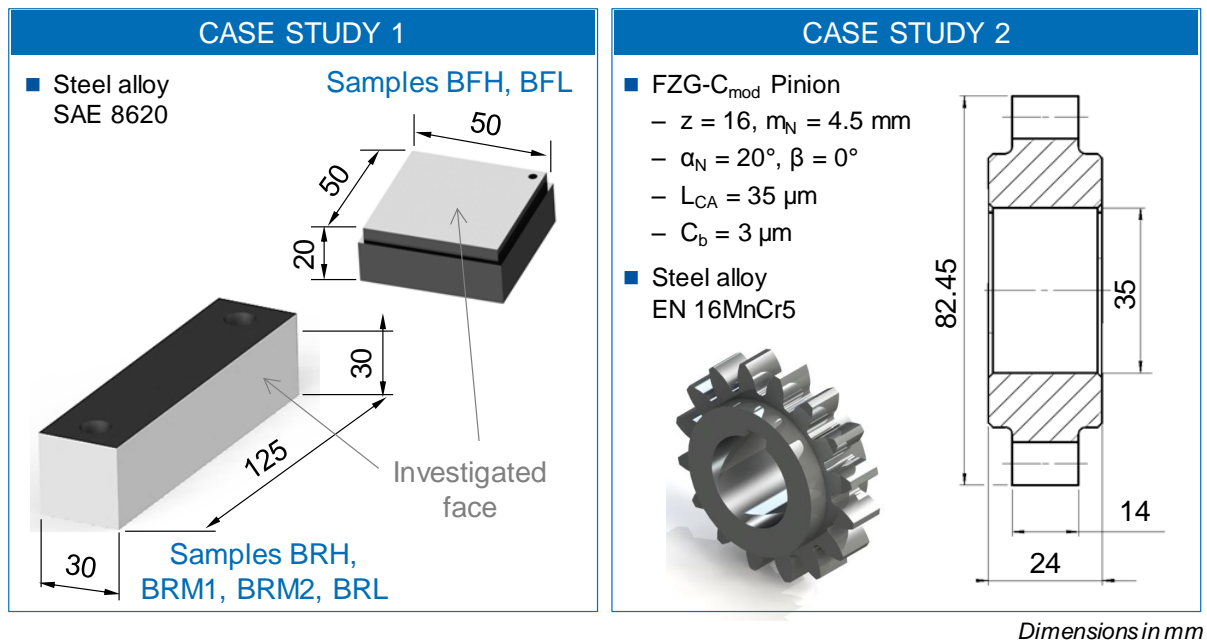


Figure 4.3 – Blocks and gears as respective specimens for the case studies 1 and 2.

Although presenting different dimensions, the specimens are produced out of the same material, the steel alloy SAE 8620 (DIN 20NiCrMo2 equivalent). This alloy is a typical material for the production of gears that must be case hardened. The reason is found on its low content of carbon, together with the addition of the hardening elements Mn, Cr and Ni. The low carbon content provides high potential for enhancing the carbon diffusion at the

surface during the carburizing process, while it keeps a soft and thus machinable core. The alloy elements increase the steel hardenability, by slowing down the martensitic transformation and by generating the precipitation of carbides (RAKHIT, 2000). The isothermal transformation diagram of the SAE 8620 alloy is available in the Attachment “C.1 Blocks, SAE 8620”. Likewise the explanation of the design change, the investigation progress demanded purchasing the material at different moments. Although coming from distinct batches, the material specification for both block designs is the same.

Under the perspective of the manufacturing loads and the residual stress origins, the concept of gears teeth cutting can be simplified to a milling process. This is even reinforced by the fact that milling itself is one of the teeth cutting alternatives. The heat treatment process setup is also not substantially altered only due to the existence of teeth. The process must only be adjusted to the specimen volume. The blocks’ designs were carefully defined to be volumetrically similar to gears usually treated at the adopted furnace. These considerations allowed performing experiments with the block geometry, whose manufacturing requirements could be complied by the facilities of CCM-ITA.

The second case study is conducted with the facilities of the gear department of the WZL-RWTH. Consequently, no manufacturing assumptions were necessary and the specimens for the interaction between shot peening and grinding are gears. The design of a gear itself was still necessary to perform the contact fatigue tests to investigate the relevance of the interaction effects. For this purpose, it was selected the gear geometry of standard procedures performed at the test rigs of WZL. The FZG-C model is a spur gear designed for the investigation of contact fatigue failure modes. The specimen is the driver unit of the gear pair, hereafter just called as pinion. The pinion has 16 teeth and its loaded flanks are the investigated surfaces. A microgeometry modification was set with a tip relief of 35 μm and a lead crowning of 3 μm (visual description in the appendix “A.1 Gear Nomenclature for Macro and Micro-Geometry”). The specific geometry is determined to avoid generating other flank failure modes rather than contact fatigue, such as flank breakages and scuffing. This selected design is based on the model identified as FZG-C_{mod} (BAGH, 2015), being depicted in the Figure 4.3 and detailed in the Appendix “B.3 Gears: FZG-C_{mod} Pinion”. The material selected is the alloy steel DIN 16MnCr5 (SAE 5115 equivalent). Analogous to the blocks’ material, this alloy is largely used for the gear production due to the low carbon content and to the alloy elements to increase its hardenability. Its composition and its isothermal transformation diagram, for different carbon contents, are available in the Attachment “C.2 Gears, DIN 16MnCr5”

4.2 Manufacturing of the Specimens

Four processes compose the monitored steps to identify the residual stress interaction, two in each case study. The previous processes to the analyzed ones will also be described. Nonetheless, the focus is kept over these four processes, to be introduced in the sequence.

4.2.1 Soft Machining

As revised in the topic 2.1.3, the soft machining processes for cutting teeth can also be represented by a roughing and a finishing step. Both are not necessarily conducted at the soft machining stage. The finishing before the heat treatment, such as the shaving process, is usually not performed when a hard finishing process like grinding is already planned. This chain variation creates an investigation opportunity in the context of the convergent experimental scope. The type of soft machining was thus the first definition to induce different residual stress states before the case hardening process. The specimens labelled as BFH and BFL are finished, while the samples from groups BRH, BRM1, BRM2 and BRL are roughened. The parameters that essentially represented this manufacturing difference were the radial and axial depths of cut (a_e , a_p). The determination of the cut depth for the roughing process was based on the publication of Gerth et al. (2009). The authors proposed a simplification model from the gear hobbing to the milling process, which goes towards the approach of this thesis. The radial and the axial depths of cut are respectively selected to be equal to 1.0 mm and 3.0 mm. A much reduced value characterizes the milling of the finished specimens: 50 μm in both directions. It appears in the same order of, although still above, the depth of cut considered for the gear shaving process (DAVIS, 2005; SCHRÖDER, 2007).

The definition of the further manufacturing parameters achieved a critical point, especially due to the divergences found in the literature about machining residual stresses. This conflict is exemplified by the investigations of the feed rate and the cutting speed. While the studies of Navas et al. (2012), Grum (2010) and Thiele et al. (2000) register a more tensile residual stress state with the increase of the feed rate, the opposite behavior is observed by Lazoglu et al. (2008). Also for Navas et al. (2012), the reduction of the cutting speed induced more tensile residual stresses. However, the residual stress increasing trend is published by Jang et al. (1996) and Outeiro, Umbrello and M'Saoubi (2006) when the cutting speed is

indeed increased. All of the mentioned studies worked with steel, although not with the same alloys.

The conflict was solved with two different approaches, along the evolution of the thesis. In a first moment, for the BFH and BFL specimens, the cutting parameters were selected by considering the published database on similar manufacturing conditions. For the exposed divergences, the studies performed with low-alloy steels were defined as reference. In order to create the distinct stress states, through a finishing condition of cut depth, the parameters were defined as shown in the Table 4.1, also including the explanation for the samples' nomenclature. All of the specimens are represented by a BFL, due to the geometry of a block, and by a "F", which assigns the finishing setup. The two setups were finally named according to the expectation of mechanical load during the process. For each machining group, five specimens were produced, starting with new tools.

Table 4.1 – Process parameters for the groups representing the finishing machining condition.

Parameter	Finishing specimens 50x50x20 [mm]	
	BFH	BFL
f_z [mm/tooth]	0.10	0.05
v_c [m/min]	80	250
a_e [mm]	0.05	0.05
a_p [mm]	0.05	0.05
Direction	Up-cut	Down-cut

```

graph LR
    B[B] --- BS[Block Sample]
    F[F] --- FS[Finishing Setup]
    EML[ ] --- EMLD[Expected Mechanical Load]
    EMLD --- H[“H” – Higher]
    EMLD --- L[“L” – Lower]

```

Expected Mechanical Load
“H” – Higher;
“L” – Lower

Finishing Setup

Block Sample

The second approach, for the specimens BRH, BRM1, BRM2 and BRL, is based on the phenomena that connect the process to the stress state. As described in the literature review topic, the residual stress state is defined over three physical phenomena: mechanical loads, thermal loads and structural modifications. The selection of a manufacturing process parameter can promote different intensity levels for each one of them. Where the residual stress state is resultant from the coupling of at least two phenomena, the parameters' analysis cannot be lonely approached. The comparative importance of each phenomenon in the final stress state must be understood. Generally, the researches over manufacturing residual stresses investigate the direct influence of a process parameter over the residual stress profile. Although valid in the specific published study, it may not be reproduced proportionally under other boundary conditions. Another, and even similar, experiment will represent slight changes in the material composition, process parameters or even in the depth zone under

analysis, which is function of the failure mode studied. That is the point where crossed effects can occur: The balance of these slight changes will be hidden behind a residual stress profile measured and imprecise conclusions from individual changes can be taken.

Considering that a residual stress measurement is highly time and money consuming, the incorrect conclusions from crossed effects must be avoided. Therefore, a method with focus in the origins of residual stresses is here proposed (Figure 4.4). Samples with different process parameters configuration are produced and the selection for residual stress measurement is determined upon the examination of each phenomena applied to that process. This implies the measurement of force and temperature during the samples production. After the process completion, a material investigation must be performed on the workpiece. The method increases the chances of selecting sample groups with statistical differences in the residual stress state.

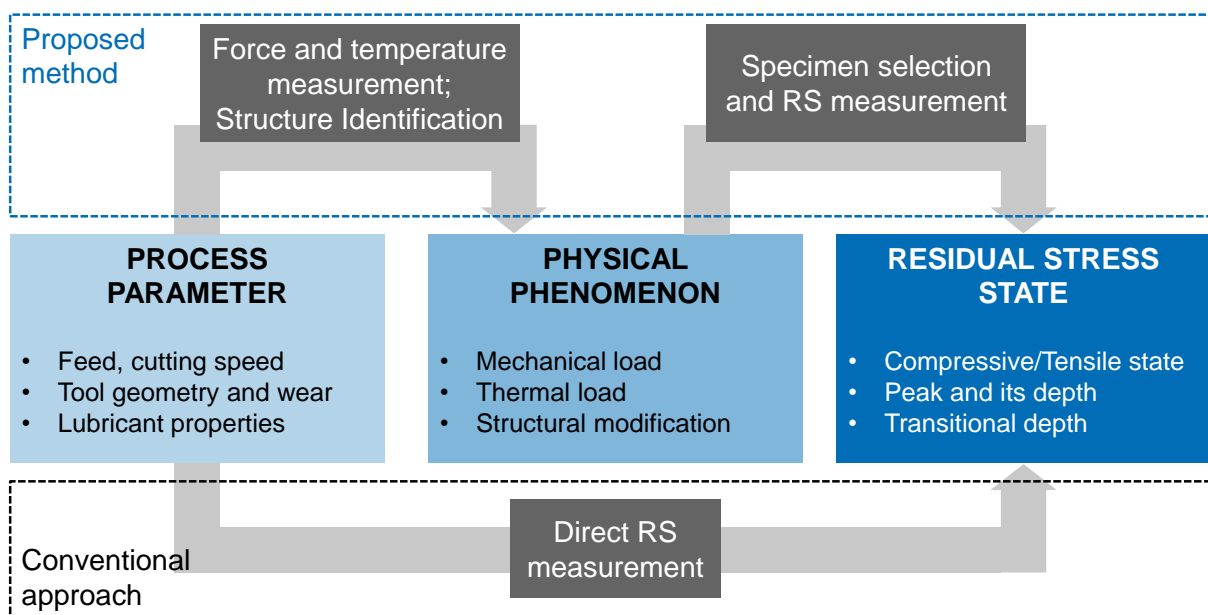


Figure 4.4 – Proposed method for selecting samples to be submitted to the residual stress measurement.


Towards increasing the thermal load, the first definition was to reduce the feed rate. The temperature in the cutting process rises due to generated shear and frictional heat and decreases during the non-cutting period due to the forced convection of the air. By reducing the feed rate, the heat change is reduced in the near cutting region and convection has less efficiency in cooling the workpiece. While the feed rate is selected due to its effects on the non-cutting period, the tool wear is considered due to the loads of the cutting period. When


the tool loses its sharp frame, shear forces are gradually replaced by frictional forces. Thus, it promotes temperature rising in the tool-workpiece contact. The groups targeted to have higher thermal loads were therefore manufactured with worn inserts.


On the other hand, the induction of a more compressive state was mostly guided by the determination of the mechanical load. It was then necessary set the process up to a condition in which the surface is stretched, or submitted to plastic deformation to expand the surface, like the concept presented in the Figure 2.12. This surface stretching behavior can be differentiated by up-cut and down-cut milling conditions. These two concepts apply different force directions to a material point behind the tool movement, but still under the strain influence of the process. The down-cut still compresses this point behind the tool, while the up-cut is now stretching this region. This rationale goes in agreement with what is shown by Ericsson (2002) and Brinksmeier et al. (1982). Yet on the understanding of the cutting mechanical load, the feed rate is again considered. A larger feed increases the material removal rate, promoting a higher cutting energy. The consequence is the generation of higher cutting forces.

The Table 4.2 summarizes the parameters' decisions for creating the desired differences to the residual stress states, through a roughing condition of cut depth. For each of the groups BRH, BRM1, BRM2 and BRL, fours specimens were produced. Their nomenclature is shown according to the legend of the Table 4.2, in which "B" is still representing the block as the sample geometry. Due to the roughing setup, the code is followed by a letter "R". At the end, also the expected mechanical load is represented. The process applied was face milling, and a 25 mm diameter tool with three carbide milling inserts *SANDVIK CoroMill R390-11 T3 08M-PM GC1030* was used into a dry condition.

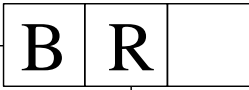
Table 4.2 – Process parameters for the groups representing the roughing machining condition.


Residual Stress 

Force 

Temperature 

Parameter	Roughing specimens 130x30x30 [mm]			
	BRH	BRM1	BRM2	BRL
f_z [mm/tooth]	0.15	0.10	0.10	0.03
v_c [m/min]	100	250	250	400
a_e [mm]	1	1	1	1
a_p [mm]	3	3	3	3
Condition	Up-cut	Down-cut	Up-cut	Down-cut
Tool life	New	New	Wore	Wore

Block Sample  Expected Mechanical Load
 “H” – Higher; “L” – Lower
 “M1” and “M2” – Medium

Roughing Setup 

The proposed method required also the instrumentation of the milling machine, a 5-axes vertical CNC machining center *Hermle model C600 U*. In order to acquire the force during the milling process, the machine was equipped with a piezoelectric dynamometer *Kistler 9265B*. This load cell is designed to enable measuring the three orthogonal force components (Figure 4.5b). The temperature assessment was supported by thermocouples and a thermal camera. Bores with 1.5 mm diameter (Appendix “B.2 Blocks for Sample Groups BRH, BRM1, BRM2 and BRL”) accommodated three K-type thermocouples were positioned internally to the specimen. The distance from the thermocouple’s extremity to the machined surface is, before the process starts, 5 mm. The temperature signal was also captured with a thermal camera *FLIR E60* positioned in front of the machining center. The camera was adjusted to capture an image from a similar angle than the one shown on Figure 4.5c.

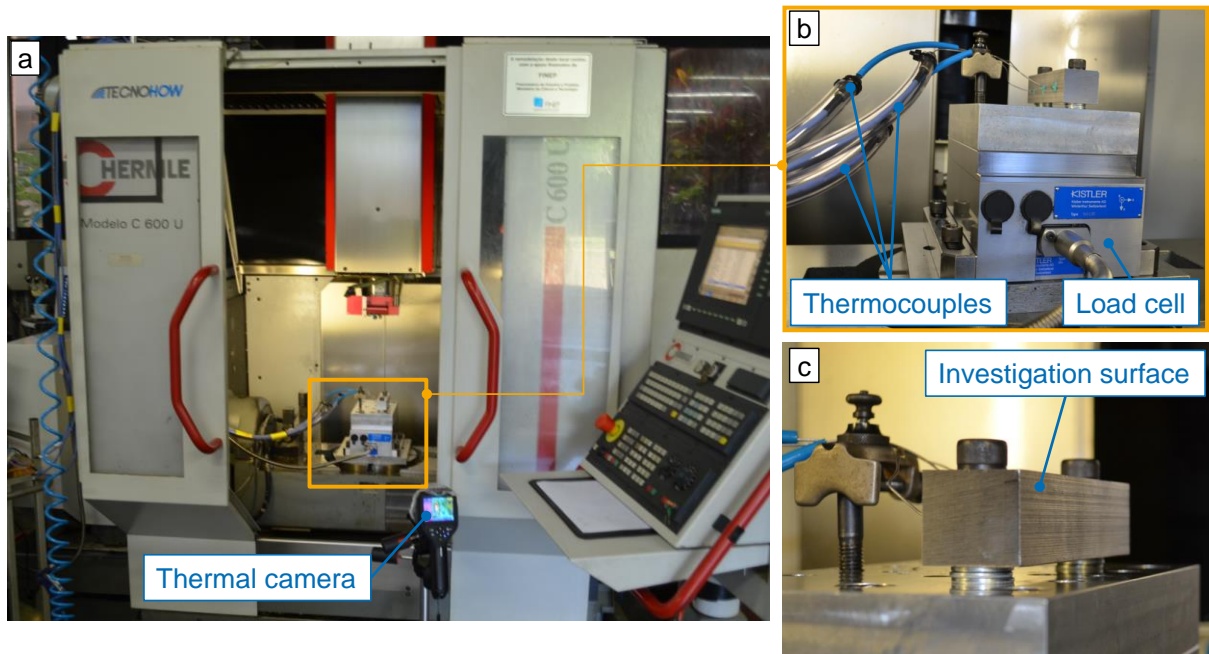


Figure 4.5 – Production of the machined samples: *Hermle C600 U* equipped with *Kistler* dynamometer thermocouples and assisted with a thermal camera; (b) Instrumentation detail; (c) Specimen's face to be machined.

4.2.2 Heat Treatment

The convergence of the first case study forwards machined blocks with different residual stress states to the same heat treatment process. It requires a planning of this second manufacturing step with a special attention to minimize process variations among the specimens. Particular considerations were taken to the definition of the cycle, the preparations for the process and even the selection of the furnace.

Likewise the definition of the machining parameters, the heat treatment was planned to the blocks to create similar conditions of a process usually applied to gears. The process was defined as a sequence of gas carburizing, oil quenching and tempering. The carbon content for the carburizing process was provided by methane as the carrier gas, with propane as the enriching gas. A two-stage carburizing process was applied, also referred as the boost-diffuse method. The first stage is conducted with higher temperature and carbon potential values, in order to speed up the carbon diffusion into the workpiece's surface. Both values are reduced for the second stage, which provides a more flat carbon distribution in the surface and a deeper diffusion towards the core (KRAUSS, 2002; RÉTI, 2002). The determination of the temperature, carbon potential and time for each heat treatment phase were set according to the

blocks' design specification. To ensure that the specified treatment would comply with the design requirements, preliminary tests were conducted with some of the specimens. After an approval regarding the inspection of the hardness profile and the amount of retained austenite, a final cycle was fixed, as displayed in the Table 4.3. All the specimens were treated in a single charge.

Table 4.3 – Parameters for each phase of the heat treatment process.

Phase	Temperature [°C]	Time [h]	Carbon Potential
Carburizing (Stage #1)	930 ± 10	8.50	1.00%
Carburizing (Stage #2)	840 ± 10	1.00	0.72%
Quenching	90 ± 5	0.33	
Tempering	180 ± 5	2.00	

The heat treatment process was conducted in a furnace of the *Companhia Industrial de Peças* (CIP), in Guarulhos, Brazil. A batch atmospheric furnace was selected due to the flexibility of adjusting the process to the specific needs of the experiments. Additionally, the smaller dimensions of this furnace concept enable quicker temperature stabilization and therefore enhanced temperature homogeneity inside it (Figure 4.6a).

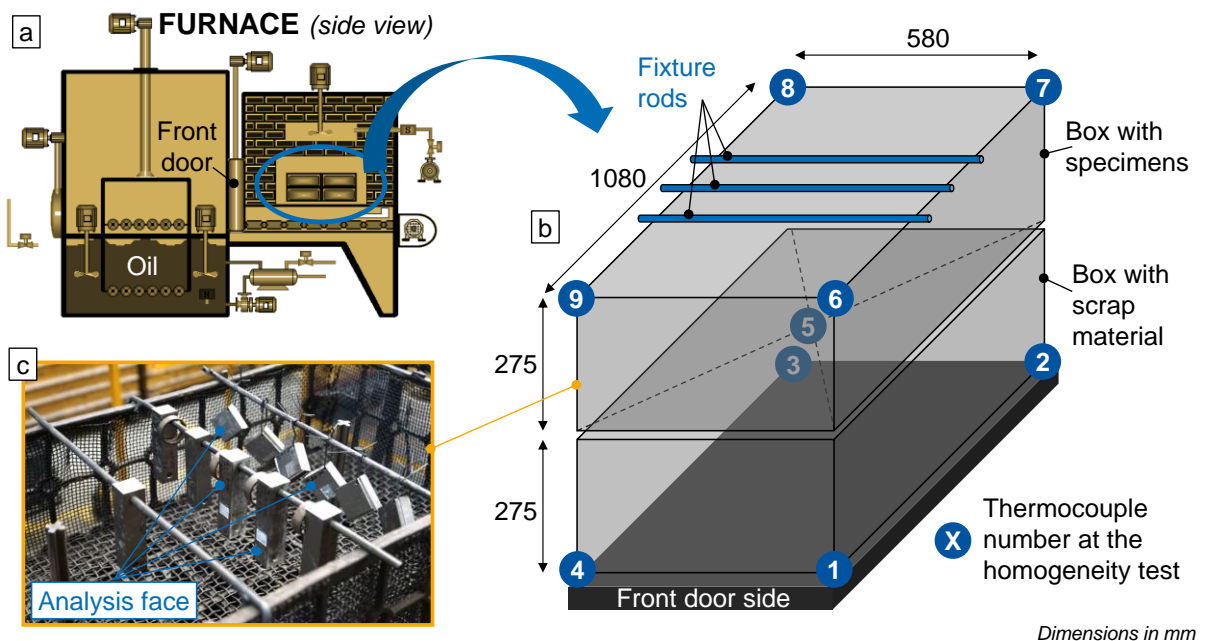


Figure 4.6 – Heat treatment process: furnace concept, dimensions and the batch arrangement of the specimens.

The temperature homogeneity is directly linked to the concern of having similar loads for all the specimens at the second process of the case study. The selected furnace had been recently approved according to the AIAG CQI-9 standard, which comprises a furnace homogeneity test (AIAG, 2011). For the temperatures of 800°C and 900°C, nine thermocouples in different positions of the chamber (Figure 4.6b) had to demonstrate that the temperature would not exceed the range of $\pm 15^\circ\text{C}$. The results enabled the process to be established even with a lower tolerance, of $\pm 10^\circ\text{C}$ over a nominal value higher than 900°C.

Even with the equipment certification, the disposal of the specimens in the chamber was carefully defined. The parts were positioned in the longitudinal center of the charge. The regions close to the front and the rear walls are submitted to a higher heat transfer, thus potentially increasing the temperature variation. The statement is even supported by the results of the thermocouple #5 (Figure 4.6b). In a centered position, it resulted in one of the lowest temperature deviations during the furnace certifying tests. The specimens were also loaded considering the face of analysis oriented towards the same direction. The roughing machining specimens were fixed through rods, while the finishing machining specimens were suspended by a wire, tied to one of the rods (Figure 4.6c). Finally, the attention with the treatment preparation was to load additional generic parts (scrap material) that would lead the overall mass that matches to the volume of carburizing gas demanded in such a furnace.

4.2.3 Shot Peening

The shot peening is the first process from the interaction analysis of the second case study. However, it represents also the latest of a processes sequence not yet concluded to produce the gear specimens. The production started with forged cylindrical blanks, which were then machined to achieve the dimensions of width, and outer and inner diameters. The teeth cutting was performed by gear hobbing with a *Liebherr LC120* gear cutting machine. The involute was generated with one single pass, and fifty samples were manufactured. Before submitting the samples to the heat treatment, their keyways were broached. The case hardening process applied was the atmospheric carburizing, followed by quenching and tempering. The cycle setup was defined to achieve the case properties specified in the drawing of the Appendix “B.3 Gears: FZG-C_{mod} Pinion”. The samples displacement inside the furnace was registered. Parts positioned both in the center of the furnace and close to its walls were taken for the inspection. The depth profiles of hardness and residual stress were measured in order to verify the uniformity of the heat treatment applied to the samples. Even with this

control, a pre-grinding process of the flanks was applied as a last step before the shot peening. The purpose was to compensate the different distortion levels among the samples.

The role of the shot peening in the convergent interaction approach of this thesis is to be the source of the different residual stress states for the second case study. Since the outer layer of a peened surface is always under compression, the definition of the shot peening parameters was taken to create distinct stress distributions. Regarding to the intensity distribution factors, the maximum compressive intensity (peak) and its depth level are the targets. They are complemented by the heterogeneity state as a surface distribution aspect.

The process parameters used for differentiating the stress states are essentially the media size and the coverage level (Figure 4.7). Three media diameters were used based on the specification of cut wire spherical material with a hardness of 60 HRC. As the media is enlarged, the shot kinetic energy increases as well. Similarly, as the energy during contact is increased, the plastically deformed region grows. Consequently, the residual stress intensifies and grows deeper (KRITZLER; WÜBBENHORST, 2002; GUAGLIANO; VERGANI, 2004; SHIVPURI; CHENG; MAO, 2009). The different media sizes enable the specification of another process parameter that increases proportionally to the residual stress amplitude: the *Almen* intensity. This method, defined by the standard SAE J442, infers the residual stress level by the deflection measurement of a thin strip (SAE, 2001). Accordingly, the tests were planned in such a way that the diameter increase was followed by a consequent rise on the *Almen* intensity.

The diameters were still considered for the application of a single or a dual peening process. For the gears in which the dual peening was applied, a media with smaller diameter made out of glass was used as the second process step. The dual peening process produces a more uniform surface, since the second step aims at homogenizing the deformations created by the first one (MOLZEN; HORNBAACH, 2000; REGO; GOMES; BARROS, 2013).

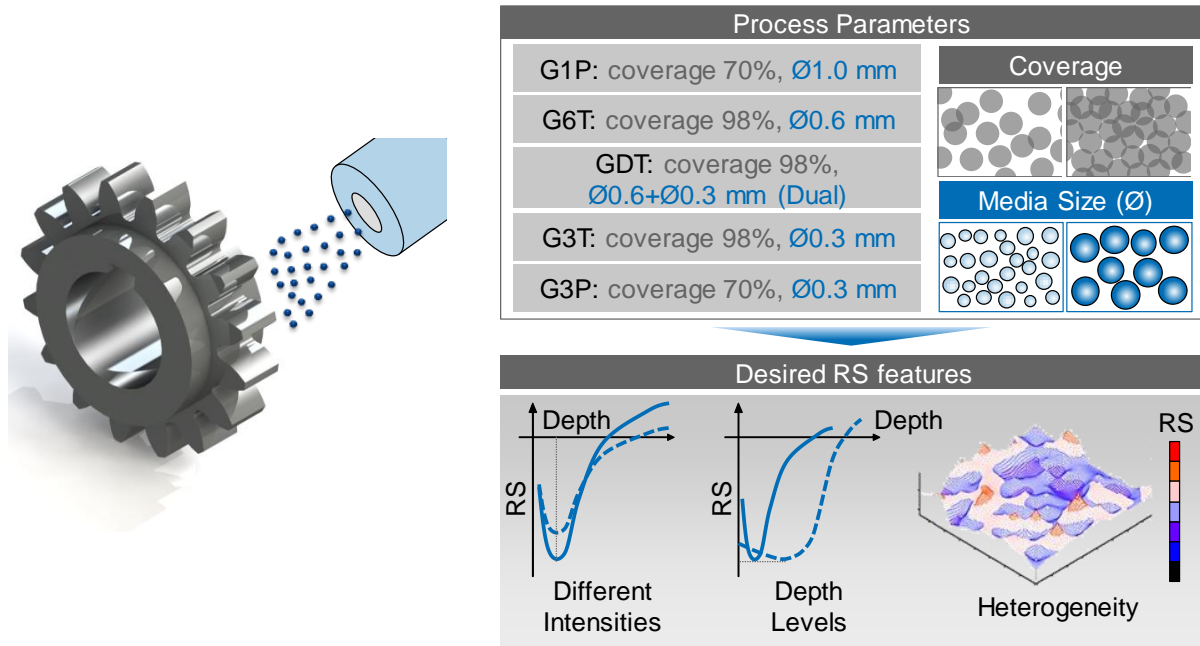


Figure 4.7 – The shot peening parameters were defined to induce different residual stress distributions along the depth and across the surface.

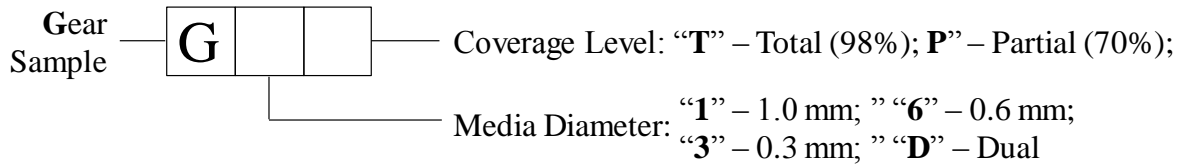
Following the concern on the heterogeneity stress state introduced by the dual peening, different levels of coverage were determined. The coverage is a percentage value to define the effectively indented area of the peened surface (Figure 4.7). As a natural consequence, the more covered the surface is, the better distributed will be the pattern of deformations. The coverage is essentially controlled by the exposure time of the workpiece to the process. But regardless to the exposed time, it is never assured that the surface reaches the level of 100%. A fully covered surface is then defined with a value of 98% (KIRK, 2002; BAGHERIFARD; GLELICH; GUAGLIANO, 2012). In this context, two coverage levels were selected. A coverage of 98% for a more homogeneous surface, against a process set to reach 70% of coverage, and thus induce a higher heterogeneity residual stress state.

Five different groups were peened and, according to the process setup, the wheel-propelling machine or the pneumatic nozzle-type machine were used. The peening machine concept does not necessarily produce significant differences on the workpiece surface integrity, as demonstrated by Köcher (1996). All the process facilities were kindly provided by the company *OSK-Kiefer*, located in the city of Oberhausen, Germany. The Table 4.4 summarizes all the conditions considered to manufacture the gears with distinct intensity and heterogeneity of residual stresses. It also provides an explanation to the symbolic

representation of each group. All groups start with a “G”, representing the gear as the specimen. The next two codes respectively refer to the media size and to the coverage level.

Table 4.4 – Shot peening parameters defined for inducing different intensity and heterogeneity levels of residual stress.

Group	Manufacturing Process	Machine Concept	Media Diameter [mm]	Media Material	Almen Intensity [mm Almen A]	Coverage [%]
G1P	Shot Peening	wheel	1.0	Cut Wire	0.50 → 0.60	70
G6T	Shot Peening	nozzle	0.6	Cut Wire	0.35 → 0.40	98
GDT	Dual Peening	nozzle	(1) 0.6	(1) Cut Wire	(1) 0.35 → 0.40	(1) 98
			(2) 0.3	(2) Glass	(2) 0.35 → 0.40	(2) 98
G3T	Shot Peening	nozzle	0.3	Cut Wire	0.20 → 0.25	98
G3P	Shot Peening	nozzle	0.3	Cut Wire	0.20 → 0.25	70



4.2.4 Grinding

The grinding is not only the last process of the second case study, but also the last on the entire specimens’ manufacturing chain. That confers to the grinding the accumulated variability of the whole production. As consequence, a complex situation is created for its role to be statistically the same for all the prototypes in the convergent experimental approach.

The first measure taken for the variability consideration was to select the profile grinding process to be applied to the prototypes. Differently than the generating grinding process, the profile grinding actuates individually to each tooth gap. Through it, an individual control and monitoring of each flank is enabled. A flank control matches the investigation scope of most part of the experimental techniques to be here utilized, which turns the teeth into the actual specimens. The profile grinding was performed with a *Kapp KX-500 Flex* gear grinding machine. A grinding wheel made of sintered Al_2O_3 with a diameter of 200 mm and a thickness of 20 mm was used in the experiments. The process parameters were set to gentle conditions, in order to avoid temperatures that could lead to surface phase transformations. The process was performed with flood of coolant, a speed of 35 m/s and a feed rate of 500 mm/min. For each produced specimen, the grinding wheel was dressed. The depth of cut was

just selected after the residual stress measurements of the peened surfaces. The decision is based on the directive of establishing different depth profiles of residual stress to feed the interaction analysis. Nevertheless, the removal was performed by one single pass. The further process parameters were defined to provide the pinions a geometric quality level 6, according to the standards ISO 1328 and DIN 3962 (DIN, 1978b; DIN, 1978c; ISO, 1995).

In the search for the same loads applied during the process, special procedures were taken even before the grinding itself. The first of them was the application of a pre-grinding process immediately after the heat treatment. The precautions taken during the heat treatment cannot be considered enough for stating that the distortion level of the specimens are the same. As a preliminary grinding stage, a shallow layer of around 40 μm was removed from the flanks of each gear. The pre-grinding is not an unusual practice on finishing gears. Due to the stock removal limitation, the grinding is normally applied through a step of roughing, followed by a finishing step (KARPUCHEWSKI; KNOCH; HIPKE, 2008). The difference herein adopted was to perform this roughing (pre-grinding) before the shot peening. This action allowed having gears, immediately prior to the grinding process, with different residual stress states and similar distortion levels.

The definition of a same distortion level needed still to be reinforced. Even the pre-grinding application was not a guarantee that the teeth would be geometrically equal, due to the progressive wear of the grinding tool and the intrinsic errors of the machine. The gears were then measured in order to classify the specimens into groups with restricted tolerance for these deviations. The tooth span, symbolized by W_K (Figure 4.8), was the characteristic defined for this control. It is the most direct gear geometry inspection feature to define the heat treatment distortions and to feed the grinding programming (DIN, 1980; GOCH, 2003). The measurement considers the distance between flanks of different teeth, with reference to the base diameter of the central tooth. In the case of the investigated gear design, this measurement is conducted between three teeth. The value taken from the procedure includes the standard deviation of all the sequences of three teeth measured on one gear. The classification was determined before the shot peening. In this way, there was possible to define the peening setup for each sample, assuring that all the groups of tooth span receive the different residual stress states to be induced after the shot peening.

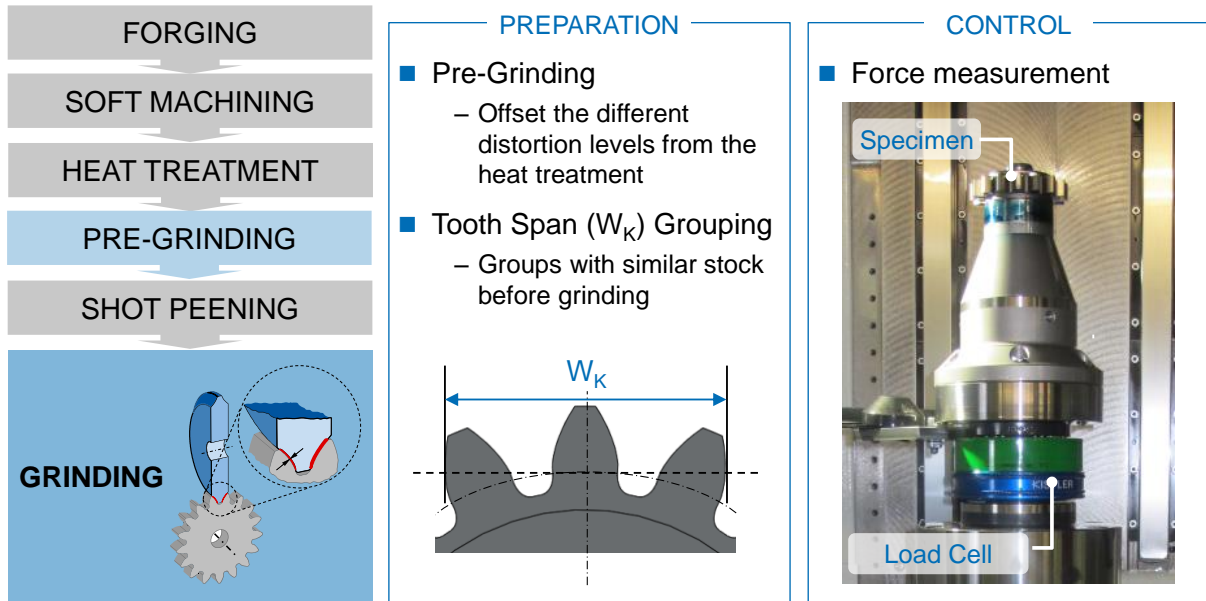


Figure 4.8 – Procedures adopted to select ground samples with the same process loads.

The final control action was employed during the execution of the grinding process. Over the machine's fuse, a load cell was installed in order to measure the grinding force. The load cell used was a rotary dynamometer *Kistler 9123C*. It was installed with the closest distance to the gear, with safe conditions to avoid collisions from the grinding wheel travel during the process (Figure 4.8). The measured value cannot be taken for absolute considerations of the cutting force. The countershaft needed to be used to provide stiffness and to enable the finishing quality required for these gears. Consequently, a fraction of the force coming from the wheel is also supported by the countershaft's bearings. However, the objective is to assure the selection of flanks ground with statistically equal forces. Therefore, for this comparative approach, the issue with the absolute value does not become an obstacle to the present study.

The forces were acquired according to three orthogonal directions along the complete grinding cycle. They are two radial components, which changed according to the gear position along the process, and an axial component. The analysis is performed with the equivalent value of the radial grinding forces. The axial force was used as the reference to identify the beginning and the end of the cutting cycle. It was thus possible to state the background values individually per flank, compensating the axes center movement with the gear repositioning to face the wheel.

4.3 Surface Integrity Assessment

After both manufacturing processes of each case study, the specimens were submitted to a surface integrity assessment. The examination covered residual stress measurements, topography and dimensional analyses and material investigations. The gears of the second case were still submitted to fatigue tests. The procedure of each mentioned analysis is described along the following topics.

4.3.1 Residual Stress Measurement

For the two case studies, the residual stress profiles were measured by means of X-ray diffraction (XRD). The XRD appears as the most practiced technique for measuring residual stresses, especially in the machinery industry (LU, 2002; LAW; LUZIN, 2011). As for all of the residual stress determination methods, the stress is not directly measured. The XRD is governed by the Bragg's law, which correlates the incident X-Ray properties with the interplanar atomic spacing, through the diffracted beam angle (2θ). The strain is therefore measured and used for the residual stress calculation. The calculated stress is not only resulting from one single measured angle. The measurement must be representative of the wide scatter of grain's lattice orientations inside the material. Different beam incidence (Ψ) angles are induced, both with positive and negative references, so also the shear stresses can be considered. Even the 2θ value is taken from several sequential measurements. The technique works by scanning the area around a standardized diffraction angle, according to the material phase under examination. The results of the detection are curves relating the detected intensity along the diffracted angle values. For the calculation of the residual macrostress, the maximum value (peak) of each curve is considered. The overall calculation is dependent on the peak position difference. This means the difference of the 2θ value, corresponding to the intensity peak, between all the Ψ -angle curves. The above described concept, shown in the left panel of the Figure 4.9, is named as the "Peak Shift" method (CULLITY, 1978; SPIEß, 2009; RUUD, 2002). The method is usually applied over surface layers along the depth, and the residual macrostress is represented by a depth profile.

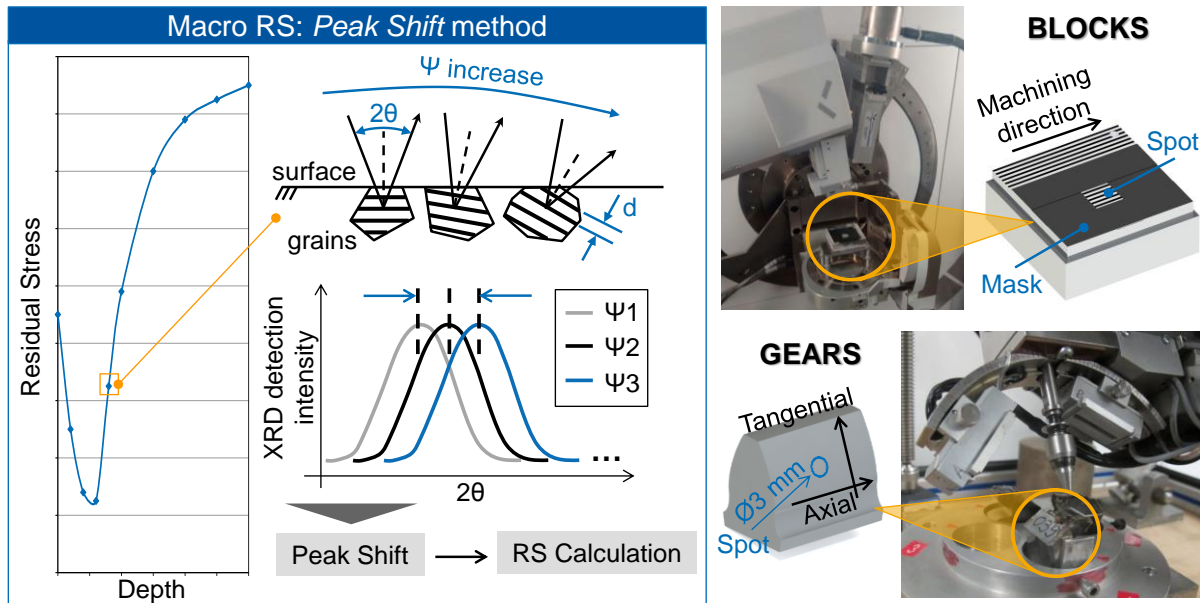


Figure 4.9 – Residual stress measurement: Calculation method and procedures applied.

For the first case study, the measurements were performed with a *PANalytical Empyrean* stationary diffractometer. The equipment is available at the Institute *SENAI of Innovation (ISI) on Manufacturing Systems*, in Joinville, Brazil. The residual stress setup of this equipment consists of a Cr K α 1 anode radiation with a vanadium filter. The radiation tube was adjusted to the point focus mode, through a crossed slit collimator with maximum aperture of 4 x 4 mm. The spot was ensured by covering the assessed surface by a mask made of tape, restricting the area of the beam's incidence (Figure 4.9). In the path of the diffracted beam, a parallel plate collimator was employed.

The blocks were always measured following the cutting direction, and for the α -Fe phase, the predominant structure after the two analyzed processes. The crystal orientations (Ψ) sampled were $\pm 0^\circ$, $\pm 16.8^\circ$, $\pm 24.1^\circ$, $\pm 30.0^\circ$, $\pm 35.3^\circ$, $\pm 40.2^\circ$ and $\pm 45^\circ$. The diffraction plan of each material is defined to be the one with the higher detection intensity considering the anode radiation employed. With a CrK α radiation, this condition is satisfied for the α -Fe through the diffraction plane (211), with a diffraction angle of 156.07° . The scanning range of this phase was thus set from 148° up to 163° . It was defined a step scan mode with a diffraction angle scanning range with steps of 0.10° . The scanning arrangement was set to comply with the recommendations for properly determining the background level. The residual stress calculation is finally made according to the *Dölle-Hauk* method (SAE, 1971, HAUK, 1997).

For the depth profile representation, the outer surface and six depth layers from 20 μm to 250 μm were evaluated. The layers' removal was performed by means of the electropolishing process, with the equipment *Buehler Electromet 4*. The polishing solution is a composition of perchloric acid, 2-Butoxyethanol and ethanol. This process is considered to induce non-significant stress changes during the layers' removal. Differently from the electrolytic etching, the electrolytic polishing removes material from both the grains and their boundaries. The result is a considerably more uniform surface, avoiding an improper spread of the X-Ray diffracted beam due to surface unevenness (PANGBORN; WEISSMAN; KRAMER, 1981). The depth values were measured, after each removal process, with the CMM center *Mitutoyo Crista Apex C7106*.

Similar conditions were applied to the examinations of the second study, and the few differences are now described. The experiments with the gear specimens were performed with the *Stresstech X3000* diffractometer from WZL-RWTH. As the main differences to be highlighted, this equipment is portable and built with two symmetrically positioned detectors. In this case study, the stresses on both material phases were measured, since no phase transformation is expected by the grinding process. For the assessment of the γ -Fe, the diffraction angle of 128.17° corresponds to the (220) diffraction plane. This property demanded a scanning procedure between 115° and 145° . The determination of the residual macrostress, according to Equation (2.3), required also the determination of the amount of retained austenite. Not only the main manufacturing direction, axially oriented, was taken for these measurements. Since the specimens were planned to perform functional tests, the rolling direction of the gear mesh was assessed. The rolling direction is oriented tangentially to the tooth involute profile, and therefore perpendicular to the axial orientation. A circular collimator with a diameter of 3 mm was used to define the measurement spot (Figure 4.9). The measurements were done over the tooth flank, around its pitch diameter. The specimens were prepared by cutting a sample of two teeth out of the pinion.

The same crystal orientation angles were assessed, but also introducing an oscillation of $\pm 2^\circ$ in the Φ -direction for increasing the quantity of crystals assessed at each Ψ -angle. The scanning range was slightly widened, when compared to the blocks' assessment. For the α -Fe, the range was set between 135° and 164° . Also the scanning steps could be collected in smaller intervals, of 0.06° . The depth profile covered, in addition to the outer surface, seven layers from 10 μm to 500 μm . The equipment used for the electrolytic polishing process was a *Struers MoviPol-4*, using the same solution applied for the blocks.

All the measurements were preceded by the calibration of the diffractometer. This step was conducted with *Stresstech* powder specimens certified for being free of residual stresses. Further measurement and analysis features not here described, such as polarization and absorption corrections, were set according to the procedure established by the standard SAE J784a (SAE, 1971).

4.3.2 Topography and Dimensional Analysis

The residual stresses comparison between processes is the main experimental outcome of the proposed scope. However, the understanding of the phenomena occurring must be supported by complementary analyses. Among them, and according to the experimental planning of the Figure 4.2, topography and dimensional analyses are conducted in the manufactured specimens.

The dimensional analysis is essentially the procedure for the distortion observation. It is known that the residual stress relieving is followed by dislocations movement and consequently geometric deformation (ERICSSON, 2002; LU, 2002). Therefore, the distortion analysis was performed before and after each manufacturing process under analysis. It is an indirect method to monitor the variation of the surface state not directly converted in change of the residual stress intensity.

The topography analysis was composed by the collection of amplitude, spectral and functional roughness parameters. At least for processes defined by predominant mechanical loads, such as shot peening, there is a strong relationship between the roughness pattern and the residual stress uniformity (ZHAN; JIANG; JI, 2013; REGO; GOMES; BARROS, 2013). This is indispensable information to the interaction analysis under the perspective of the heterogeneity state of residual stresses. Nevertheless, even for surfaces submitted to manufacturing processes with coupled loads, such as the machining, the roughness pattern is an indication of the process parameters set. In this scenario, the topography measurements contribute to the definition of the specimen groups that must be selected for residual stress measurements.

Concerning the measurements of the first case study, both distortion and roughness were analyzed with the same technique, the chromatic aberration confocal microscopy (Figure 4.10). This technique is based on the principle of colors' different wavelength for determining the depth under analysis. The confocal microlenses are responsible for creating the chromatic aberration over the light beam generated by the system. The light is spread in full spectrum

lighting and, thus, distinct wavelength rays. These incident lighting rays are reflected in the surface to several different directions, including back to the system detector. Depending on the sample topography on the analyzed region, there is higher detection intensity for one specific color. This color information is used for determining the wavelength to be input in the real depth calculation (TIZIANI; WEGNER; STEUDLE, 2000; SHI et al., 2004). The equipment used, according to the described principle, is a *Cyber CT 100*. For the purposes of topography and distortion, two regions of each block were measured with different specifications. An area of 3 x 10 mm was measured with a lateral resolution corresponding to steps of 2 μm , for assessing the roughness profile (Figure 4.10). The distortion assessment did not require such a high resolution, and it could be set to a lateral step of 100 μm . On the other hand, it demanded covering an extended area, with dimensions of 90 x 15 mm in the case of the roughing machining specimens and 43 x 37 mm for the finishing machining blocks.

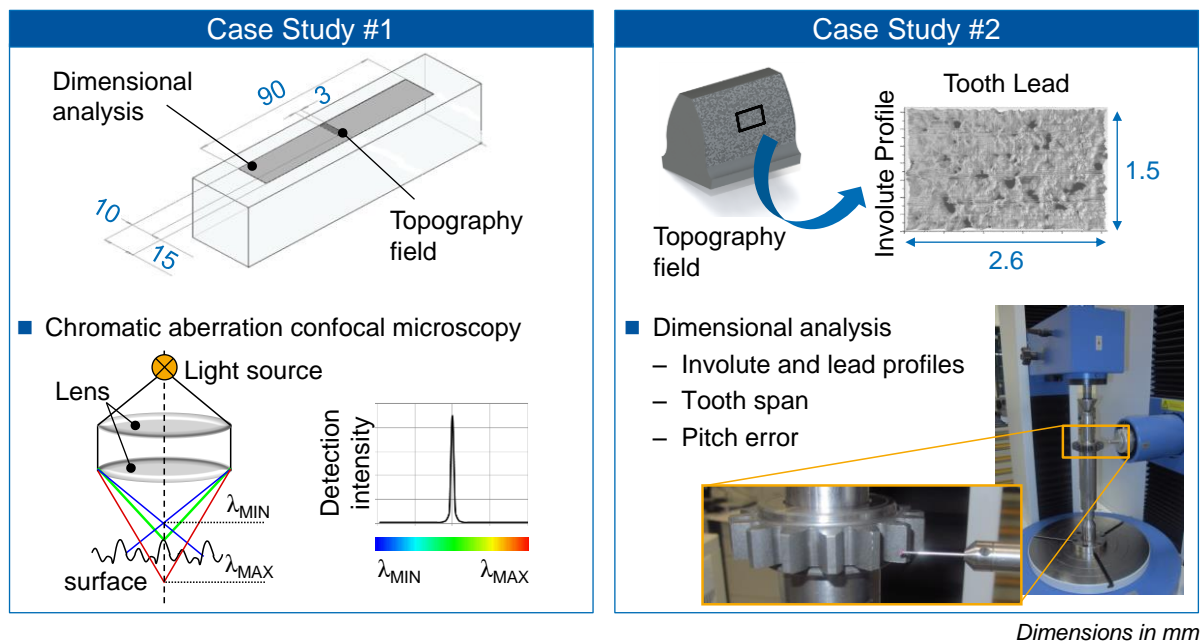


Figure 4.10 – Techniques and procedures used for topography and dimensional analyses.

The same equipment was also applied for the monitoring of machined specimens' production. As presented in the topic 4.2.1, one of the parameters for defining the machining groups is the tool wear. The chromatic aberration confocal microscopy is therefore applied for a dimensional evaluation of the wear evolution over the inserts cutting edge. With a section profile extracted from the cutting surface, it is possible to measure the edge radius of the insert created due to the tool's usage.

The topography measurements with the gears were performed with a tactile profilometer *Hommel-Etamic Nanoscan 855*. The teeth flanks were measured by a metering needle with radius of 5 μm and a tip angle of 90° . The measurement was planned to cover an area of 2.6 mm in the direction of the tooth lead by 1.5 mm in the direction of the tooth involute profile (Figure 4.10). To the respective directions, the resolutions selected were 5.0 μm and 0.1 μm .

For both case studies, the measurement and analysis definitions were guided by the requirements of DIN EN ISO 4287, DIN EN ISO 4288 and ISO 13565-2 (DIN, 2010; DIN, 1998; ISO, 1996). Besides the conventional two-dimensional metrics, areal parameters were as well computed, according to the recommendations also known as “The Birmingham 14 parameters” (DONG; SULLIVAN; STOUT, 1992; DONG; SULLIVAN; STOUT, 1994). *Gaussian* and polynomial filters were applied to separate the patterns of roughness, waviness and form error. The filter, likewise the cut-off value to separate the mentioned geometric orders, was individually selected for each surface manufacturing pattern, but equally applied to the samples after each process.

The dimensional analysis for the second case study could not be simply performed with the same surface of the topography measurements. The distortion on gears is an effect that refers the teeth to the gear hub and in-between them. Therefore, a complete measurement under the same coordinate system was required for this dimensional analysis. A *Klingelnberg P40* gear measuring center, which has the concept of a Coordinate Measuring Machine (CMM) but also equipped with a rotary table, was used for the measurements (Figure 4.10). The involute and lead profiles from four out of the sixteen pinion’s teeth were measured, both in the right and left flanks. The pitch error and the tooth span (Figure 4.8) are calculated based on a measurement involving all the pinion’s teeth. All the measurements and the results’ assessments followed the standard DIN 3961 (DIN, 1978). A reference tooth was adopted to be the first measured flank, enabling the dimensional comparison after each of the manufacturing processes of this case study.

4.3.3 Material Investigation

According to the complete comprehension model of the residual stress state evolution, the discussed topography and dimensional analyses can be seen as traces. They are mainly consequences of manufacturing loads and their corresponding stress state alterations. However, this comprehension model demands also the root causes that drive the interaction

in-between the manufacturing processes. Part of these explanations should be possible to be investigated through evidences of a material investigation.

The most fundamental examinations were conducted with metallography, by means of optical microscopy. Structural aspects such as the grain size and its dispersion, texturing effects, phase's identification and precipitates existence are the focus of this step (Figure 4.11). They can indicate the event of phase transformation after each analyzed process, and provide explanations to potential differences observed on the residual stress state between measurement directions. Additionally, these features directly reflect phenomena in the same domain level of residual microstresses. The metallographic analyses were done over the depth profile of the samples. The specimens were polished and then etched with a 3% Nital solution (3% HNO_3 + 97% alcohol). The blocks were assessed with a *Carl Zeiss Ultraphot III* microscope while the gears' pictures come from a *Carl Zeiss Axio Imager.M2m* microscope.

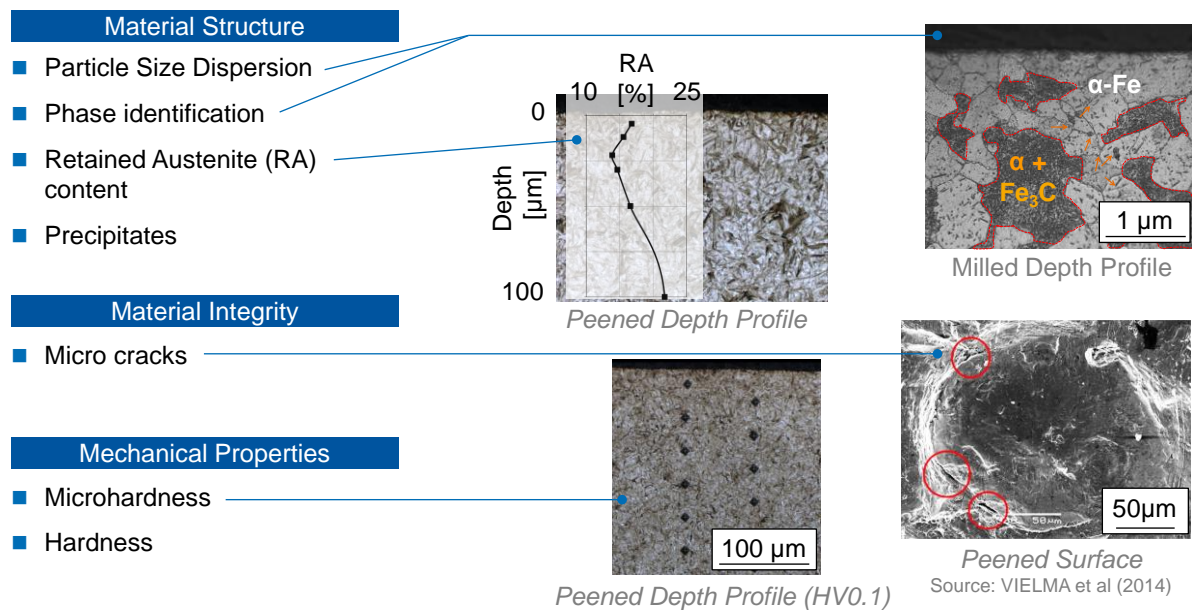


Figure 4.11 – Methods for the material investigation.

The identification of the steel phases in the specimens was still complemented by its quantification, and, in this specific case, of the retained austenite content. The value is necessary to calculate the residual macrostress, as shown by Equation (2.3). The quantification could be even done with the optical microscope through statistical sampling. However, a low content of retained austenite, of about 15%, is expected for the specimens of the present study. At this level, the quantification reliability with microscopy methods

decreases significantly. This scenario requires the employment of the X-ray diffraction technique. A wide diffraction angle range containing the reference peak positions for each phase is scanned. The assumption for the materials herein made, after the case hardening process, is the formation of a dual-phase composition of martensite and retained austenite. The volume fraction is thus calculated by considering the relationship between the integrated diffracted intensity of the profile from the both phases. Part of the determination procedure is also dependent on constant values of each phase, such as the *Miller* index and the diffraction angle itself (CULLITY, 1978). Before and after each manufacturing process under investigation, the specimens were submitted to the XRD technique for assessing the contents of each phase. The equipment and the accessories used are the same than the ones described for the residual stress measurement procedures. The volume fraction of retained austenite was assessed as a depth profile, according to the layers already removed for the residual stress measurements (Figure 4.11).

Microhardness measurements were conducted in the same samples, in order to assess the intensity of the work hardening along the depth. The work hardening is considered to influence the diffraction profiles, and the microhardness results can be used to verify how much of this influence is actually originated from the strain hardening effect (KIM et al., 2005; SOADY et al., 2013). For every sample already case hardened, *Vickers* indentations with a load of 100 g were used (HV0.1). For the machined samples, the lowered surface hardness value demanded the usage of a load of 50 g (HV0.05). The measurements of the blocks were performed with an *Emco-Test DuraScan 50* hardness testing machine. For the second case study, the gears were measured with a Fischerscope HM2000. The further definitions about the microhardness depth profiles (Figure 4.11) followed the standard DIN EN ISO 6507-1 (DIN, 2006b).

The studies of Kim, Cheong and Noguchi (2013) and Hassani-Gangaraj et al. (2014) alert to the possibility of microcracks appearance due to severe shot peening parameters (Figure 4.11). The open space created by cracks redistributes the local residual stresses and therefore influences the diffraction broadening analysis. The surfaces of the gear specimens, after the shot peening process, were thus investigated with high magnification, by means of the Scanning Electron Microscopy (SEM) technique. The samples were examined with a *Cambridge Scan S2* microscope.

4.3.4 Fatigue Tests

The content of the third question established in the topic “Objective and Approach” refers to the relevance of the residual stress interaction to the fatigue strength. For this purpose, fatigue tests were conducted with the specimens of the second case study. Since the flanks of the gears were the surfaces under investigation, the specimens were submitted to rolling contact fatigue tests. The fatigue strength was approached into two contexts: performance and behavior. The first topic had as focus to register the different lifetime provided by each group of specimens. At the second one, aspects of the damage morphology and evolution were collected with a linking purpose to the surface and material analyses previously described.

The fatigue tests were performed with a power-recirculating gear test rig (Figure 4.12). In this bench concept, a test gear set and a slave gear set are assembled at the rig opposite ends. One shaft connects the test driver gear to the slave driven gear. The power loop is closed since the other shaft connects the slave driver gear to the test driven gear. One gearbox is loaded against the other by twisting the shafts through a toothed wheel, to create a locked-in torque at the coupling flanges. This rig is also known as “four-square” or “FZG”, in attribute to their concept inventors, the laboratory *Forschungsstelle für Zahnräder und Getriebebau*. The locking system allows the application of a static torque, representing the required load on the test gear. The entire loaded arrangement is driven by an electric motor at the required speed, which needs only to supply power for friction and inertia losses (DAVIS, 2005).

The specific rig employed has a center distance of 91.5 mm and it is equipped with an electric motor of 14 kW. The torque is manually applied through a lever and a set of weight-calibrated disks. The corresponding amount of hanged disks to the desired torque level is specified by the standard DIN ISO 14635-1 (DIN, 2006).

Three tests for each group were conducted with a fixed torque intensity of 534 N·m. This is the input torque of the samples, once the pinion is directly assembled on the torque application shaft. The meshing gear has 24 teeth, creating a transmission ratio of 1.5:1. They were also ground and manufactured according to the FZG-C_{MOD} design. The motor speed was set to rotate at 3,000 rpm, and thus 4,500 on the shaft where the pinions are assembled. With this setup, each hour of test represents 270,000 cycles. The overall preparations for the tests were guided by the recommendations of the report FVA 563-I, from the *Forschungsvereinigung Antriebstechnik* (TOBIE; MATT, 2012).

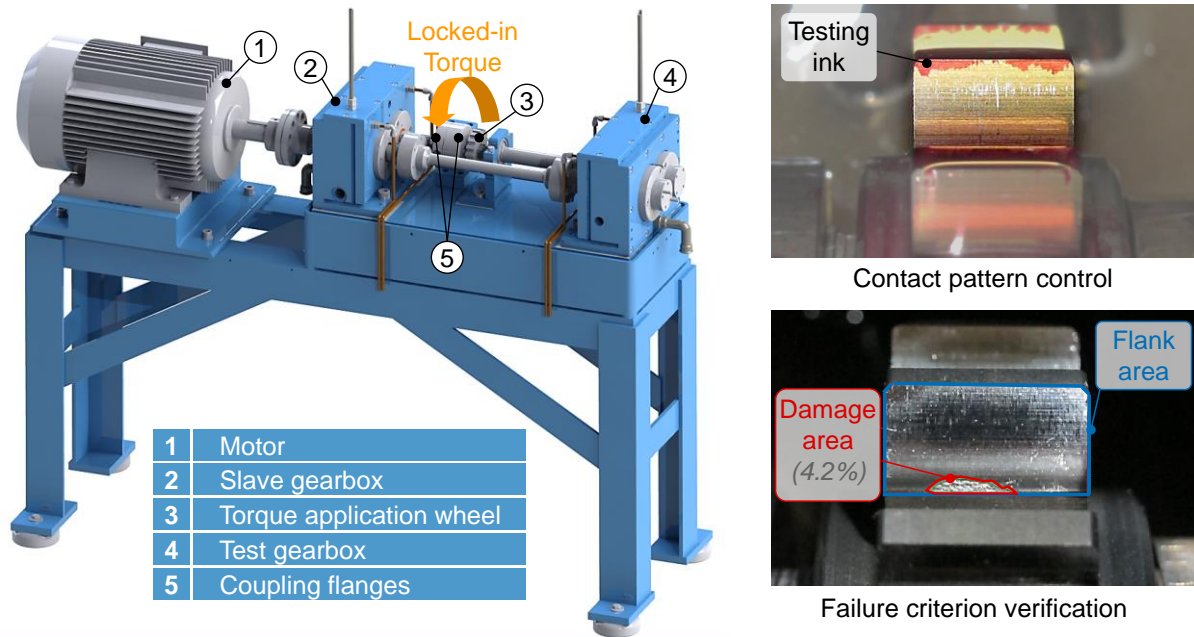


Figure 4.12 – Gear fatigue test: power recirculating test rig and the visual inspection procedures of the tested pinion.

The test starts with a control of the contact pattern. After the gears assembly, an appropriate ink is applied over the flanks, and the rig, already loaded with a torque intensity of 135 N·m, is manually rotated. The regions where the ink is removed reveal the contact pattern (Figure 4.12), and indicate whether any mistake coming from the assembly or even from the manufacturing is present. The same torque intensity is kept for the run-in procedure. At a motor speed of 3,000 rpm (pinion speed of 4,500 rpm) and an oil temperature of 60 ± 1.5 °C, this step lasts one hour. It has as purpose to provide conditions for a stable operation, by removing uneven roughness patterns and accommodating the stresses introduced by the assembly. The oil selected to be used inside the test gearbox was a *Shell Spirax ASX 75W90* (“Attachment D – Testing Specification”).

After the run-in procedure, the temperature is risen to 90 ± 1.5 °C and the rig is loaded to the desired torque intensity. Under the same previous conditions, the test is started and the register of cycles is initiated. A relaxation of the load is expected due to the elastic stresses distributed along every part in contact inside the rig, aside the wear itself. Due to this reason, with the first fourteen hours completed, the test is interrupted and the load level is verified. The verification is performed in such a way the torque is not relieved, only uploaded to the planned initial level. Once restarted, the test is run up to the failure. The criterion that defines the completion is the percentage of the surface already damaged. According to the report FVA

563-I (TOBIE; MATT, 2012), this limit is set to 4% of the flank area, as depicted by the example of the Figure 4.12. A visual inspection is performed at each seven hours, with a photographic register of the flanks. The rig is also provided of a vibration sensor. Its setup enables the interruption of the test in case the damage size overcomes the specified limit of damaged area within the inspection interval of seven hours.

The second investigation aspect refers to the morphology of the damage. The objective is to characterize the failure region, in order to verify potential correlations with the residual stress state. The task is basically composed by identifying the fatigue crack mechanism, measuring specific geometric features of the removed material portion and by monitoring the damage evolution along the test.

After the test is completed, the gear is cut to separate the several teeth with damages over the surface. For each tooth, a surface map around the region of the damage is created with a *Keyence VK-X100* confocal microscope. Geometric features from the removed material portion such as the maximal depth, the total removed area and volume and the angle of the damage walls are collected. An example of the measurement is shown in the bottom left corner of the Figure 4.13

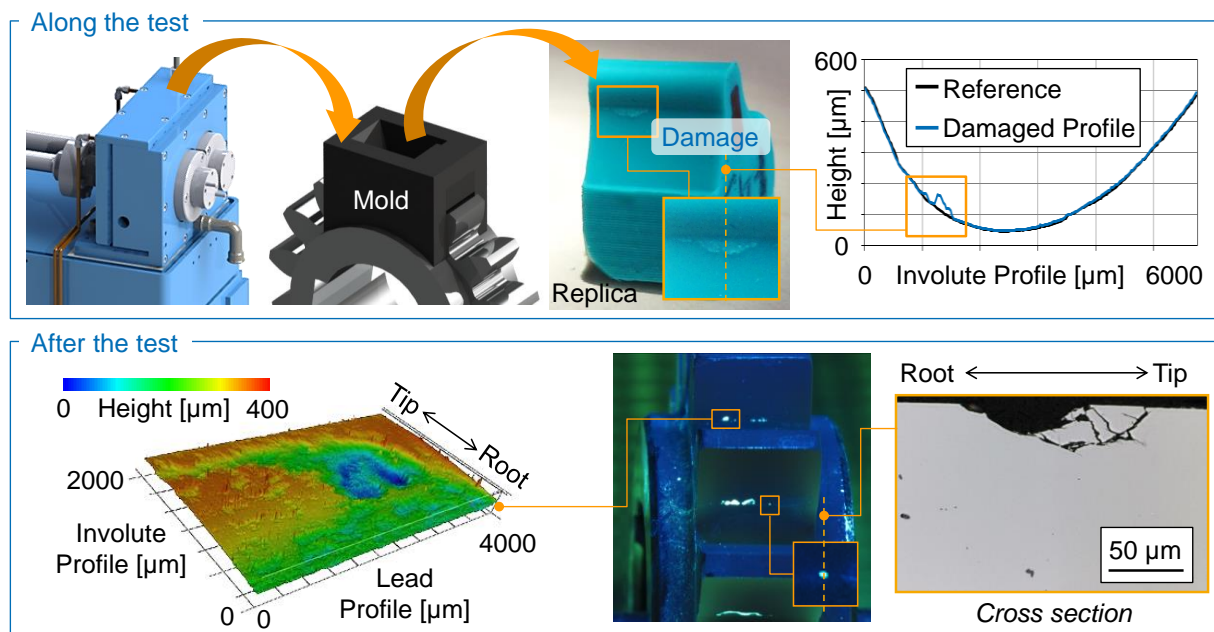


Figure 4.13 – Procedures for the damage morphology analysis during and after the test completion.

However, not always the information can be taken from the area where the material is removed. As the created damage keeps in contact along the test performance, further deformation can be superposed, hindering the identification of features that characterize the original failure mechanism. Hence, the applied method concentrated on finding regions where the fatigue cracks still did not lead to the material removal. Or, at least, where there were small damages such as the one shown in the Figure 4.13. The search for the described regions demanded the application of a crack inspection method. The failed gears were submitted to a liquid penetrant test, according to the standard DIN EN ISO 3452-1 (DIN, 2014). A fluorescent liquid, in combination with an ultraviolet lamp, highlighted the areas where the fatigue cracks were connected to the surface. With this picture, cross sections were made on regions directly besides the end of a large damage, or over regions with a small-scale material removal (Figure 4.13). The samples, polished but not etched, were then observed with the same optical microscope described for the material investigations. The images were also used to identify the crack propagation mechanism. By considering a statistical approach with ten identified cracks from each manufacturing group, their geometric features were mapped, with special attention to the crack depth.

Finally, the mentioned geometric features were examined regarding to their evolution along the test. A non-destructive method was utilized through the production of replicas from the damaged flanks. At the first inspection that a surface failure was observed, the procedure was applied, without removing the pinion out of the gearbox. With the reduced gearbox temperature, the replica material *Panasil contact two in one Light* was applied to the flank. The referred material proved to demand only a few minutes to satisfactorily reproduce the surface structure. The material was fulfilled into a customized mold for the pinion design, produced by means of the FLM (Fused Layer Modeling) additive manufacturing process (Figure 4.13). A surface analysis, with the same equipment and with an analogous procedure to the method described for the teeth after the test, was conducted with the extracted replicas. After the first instance when the damage was observed, the visual inspection interval was shortened to half of the time (3.5 h). At each inspection up to the failure criterion was achieved, replicas of all damaged flanks were produced. The evolution of the damage geometric features was analyzed as a comparative approach between the pinions produced with different residual stress states.

5 Results and Discussions

All the results and the corresponding discussions are organized in three topics inside this chapter. Each topic is related to one of the research questions introduced at the “Objective and Approach”.

5.1 The Role of the Residual Stress Intensity on the Processes' Interaction

Guided by the first research question, the two case studies were set to explore the various features of a residual stress depth profile. Among the targets, the surface value or the maximum intensity and its depth can be mentioned (Figure 5.1). Considering the both chain stages analyzed, different results were successfully achieved as input profiles to the interaction investigation. The case studies were equally reported in two steps. Firstly, there is a description of how the distinct residual stresses were induced by the first process of the interaction. In the sequence, the surface integrity out of the second process is explained, and attempts to connect it to the prior residual stress state are established. An overall physical explanation closes the chapter, unifying the outcomes of both case studies.

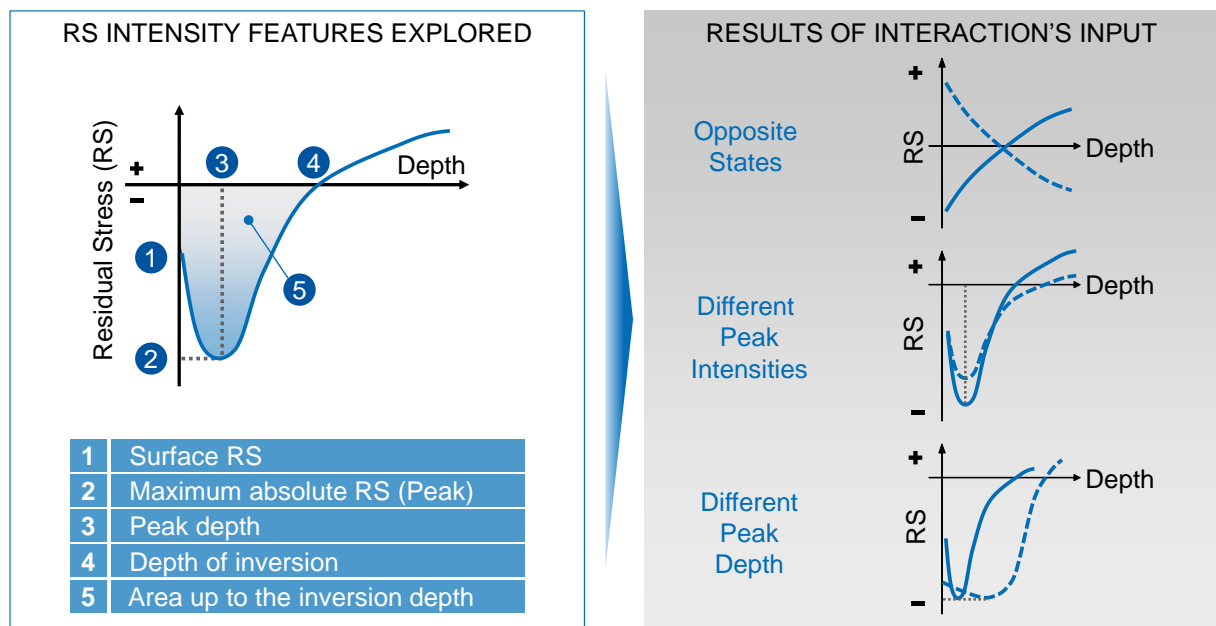


Figure 5.1 – The residual stress intensity features explored and the results achieved for the input of the interaction analysis.

5.1.1 Inducing Different Stress States through the Soft Machining

The induction of the residual stress state on the finishing specimens was directly conducted by the definition of the cutting parameters, such as described at the last chapter. For the roughing specimens, the surface integrity analysis was preceded by the phenomenon investigation. The specimens' selection was hence decided based on the information of the mechanical and thermal loads, as well as of the material structure.

The analyzed cutting forces were oriented towards the radial depth of cut (F_x , normal to the plane) and the feed direction (F_y , longitudinal to the plane). The axial depth of cut component (F_z , transversal to feed, but contained in the plane) was disregarded in the analysis once the piece of material subjected to this magnitude is removed in the forthcoming pass. The force components behaved fairly constant along the cutting operation. The analysis was therefore zoomed into a small period in which the three inserts exerts force over the surface. The results of the forces in the radial depth of cut and feed directions are shown in the Figure 5.2.

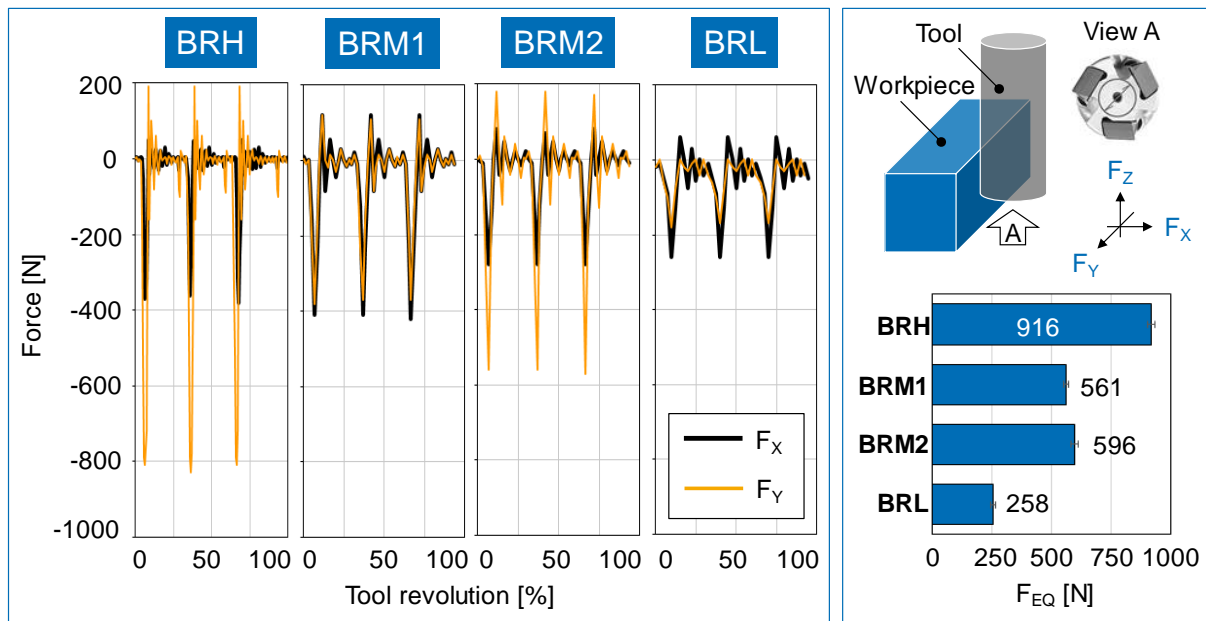


Figure 5.2 – Results of the mechanical loads assessed for each roughing group.

The first observation of both charts is that the comparison between groups does not behave equally between the normal and the longitudinal components. The lowest force is found for both components in group BRL. However, the highest force in the radial depth of cut direction occurs in group BRM1, while the highest feed direction force is from group

BRH. The explanation refers to the comprehension of the up-cut and down-cut mechanisms. The chip thickness for the down-cut milling is larger in the outset of the cutting, gradually reducing up to the chip removal. The opposite happens with the up-cut milling, in which the chip thickness is increased along the cutting period. The tool contact force is more oriented to the normal direction in the down-cut milling than in the up-cut milling. Analogously, the up-cut milling force direction has predominance in the longitudinal direction. This rationale goes in agreement with results from F_Y (Figure 5.2).

The influence of the further parameters can be observed through the comparisons with the same cutting direction (BRHxBRM2 and BRM1xBRL). It is possible to see in both comparisons the reflection of the cutting speed and the feed rate to the force intensity along both directions. The most important conclusion from these charts comes when considering the magnitudes in both directions simultaneously. A combined analysis considering the equivalent forces is shown in the Figure 5.2. The equivalent force is calculated according to the Equation (5.1).

$$F_{EQ} = \sqrt{F_X^2 + F_Y^2} \quad (5.1)$$

Where:

F_{EQ} : Equivalent force

F_X : Force in the direction of the radial depth of cut

F_Y : Force towards the feed direction

The results follow the expectation expressed by the cutting force scale depicted in the Table 4.2. Furthermore, the difference between the groups with the highest and the lowest forces, respectively BRH and BRL, is significantly large to consider potential differences in residual stresses originated from the mechanical loads.

The second criterion to highlight the potential differences between the groups is the thermal load induced to the workpieces. It was assessed through the measurement of the process temperature, by means of thermocouples and a thermal camera. In this case, the applied methods did not allow drawing conclusions as efficiently. The first issue noticed with using the thermal camera was the magnitude of the temperature values indicated. At any moment of the cutting process, the maximum temperature was in the order of 40°C (left panel of the Figure 5.3). Besides, the high reflectivity of the surface was mirroring the tool temperatures, not representing the value at the workpiece's surface. The tentative for solving

the reflectivity was to consider as procedure making the pictures in just after the cutting ended and the tool moved vertically. Even though, the pictures comparison of Figure 5.3 shows that no real difference can be considered between the groups.

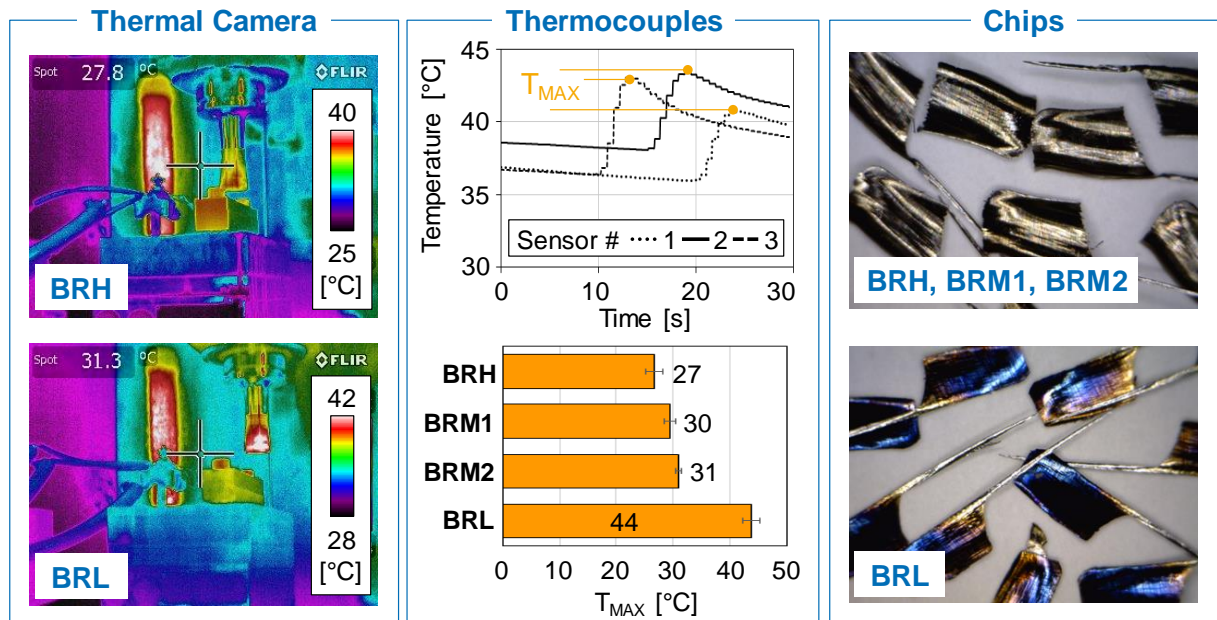


Figure 5.3 – Methods approached to investigate the thermal loads induced during the roughing process.

The potential reason for the method failure is on the camera frame rate specification. The camera used has a frame rate of 60 Hz. Similar experiments with conclusive analyses employed cameras with frame rate varying from 750 Hz up to 3,400 Hz (ASPINWALL et al., 2013; PITALLÀ; MONNO, 2011; ABUKHSHIM; MATIVENGA; SHEIKH, 2006). Additionally, by needing to wait the tool to move far away from the surface, the high cooling rate did not allow to register a value close to what must have been the maximum surface temperature. The study published by Abukhshim; Mativenga; Sheikh (2006) conducted temperature analysis in a HSC process with a thermal camera of 900 Hz. It was shown that the temperature decreased from 1,200°C to 200°C in about 0.5 s and from 1,000°C to 600°C in a distance of 0.2 mm from the cutting edge.

Similar magnitude values for the temperature measurement were obtained with the thermocouples. The results were measured along the process time with the three thermocouples, as shown in the central panel of the Figure 5.3. As awaited, the temperature was risen in the positioning sequence of the thermocouples' assembly. The variation in the

depth manufacturing of the thermocouple's bores and the fixation of the sensors inside them explain why not always the maximum value registered is the same in all the sensors. Lin et al. (2013) did a very similar experiment setup, with using thermocouples in end milling process of a 300M steel grade. The results showed the same maximum temperature order (under 100°C). The slight difference is justified by the different process parameters, material and thermocouples positioning. A summary with the maximum values acquired in each sample is displayed in the Figure 5.3. Despite not showing the expected magnitudes, the results within a comparative analysis are conclusive. As considered in the samples planning of the Table 4.2, there is a positive trend to increase the temperature in the samples from the group BRH to the group BRL.

If the maximum values of the temperature do not enable to differentiate the effects between the groups, a better understanding could be provided by the examination of the chip's color (Figure 5.3). The chips produced by the groups BRH, BRM1 and BRM2 have a silvered color. On the other hand, the color of the chips from the group BRL is a mix of blue, violet and brown. The color analysis is in agreement with the study of Ning, Rahman and Wong (2001), in which a correlation between the predicted chip temperature and its observed color was performed. The highest temperatures were characterized by a dark blue color, which is explained by a severe extent of oxidation. The same assessment can be found with regard a correlation between the color and the process parameters. The dark blue is induced by increasing the cutting speed and the tool wear (GOMES, 2001; TOH, 2005; CUI et al., 2012).

The evidence of the different thermal loads is also registered by the third aspect of the physical phenomena that bridge the process parameters to the residual stress state. The material structure of the specimens was assessed along the depth, and some images are depicted in the Figure 5.4. The main observed structure is the same for all the specimens, composed by a primary ferritic phase and a perlitic phase. The cementite is more sensitive to the Nital solution, which characterizes the perlitic grains by a dark color. This composition is expected for the alloy examined, which is a hypoeutectoid steel ($< 0.77\%$ of carbon content). But what is not the same among the samples is the outer layer formed by a few micronmeters. A white layer, approximately between 5 μm and 10 μm thick, is observed only on the images taken from the group BRL. Based on the previous results of the process' temperature, it is reasonable to confirm that the white layer is a thin austenitic-martensitic region, generated by the higher heat transfer rate deployed during the cutting process of this group. This conclusion goes in agreement with the machining integrity investigations reviewed by Grum (2010), and reinforce the outcomes from the thermal load assessment.

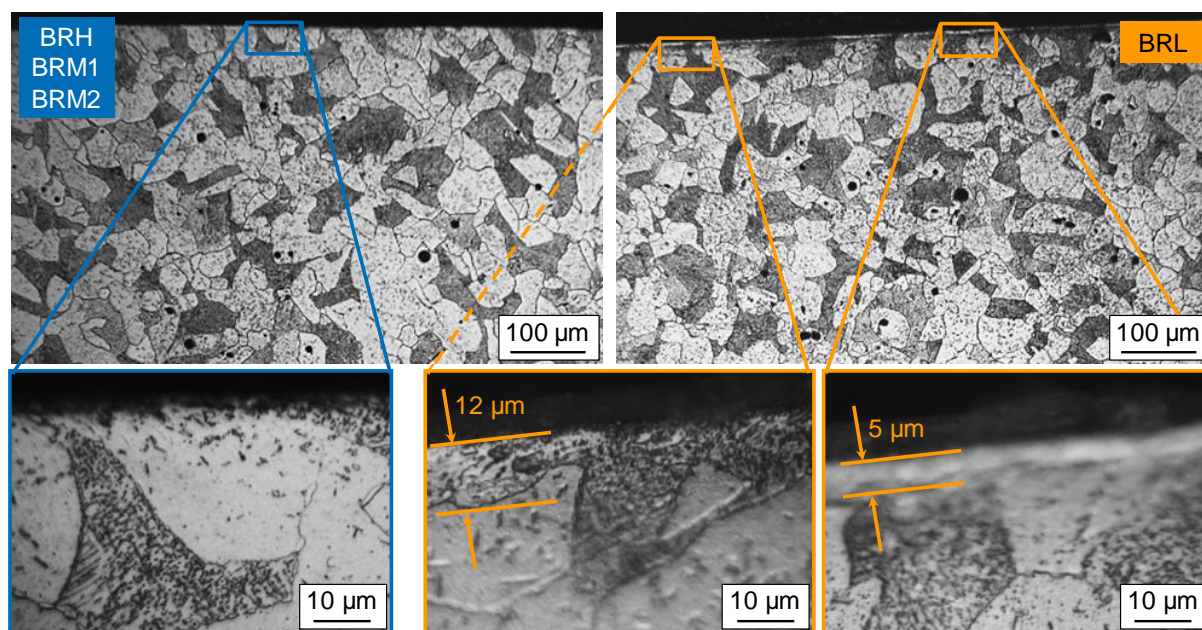


Figure 5.4 – Metallographic comparison exposes the different microstructure observed on the outer layer of the specimens of the group BRL.

Finally, all the discussions allowed the selection of the groups BRH and BRL according to the phenomenological method presented in the Figure 4.4. The specimens of the group BRH show the highest mechanical load and a trend to have received the lowest thermal gradient on the surface. On the other hand, the specimens of the group BRL registered the lowest force values, with about 27% of the intensity measured for the group BRH. Moreover, the thermocouples results, the chips color assessment and especially the microstructure observed from Group BRL are strong evidences that this machining setup induced the highest thermal loads.

Together with the finishing machining specimens (BFH and BFL), the specimens from the groups BRH and BRL were submitted to the residual stress assessment. The depth profile results are shown in the Figure 5.5, followed by the machining parameters of each group. The most pronounced difference is observed when comparing the profiles of the roughing specimens against the ones from the finishing samples. While the groups BFH and BFL assumed a compressive intensity over the outer surface, a tensile residual stress state characterizes the surface of the groups BRH and BRL.

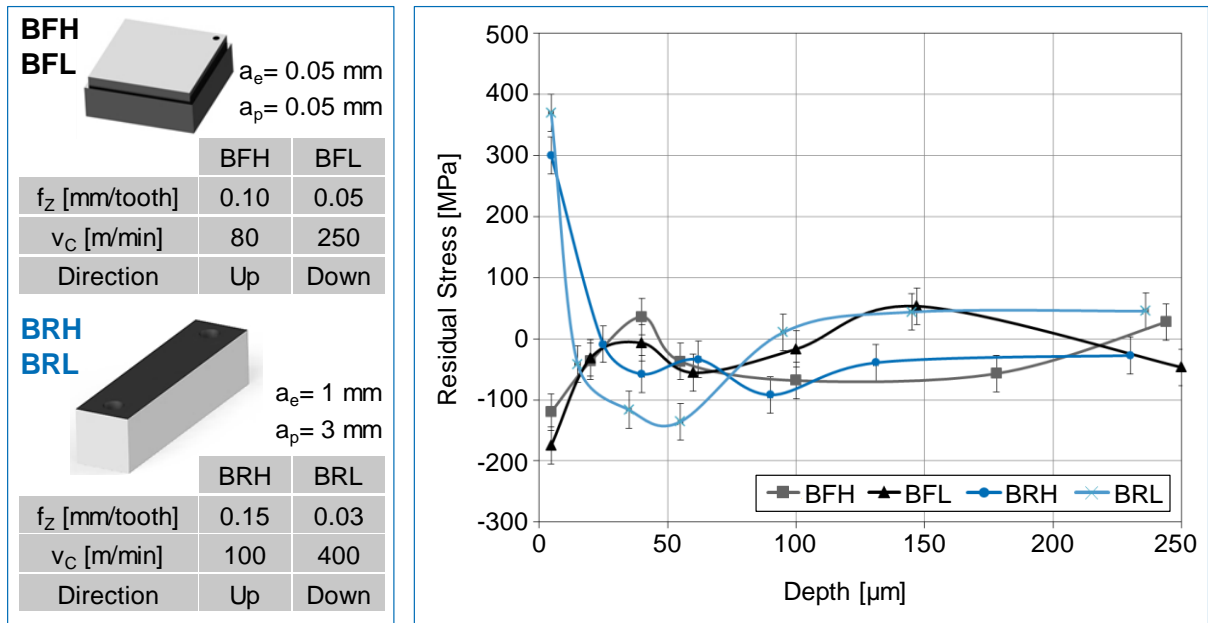


Figure 5.5 – Macro residual stress measurements of the machined specimens.

This result is representing the opposite stress states introduced in the Figure 5.1, which is the most important achievement of these machining experiments. They empower a meaningful input to the interaction analysis with the heat treatment by means of stress states positioned at the different extremities of the stress state. The opposite behaviors are particularly important to this case study. The heat treatment produces completely new steel phases, highly modifying the initial stress state. Any expectation for distinct results after the heat treatment requests thus the machining of samples differed by large differences on the residual stress intensity.

The potential explanation to the opposite states is based on the main difference between the roughing and the finishing processes, which is defined by the depth of cut (a_e). This parameter recalls the conclusions from the publication of Jacobus, Devor and Kapoor (2000), depicted in the Figure 2.15. The residual stress profile of a machined surface is dependent on the balance between the thermal and the mechanical strains in the surface and near-surface layers. The groups BFH and BFL presented residual stress profiles matching to the “Case 1” from the referred publication and figure. It means that the mechanical plastic strain was kept higher than the thermal load up to the subsurface layer. This balance changes for the groups BRH and BRL, whose profiles follow the “Case 2” of the Figure 2.15. The thermal strain over the surface was high enough to overcome the plastic strain in the subsurface layer.

The interpretation considering the depth of cut must include as well the tool edge radius (r_e). The average tool edge radii measured for the roughing and the finishing specimens along the experiments are displayed in the Figure 5.6. By comparing the edge radius to the depth of cut (a_e/r_e), distinct results can be observed between these groups. This value, hereafter called as cutting depth ratio, is linked to the cutting forces distribution, between shearing and ploughing forces. The smaller value creates a condition in which the cutting process has a larger contribution from the ploughing mechanism. This type of force actuates pushing the tool perpendicularly against the workpiece, smashing the first micrometers of the surface. This description is reinforced by the different surface patterns between the roughing and the finishing specimens. The surface height profile along the cutting direction of the specimens BRH and BRL assumes a milling conventional aspect, in the shape of the negative value of an absolute sinusoidal signal. The samples BFH and BFL, however, demonstrate a more waved pattern (central panel of Figure 5.6). Under a purely mechanical load perspective (Figure 5.6), the ploughing force promotes the stretching of the surface, leaving a compressive residual stress state. The observed connection between the cutting depth ratio and the cutting forces distribution converges with the publication from Yan, Zhao and Kuriyagawa (2009). The respective explanation around the residual stress mechanism matches the results from the profiles representing the groups BFH and BFL.

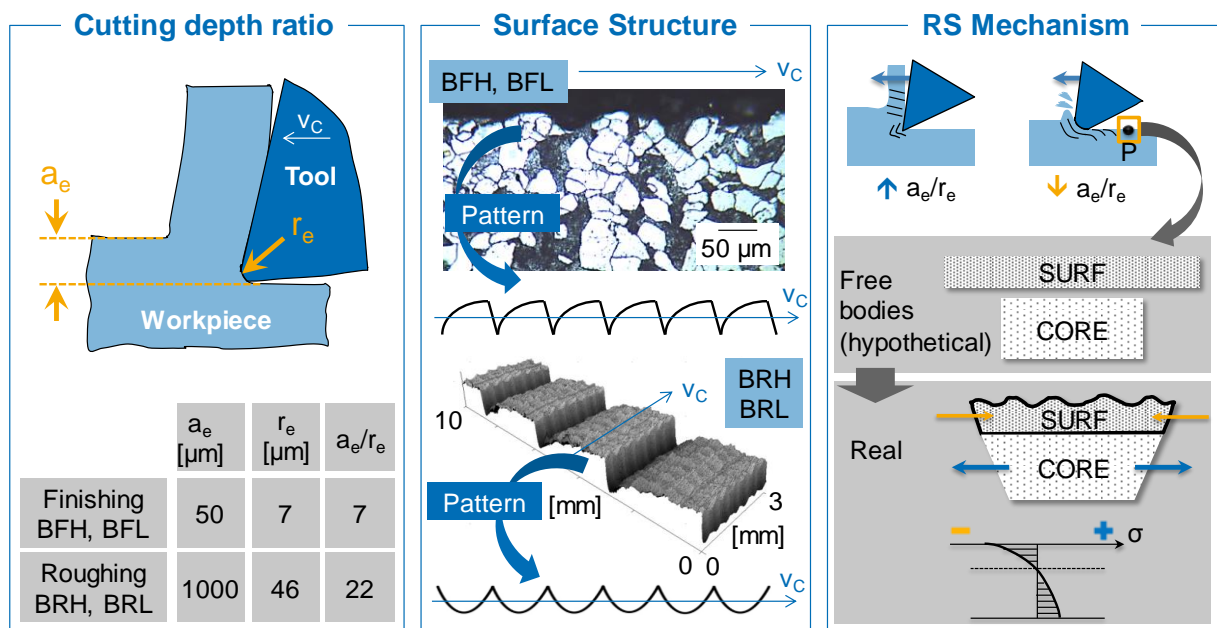


Figure 5.6 – Relationship between the depth of cut and the cutting nose radius as the influence for the opposite residual stress states observed between roughing and finishing specimens.

A next comparison is observed between the profiles from the groups BRH and BRL, driving the discussions back to the results of force, temperature and microstructure just presented. Although not largely different, the outer surface value of the group BRL is the most tensile one. This takes place right over the first few micrometers of the surface, which matches to the size of the white layer identified in the Figure 5.4. Along the following depth layers, though, the group BRL assumes a more compressive intensity, through a steep transition. This behavior inversion is a consequence of the equilibrium principle, in such a way that the higher tensile stresses of the surface are followed by a larger compressive magnitude.

A similar result from the roughing specimens was expected for the finished samples. However, the results of groups BFH and BFL do not show to be statistically different. And if a trend over the outer surface would be pointed out, it would be to state that the group BFL is provided by the most compressive magnitude. The corresponding explanation would demand a similar approach than the one conducted for the roughing specimens, by means of assessing the cutting force and temperature and the workpiece's microstructure.

A final remark is noted regarding to the different material batches from which the roughing and the finishing groups come from. Indeed, a comparison between the metallographies of the Figure 5.4 and the Figure 5.6 shows that the manner in which the carbides precipitated differs. Whereas they mainly appear on the grain boundaries for the groups BFH and BFL, they are mostly dispersed inside the grains for the groups BRH and BRL. However, these carbide arrangements are observed to be invariable along the depth. Since the stress curves of the Figure 5.6 can be considered the same from the depth of 100 μm on, at least the macrostresses show not to be impacted. Therefore, the difference is most likely to be explained by the distinct batches of material from which they come. The further material properties, such as grain size and elongation aspect and the chemical composition, are consistently the same between the groups.

Overall, the results prove to comply with the machining experiment's main goal. The produced samples are separated by a large different and still characterized by opposite residual stress states. The coexistent tensile and compressive database constitutes an adequate input to the interaction analysis with a process of high impact to the lattice deformation of the steel: the heat treatment.

5.1.2 The Interaction between Soft Machining and Heat Treatment

In this first case study, the announced convergent experimental approach is fed by the provision of parts with different residual stress states, as just described. The purpose of this topic is to explore the surface integrity outcome of submitting these parts to the same heat treatment process.

All the samples, from the roughing and the finishing process investigations, were then simultaneously case hardened, through a cycle composed by gas carburizing, oil quenching and tempering (Table 4.3). The results of the residual stress measurement along the depth, corresponding to the α -Fe phase along the cutting direction, are shown in the Figure 5.7.

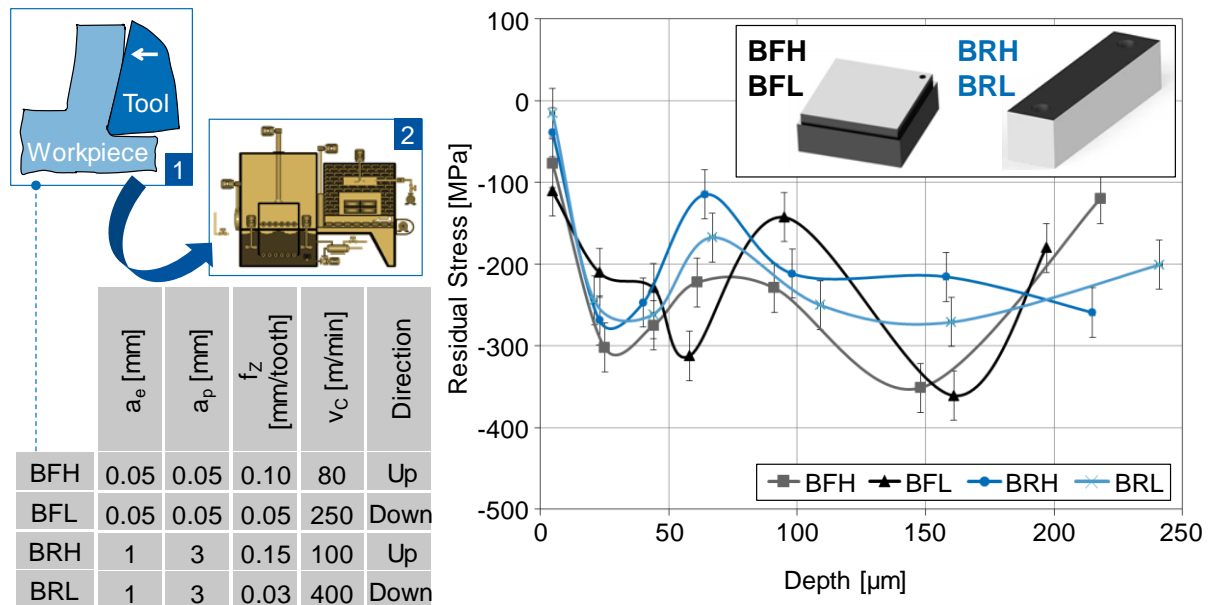


Figure 5.7 - The different residual macrostress states induced after machining do not create meaningful differences after the heat treatment.

The direct observation is that no meaningful differences can be identified among the profiles of the treated samples. At the surface, the stress of the four parts varies within a short range of 85 MPa. All the charts are then driven to an inflection point defined by a compressive value between 250 MPa and 315 MPa. The following points show an oscillating behavior, possibly representing an attempt for achieving the equilibrium principle, inside a local boundary.

In general, the main profile features fit to the conventional residual stress state of low-alloy carbon steels after a case hardening process. The value over the surface, the peak intensity and its depth converge with the outcomes of the survey of Parrish and Harper (1985), based on residual stress measurements of 70 similar carburized steel alloys. From a chain evolution perspective, the results are in agreement with the statement from Réti (2002). The carbon content decreases the temperature in which the martensitic transformation starts. It implies that the transformation evolution is from the core, whose carbon content is much lower, outwards the surface. The martensitic transformation during the cooling cycle is characterized by volume expansion and shear strain. Consequently, this carburizing mechanism shifts the existing stresses to more negative magnitudes. This behavior was observed with all the samples, as the roughing specimens assumed negative values and the finishing ones became even more compressive.

The description above exposes the results proximity between the samples, both by the intensity and by the profile's shape. It highlights that, independent on the machining-induced stresses, the heat treatment process delivers the same residual macrostress state. Formatting the statement to the thesis' objective, the effects of the processes' interaction from the early manufacturing stage are not reproduced on the final residual stress state. As described in the state-of-the-art, this result was already claimed by the publications of Barsoum and Barsoum (2009), Epp et al. (2011) and Navas et al. (2011). Nonetheless, none of them had experimentally proved this reaction by specifically submitting parts with opposite stress states to the same heat treatment.

Still, the interaction effect is to be observed for the overall surface integrity characteristics. By analyzing residual macrostresses, the geometric distortion evolution must be considered. For this purpose, the topography maps of the samples were configured to separate regions of negative and positive values. They were respectively defined to be below and above a reference average plan, which is determined by the least squares method. The negative areas are identified with the black color in the images of the finishing specimens before and after the heat treatment (Figure 5.8).

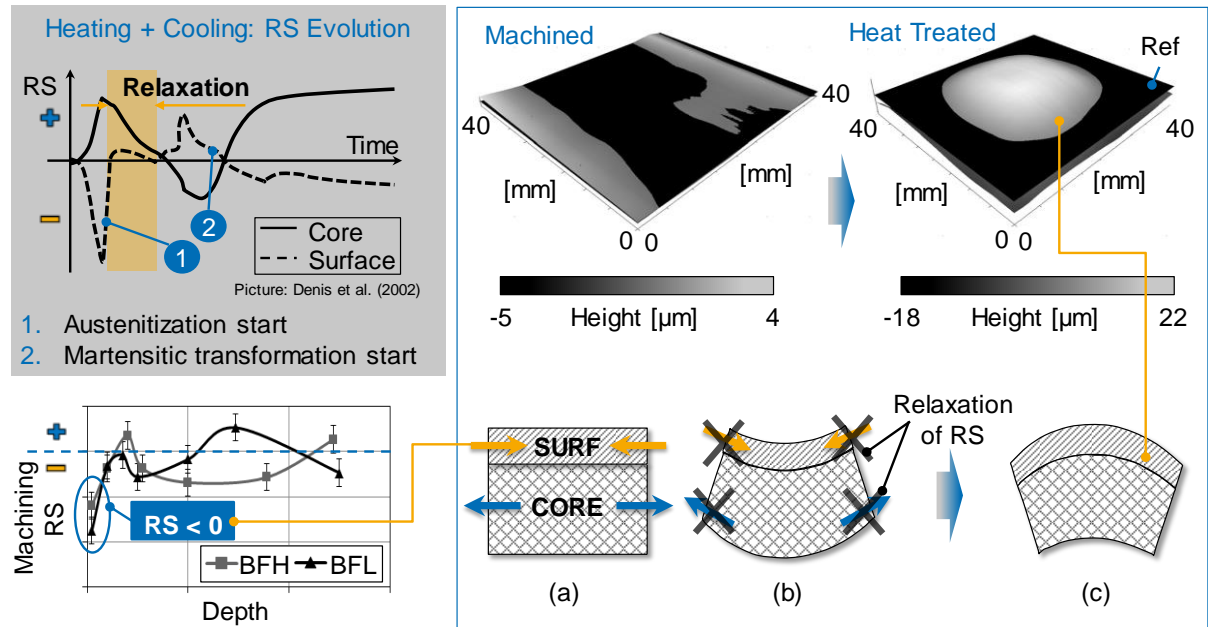


Figure 5.8 – The distortion shape is an effect of the processes' interaction: the case of machining compressive stresses, for the finishing specimens.

The images of the groups BFH and BFL illustrate the case in which the surface is compressively stressed before the heat treatment. The stress state, depicted by Figure 5.8(a), has the geometrical trend represented by the Figure 5.8(b). Within the entire case hardening cycle, the first phase transformation occurs during the heating, when the existing structure is austenitized. It is during this phase that the machining residual stress is relaxed, as shown by the simulation chart of Denis et al. (2002), Figure 5.8. The relaxation is counterbalanced by the surface displacement, and the distortion is formed. The balance drives the frame onto the opposite shape of the former situation, as it is shown by the transition from the Figure 5.8(b) to Figure 5.8(c). This mechanism, which follows the concept of the *Almen* intensity testing (ALMEN; BLACK, 1963) is a satisfactory illustration to the topography measurements.

A same approach is applied to the roughing specimens, which are submitted to surface tensile residual stresses by the machining process. Presenting an opposite stress state to the one previously described, the corresponding consequence is an opposite distortion shape (Figure 5.9). It must be observed that the machined surface had already a concave shape. That was the deflection created by the combination of the tool force and the specimen design with fixation points only at the extremities (Appendix B.2 Blocks for Sample Groups BRH, BRM1, BRM2 and BRL). The distortion assessed after the heat treatment takes place, however, along the transversal direction. This is the mostly like to deform due to its lower length and hence lower moment of inertia.

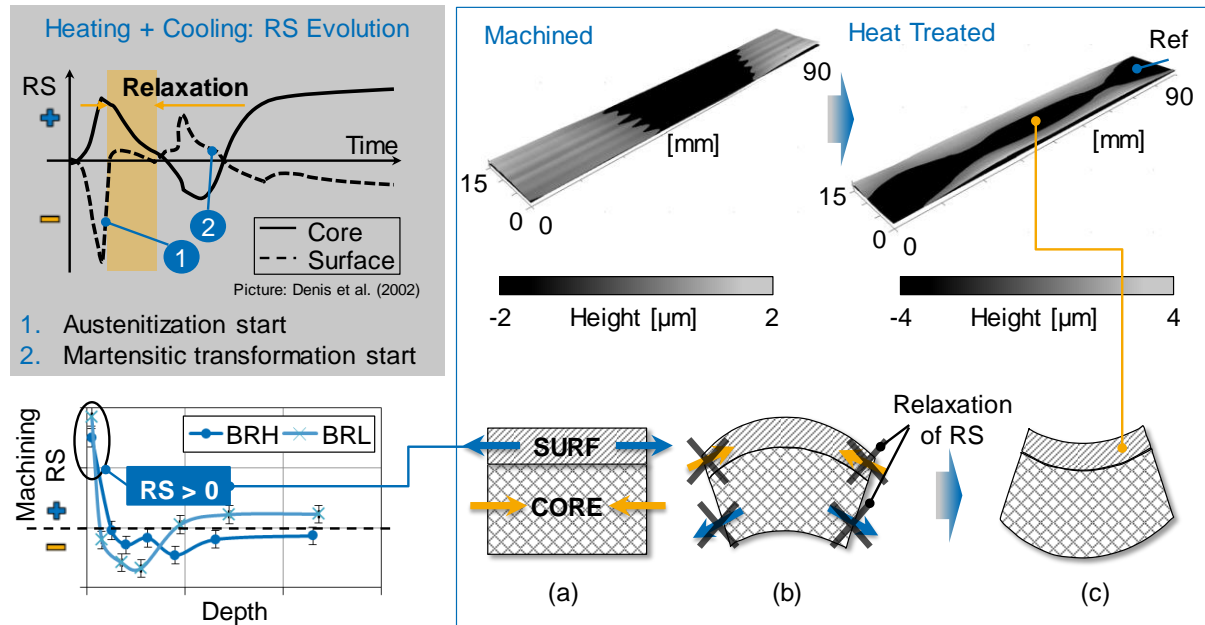


Figure 5.9 – The distortion shape is an effect of the processes' interaction: the case of machining tensile stresses, for the roughing specimens.

The conclusion out of the comparison between the roughing and the finishing specimens highlights the first important aspect of the processes' interaction. The shape of the distortion is a direct result of the residual stress state prior to the heat treatment. It becomes a relevant outcome for functional surfaces. If the surface is to be in contact with a matching part by a centered and symmetric pattern, the convex form is desirable. The distortion following this shape is hence to a certain amount tolerable. However, the same surface would not afford a concave distortion shape. In this case, the machining setup must be designed to induce either no residual stresses or compressive ones.

In addition to the shape, the topography maps enable also that the distortion is quantitatively analyzed. Since the observed geometric deviations do not behave symmetrically, the distortion was evaluated based on a volumetric approach. The total volume, as the sum of the positive and the negative (absolute) magnitudes, was measured for each sample at each manufacturing condition of this case study. The same described reference plane is the basis for separating positive from negative values. With the interaction under the spotlight, the evolution of the total volume was considered as the difference between the machined and the heat treated conditions. The concepts are summarized by Equations (5.2) and (5.3).

$$V_{TOT} = V_{POS} + |V_{NEG}| \quad (5.2)$$

$$\Delta V_{TOT} = V_{TOT}^{HT} - V_{TOT}^{MAC} \quad (5.3)$$

Where:

V_{TOT} : Total volume

V_{POS} : Positive volume

V_{NEG} : Negative volume

ΔV_{TOT} : Volumetric variation between the analyzed manufacturing processes

V_{TOT}^{HT} : Total volume of the heat treated surface

V_{TOT}^{MAC} : Total volume of the machined surface

The information about the volumetric variation brings the analysis back to the objective of the thesis. The first research question searches for a factor from the previous residual stress state that influences the final integrity state. The volumetric variation is then taken as the base to identify a potential correlation.

That the distortion is a consequence from the initial residual stress state, several earlier publications have already proved. On the other hand, it was not only the convergent approach with initial opposite stress states that conferred originality to these results. The usual correlation established in this purpose refers to the residual stress values assessed only over the outer surface layer. This experimental scope can be found in the studies of Nowag, Sölter and Brinksmeier (2007), Klein and Eiffer (2010), and Brinksmeier et al. (2011). By comparing the volumetric variation with the surface stress, it is possible to observe that the usual relationship is not fully achievable for the results herein presented. In the case of the roughing specimens, the group BRL has the highest surface residual stress, whereas its distortion is about as half of the one of the group BRH (Figure 5.10).

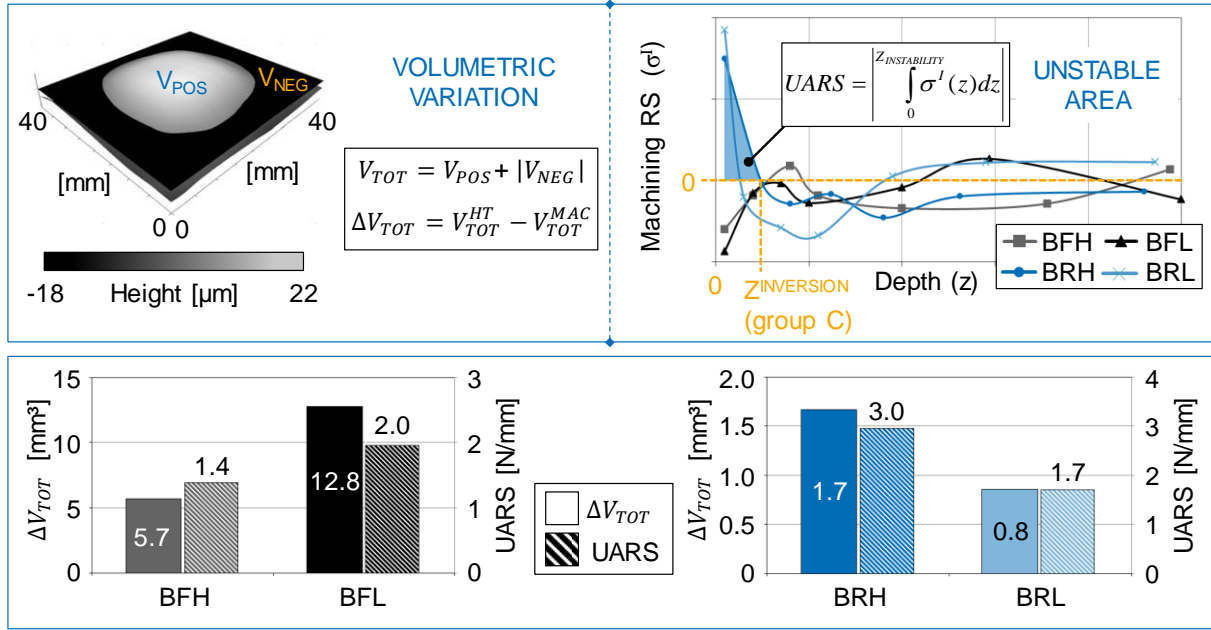


Figure 5.10 – The intensity of the distortion after the heat treatment follows the same trend than the unstable area of residual stress from the machining process.

The outcomes of the Figure 5.8 and the Figure 5.9 highlighted the importance of the sign of the surface residual stress over the surface. Likewise, the depicted treatment cycle exposed the relaxation as a function of the initial existing stress state. In this direction, not only the external stress value should be considered, but the entire region that leads to the same distortion behavior. This means the depth extension to which the residual stress level is kept under the same sign. For a relaxation consideration, the austenitizing turns it into an unbalanced area, where the surface equilibrium is mostly disturbed. Mathematically, this area is hereafter defined as the “Unstable Area of Residual Stress (UARS)”. It is from this part of the material that the relaxation will define the distortion shape. The metric is calculated simply as the absolute value of the integral of the residual stress profile. Its boundaries cover from the depth of the equilibrium disturbance up to the end of the unstable area, Equation (5.4). In this case, they respectively represent the outer surface and the depth point of the sign inversion.

$$UARS = \left| \int_{Z_{DIST}}^{Z_{STAB}} \sigma^I(z) dz \right| \quad (5.4)$$

Where:

UARS: Unstable Area of Residual Stress

σ' : Residual macrostress

z: Depth

Z_{DIST} : Depth of the initial disturbance of residual stresses

Z_{STAB} : Depth of the end of the unstable area of residual stresses

This metric is used as a new attempt to correlate the machining residual stress to the heat treatment distortion. Now, revisiting the Figure 5.9, even the roughing specimens respect a proportional relationship. For all the samples, the largest UARS leads to the highest volumetric variation. As a remark, unequal axis' scales were intentionally applied for the charts of the roughing and the finishing specimens. The specimens have meaningfully distinct designs, and the distortion between them cannot therefore be compared.

Profiles with different rates from the surface stresses to the sign inversion are the clear case in which the UARS overcomes the surface magnitude in importance to predict the distortion intensity. The steeper gradient provided by the group BRH enabled to differentiate the herein assessed data from the results hitherto published. On account of these findings, the UARS can be defined as the interaction factor searched to influence the final integrity state. The conclusion is so far valid for the first case study of the thesis. However, it becomes a value to be investigated in the second case study, to be explored in the sequence.

5.1.3 Inducing Different Stress States through the Shot Peening

Face to the first discussed case study, the interaction analysis to be now presented brings the confrontation of two different stages of the manufacturing chain. The next two approached processes are not only at the end of the chain, but also both are in the same condition of case hardening. Particularly to the first step of this analysis, the shot peening, different assumptions are made for generating the input of this interaction. Differently than for the machining, the residual stress profile from the shot peening is always compressive at the first surface layers. Also, it never achieves its maximum value at the outer layer.

On the one hand, it has the complexity onto producing profiles with meaningful differences for the maximum residual stress intensity. On the other hand, it provides the opportunity of positioning this maximum value at distinct depth values. Consequently, other depth profile magnitudes change, such as the area below the chart or the depth of compression-tension transition. Possible different combinations allow the determination of

which profile factors mostly influence the residual stress state after the following profile, as stated by the first research question.

The five peened groups were produced by combinations of different media sizes and coverage levels. The residual stress profiles were measured both along the tangential ($\Phi = 0^\circ$) and the axial ($\Phi = 90^\circ$) directions. The results for the α -Fe phase are shown in the Figure 5.11. As a first observation, valid for all the groups, the results are barely the same when comparing the both measured directions. The collision of the media against the surface causes radially symmetric strains, in case the incident angle is exactly normal to the surface and the material is isotropic. Since this angle condition is not feasible for the process execution, the results showed that the peening incident angle was low enough to not induce a textured surface.

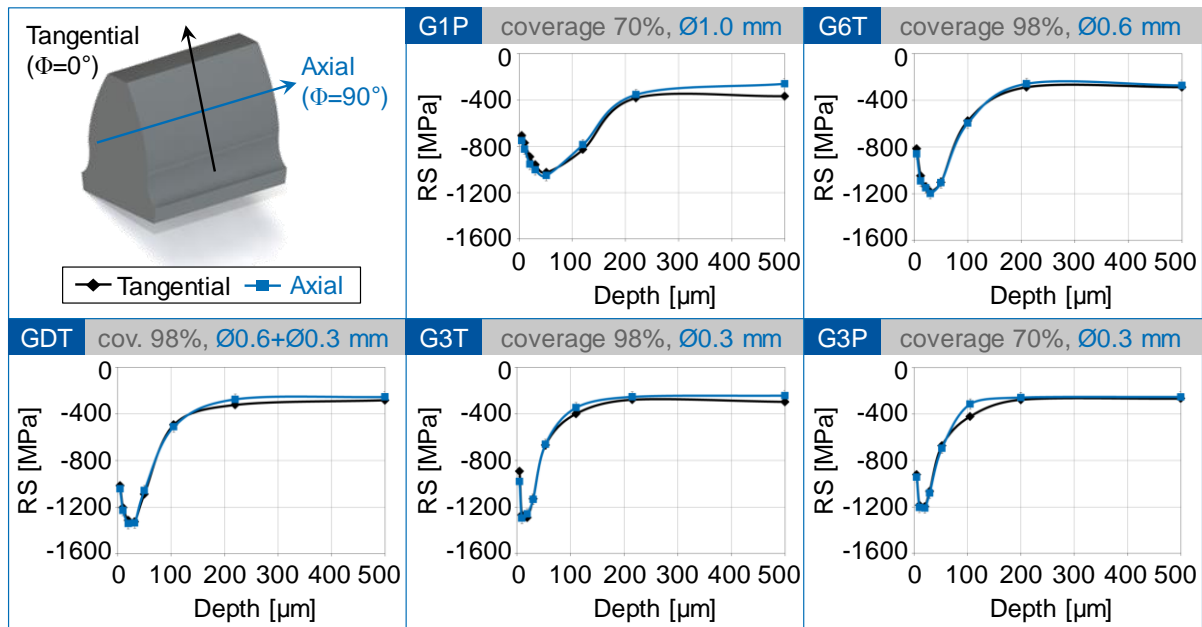


Figure 5.11 – Residual stress measurements on the peened samples on both axial and tangential directions.

The groups were assessed also for each one of its constituent phases. Together, they provided the value of the residual macrostress, according to the Equation (2.3). Individually, they compose the input database for the microstructural connection to the residual stress interaction. The results along the depth of the retained austenite content, as well as the residual stress for both the α -Fe and γ -Fe, are shown in the Figure 5.12. The stress results refer to the axial direction, but as just discussed, are representative for both directions.

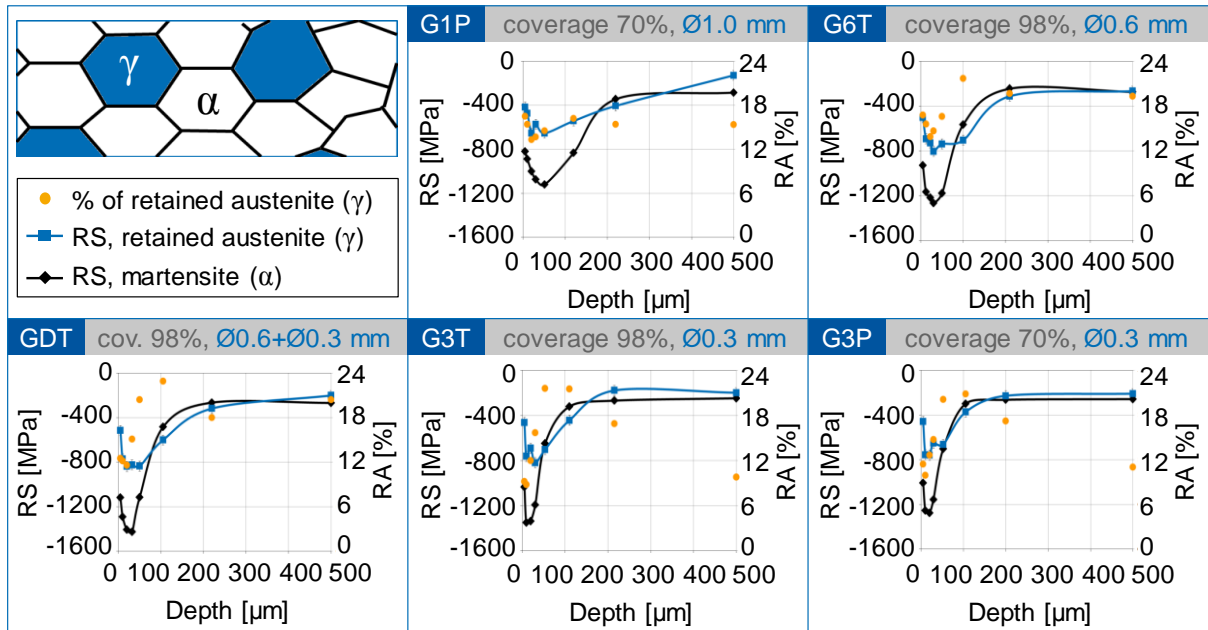


Figure 5.12 – Steel phase approach for the residual stress state of the peened samples: retained austenite fraction and the axial stress measurements on both phases.

For all the groups, the amount of retained austenite varies between 8% and 23%. The largest oscillations are observed in the depth layers where the residual stress shows to be mostly influenced by the shot peening, which occur up to a depth of 100 μm . Within this range, the larger the intensity of the induced residual stress is, the most reduced will be the content of the retained austenite. The statement, observed by considering most of the groups, was expected, and is in agreement with the review of Funatani (2002). The transformation of the austenite in martensite is diffusionless, and enabled by shear stresses. It is based on the balance of free energy between the phases to start the transformation into the respective structures. This balance is altered by the deformation energy added to this system by the shot peening. The required internal strain necessary to the martensitic transformation is lowered, and the phenomenon can take place in a lower temperature. In a mechanism called as deformation induced martensitic transformation (DIMIT), the microstructure changes from a face centered cubic structure to a body centered tetragonal frame. (SHIN; HA; CHANG, 2001). Hence, an intense peening energy is related to the reduced amount of retained austenite (FUNATANI, 2002).

A difference in the stress levels between the phases is found within the same depth range. For all the groups, the measurements in the α -Fe phase indicate a larger compressive intensity. A potential explanation to the observation is based on the DIMIT mechanism. With

the deformation energy induced by the peening, part of the γ -Fe content is transformed. However, the non-transformed content could have already started the transformation mechanism, and the partial transformation may have relaxed the residual stress intensity.

These results input the residual macrostress calculation, and a comparative analysis along the axial direction is depicted in the Figure 5.13. The five groups created a database with both the maximum compressive stress (peak) and its depth on distinct levels. The values of these two depth profile factors for each group are also shown in the Figure 5.13. They prove to achieve the peening experimental goal, as introduced by the Figure 5.1

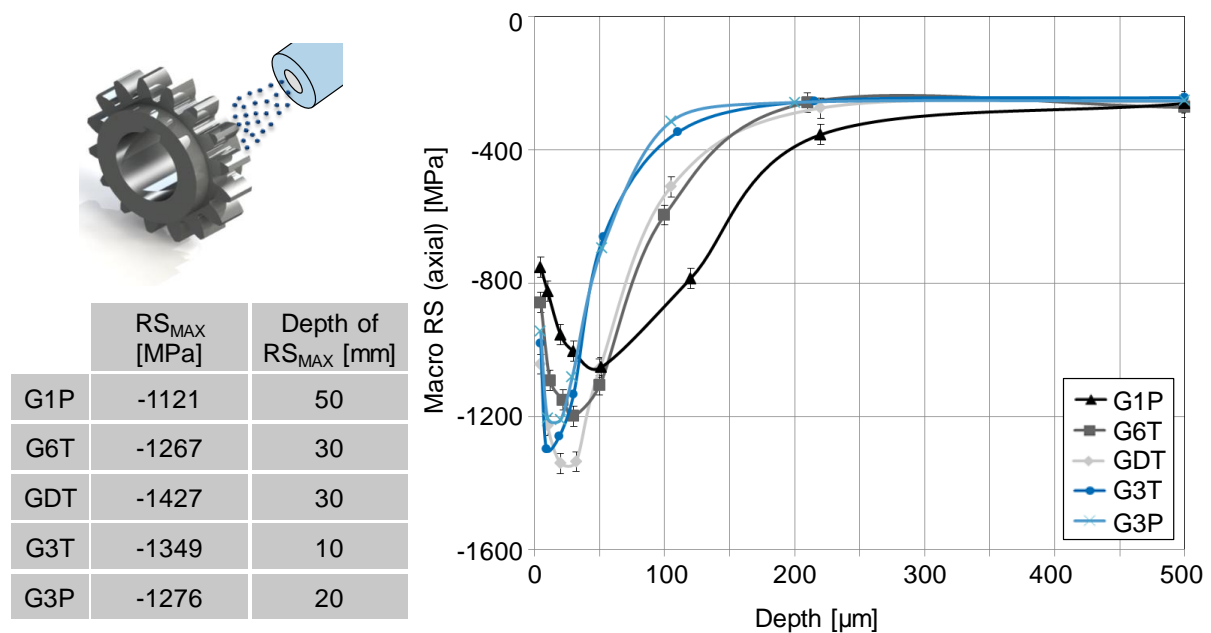


Figure 5.13 – Different depth profile features achieved with the residual macrostress profiles of the peened pinions.

In a first approach, the groups are compared regarding to the depth of the maximum residual stress. The results of peak depth were directly proportional to the media diameter. The group G1P, set with a media diameter of 1.0 mm, has the deepest peak while the shallowest ones are represented by the groups peened with 0.3 mm media (G3T and G3P). The larger media characterizes a larger kinetic energy and thus a larger deformation energy. A high energy magnitude is not only inducing a deeper peak but also pushing the point where the stress stabilizes to a deeper level. The results match to the publications of Guagliano and Vergani (2004), Hong, Ooi and Shaw (2008) and Rego, Gomes and Barros (2013). As a common observation, the groups find stabilization around a depth of 200 μ m. The intensity,

which is for all the groups around 300 MPa at 500 μm , will move gradually towards a tensile state up to the core, due to the equilibrium principle.

The shot peening state-of-the-art is not convergent when it comes to the influence of the media size to the peak intensity. The discussion is whether the peak is increased or kept constant with the enlargement of the media. Restricting the comparison to the single peening treatments, the maximum intensity of groups G6T, G3T and G3P are reasonably similar, although represented by different media classes. However, the peak of the group peened with the largest media (G1P) is the one with the lowest maximum residual stress. The reason must be especially related to the low coverage level. But since it assumes a lower peak than another group with similar coverage (G3P), part of the explanation may also be related to the peening machine concept. The samples of the group G1P were, due to technical specifications of the available machines, the only to be peened by means of a wheel-type machine.

The comparison between the groups G6T and GDT demonstrates the actual effect of the dual peening. The dual peened sample brings additional effects to the residual macrostress profile only up to its maximum absolute value, about 30 μm deep. Already from a depth of 50 μm , both profiles merge and present the same trend. This effect is connected to the explanation given to the media size influence to the peak depth. The second step media, which is smaller (0.3 mm), has the function of homogenizing the residual stress induced. With this diameter, its effect is limited to the first depth layers, as observed. The results meet the expectation and are in agreement with the previous studies from Molzen and Hornbach (2000) and Rego, Gomes and Barros (2013).

As a main conclusion, the peening experiments allowed the accomplishment of this specific goal. An input database was produced with different depth profiles of residual stress. These combinations of features compose the plan to determine which characteristics of the residual stress state are mostly relevant to the surface integrity after the following manufacturing step. Consequently, they drive the definitions for the setup of the second process of this interaction analysis, the profile grinding.

5.1.4 The Interaction between Shot Peening and Grinding

Differently than the previous study case, this interaction involves a partial removal of the surface layers examined after the first process. The topic starts with describing how the

material removal had to be carefully monitored, so its effects could be considered negligible to the peening comparative analysis.

The definition of the stock removal was based on the residual stress factors of intensity and heterogeneity. For the definition of this grinding parameter, the first activity was to mathematically represent the peened residual stress profiles. Each curve was represented by two regression functions. These functions refer respectively to the two peening mechanisms that induce the residual stress state. Over the first layer, the *Hertzian* stresses are the predominant effect, followed in depth by a profile shape mostly defined by the stretching effect (KRITZLER, WÜBBENHORST, 2002). The used functions are based on the analytical calculation published by Li et al. (1991) and Rego, Gomes and Barros (2013). The goodness-of-fit for all the regressions were in average represented by a R^2 value of 94.5%. The results are depicted in the left panel of the Figure 5.14.

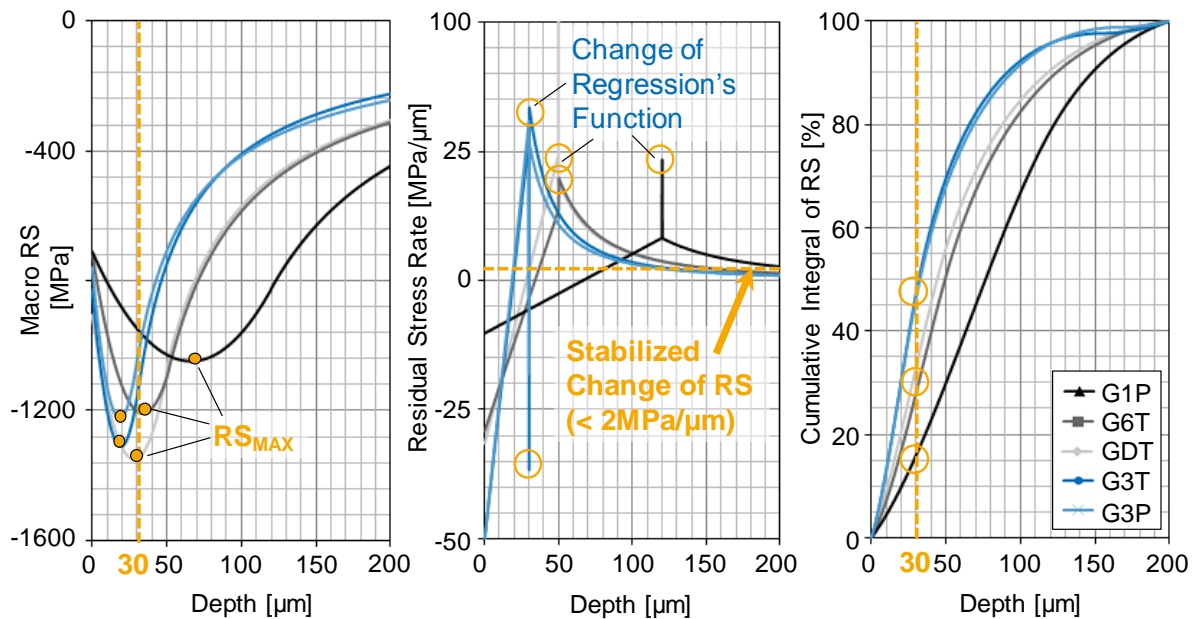


Figure 5.14 – Criteria to define the stock removal of 30 μm .

The profile functions enabled the calculation of the residual macrostress integral, a value defined by the area below the curve. The area is calculated from the curve value to a constant intensity representing the residual stress at the depth where its magnitude is stabilized (Z_{STAB}). This value does not mean that the stress is kept the same up to the core, since the equilibrium principle will drive the profile to a tensile state at a certain depth. But it symbolizes a region in which the change of stresses has a much reduced rate. The stabilization

is defined by a rate calculated to be up to 2 MPa/μm. This threshold is depicted in the central panel of the Figure 5.14, where the pronounced peaks are simply a mathematical resultant of the depth where regression's function is changed. The Z_{STAB} was identified to be around 200 μm, which matches to the observation of the Figure 5.13. The residual stress integral is then converted to a percentage value, in order to account the contribution of certain cumulated layers to the total amount calculated. Considering the stabilization depth as 100%, the cumulated integral value is plotted, as shown in the right panel of the Figure 5.14. The cumulative integral of residual stresses (CIRS) is defined by the Equation (5.5).

$$CIRS = \frac{\int_0^{Z_{STAB}} \sigma^I(z) dz}{\int_0^z \sigma^I(z) dz}, z \leq Z_{STAB} \quad (5.5)$$

Where:

CIRS: Cumulative Integral of the Residual Stress profile

Z_{STAB} : Depth of stabilization

z: Normal direction to the surface (depth)

The stock removal (Z_{STOCK}) was defined to be 30 μm, based on the information of both charts of the Figure 5.14, and with three justifications. At a first instance, this depth level separates the groups in regard of the peak positioning. The value of 30 μm is lower than the peak depth of the G1P, higher than the peaks of G3T and G3P, and practically over the maximum intensity depth from G6T and GDT. The adoption of this value goes towards the verification of the peak depth as one of the residual stress intensity factors to the interaction analysis. This value reflects, at a second aspect, also the cumulative integral of the residual stress intensity. The shallower peaks achieve values close to 50% of the CIRS, while the group G1P has not yet achieved 20%. The third reason binds both the first two described. The selected depth registers the meeting of curves with different profile features. At 30 μm, the residual stress assumes almost the same intensity for the peened samples of G6T and G3T.

Already after the pre-grinding, and thus before the grinding process has started, the peened gears received a second classification label, according to the tooth span (W_K). Within a spread range of 12 μm, four classes were defined and identified by a roman algorithm (Table 5.1). The difference between the maximum and the minimum limits of the tooth span are never higher than 5.0 μm. Some of the classes have superposed ranges, since they were

established to have at least one sample from each different peening group. After the pre-grinding, this classification defined the second action taken to offset the distortion and to characterize the grinding process as equally applied to the different samples.

Table 5.1 – Samples classification according to the tooth span measured after the pre-grinding.

Class	Tooth Span (W_K) [mm]		W_K range within the class [μm]
	MIN	MAX	
I	34.878	34.883	5.0
II	34.871	34.875	4.0
III	34.876	34.880	4.0
IV	34.872	34.877	5.0

With the samples classified according to the peening treatment and the tooth span, the profile grinding process was performed. The stock removal was equally applied to all the pinions. This demanded to define individual tooth span values to the grinding setup, based on the measurement of each specimen before grinding.

As the final action for controlling the grinding load, with the mindset to characterize the process as the same for all the specimens, the grinding force was acquired. The load cell provided the force on the three Cartesian directions. Since the load cell was fixed to the shaft, only the axial direction (F_Z) was always kept towards the same orientation. The radial directions (F_X and F_Y) varied according to the gear movement along the process, dictated by the tooth gap being ground. The axial direction was therefore used as the reference to define the region of the force analysis, when there was full engagement between the tool and the flanks (Figure 5.15). For a comparison among all the teeth, the radial forces were analyzed according to their absolute values. Based on the signal of the axial direction, it was possible to determine the background values and to remove it respectively from the radial force curves. Likewise applied for the machining analysis, an equivalent force based on the radial force components was calculated, Equation (5.1). The analysis was individually performed for every ground gap, as shown by the chart in the right top corner of the Figure 5.15.

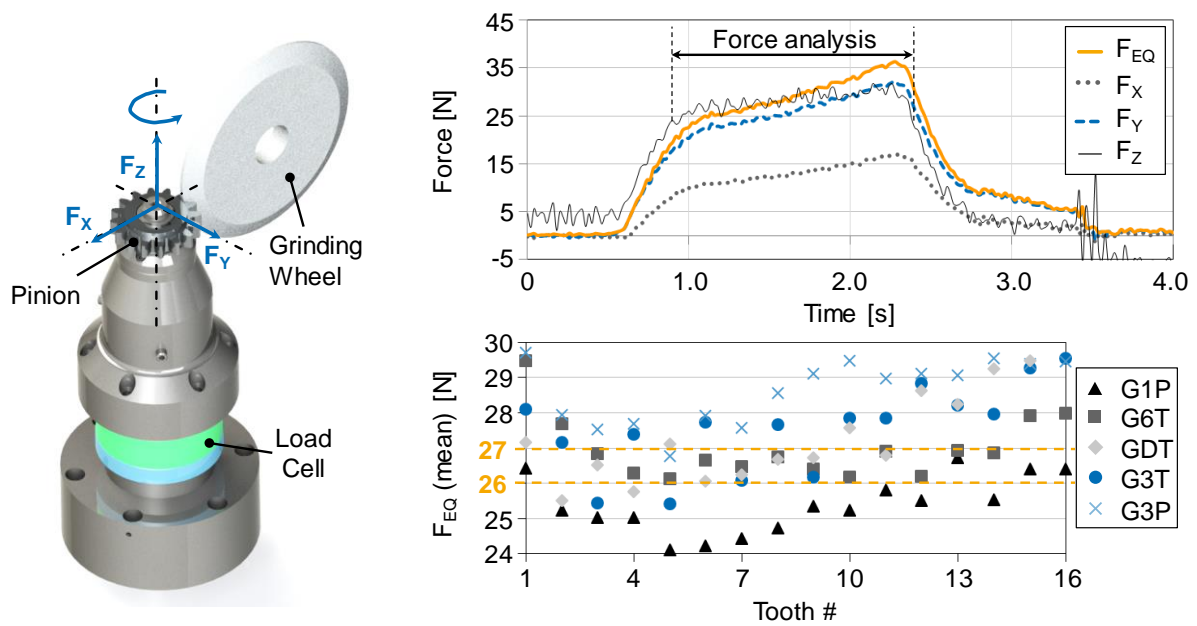


Figure 5.15 – The measured grinding force and the method for selecting the flanks for the surface integrity analysis.

The selection of the flanks to be submitted to the surface integrity analysis was taken from the calculated equivalent force. Within the force analysis range, the mean value was considered to represent each flank. The results for all the teeth of one gear, from the five peening treatments, and also defined as tooth span class III (Table 5.1), are shown in the right bottom chart of the Figure 5.15. An overall view of this chart justifies the execution of the force measurement. Without this approach, the flanks selection would be taken randomly, and the flanks representing the lowest and the highest force could be the chosen ones. In this case, the mechanical load difference between the gears would be in the order of 25%. However, by applying this selection criterion, it was possible to find at least one flank from each peening treatment within a range of 1.0 N. This represents a difference of 4% and effective control to isolate the grinding intrinsic deviations for the interaction analysis.

The selected flanks were finally assessed with the XRD method, following the same procedure applied after the peening process. The depth profiles for the α -Fe and γ -Fe phases, together with the austenite content, are shown in the Figure 5.16.

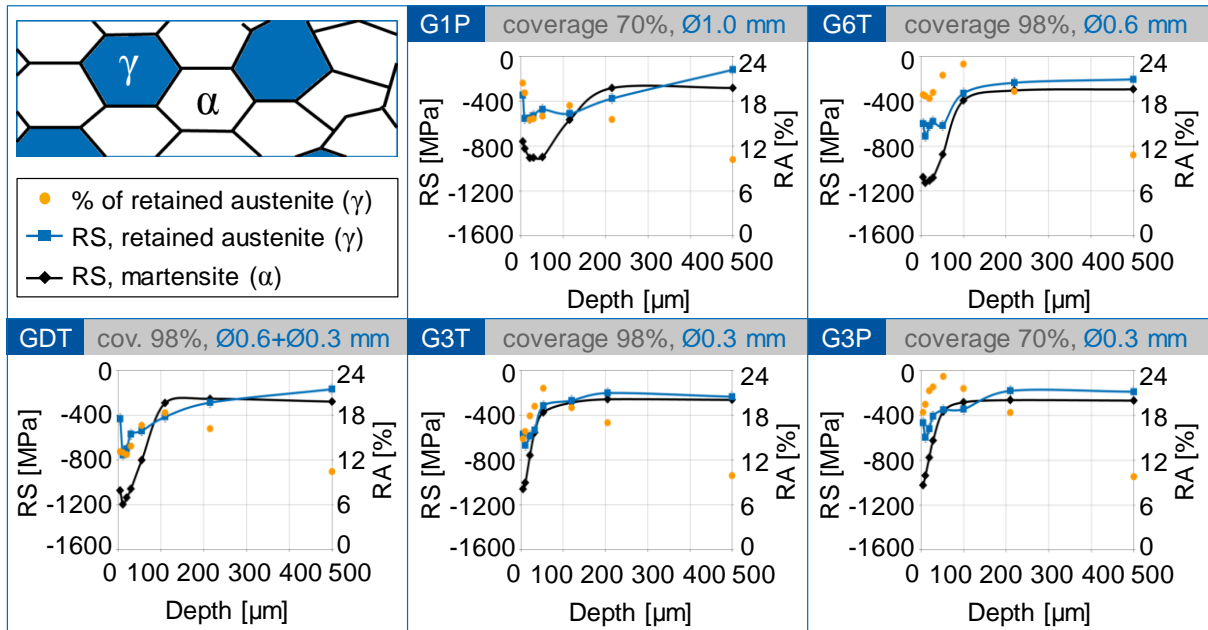


Figure 5.16 – Phase residual stresses and retained austenite fraction after the grinding process.

A glance at the different results of stresses recovers the base of the problem stated in the introduction of this thesis. The groups' samples were peened with distinct treatments and then ground with the same conditions, defined and monitored. According to the state-of-the-art, the residual stress optimization investigations are conducted without considering the influence of the stress state before the analyzed process. With this mindset, the previous surface would be negligible and the same grinding process would thus induce the same residual stress state for all the groups. However, the results of the Figure 5.16 prove the conclusion of the Figure 1.1 to be true. Especially observing the charts referring to the α -Fe phase, the difference between the groups is clear and not limited to distinct intensities. The profile shapes are also contrasting along the depth. The profiles from the G3T and the G3P achieve their maximum compressive magnitude directly over the surface, as it would be expected for a ground surface (BRINKSMEIER; GIWERZEW, 2005; SCHWIENBACHER, 2008; REIMANN, 2014). On the other hand, the other three groups are still shaped with a subsurface peak, like the stress profiles after the shot peening process. This statement is better perceived when computing the residual macrostress, in a comparative analysis between the two different manufacturing steps of this interaction study (Figure 5.17).

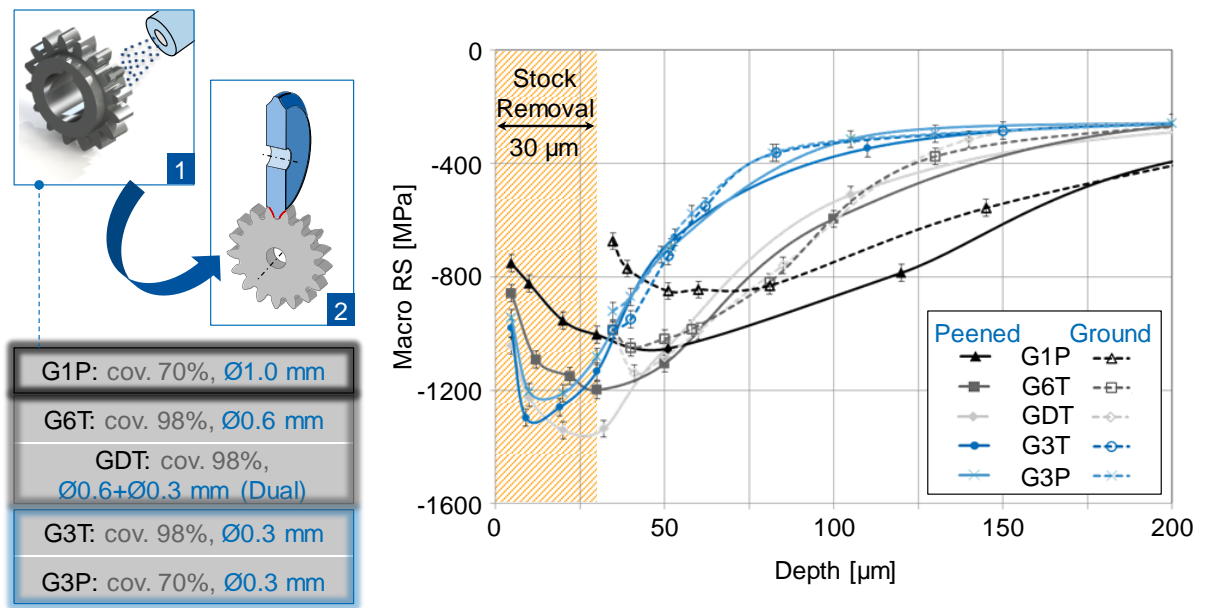


Figure 5.17 – The residual macrostress differs between the groups treated with different peening conditions and the same grinding process.

In the chart of the Figure 5.17, the axial residual stress results of both manufacturing steps are plotted along the same depth axis. With the information of the stock removal, there should be understood that the first point of the dashed lines are the measurements done over the outer surface of the ground samples, albeit laying on the axis depth level of around 30 μm . This chart arrangement highlighted the meaningful influence of the previous process to the final residual stress state. For the profiles of samples G3T and G3P, the ground stresses are quite similar to the peened results. And for the first three groups (G1P, G6T and GDT), the convergence takes place after the peak depth of the grinding profiles.

The different behavior between the groups motivated a detailed analysis towards the goal of finding which profile features mostly drive the verified interaction influence. For this purpose, the arrangement of the chart was once more changed, in order to individually compare the stress states after each manufacturing step. Three groups were sorted to represent all of the five treatments. A similar behavior enabled to jointly analyze G6T and GDT, as well as G3T together with G3P. These three classified behaviors are respectively marked in the Figure 5.17 with the colors black, gray and blue. The described individual approach is shown in the Figure 5.18. Also in these charts, the peened profiles are plotted just starting from the corresponding depth to the stock removal. Hence, the depth axis of the ground profiles at the outer surface layer is aligned to the peened axis starting from the stock removal depth level.

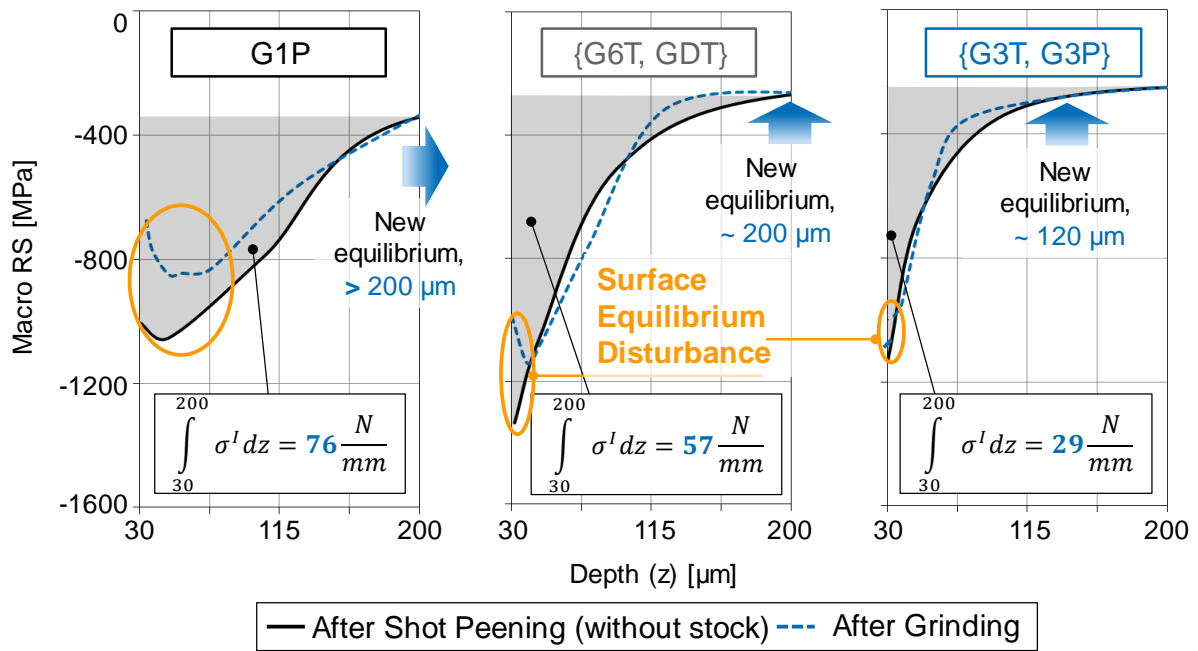


Figure 5.18 – The remaining area as the meaningful residual stress profile feature to influence the interaction between shot peening and grinding.

In these comparative charts, the first observation has focus on the intensity difference between the two manufacturing steps. A common phenomenon is observed on the three sorted groups, which is an oscillation of the ground profile around the peened one. A larger intensity change occurs over the outer layer of the surface, and the oscillation is gradually reduced along the depth. It goes up to a point where the two curves are again convergent. The behavior is an indication that the basic rule of residual stresses was respected: the equilibrium principle. The stable condition after the shot peening was disturbed by the material removal, and the oscillation is an evidence of the search for a new equilibrium point after the grinding process.

The three charts of the Figure 5.18 also display the difference between the sorted groups. The new equilibrium depth finds its shallowest depth on the panel of the group G3T and the group G3P, while the deepest point is characterized by the group G1P. This statement can be seen as the consequence of the intensity change at the outer layers, simply defined as the “Surface Equilibrium Disturbance”. The larger this disturbance is, the deeper will be the new equilibrium point. The concept reveals a tightened relationship between the both case studies under investigation. It is the once more the loss of the system stability that shows to bring an answer to the interaction effect. While the disturbance for the machined samples was

represented by a thermal load followed by phase transformation, it is now, for the peened specimens, the mechanical removal of the stock material.

This inference takes the analysis onto the comprehension of the surface disturbance. For this purpose, the UARS metric is recalled from the first case study and applied to the peened gears, Equation (5.4). The regression functions of the peened residual stress profiles are here useful. The UARS is for this case calculated on the remaining area of the peening curves, which is extended from the stock removal depth up to the stabilization depth (Z_{STAB}). For this second case study, the unstable area appears as the remaining area of residual stresses. Analogously, the depth of the initial disturbance (Z_{DIST}) is the grinding stock depth.

The application of the UARS value shows exactly the same trend as the surface equilibrium disturbance. As shown in the Figure 5.18, the highest UARS value refers to the G1P and the lowest to the G3T and G3P. The statement validates a quantitative representation of the interaction effect for a manufacturing chain sequentially composed by the shot peening and the grinding processes.

Summarizing the latest drawn connections, the unstable area proportionally disturbs the equilibrium, which directly drives its new depth point. This observation goes in the direction of the first research question, of finding the parameters from the previous process that interact with the following one. Moreover, it defines a parameter from the first process that proves to be similarly applicable for both case studies. Differently, the impact to the heat treated samples is the geometric distortion and for the ground gears is the residual stress state itself.

The hitherto presented results indicate that the UARS value appears to be the most suitable answer to the question. But even the distinct effects that the interaction promotes to each case study open an opportunity to further comprehension of the phenomenon. Therefore, it is required a physical explanation to certify the reliability of the established connection.

5.1.5 A Physical Model to the Residual Macrostress Interaction

A description of the influence of the residual macrostress interaction to the final surface integrity brought as outcomes the geometric distortion and the change in the residual stress state. In both cases, the UARS value showed to be the main driver to the results after the second process. A fundamental approach to these statements outlines the following points:

1. Distortion and stress refer to displacement and force. The bond between them forms the basis of the mechanical energy conception.

2. The unit of the UARS, calculated in this case as N/mm, is a metric of stiffness.

A raw observation to the combination of the two exposed points recalls the early potential energy model proposed by Heyn (1914). Based on springs, the model aimed at physically explaining the event of residual stresses. In this model (top of Figure 5.19), a symmetric component is represented by a cross section, where the surface is positioned at the section's extremities and the core over its center. For the given example, this part is submitted to surface compressive residual stresses. Hence, the model is composed by springs under compression at the extremities. The spring model matches the residual stress behavior exactly by its equilibrium principle. Consequently, a central spring under tension balances the existent compressive energy coming from the surface. The herein presented study proposes that this model should be considered in a derivative approach, to such a degree that the surface is represented by several layers (bottom of Figure 5.19). Each layer has its specific stiffness, corresponding to the residual stress integral of the respective depth range. It is important to highlight that the layers are represented by an equivalent energy to the unique spring from the model of Heyn. Due to this reason, it is referred as the “Equivalent layers model” (ELM). Analogously to the model of Heyn, the ELM keeps respecting the equilibrium, since the total energy of the part is still nil.

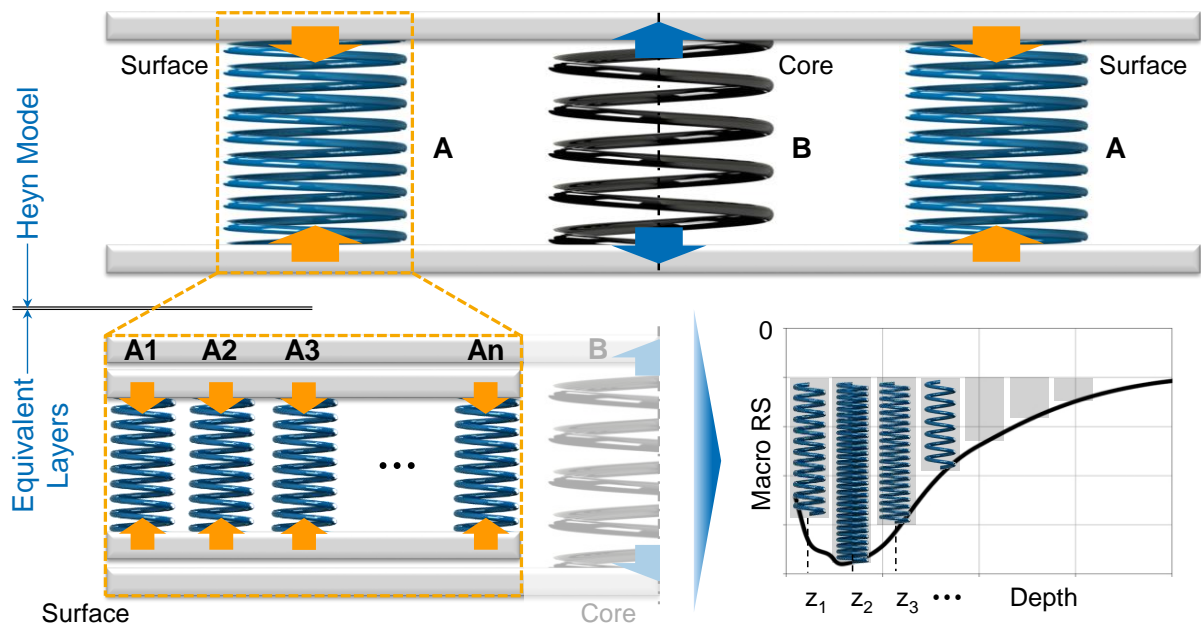


Figure 5.19 – Springs model to describe the residual stress behavior: model of Heyn (1914) and the proposed adaptation of equivalent layers (ELM).

The reason for the derivative approach of the ELM is comprehended when considering the second manufacturing process of each case study. Respectively, the phase transformation and the stock removal act as an external source for disturbing the equilibrium. The machined layer under the same sign and the stock material are then taken as the outer layer of the Equivalent Layers Model. The completion of the disturbing manufacturing processes represent the extraction of the external spring. The Figure 5.20 analyzes the extraction effect for two scenarios, each one with a different UARS. The model for both the scenarios starts with a stable system, represented by the surface after the machining or after the shot peening process. This stability is lost together with the surface phase transformation and the stock removal, respectively. The system will thus search for a new equilibrium state, and at this point, the two scenarios differ. The higher UARS means a higher stored energy, symbolized in the first scenario by more compressed springs. The intensity of the stored energy is proportional to its release, and therefore to the system disturbance.

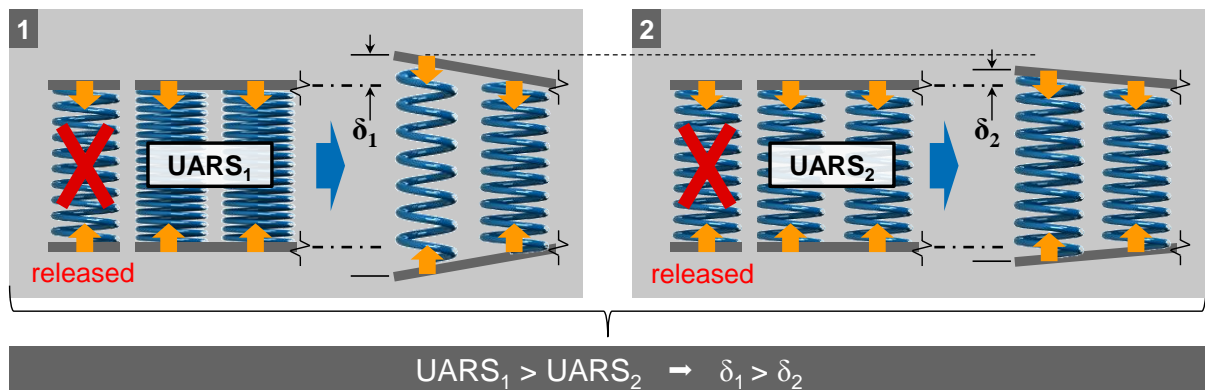


Figure 5.20 – The unstable area of residual stress (UARS) as the driving factor to the residual stress interaction. The larger is the UARS, the larger will be the surface equilibrium disturbance.

The Figure 5.20 illustrates the mechanism by comparing the disturbance by through the “ δ ” symbol. As a first impression, it may take the reader to an exclusive perception of distortion as the outcome of the equilibrium disturbance. Indeed, the surface distortion is one possibility to reflect the release of the stored energy after the loss of stability, as it was observed after the heat treatment process. However, dealing with the model of springs also open the possibility of reflecting this release of energy on the residual stress state itself. That was the reaction observed for the interaction between the shot peening and the grinding. The

measurement of the tooth span (W_K) after the grinding did not confirm a statistical difference when running a hypothesis test between the sorted groups ($P\text{-value} = 0,566$). A slight trend is actually pointed out to this direction, but the data dispersion hinders the validation.

The potential energy model of a spring is composed by its stiffness (k) and the displacement (δ), herein read as the distortion. If there was no clear difference from the distortion assessment, then the release of the stored energy should have been converted in a change of the stiffness. This statement drives the analysis finally back to the UARS metric. The stiffness represents the internal stress state and its change will be the disturbance on the residual stress intensity (Figure 5.21).

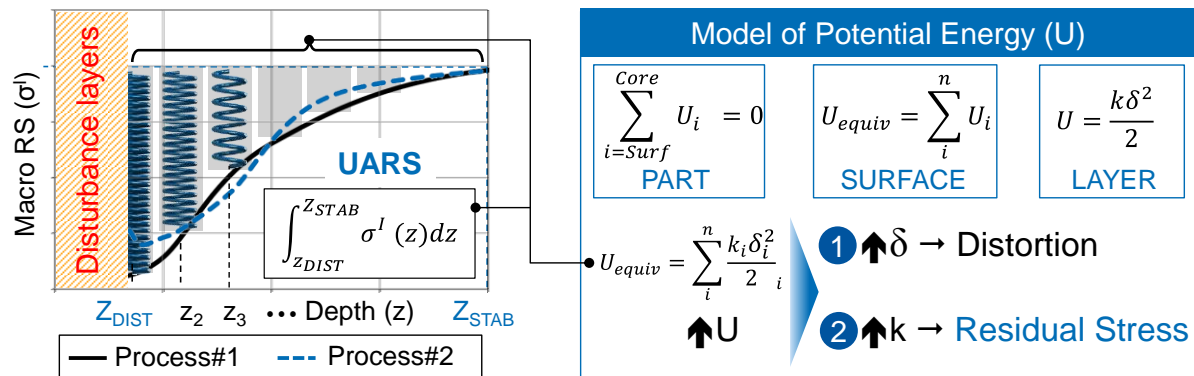


Figure 5.21 – The release of the stored potential energy converts the disturbance in distortion and/or internal stress change.

It is supposed that the disturbance mechanism is determinant on the definition whether the energy is released as geometric or stress change. During the heat treatment, there is no physical obstacle to hold the surface material displacement. For the grinding, however, the same wheel that disturbs the equilibrium also works as a load support. It removes the surface degrees of freedom to a certain magnitude, hindering the surface to freely move. This restraint favors the disturbance to be converted to a change in the residual stress state.

Considering the second case study, the expected residual stress introduced by the grinding is lower than the actual peening one (BRINKSMEIER; GIWERZEW, 2005; SCHWIENBACHER, 2008; REIMANN, 2014). Hence, this stored energy tend to be relaxed and the disturbance is initially moved towards the tensile state, as observed in all the charts of the Figure 5.18.

The explained model brings a physical meaning to the observed results, enhancing the robustness of the drawn conclusions. The findings meet the goal of the first research question,

by characterizing the UARS as the intensity factor of the previous residual stress state with the largest influence on the profile after the final process. How the change is distributed between distortion and residual stresses for different manufacturing interactions, it consists of an outlook of this study.

5.1.6 Summary

The first research question established a goal of identifying factors from the residual macrostress state along the manufacturing chain that influences the final integrity state. Through two case studies, different factors composing the stress depth profile could be examined. The machining process was used to create residual stresses of opposite signs. The monitoring of the mechanical and thermal loads supported the selection of the appropriate process design for the analysis. Due to the compressive nature of the stresses induced by shot peening, the generated profiles of the second case study were set to provide distinct combinations of intensity and depth level. If the furnace temperature homogeneity had to be assessed for the case hardening, the grinding control was certified by a selective definition of the investigated gear flanks according to the measured cutting forces.

On the one hand, surfaces compressively or tensely stressed by the machining are characterized by the same residual stress state after the heat treatment process. The phase transformation of the austenitizing phase promotes a complete relaxation of the existing stresses. On the other hand, the application of the same grinding conditions was not enough to provide a unique residual stress profile. The clear influence of the shot peening rectifies the introduction's statement that the intermediate process cannot be neglected to the final integrity state.

By means of the machined opposite stresses, the interaction proves to be significant to another property of the surface: the geometric distortion. The previous stress state drives the shape and the intensity of the surface displacement. Confronting the state-of-the-art, the results show that not only the residual stress of the outer layer promotes this effect. The heat treated distortion is a function of the entire area before the transition to the opposite stress state. The finding established the metric defined as the Unstable Area of Residual Stresses (UARS). It represents mathematically the area below the residual stress profile along the region of equilibrium disturbance. The value is also valid to determine changes in the residual stress profile itself. Calculated for the peened state, the UARS correlates well with the magnitude of the surface equilibrium disturbance after the grinding.

The effect on both the distortion and the stresses indicated a physical model to explain the interaction mechanism. An adaptation of the classic residual stress model of springs is proposed to consider a derivative approach. Each depth layer is represented by a spring with a specific stiffness, according to an equivalent layers model (ELM). The disturbance of the surface symbolizes the removal of one of these springs. In the presented case studies, the removal was featured by phase transformation and by material removal. The stored energy coming from the previous process, quantified by the UARS, is proportional to the surface modifications on the final integrity state. The changes are developed either as distortion or as a variation of the residual stresses.

The unstable area of residual stresses appears as the main answer for the first research question. It motivates future studies on the compromise between the affected distortion and stresses on different manufacturing chains. Finally, it encourages the exploration of the deviations of the mean and macro stresses for the interaction perspective. The role of this residual stress heterogeneity in-between the processes is the content of the following topic.

5.2 Residual Stress Heterogeneity: Assessment and its Influence

The first chapter of results demonstrated the influence, the most important factor and the mechanisms driving the residual stress interaction under the stress intensity perspective. The concern is now taken to a statistical approach, in which these stress profiles cannot be assumed to be constant across the surface. The focus is now over the deviations of the residual stresses, its heterogeneity state. The present chapter starts with the development of a feasible to method to assess the residual stress heterogeneity. The validated method is then applied to the two case studies, in order to verify whether and how the surface heterogeneity can influence the process interaction.

5.2.1 Local Residual Stress Deviations

The challenge of inducing compressive residual stresses is not restricted to the manufacturing feasibility of increasing the intensity to the desired level. The high variability observed on the measured values is a daily fact faced by the industry. The statement can be quantified by the scatterplot chart previously introduced in the Figure 1.1. The variability of

the manufacturing processes, an irregular material microstructure and the measurement equipment's intrinsic errors can contribute to such a poor repeatability level. Also among these potential reasons, the measurement method must be considered. In most cases of the mechanical industry, the residual stresses state is determined by means of XRD (LU, 2002; LAW; LUZIN, 2011). The XRD measurement spot is, commonly for gears applications, in the order of a 1-3 mm diameter circle. The size relationship between the spot and the heterogeneity state can bring two consequences (Figure 5.22):

1. Punctual feature: the spot is too small compared to the local deviations. The measurement is performed over a position that may not reproduce the stress variations along the entire surface.
2. Mean value: the spot is too large compared to the local deviations. The assessed residual stress is represented by one averaged value inside the spot. The measured value is, additionally, an average of the microstructural stress level.

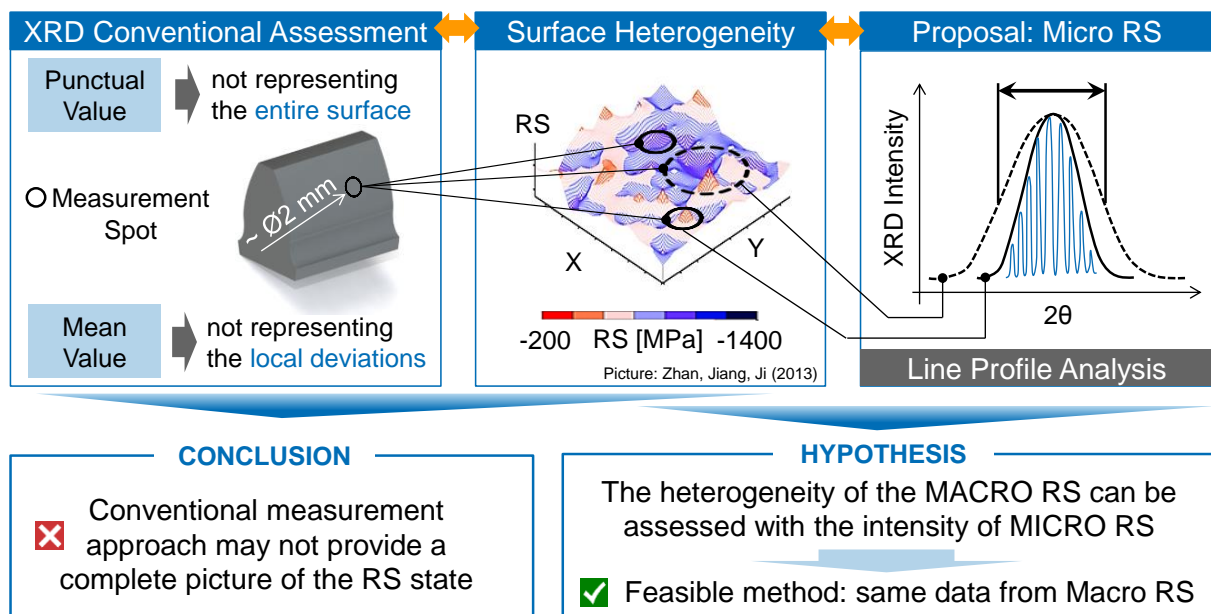


Figure 5.22 – The large variability of macro RS is also influenced by its heterogeneity state.

The studies of Valiorgue et al. (2012) and Zhan, Jiang and Ji (2013) support the discussed concern. They show how wide the stress distribution can be, respectively for machining and shot peening. Moreover, this wide stress distribution can be functionally

critical to a surface, since the measurement results may hide the appearance of tensile stresses. It represents a warning since tensile stresses can appear in an average compressive state, as already highlighted by Hu et al. (2009) and Nedin and Vatulyan (2013). They finally lead to the conclusion that the conventional mean, macro and punctual residual stress analysis may provide an incomplete comprehension of a component's fatigue life prediction. Despite to the highlight given by these publications to the heterogeneity stress state, an experimental assessment methodology was not investigated.

As an alternative, the solution for the punctual evaluation issue would be delivered by the creation of a residual stress map. That would be possible if a matrix with several surface points on each depth layer is set for the measurements. Possible, but quite not feasible at the industrial scenario. The procedure at each point is highly time-consuming, thus not affordable. Furthermore, it does not bring information regarding the microstructural level of stress. The interpretation of the stress deviations at the microstructure defines a second alternative, through the quantification of residual stress in each steel phase. This method allows identifying how different the stress states are between the material phases (HAUK, 1997). However, it is neither covering a representative area for assessing the surface nor providing the deviation level for evaluating the heterogeneity at each phase.

The exposed disadvantages leave a gap to which an alternative is herein explored. As reviewed in the topic 2.2.3, the residual stress state is classified from macro to microstresses into three levels, depending on the domain size of analysis. Starting from a macro level, the subsequent microstress levels are defined as a deviation from the respective previous level. It is under this perspective that the hypothesis for a new analysis method is established: the residual stress heterogeneity state can be assessed through the intensity of its lower levels, the residual microstresses. These last, as described in the following topic, can be quantified through the broadening of the diffraction curves (Figure 5.22). It means that most part of the data is already provided by the residual macrostress measurement. Consequently, if the proposal is validated, it represents a feasible assessment solution even within industrial constraints.

This approach of linking the residual macrostress heterogeneity to the intensity of the microstresses was however not yet explored. The microstress analysis is usually applied with the focus of investigating work hardening intensity and dislocations density (PANGBORN, WEISSMAN, KRAMER, 1981; RUUD, 2002). The topic is still motivated by the outcomes of the earlier publications from Mittemeijer (1983) and Delhez, De Keijser and Mittemeijer (1987). They call the attention to the importance of the residual microstresses to the fatigue

performance, but without connecting them to the deviations of the residual macrostress state. The relevance of localized stresses to the fatigue behavior was recently reinforced by the state-of-the-art review of Lunt et al. (2015) and the study of Löpenhaus (2015).

5.2.2 The Proposal of a Feasible Assessment Method

The objective explored in this topic is the definition of a feasible method for evaluating the heterogeneity state of the residual stresses induced by processes of the gear manufacturing chain. The main goal is to correlate the macrostress deviations with the microstresses assessed through the XRD curves' broadening analysis.

The XRD technique's outcome is a curve relating the detected X-Ray intensity along the diffracted angle (2θ) values. For the calculation of the residual macrostress, the 2θ value regarding to the peak of the diffracted curve is searched. The calculation is dependent on the difference of this 2θ value between different grains' lattice orientations (Ψ) inside the material (CULLITY, 1978; LU, 2002; RUUD, 2002). The diffracted profiles still provide more information than the peak position. The broadening of these profiles is the key-parameter for the assessment of the residual microstresses (DELHEZ, DE KEIJSER, MITTEMEIJER, 1987). From a generic signal treatment perspective, the broadening can be seen as the product of several adjacent peaks of unequal intensities (Figure 5.22). This supports the hypothesis of binding the residual microstress with the heterogeneity of the residual macrostresses.

The broadening analysis, often named as "Line Profile Analysis", finds its simplest approach with the concept of the Full Width at the Half Maximum (FWHM). It is determined by the width of the diffracted curve at the intensity given by the half of the maximum intensity detected. Although allowing a quick and practical analysis, it has two meaningful limitations. Since it is a value coming from a single line, it may not differentiate effects such as asymmetry, a multimodal profile or different profile shapes. Additionally, it cannot directly refer to the microstrain. The material's particles size dispersion and the instrumental systematic errors are further significant influences on the diffracted profile width (MITTEMEIJER, 1983; GENZEL, 1997).

According to the Line Profile Analysis (LPA), the different procedures for isolating the individual influences are classified as the *Fourier-Space* and the *Real-Space* methods. The assumption according to these concepts is that the overlap between these effects is mathematically represented by convoluted functions. The desired analysis curve ($f(x)$) is the deconvolution of the measured profile ($h(x)$) from the profile that defines the instrumental

effects and the X-Ray wavelength distribution ($g(x)$). Analogously, the desired profile is the convolution from the material size dispersion and from the residual microstrain contribution. As part of the Real-Space methods, it is assumed that the measured profile represents a *Voigt* function, which is the convolution of the *Cauchy* (*Lorentz*) and the *Gaussian* distributions. Respectively, these probability functions describe the material size dispersion and the microstrain influence (LANGFORD, 1978; DELHEZ, DE KEIJSER, MITTEMEIJER, 1987; GENZEL, 1997).

The analytical procedure for conducting the deconvolution of the *Voigt* function characterizes the Real-Space methods. For each probability function, they are based on the calculation of the integral breadth, a concept defined as the profile area divided by its maximum height, Equation (5.6). The integral breadths for the *Cauchy* and *Gauss* functions are determined following the empiric Equations (5.7) and (5.8) (DELHEZ, DE KEIJSER, MITTEMEIJER, 1987).

$$\beta = \frac{\int_{2\theta_i}^{2\theta_f} I(2\theta) d2\theta}{I_{MAX}} \quad (5.6)$$

$$\frac{\beta_C^h}{\beta} = 2.027 - 0.4803 \times \left(\frac{2w}{\beta} \right) - 1.7756 \times \left(\frac{2w}{\beta} \right)^2 \quad (5.7)$$

$$\frac{\beta_G^h}{\beta} = 0.6420 + 1.4187 \times \left(\frac{2w}{\beta} - \frac{2}{\pi} \right)^{0.5} - 2.2043 \times \left(\frac{2w}{\beta} \right) + 1.8706 \times \left(\frac{2w}{\beta} \right)^2 \quad (5.8)$$

Where:

β : Integral breadth

β_C^h : *Cauchy* integral breadth of the measured profile

β_G^h : *Gauss* integral breadth of the measured profile

I: Diffracted intensity

I_{MAX} : Maximum diffracted intensity

$2\theta_i$ Initial diffracted angle for the LPA

$2\theta_f$ Initial diffracted angle for the LPA

$2w$ Full Width at the Half Maximum (FWHM)

The separated integral breadth values can be then used in the Equations (5.9) and (5.10) for removing the effects of the instrumental systematic errors (LANGFORD, 1978; DELHEZ, DE KEIJSER, MITTEMEIJER, 1987; GENZEL, 1997).

$$\beta_C^f = \beta_C^h - \beta_C^g \quad (5.9)$$

$$(\beta_G^f)^2 = (\beta_G^h)^2 - (\beta_G^g)^2 \quad (5.10)$$

Where:

β_C^f : *Cauchy* integral breadth of the desired profile

β_G^f : *Gauss* integral breadth of the desired profile

β_C^g : *Cauchy* integral breadth of the instrumental calibration profile

β_G^g : *Gauss* integral breadth of the instrumental calibration profile

The utilization of an analytical procedure simplifies the solution for assessing the microstress state. It was therefore the herein selected method for the proposal for feasibly assessing the residual macrostress heterogeneity. Despite of its straightforward nature, it must be conducted through rigorous boundary conditions. Firstly, the calibration profile is raised over a standard specimen certified to be without residual stresses. This data must be collected at each new setup of the diffractometer, which includes the procedure for sampling the different material phases. Both measured and calibration curves are then submitted to a signal treatment. The background level, the initial ($2\theta_i$) and the final ($2\theta_f$) diffraction angles (tail ends) as well as the $k\alpha$ -2 parameters must be defined and equally applied to all the data. That allows the required profile symmetry that supports the *Voigt* theorem (DELHEZ, DE KEIJSER, MITTEMEIJER, 1987). This procedure was applied to all of the measured Ψ -angles, in order to increase the chance of gathering more local deviations. The procedure was calculated for each depth layer and each evaluation direction. The high amount of data required the development of a routine to apply the entire procedure for each sample. The outlined steps are the basis of the proposal that aims at calculating the residual microstress parameters (Figure 5.23).

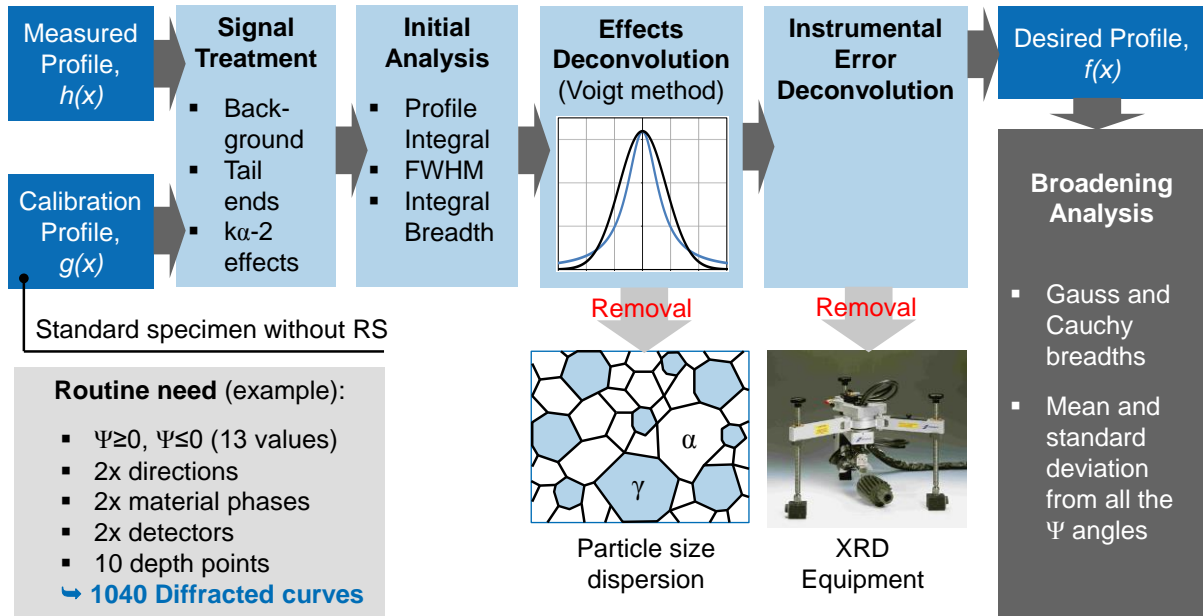


Figure 5.23 – Main steps composing the developed method and its application routine.

5.2.3 Method Validation

The validation of the proposal is established in the correlation between the macrostress heterogeneity and the microstress intensity. The database for the correlation is composed by topography measurements, and residual macrostress maps built by means of the XRD technique. Each technique is applied for identifying how uniform the surface state is. The described microstress assessment method is then utilized for defining a broadening parameter to reproduce the surface heterogeneity. The results' interpretation is supported by the integrity verification over and underneath the surface.

The specimens of the second case study, the pinions of the FZG-C gear model, were used for the validation. The three first peening groups (G1P, G6T and GDT) were the selected treatments for the experiments (Table 4.4). The process parameters defined for differentiating the stress state were essentially the media diameter and the coverage level. The different media diameters were simultaneously considered by the application of a single or a dual peening process. A decreased coverage creates a higher heterogeneity state, and the dual peening process produces a more homogeneous surface (MOLZEN; HORNBACH, 2000; REGO; GOMES; BARROS, 2013; ZHAN; JIANG; JI, 2013).

The topography maps of the three distinct peening treatments are shown in the maps of the Figure 5.24. The map of the group G1P exhibits larger rounded regions, corresponding to the larger media indentation. And the observation of GDT points out to a larger amount of

points in the highest values of the height scale. These points are also characterized by smaller individual areas. This is the outcome of the second step's glass beads, which are able to deform the peaks created during the first peening step.

The subjective perception was not converted in quantitative results in a straight way. Since the peaks are in a high number, it was not a height or a functional roughness parameter but a frequency value that could quantify this behavior. This was identified when the surfaces were evaluated from a peak density perspective. The peak density value is representing the amount of points over the total area corresponding to the 5% highest values of the height scale. The bars chart of the Figure 5.24 demonstrates the increasing trend from group G1P to group GDT. The lower density values indicate that the peaks are sparse and the respective surface is thus more heterogeneous.

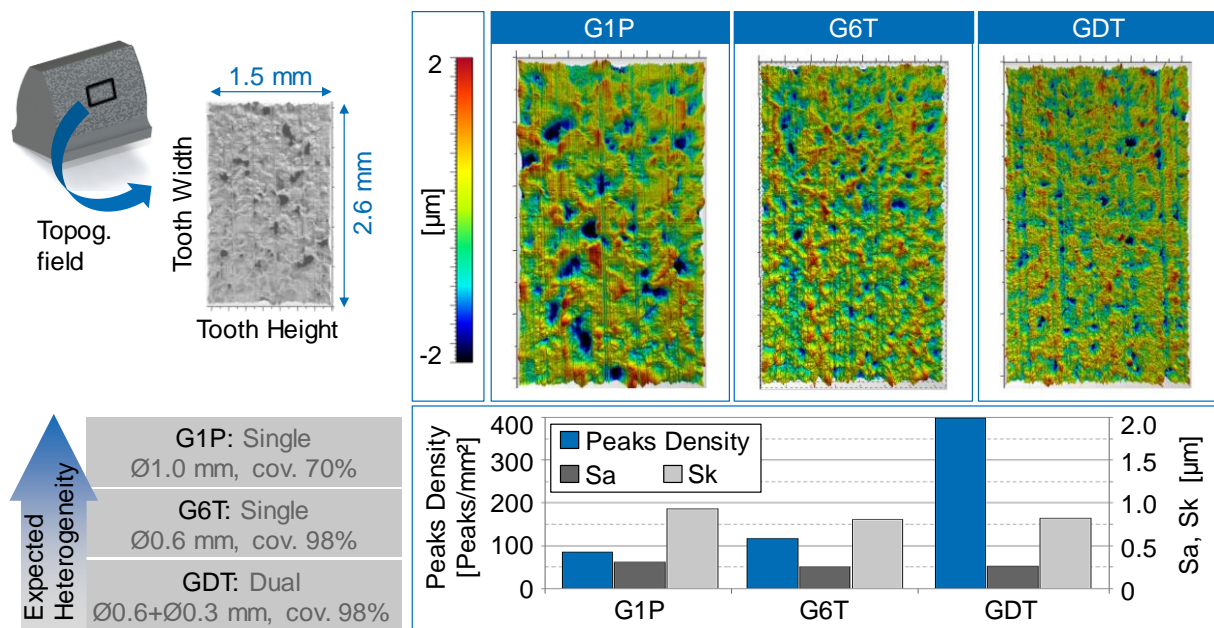


Figure 5.24 – Topography analysis of the gears produced with different shot peening configurations.

The existing difference between the group G1P and group G6T can be further explained by the distinct peening coverage levels. The valleys area is not the same for the three groups, therefore it does not demand the density assessment. With the support of the topography maps' scale, the valley depth was determined as a fixed common distance of 2.5 μm from the peaks height. At this level, the area of each sample was collected (Figure 5.24). The higher value of valleys area intensity presented by the group G1P is the representation of

the plastification produced by a larger media diameter. Both results come in the direction of the expectation. The peaks are better distributed and the total profile height is lower when coming from the group GDT to the group G1P.

The topography results indicate the expected heterogeneity behavior, but it must be still proved through measuring the deviations of the residual stress state. For this purpose, collimators with different diameters were used for comparing the effect of the distribution of local stresses across the surface. The selection of the collimator size defines the measurement spot diameter. The mapping was planned in such a way that seven fields of 1 mm diameter would fit inside a 3 mm diameter spot (Figure 5.25). The fields' disposition plotted against a topography image confirmed this purpose. The smaller spot was small enough for registering different surface profiles between them. And the large spot was including all these surface deviations. The residual stress mapping was conducted only over the outer surface layer.

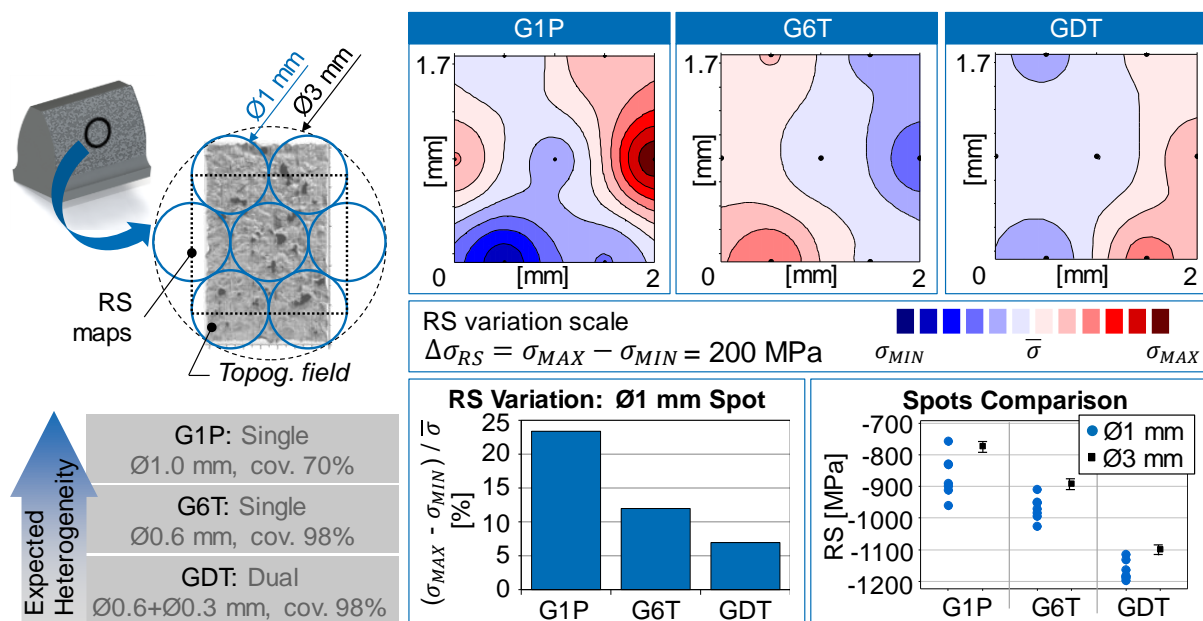


Figure 5.25 – Residual macrostress maps, the variation bar chart and a scatterplot indicate that the heterogeneity state increase from group GDT to group G1P.

For each sample, the results of the smaller spot measurements were plotted as a contour chart, according to the fields' positioning (Figure 5.25). The maps were built over a linear interpolation between the center positions of the seven measured points. The charts were defined not over the same scale intensity. But over the same scale range of 200 MPa, symmetrically distributed over the center value of each group. This was determined in order

to compare the residual stress variation between the three groups. The contour maps indicate that the surface state of group G1P is the most heterogeneous. Both the amount of contour lines and the colors difference are more highlighted in this group than in G6T and GDT.

This difference between the last two groups was lastly revealed by the examination of each mean value. As a weighted analysis, the total stress variation was divided by the respective mean value of each group. The weighted variation values are illustrated with a bars chart, Figure 5.25. A decreasing trend is observed from G1P to GDT. It shows that, as expected (MOLZEN; HORNBACH, 2000; REGO; GOMES; BARROS, 2013; ZHAN; JIANG; JI, 2013), the heterogeneity of the residual stress state is continuously increasing from the group GDT to the group G1P.

The Figure 5.25 still compares a scatterplot with the measurements from the different spot diameters. Besides the scatterplot of the smaller spot, three replications of the 3 mm spot diameter are represented by a point with an error bar. Even repeating the procedure with the larger collimator, it cannot cover all the variations indicated by the smaller one. It demonstrates how the punctual evaluation is limited regarding to reproducing the deviations of the residual stress state. The explanation for the difference between the mean values generated by each spot size may lay on the influence of the surface curvature to the height positioning of the collimator. All the charts of this figure report to the tangential direction of the measurements, but they reflect as well the behavior of the axial direction.

For the depth profile measurements of the macro and the microstresses, only the collimator that defines the 3 mm diameter spot was used. The same data acquired for the macrostresses were herein considered as input for the application of the proposed method. They were complemented by the calibration files, used for removing the equipment's systematic errors. The expectation was to find a parameter from the deconvoluted *Gauss* profile, which describes the influence from the microstrain. And the most suitable results came with the *Gauss* integral breadth. Based on the relationship between the diffraction profile area and its maximum intensity, this value was calculated by considering the average of all the measured grain orientation angles (Ψ). Within the proposed interpretation, the higher this parameter is, the more heterogeneous the residual macrostress state is.

The *Gauss* integral breadth profile along the depth is exhibited in the Figure 5.26. Up to a depth of 50 μm , the values match the confirmed heterogeneity state order: the minimum value is represented by the dual peened group (GDT); the maximum value, by the group peened with the larger media and lower coverage (G1P). The first profile's point presents a smaller magnitude difference, possibly due to the sensitivity of the diffracted profiles to

roughness, impurities and other surface preparation aspects. After the depth of 50 μm , the residual stress state is not anymore majorly driven by the peening process, as observed with the profile of residual macrostresses (Figure 5.13). For these reasons, the searched effect is concentrated in a range defined as the “Peening zone”, over both charts of the Figure 5.26.

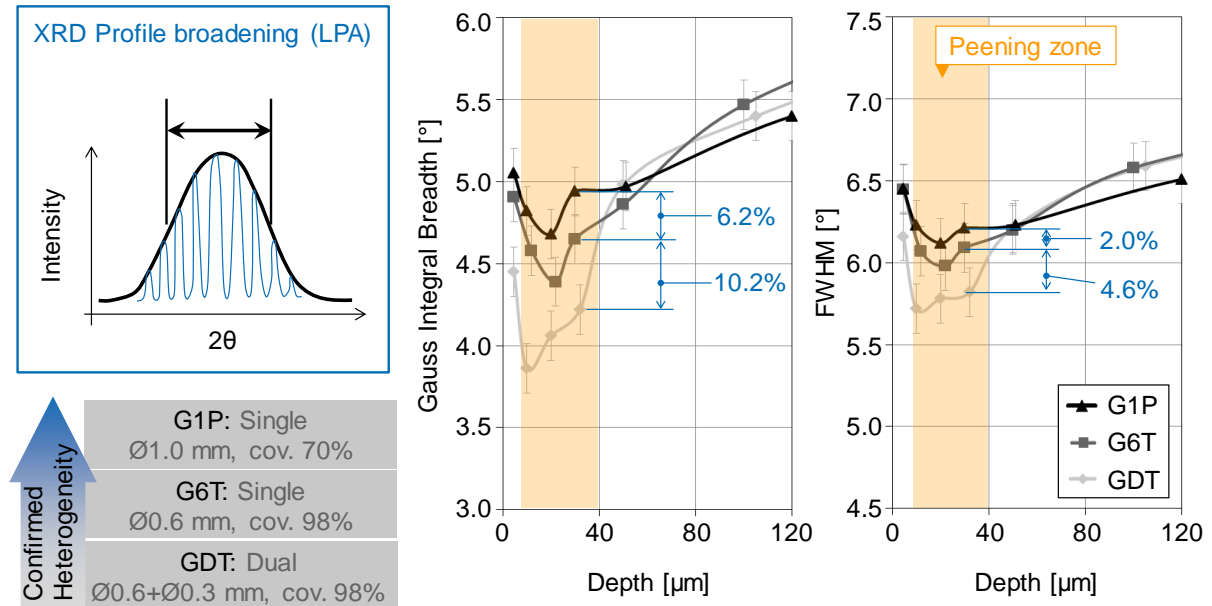


Figure 5.26 – The *Gauss* integral breadth matches the previous analyses and the order of the RS heterogeneity state, indicating a more reliable result than the FWHM.

The Figure 5.26 also comprises the results of the FWHM value. Its scatter inside the peening zone is meaningfully smaller than for the *Gauss* integral breadth. This is confirmed with the lower FWHM difference between the groups, demonstrated with percentage values through an example at the depth of 30 μm . Moreover, the relationship between the two comparative values of both parameters is not proportional. The two FWHM percentage values shown are in the order of more than the double-size (2.3% and 4.7%). The same relationship for the *Gauss* integral breadth is about 60%. These relationships vary along the peening zone and there is never a direct proportion between these both profile parameters. It indicates that the *Gaussian* parameter is adequately isolating other effects that broaden the profile, as proposed by Langford (1978), Delhez, De Keijser and Mittemeijer (1987) and Genzel (1997).

Even isolated the microstrain effects, other material and surface properties rather than the residual macrostress heterogeneity could lead to the diffraction line broadening. That would happen for the existence of microcracks, in the case of textured materials or due to

different work hardening effects. These three effects are now discussed for verifying the hypothesis herein proposed.

The studies of Kim, Cheong, and Noguchi (2013) and Hassani-Gangaraj et al. (2014) alert to the possibility of microcracks appearance due to severe shot peening parameters. The open space created by cracks redistributes the local residual stresses and therefore influences the diffraction broadening analysis. Both surface and the depth profiles were thus investigated in order to verify the existence of microcracks. The results for each one of the groups are depicted by the optical microscopy and SEM analysis of the Figure 5.27. No microcracks were observed over and underneath the surface, and this influence can be eliminated from the interpretation of the microstress analysis. Some black dots were observed on the sample's surface of the group GDT. They are residual material from the glass beads of the second peening step. This effect may not influence the broadening analysis, since the measurements are related to the respective diffraction angle of each steel phase. In any case, they would be not altering more than the results of the first depth layer. On this concern, the depth profile pictures show no meaningful difference between the groups.

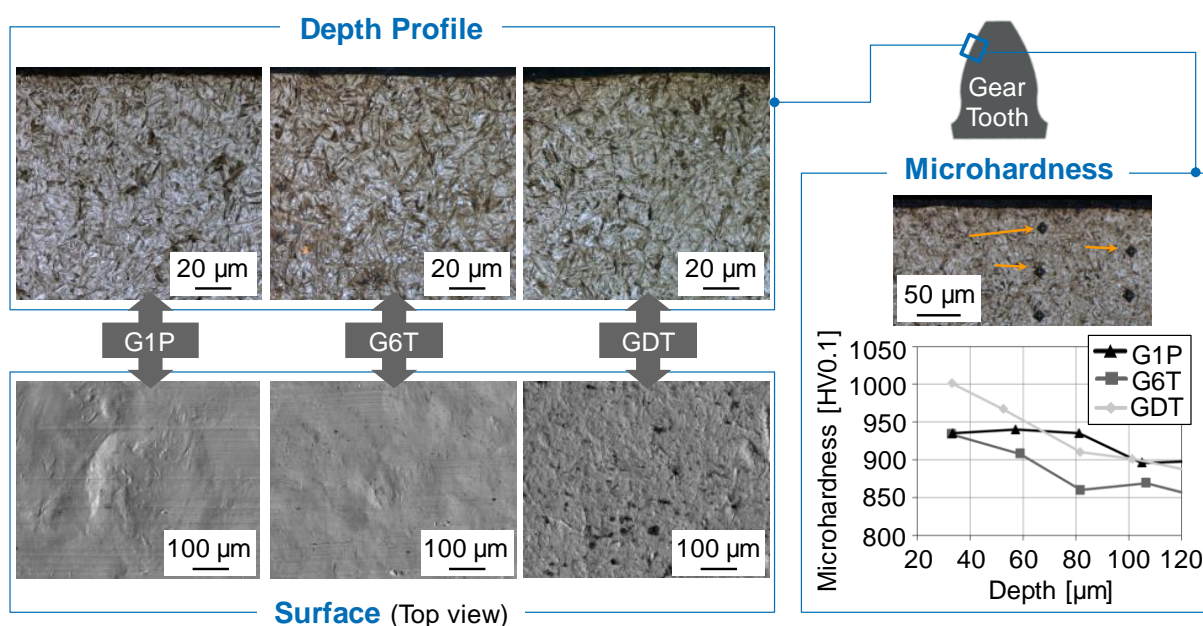


Figure 5.27 – Metallographic and SEM analyses revealed no microcracks; the microhardness results do not match with the micro RS analysis; Results support the study's hypothesis.

The depth profile images of Figure 5.27 show a conventional plate-martensitic structure of case hardened steels (SVERDLIN; NESS, 1997; BRAMFITT; BENSCOTER,

2002). The random disposal of the plates does not indicate the preferred grain orientation that characterizes textured materials. According to Perlovich, Isaenkova and Fesenko (2010), the texture should be also identified with distinct values of FWHM towards different azimuthal angular direction (Φ). The measurements conducted for the three groups on axial and tangential directions ($\Phi = 0^\circ$ and $\Phi = 90^\circ$) presented very similar FWHM results. Between these directions, the difference was mostly below 1% and never exceeded the value of 2%.

Analogously, the broadening could be a major consequence of the work hardening effect (PANGBORN, 1981; RUUD, 2002). In this case, it should be expected that the highest compressive residual stresses would lead to the highest values of FWHM or integral breadth (KIM et al., 2005; SOADY et al., 2013). However, the comparison between the results of the Figure 5.16 and Figure 5.26 indicates that the highest compressive stresses are linked to the smallest profile broadening values. Additionally, when revising that the groups G6T and GDT were produced with similar parameters and *Almen* intensity levels, being the group GDT distinguished by a second and low-intense peening step. These observations are finally supported by the results of microhardness measurements, as depicted in the right panel of the Figure 5.27. The microhardness profiles do not follow the same trend shown with the parameters of the line broadening analysis. It shows that the line broadening is not here exclusively influenced by the work hardening effect.

The isolation of these three potential factors becomes additional evidence towards the validation of the relationship between the residual macrostress heterogeneity and the residual microstress intensity. It is suggested that this relationship was not previously reported, since the FWHM is the most usual parameter for describing the diffraction profiles. With such small differences, as depicted in the Figure 5.26, either the differences were not observed or the conclusions were not statistically possible.

The results of this topic turn the *Gauss* integral breadth the residual microstress parameter that can be correlated to the residual macrostress heterogeneity state. Despite of the positive results, the method was validated according to the same material conditions. It is not yet possible to state whether the correlation would be valid also for different materials simultaneously compared. The particular microstructural arrangement, the volume and the strain properties of each material phase would also actuate as influences for broadening the diffraction profiles.

The validation conducted through the pinions was concentrated on the material and on the surface properties of the analyzed parts. The proposed approach is then applied for supporting a better understanding of the role of the residual stress heterogeneity for fatigue

failures. A *Two-Discs* fatigue contact test procedure was used for evaluating the parts' lifetime. The test is designed to enable the tested discs to be correlated to gears. The specimens were 42 mm diameter discs with a width of 18 mm. Produced out of a steel alloy 16MnCr5, they were equally machined and heat treated, but submitted to different grinding process parameters. Two groups of specimens were ground both through two steps, a roughing and a finishing process. The discs identified as "A" were produced with higher grinding speeds than the ones designated for the "B" specimens. The procedure consisted of an angular speed of 3000 rpm, a slippage of 28% and a normal force corresponding to a Hertzian pressure of 2500 MPa. The test interruption criterion was the appearance of contact fatigue failure modes (TOBIE; MATT, 2012). Each grinding group was tested a total of three times. In parallel to the fatigue tests, the residual stress was analyzed along the depth with the same equipment and procedure from the peened gears' investigation.

An illustration of the specimens, an enlarged view of the contact fatigue failure, the grinding parameters and the average fatigue lifetime appear in the Figure 5.28. In the left panel of the Figure 5.28, the results of the residual macrostresses measured along the depth on the α -phase are displayed. These results were already provided by a recent study of WZL (BRECHER; BRUMM; GRESCHERT, 2014), and then used as database for the method validation. The selected collimator was the one for a 2 mm diameter measurement spot. This conventional residual stress analysis points out to a conflict. The expectation is that a part with higher compressive residual stresses leads to a better fatigue performance. However, it is possible to see that the specimens "A", which had earlier fatigue failures, are actually submitted to a more compressive stress state than the specimens "B".

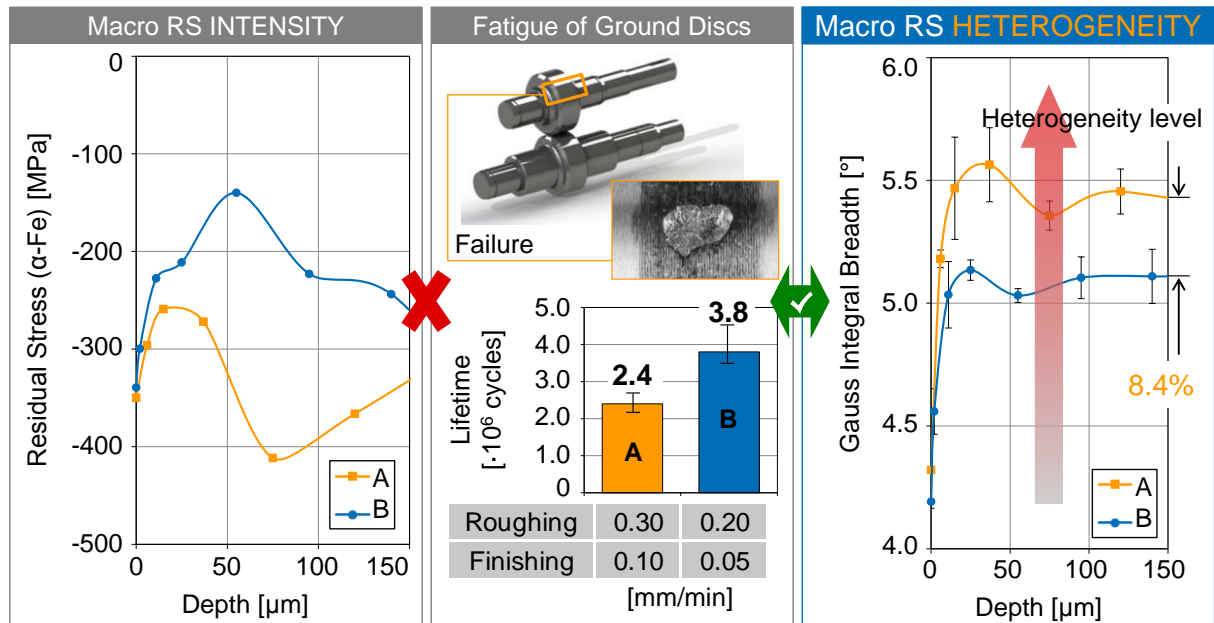


Figure 5.28 – The fatigue results of ground discs conflict with the expected behavior of the residual macrostresses. A potential explanation is given with the RS heterogeneity, by means of the *Gauss* integral breadth.

The mentioned conflict motivated the application of the validated model to this case. It was again the *Gauss* integral breadth that provided a potential explanation. The values of the *Gauss* integral breadth of the specimens “A” are definitely higher from the depth of about 15 μ m, Figure 5.28. Following the conclusion of the validation investigation, it is indicating that the residual stress state of the specimens “A” is more heterogeneous than the one of the Specimens “B”. The conclusion is coherent when analyzing the grinding parameters of each group. The higher grinding speeds represent a more severe treatment to the surface, which cannot behave within such a uniform stress pattern. As a consequence, despite of having a more compressive mean stress state, its higher deviations might have probably led to the deleterious fatigue behavior.

The mean difference of 8.4% between the specimens regarding to the *Gauss* integral breadth may not initially seem high. However, the studies of Batista et al. (2000), Xie, Jiang and Ji (2011) and Vielma, Llaneza and Belzunce (2014) show that a delta of about 10% regarding to integral breadth or microstrain can describe very different surface integrity states. This statement is reinforced by the results of the same order observed with the peened gears, during the validation analyses. In the same direction of the peened gears’ evaluation, an analogous conclusion might not be possible with a FWHM analysis. By means of it, the relative difference is only of 2.8% in average along the depth, again at a 15 μ m deep layer,

starting from surface. The smaller difference indicates that not only the residual microstresses broadened the diffracted curves. This comparison is an additional motivation for the application of the proposed method.

In summary, the results highlight the importance of assessing the heterogeneity state for an enhanced comprehension of the residual stress role in the fatigue strength. The method is not proposed as to overcome the importance of the residual macrostress intensity to the part lifetime. It appears as a statistical complement in order to add deviation information to the mean value provided by the XRD measurement.

As an outlook for this specific study, which was published as Klocke et al. (2016), it is planned a robustness enhancement model. Since these initial results presented a positive trend, additional mathematical developments can be implemented, such as the *Fourier-Space* procedure for the effects' deconvolution.

5.2.4 The Interaction between Soft Machining and Heat Treatment

The validation of the demonstrated method represented as well the feasibility of including the heterogeneity state in the residual stress interaction analysis. This topic covers the application of the method on the early manufacturing stage, where the machining and the heat treatment processes are investigated. It will not only be explored according its heterogeneity meaning. Since the *Gauss* integral breadth is a parameter related to residual microstresses, the collected results will also be used to support the comprehension of effects observed within local boundaries.

The same data generated for the machining macrostress discussion is taken into the developed routine to calculate the induced microstresses. The *Gauss* integral breadth was calculated for each machined sample, and the results are plotted along the depth in the Figure 5.29.

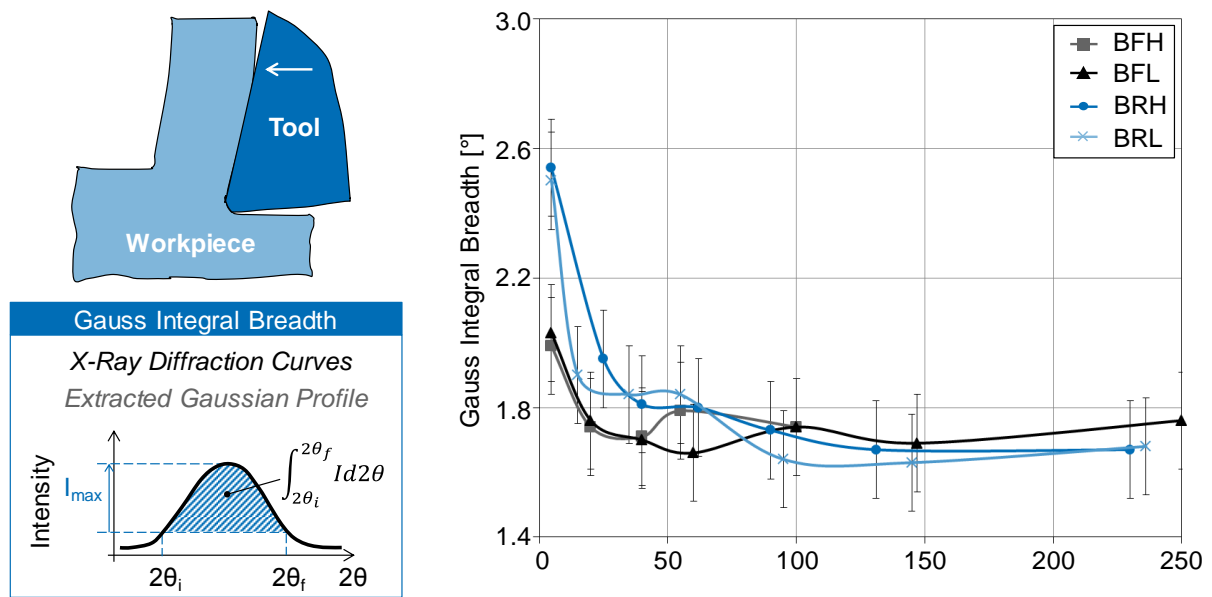


Figure 5.29 – The *Gauss* integral breadth along the depth for the groups after milling.

The chart indicates that no meaningful differences exist among the roughing specimens nor among the finishing parts. On the other hand, the distinction between these two is noticeable over the first two layers. Out of this comparison, it is once more the depth of cut that shows to play an important role to the stress state. Contrary to the directional focus given to the macrostress analysis, these results must be understood as the overall effects captured by the XRD inside the measurement region. Considering the measured area has an area of 4 mm by 4 mm, the measurements of both the roughing and the finishing samples certainly included more than one milling pass. The topography maps of the Figure 5.30 expose the surface difference induced by the axial depth of cut, quantified by a comparison between their corresponding roughness metrics. The lower a_p set for the groups BFH and BFL promoted a larger superposing effect of the passes. After one pass was concluded, the tool movement was small enough to cover a meaningful area of the previous pass. The opposite outcome is observed on the surface of the groups BRH and BRL, in which a pronounced separation of the passes appears as product of the larger a_p .

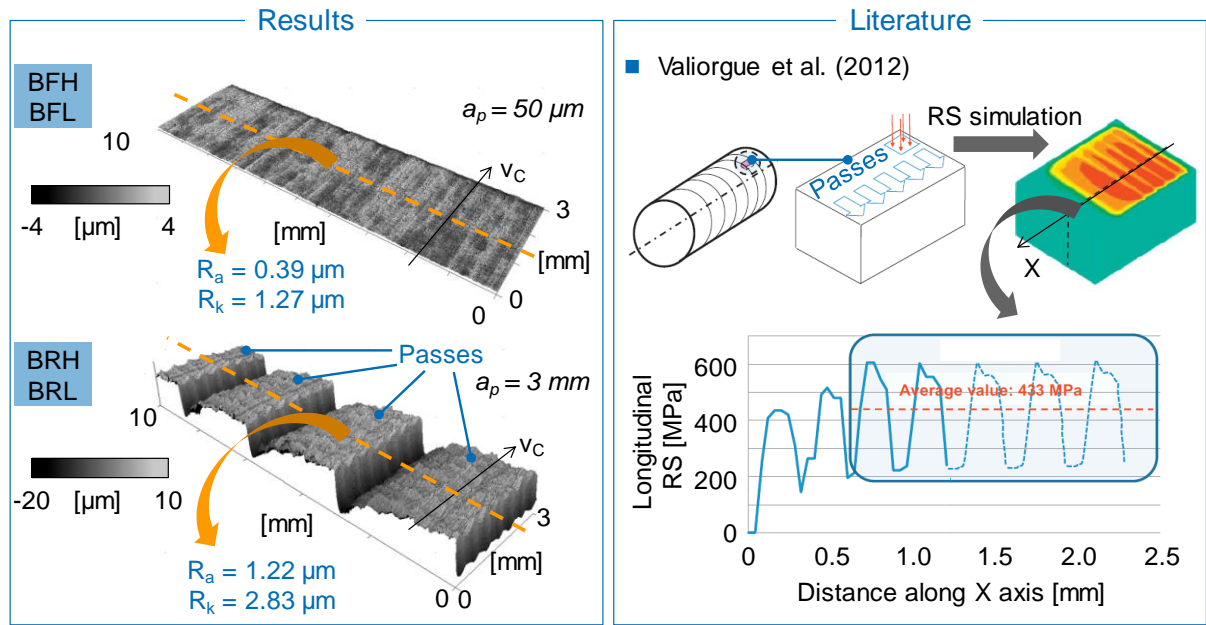


Figure 5.30 – Results and literature converging to the influence of the depth of cut on the heterogeneity state of residual stresses.

The passes' isolation exposes the deformation profile variation created by the tool into one pass, and thus the residual stress heterogeneity pattern. The topography analysis alone does not fully express the residual stress state, since the machining has also a thermal stress origin. But it works as evidence to connect the thesis to further publications' results considering all the load sources from the machining. The simulations of Valiorgue et al. (2012), summarized in the Figure 5.30, clearly display the residual stress deviations generated by sequential passes of a turning process. This is the same phenomenon that may explain the *Gauss* integral breadth results herein obtained.

For the interaction analysis, the stated differences between the groups are an achievement of the goal to produce distinct input database for the second process. The same samples were taken to the heat treatment cycle, and the depth profile of the Gauss integral breadth is presented in the Figure 5.31.

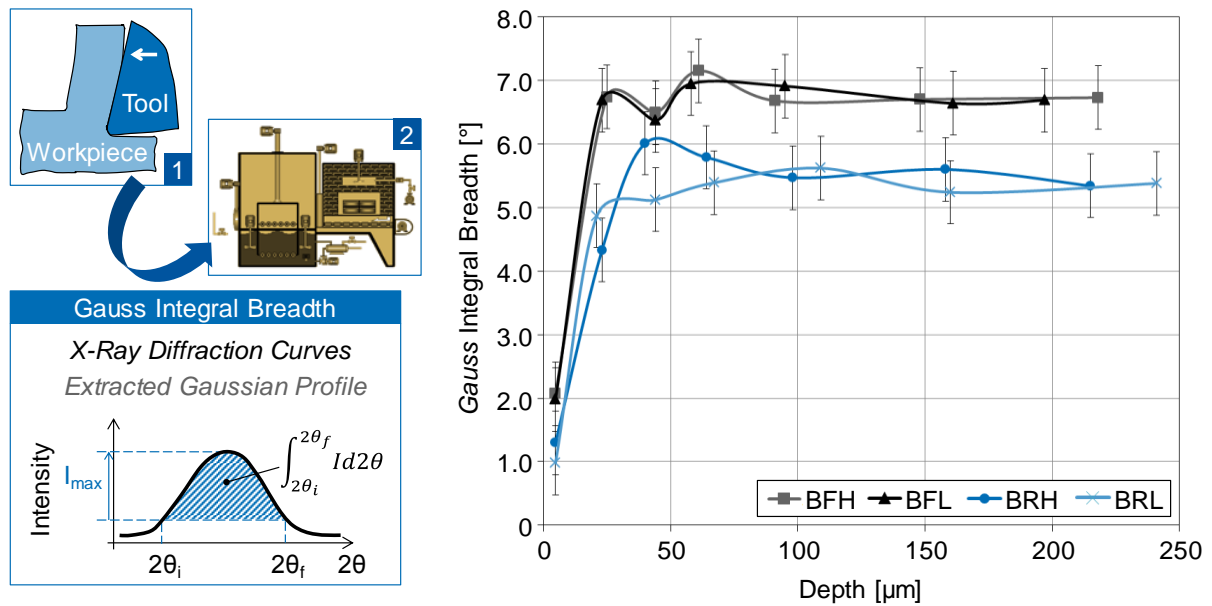


Figure 5.31 – The *Gauss* integral breadth along the depth after the heat treatment process.

Following the rationale behind the results of the residual macrostress, a complete relaxation during the heating should also equalize the microstresses. Contrarily, two groups of samples differ, being the finishing specimens now the owner of the largest *Gauss* integral breadth.

If the expected interaction should be a function of the machining process, three observations are outlined in contrast to this expectation. Firstly, the microstress difference remains up to the last assessed depth point, of around 200 μm. As shown by the Figure 5.5 and the Figure 5.29, the effects of the conducted machining experiments were likely to induce meaningful changes to the integrity up to a depth of approximately 50 μm. A second aspect is taken when assessing the microhardness profile after the heat treatment (Figure 5.32). This chart exhibits that, such as for the microstress profile, the finishing groups (BFH and BFL) and the roughing groups (groups BRH and BRL) are separated, in a trend that extends up to deep levels. These first two points raise some indications to manufacturing processes even before the machining. It takes then the analysis to the third remark. As stated earlier, although ordered and verified to be from the same chemical composition (Attachment “C.1 Blocks, SAE 8620”), the finishing and the roughing groups come from two different material batches, respectively.

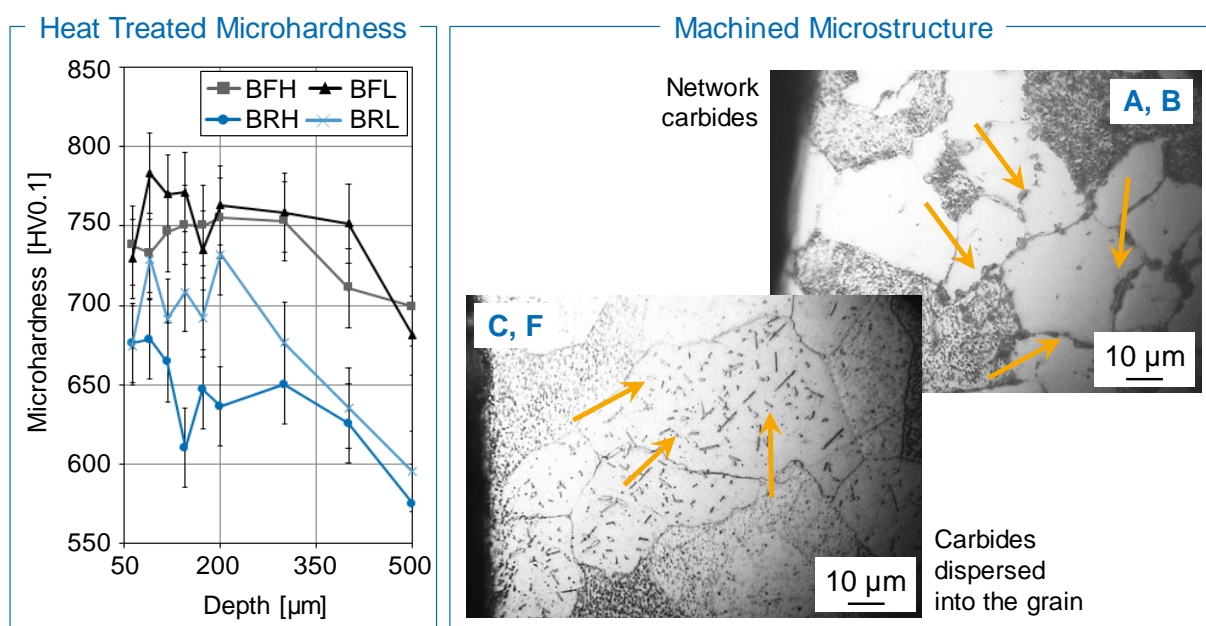


Figure 5.32 – The microhardness after the heat treatment and the microstructure before it reveal the reason for the different microstresses of the hardened samples.

The three presented statements recall the microstructural difference observed before the heat treatment in the topic of the machining macrostresses (5.1.1). Observing the images at higher magnifications (1000X), the structural difference between the two groups is highlighted (Figure 5.32). For the specimens of the groups BFH and BFL, the carbides are precipitated mainly on the grain boundaries, in an arrangement named as “network carbides”. Differently, the structure referring to the groups BRH and BRL comprises carbides dispersed mainly inside the grains.

The hardness of the carbides itself is higher than the martensite-austenite matrix where it resides (Parrish, 1999). According to Bramfitt and Hingwe (2002) and Przylecka et al. (2008), the network arrangement reduces the potential for the redissolution of the carbides during the heating cycle. These remaining network carbides result in a brittle and hard structure. The hardness effect is not only reinforced by Lampman (2002) but it also shows to match the microhardness measured on the treated samples. The groups with the network carbides prior to the case hardening are also characterized by the harder surface layers in the Figure 5.32.

As discussed during the validation of the heterogeneity assessment method, the *Gauss* integral breadth can also be influenced by the work hardening effect (PANGBORN, 1981; RUUD, 2002). Additionally, Parrish (1999) states that large differences between the carbide

and the matrix induce large microstresses after quenching. Brought to this comparison, a dispersed carbide arrangement creates a better distribution of residual stresses inside the lattice, and thus a smaller heterogeneity state. The combination of this information connects back the microstress results to the microstructural examination. The samples with the network carbides are exactly the one with the larger *Gauss* integral breadth.

The microhardness difference, such as the carbides precipitation, is observed along the entire analyzed depth range. Moreover, the manner how the carbides precipitate is primarily dependent on the austenitizing time and on the subsequent cooling rate (PARRISH, 1999; ERICSSON, 2002b). It is hence possible to affirm that the separation between the groups at the microstress assessment is not a direct influence of the milling. Also, a microstructural inhomogeneity that is not erased by the case hardening is not an exclusive role from carbides. The same effect was already observed in the case of banded structures by Navas et al. (2011).

Revisiting the second research question, the experimental scope was designed to verify the role of the heterogeneity on the interaction in-between the processes. The machining was not the generator of the different input states, but the interaction hypothesis proves to be valid. A heterogeneous feature certainly coming before the heat treatment promotes a change in its residual stress state. Adding an even more special constituent, the change is not noticed by means of the conventional macrostress assessment, but by the microstress analysis. The effect inference at an early stage of the manufacturing chain consists of an additional motivation to investigate the interaction at a late stage, as presented in the next topic.

5.2.5 The Interaction between Shot Peening and Grinding

Considering the intensity factors of the residual stress state, the topic 5.1.4 proved the interaction effect between shot peening and grinding. A driven factor was indicated and explained by means of the stored energy level of the springs' model. The interaction is now investigated, by verifying the influence of the heterogeneity state of the peening residual stresses to the integrity of the ground surface. The validated assessment method brings this analysis to a micro level, requiring the connection to further examination on a similar domain size.

The first three peening groups (G1P, G6T and GDT) were previously explored during the heterogeneity method validation. With the positive outcome from these preliminary results, the method was hence extended to the groups G3T and G3P. The residual microstress metric is simultaneously plotted for all of the groups in the Figure 5.33.

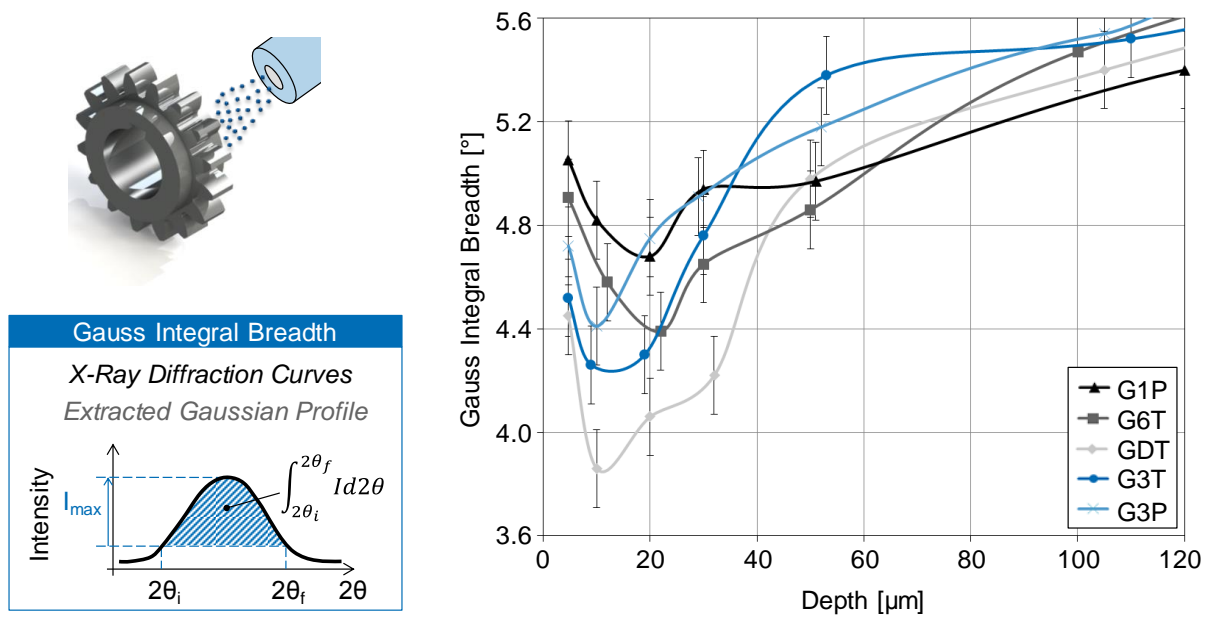


Figure 5.33 – The *Gauss* integral breadth along the depth for the groups after shot peening.

Two main observations can be taken out of the chart of the Figure 5.33, by the introduction of the groups peened with the smaller media (G3T and G3P). Firstly, following the macrostress results, the largest effects of the just mentioned groups are visible in a shallower range. Their lower media diameter brings the earlier defined “Peening Zone” from a maximum depth of 50 μm to 30 μm. Therefore, it is within this depth range that the conclusions about the heterogeneity of these two groups are drawn.

The second aspect refers to the comparison among the two added groups. They allow, for the first time, that only the influence of the coverage level can be analyzed. The only difference between them is that the group G3T was peened with 98% coverage against a level of 70% for the group G3P. As expected, the lower the coverage is, the larger the heterogeneity will be. The statement is reflected on the just defined depth range of the chart in the Figure 5.33, in which the *Gauss* integral breadth of the group G3P shows to be approximately 14% larger than the group G3T.

The media size influence can be discussed when now considering these two groups in a comparative analysis to the other three. Fixing the coverage to individual levels of 70% and 98%, contrasting diameter scenarios are exposed. The group G1P shows a higher *Gauss* integral breadth than the group G3P, whereas the same value is larger for the group G6T, taking as basis the group G3T. In both cases, the larger diameter is responsible for the higher heterogeneity state. The result is coherent, since the larger diameter induces higher plastic

deformation in the surface. Also, highly compressed areas must be, according to the residual stress equilibrium principle, balanced by an equivalent tensile region. These both stress extremities are increased, extending the deviations and increasing the heterogeneity.

Finally, the diameter of 0.3 mm could still be taken for comparing the dual and the single peening processes, respectively groups GDT and G3T. In this case, the dual peening has a previous step with a larger diameter and, even though, it has the least heterogeneity state. The function of the smaller media for the dual peening is indeed to homogenize the surface generated by the first step. When the second-step media collides against the surface, it finds already a highly compressed state. Its role is thus extracting further deformation potential, by inducing stresses in the regions that can still be strain hardened. The result is a closer stress intensity between the neighboring areas across the surface. In an analogy to the machined surface, the second step exerts the function of a superposed milling pass.

The observed differences enable the five groups to be fed in the heterogeneity residual stress interaction analysis. All the groups were submitted to profile grinding and their respective values of the *Gauss* integral breadth are displayed in the Figure 5.34. Likewise the intensity interaction analysis, the result allows to confirm the basic statement of this thesis. Would the previous processes not be meaningful to the final integrity state, the residual microstresses should be the same after the grinding. However, the difference between the largest and the smallest values on the first subsurface layers of the Figure 5.34 is in the order of 23%.

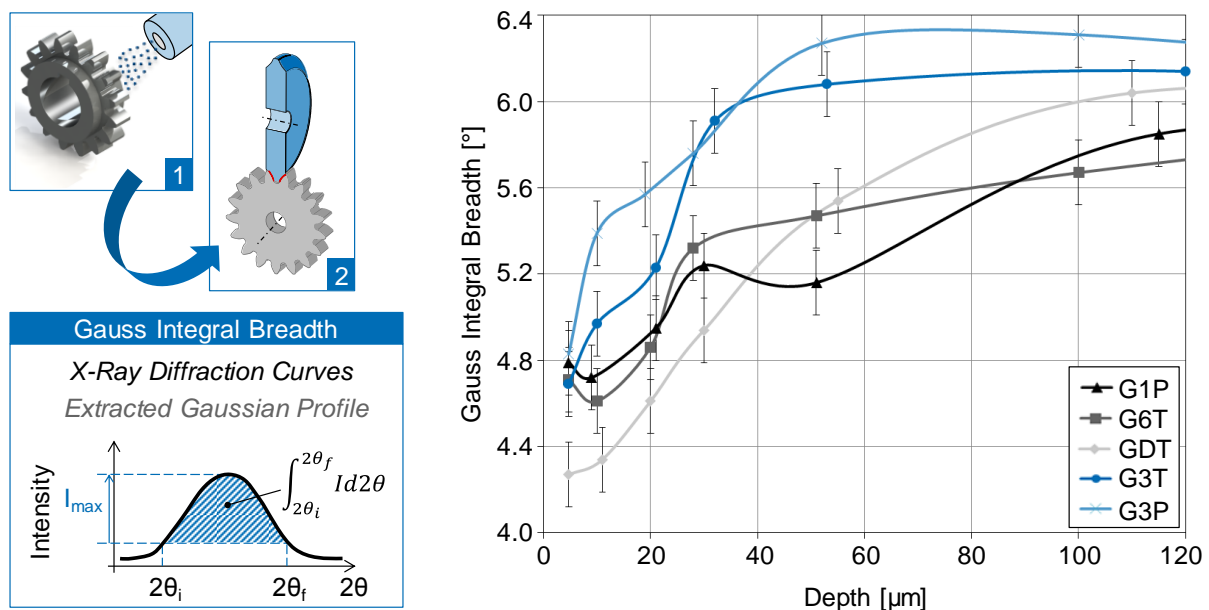


Figure 5.34 – The *Gauss* integral breadth along the depth for the groups after grinding.

Differently than the approach assumed for the stress intensity, the heterogeneity interaction analysis has to be locally performed. This means a comparison over compatible depth levels between the two manufacturing steps. The compatibility is defined by the grinding stock removal of 30 μm , and the defined “Peening Zone” must be considered. Hence, the *Gauss* integral breadth of the peened surface between 30 μm and 50 μm is compared to the same value of the ground surface from the outer layer to a depth of 20 μm .

The influence of the interaction is seen within a limited boundary. It requires that the five groups are separated into two classes, one containing the three largest and the other containing the two smallest peening media sizes. Recalling the peened profiles at a depth level of 50 μm (Figure 5.33), a class with the 0.3 mm media diameter groups (G3T and G3P) is detached from the other class, in which the further groups behave similarly. When now using this separation to observe the ground profiles (Figure 5.34), the compatible depth around 20 μm provides a convergent outcome. Also the groups G3T and G3P have the largest *Gauss* integral breadth, while the smallest ones appear for the groups G1P, G6T and GDT.

In a direct comparison between the groups of each isolated class, however, common trends are not observed. The statement defines that the sensitivity of the interaction to the heterogeneity factor is less intense than for the intensity of the residual stress. Larger differences in the previous stress state are necessary to reflect the result out of the final surface.

An attempt to collect more information for the comprehension of this partial influence brings the analysis to the outer layer of the ground samples. Whereas at least four ground groups are characterized by almost the same surface value, the compatible depth of 30 μm (Z_{STOCK}) on the peened profile provides more distinct results. It indicates that the stress alteration between the two manufacturing steps occurred as different ways for each group. Following the potential energy model, a residual stress change must be analyzed simultaneously to distortion, geometric deviations. In this case, the geometric deviation has to be consistent with the residual microstress domain. It signifies the size of a grain or less than that. The microstructure of the ground specimens is, analogously to the presented peened ones, composed by a predominant martensitic phase, and partially by retained austenite. The martensitic phase is in the form of plates, as seen in the Figure 5.35. The martensite plates can be used to approximately derive the grain size, since its growth is limited to the boundaries of its former austenitic grain (SVERDLIN; NESS, 1997; BRAMFITT; BENSCOTER, 2002). The same figure shows that the grain size, and hence the geometric level to examine the distortion, is less than 9 μm .

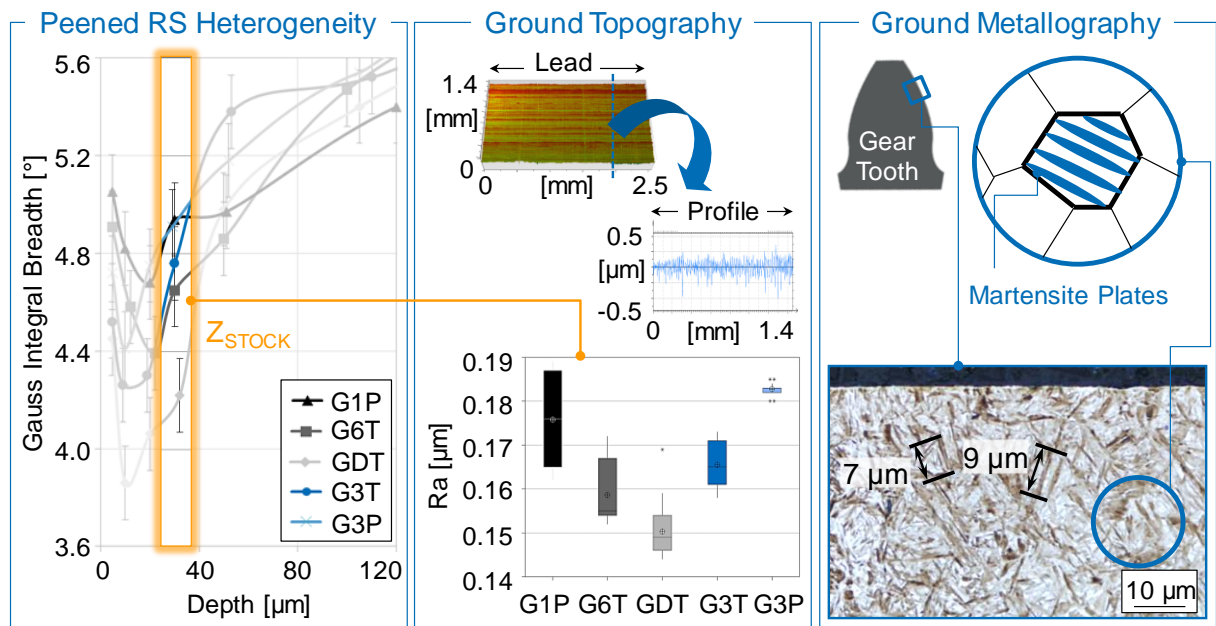


Figure 5.35 – The residual microstress of the peened surface influences the roughness after the grinding process.

The derived size was the hint to observe the results of roughness from the ground specimens, as shown by the profile extraction of the Figure 5.35. The same figure contains a boxplot with the measurements of five profiles over three teeth from each group. Once more, contrasting to the state-of-the-art, the same grinding process was not enough to provide the same surface characteristics. More than different, the trends observed in this boxplot converge with the *Gauss* integral breadth at the mentioned depth of 30 μm (Z_{STOCK}) on the peened surfaces. The statement brings the discussion back to the interaction analysis. The hypothesis that connects the latest observations is that the microstress from the peened surface was partially relieved as local deviations, generating some direct influence on the roughness of the ground samples. This argumentation is based on the mechanism of local equilibrium. Immediately after a grain from the grinding wheel ploughs the surface, the local contact elastic stresses are relieved. Together with them, some residual stresses in the domain of the crystal lattice are also relaxed, on a search for the very local equilibrium. This additional material movement is supposed to influence the formation of the roughness features, which are in the same order of size. The alignment between the data is clear. But the influence is not major, since the observed roughness differences are minor for an approach of the absolute values.

Overall, the heterogeneity showed to influence the interaction between shot peening and grinding, although with sensitivity restrictions. Moreover, an effect on the grinding roughness can be connected to the heterogeneity of the shot peening process. This is certainly only a preliminary conclusion. It provides a motivation to apply the interaction analysis with considering the heat treatment as the first process. The steps of one treatment cycle could be changed to verify both the influence of residual stresses and the grain size dispersion. If confirmed to further processes, this concept consists of an additional directive to design the manufacturing chain when the roughness quality is a major product requirement. The control of the heterogeneity state before the analyzed process would be then turned in one more variable to support the control of the roughness afterwards.

5.2.6 Summary

The potential large dispersion of the residual stress state motivates the investigation on how the deviations depend on the manufacturing chain. The residual stress heterogeneity, under the spotlight of the second research question, was approached for the same two case studies examined for the stress intensity interaction. Described along this topic, they were still preceded by the development of a method to feasibly assess the heterogeneity state.

Within industrial constraints, the conventional approach to the XRD technique delivers a punctual and averaged measurement of residual stresses. It does not allow the proper representation of the residual stress state, exposing the demand for a method of assessing the residual stress heterogeneity state. For this purpose, a method was developed with basis on the relationship between the deviation of the residual macrostress and the intensity of the microstress. The shot peened gears were used for the validation, being their microstresses assessed by means of the diffraction profiles broadening. The reference database was composed by topography measurements, metallographic analyses and residual macrostress maps. The stress heterogeneity was reasonably correlated to the intensity of the *Gauss* integral breadth. Applied to ground discs, the correlation's parameter filled a comprehension gap between the measured residual stress intensity and observed contact fatigue failures. By using the same macrostress measurement data, the method proved to be feasibly applied.

The utilization of the method to the machined surfaces revealed the high influence of the depth of cut. Especially over the first surface layers, the roughing specimens were characterized by a more heterogeneous state. Likewise the phenomenon observed for the

macrostresses, these microstresses are relieved during the austenitizing process. The machining heterogeneity influence is hence not observed after the heat treatment cycle. A difference on the heterogeneity state of the hardened samples is, however, observed along the entire analyzed depth range. The identification of different carbide arrangements between the finishing and the roughing samples bring the difference explanation to a process even before the milling. Although not being a reflection of the machining process, the evidence of the interaction effect is observed. The residual stress heterogeneity state proves to be dependent on the manufacturing chain prior to the heat treatment itself.

For the second case study, the method confirmed the expectation in which the larger media size and the coverage level induce a more heterogeneous stress state. After the grinding process, the microstress level of the gears showed to create a difference of up to 23%. The interaction effect is identified, although the influence from the shot peening is not straightforward. The trend after the peening is indeed brought to the ground condition, but just after separating the groups with the 0.3 mm media size from the larger media groups. On the other hand, no separation was necessary to observe a relationship to the roughness after grinding. The peening microstress level at the grinding stock depth is directly proportional to the roughness after the grinding. It is supposed that immediately after a grain from the grinding wheel ploughs the surface, the local contact elastic stresses are relieved. Together with them, some residual stresses in the domain of the crystal lattice are also relaxed, on a search for the very local equilibrium.

The exploration of the heterogeneity state consists of a powerful tool to enhance the manufacturing control and the comprehension of the fatigue performance. Its role to the process interaction transcends the residual stress state itself. It shows to provide connections to both the microstructure and to the surface roughness of the neighboring processes in the manufacturing chain.

5.3 The Interaction's Relevance to the Fatigue Behavior

The two previous main topics described the importance of the manufacturing chain to the final surface integrity. In different domains, the effects were observed in distinct magnitudes. Recalling the introduction of the thesis, a meaningful motivation to conduct this

investigation is the possibility of providing an enhanced comprehension of influence of the surface integrity on the durability performance.

The mapped interaction effects of intensity and heterogeneity of residual stress can now be assessed under the fatigue perspective. The last topic of this chapter starts with a descriptive content of the results coming out of the contact fatigue tests. Later, the damage concept is examined regarding to the cracks formation and to its morphology evolution. Finally, all this information is analyzed as a holistic approach considering the outcomes of the residual stress interaction analysis.

5.3.1 Contact Fatigue Performance of the Different Manufacturing Chains

The running behavior investigation of the five groups was done by means of a low-cycle fatigue test procedure. It was represented by the application of the highest torque level according to the standard DIN ISO 14635-1 (DIN, 2006). The lifetime results are displayed by their mean values in the Figure 5.36, followed by the respective manufacturing processes of the interaction analysis. The dispersion of the group samples is identified by a MRE equal to the standard deviation. From a direct observation of the chart, the first and most important conclusion is the existent difference in the lifetime between the samples. The result converges with the basic statement introduced by this thesis. The control of the final process of a manufacturing chain is not sufficient to predict the surface integrity state and, in this case, the fatigue strength. The difference between the longest and the shortest lifetime is about 68%. And even when considering the results' scatter, it is possible to identify different orders of lifetime between the groups.

- Specimen: FZG-C Pinion
- Pinion Speed: 4,500 rpm
- Pinion Torque: 534 N·m
- Failure: damage larger than 4% of the flank's area

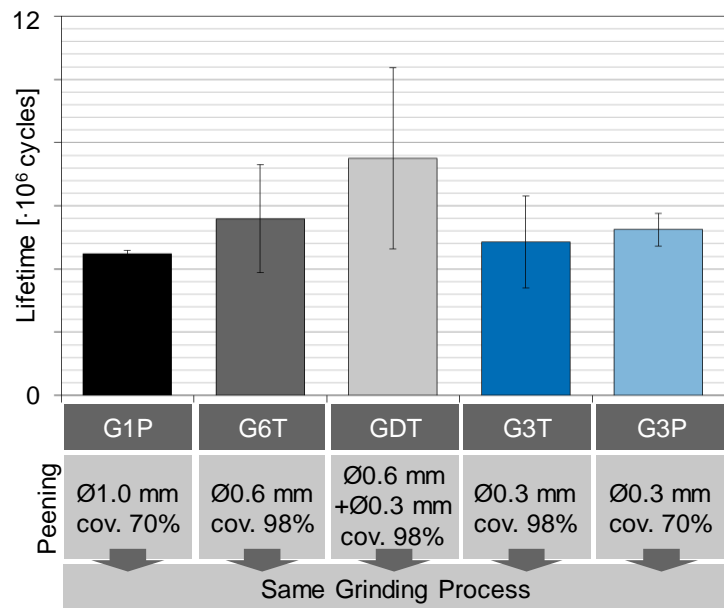
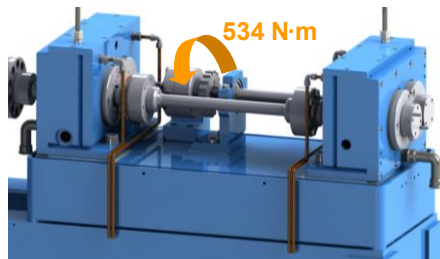


Figure 5.36 – Mean lifetime results of the different manufacturing chains.

Considering the distinct scatter intensity between the groups, a probability approach was taken to verify the mentioned initial observations. The *Weibull* extreme value distribution was the statistical function selected for the description of the fatigue performance. This function is capable of effectively describing very different lifetimes and it is especially used in the probability assessment of early failures (LECHNER, NAUNHEIMER, 1999; MCEVILY, 2002).

The *Weibull* approach requires ranking the samples within a same group, regarding to their lifetime result. Percentage levels of failure probability are assigned for this ranking, also considering the sample size of the group. This relation is described by the Equation (5-11) (HÖHN, 2010).

$$F = 100 * \left(\frac{i}{n+1} \right) \quad (5.11)$$

Where:

F: Failure probability in %

i: Lifetime ranking, with i = 1 for the shortest lifetime

n: Sample size

The failure probability is taken together with the corresponding lifetime to compose the *Weibull* diagram, as a bi-logarithmic chart. The plotted points are used to extract a regression line, according to the Least-Squares method. The point where this regression line crosses the failure probability level of 50% defines the parameter LC_{50} . This parameter is used to define the test result, enabling the comparative analysis of the fatigue performance (HÖHN, 2010). The limit of 50% is a countermeasure to offset the high scatter of a small sample size, which reduces the reliability of low and high failure probability levels (MAUCH; ZENNER, 1999). This procedure was applied to the previously presented results, and the *Weibull* diagram, followed by the LC_{50} results, is shown in the Figure 5.37.

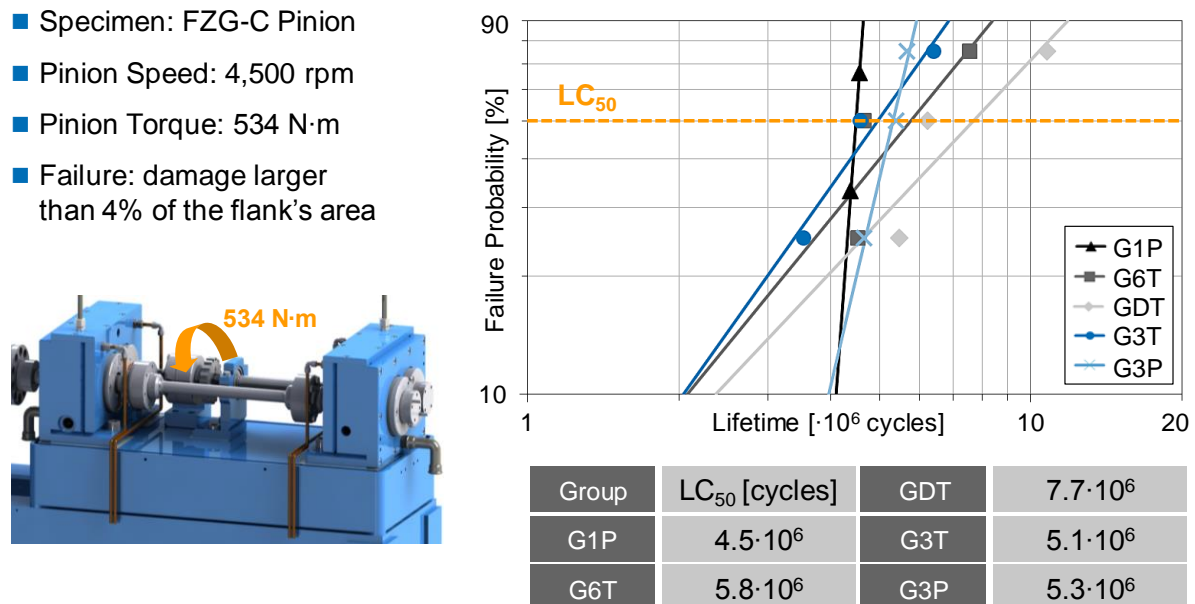


Figure 5.37 – Statistical approach to the fatigue results through the *Weibull* distribution method.

With the *Weibull* approach, the sequence of results, coming from the most to the least durable group, is kept the same than the one from the Figure 5.36. The previously described difference between the longest and the shortest lifetime has a slight increase from 68% to 71%. These conclusions support the statement of the existence of different fatigue behaviors between the groups, although manufactured with the same final process. Whether these results are compatible to the mapped residual stress states, it is still required to identify the failure mechanism in detail. This investigation is the content of the following topic.

5.3.2 Damage Morphology Analysis

In order to verify the relationship of the durability performance with the residual stress interaction outcomes, the failed surface is examined inside this topic. Face to the controversial terminology from the literature, the failure will be in a first instance described as “damage”. The investigation covers the damage morphology, using its geometric features to identify its origin and evolution along the time.

The initial approach to the damage concerns its aspect and how it progresses along the time. The first change to the surface is characterized by the appearance of small portions of material removed along a line in the bottom of the flank, close to the transition to the root. In a first evolution stage, the amount of small damages grows along this line, almost fulfilling the entire tooth width extension. The increased appearance of the small removed portions joins them into a larger damage, which grows towards the pitch line. The lead crowning promotes a higher contact pressure at the tooth width center, where the enlargement mechanism is thus concentrated. In the last stage, the damage enlargement quickly overcomes the failure criterion. Due to the stochastic influence of the several influences to the failure creation, the evolution is not simultaneous for all the pinion’s teeth. Therefore, the sequence of images representing the evolution observed along the inspections comes from different teeth (Figure 5.38, left). On these pictures, the damage was highlighted by the liquid penetrant testing.

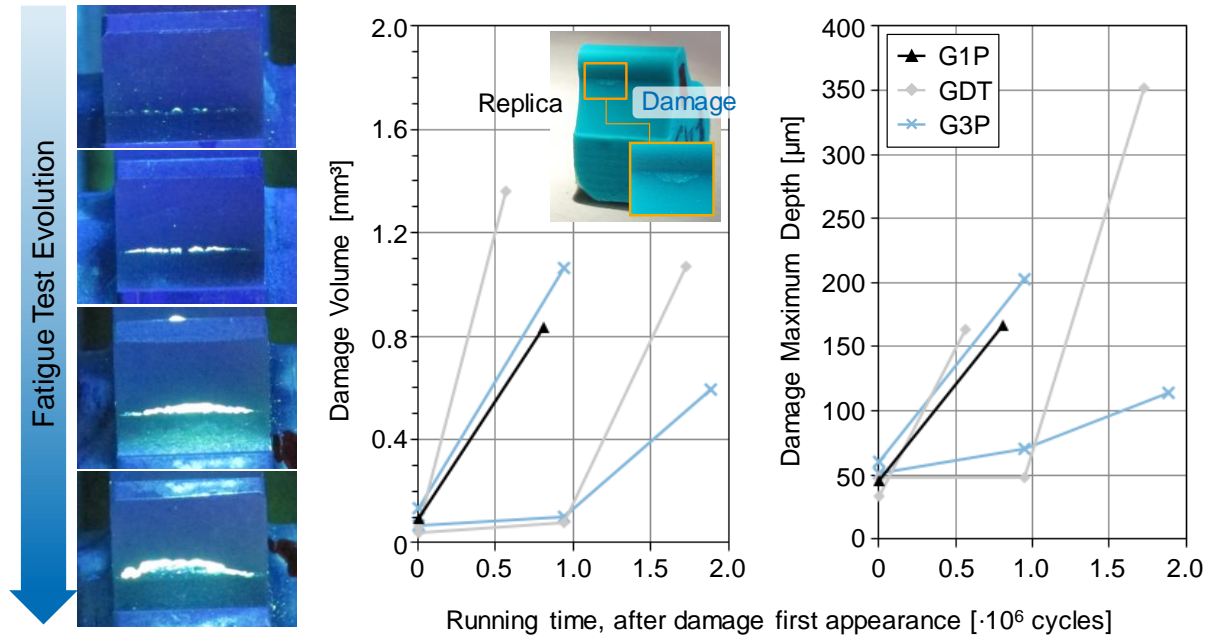


Figure 5.38 – Damage evolution along the fatigue test.

The evolution on the same flank was also monitored, by means of the measurement of the damaged surfaces reproduced by replicas extracted at the regular inspections. Out of the tested five groups, the procedure was applied to three of them, representing the three different classes of residual macrostress observed in the Figure 5.18. Both the volume and the maximum depth of the damage are analyzed along the running time (Figure 5.38). The goal of analyzing the evolution requested the first chart point to be plotted for the first inspection when a damage appears. They are hence not aligned according to the running time since the test had started. The last point refers always to the moment when the failure is characterized. With exception to the group G1P, the damage was monitored by three steps along the test. The charts show results for teeth inspected twice or three times up to the failure, taken from the best produced replica of each gear group.

The evolution rate shows a pattern that can be seen for both the volume and the depth measurements. The final stage is identified by an accelerated growth, in which the damage achieves the failure criterion in less than one million cycles. The previous features to the final stage are almost invariant, defined by a depth of approximately 50 μm and a volume around 0.1 mm^3 . The described characteristics are observed for all the monitored teeth, independent on how many inspections composed the database. For the profiles with three inspections, the interval between the first and the second points shows a minor increase, when compared to

the final stage. Had the first inspection taken place earlier, the twice monitored teeth would probably behave similarly to the three-inspection teeth.

The observations lead to two main conclusions. Firstly, the analogous results between the groups indicate that the residual stress state, and thus the interaction between the processes, has no significant influence on the late damage evolution. That means that the conventional final damage depth measurement does not explain the surface integrity state for every failure mode mechanism. As a second aspect, it requires that the investigation focus is moved to much earlier damage phases, such as the initiation and the primary propagation of the cracks.

For a further morphological comprehension, both the beginning and the final damage's status are compared to published results of tooth flank contact fatigue. Similar aspects are found when taking shot peening investigations as reference. In a first observation, the small removed portions aligned in the bottom of the flanks are also shown in the publications of Batista and Dias (2000), Guagliano, Riva and Guidetti (2002) and Lv, Lei and Sun (2015). Nevertheless, the most important outcome is extracted by their comparative observations between peened and unpeened flanks. While the peened gears are characterized by the small damages, the unpeened ones show large portions of material suddenly removed, featured by a V-shaped area (Figure 5.39). This damage, described as not only wider but also deeper, is definitely different from the failed surface observed along the tests of the present investigation. It is indeed reasonable to match the thesis' results to the publications' peened samples.

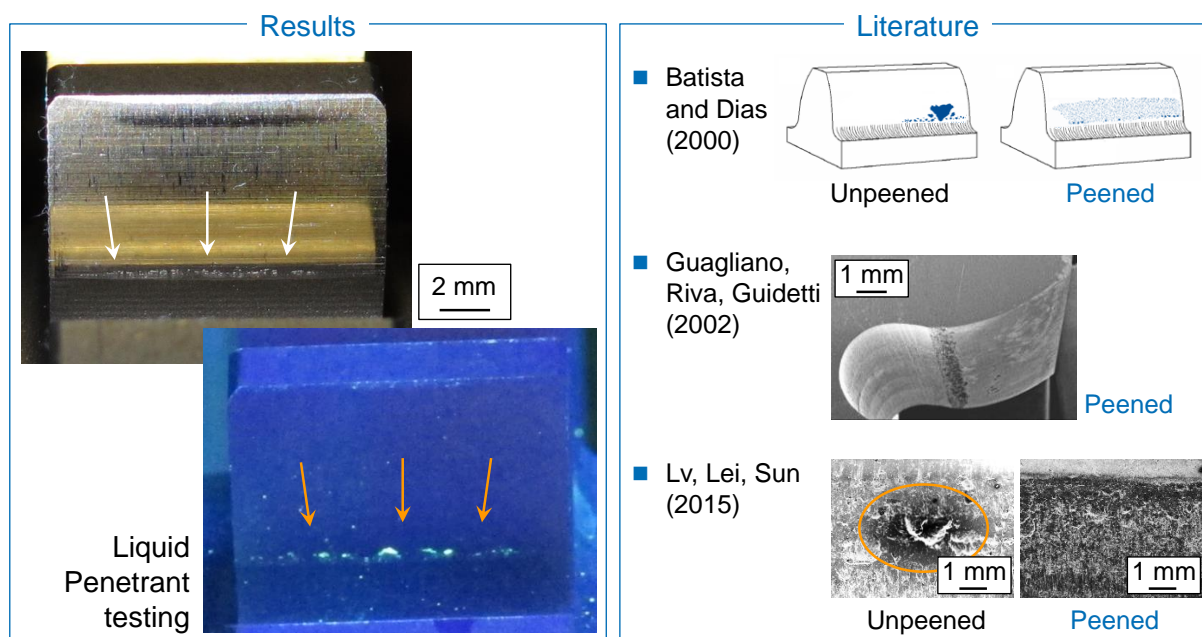


Figure 5.39 – The damage morphology found at this investigation is similar to the one from peened surfaces referred in the literature.

The authors of the referred articles assign the damage features solely to the final manufacturing process. The assignment creates then a conflict to the damage match between the publications and the thesis, whose gears are not only peened but later ground. The conflict is the key for the two conclusions out of this analysis. As shown along the present study, the tested gears still keep a residual macrostress state that is typical from shot peening, whereas its roughness pattern characterizes the grinding process. It is thus the first conclusion that it is not the peening treatment that defines the failed surface, but actually the final integrity state induced. The second statement is a consequence from the first, but it is brought to the perspective of the answer for this research question. Considering the surface integrity state as a combination of residual stress and roughness, the failure is an effect of the interaction between the processes and not only from the final manufacturing step.

As shown by the analysis of the Figure 5.38, the last damage evolution step is much accelerated by the uneven developed surface, hiding the original mechanisms of the damage's creation. Therefore, further evidences of the interaction relevance to the pinion lifetime were researched through the investigation of the beginning of the fatigue mechanism. After submitting the samples to a liquid penetrant testing, the position for making the section cut was defined. The samples were taken to a metallographic analysis, in which the fatigue cracks could be identified. The several captured images were compared to a review of the literature

on the initiation and propagation of rolling contact fatigue cracks. With this basis, the suggested explanation for the crack mechanism developed in the pinions of the thesis is organized in the Figure 5.40.

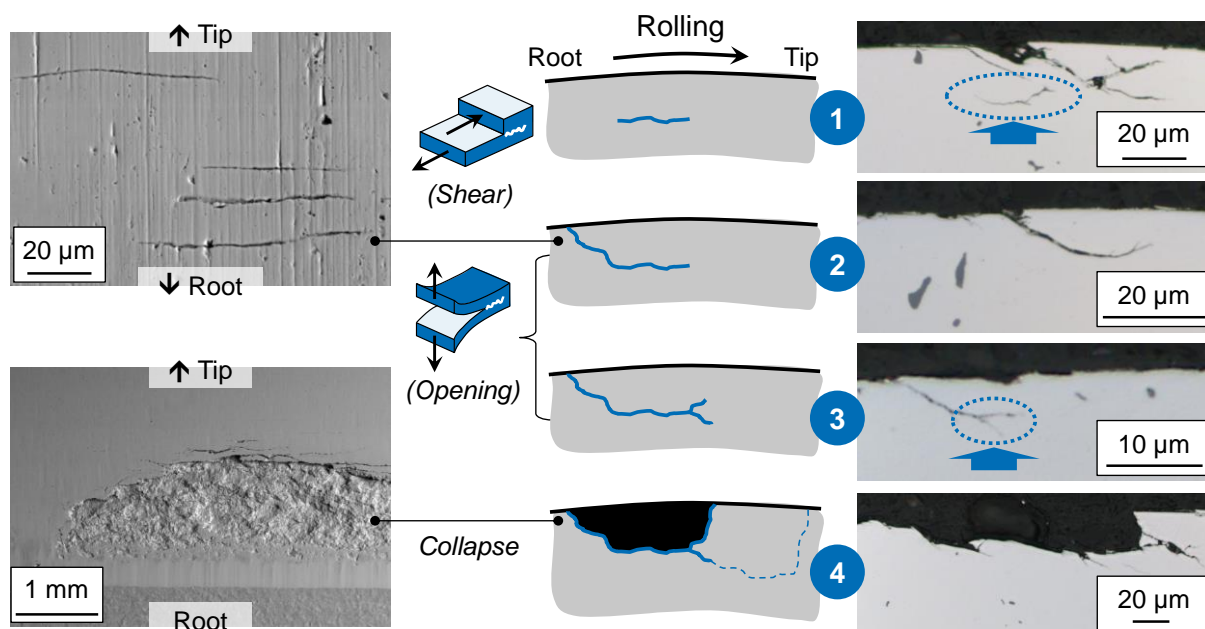


Figure 5.40 – The crack is subsurface-originated, propagates outwards the surface and when the opposite extremity finally collapses, the material is removed.

At a first stage, some material random inhomogeneities, such as structural flaws, slip planes, grain boundaries and mainly non-metallic inclusions, create a local stress concentration (MURAKAMI, 2002). The applied stress profile of a gear tooth flank usually finds its maximum magnitude beneath the surface, due to the contribution of the rolling force. The concentrators located at this region are the first presenting a trend to join, forming microcracks. They unify by coalescence and it is then with a parallel orientation to the surface that the crack shortly propagates. This is stimulated by the shear applied stresses and defined as the crack propagation mode II. This mechanism is not kept for a long time, since the crack will search for a lower energy propagation path, offered by the opening mode. Also defined as the crack propagation mode I, it takes the crack towards the surface, as the second stage of this mechanism.

These first two described steps are the basis for the definition of a subsurface-initiated crack. It is in accordance to the concepts published by McEvilly (2002), Ding and Rieger (2003) and Raje and Sadeghi (2008), although being a typically controversial topic among

researchers. However, in addition to the captured image with a subsurface crack in the right top of the Figure 5.40, two other evidences support the suggested explanation:

1. Although in a short extension, the cracks have a subsurface region oriented parallel to the surface, which indicates the shear propagation mode (DING; RIEGER, 2003; RAJE; SADEGHI, 2008);
2. The necessary energy to propagate under the opening mode is largely inferior to the one for the shear mode. As an overall physical phenomenon, the nature always searches for the lowest energy course. Thus, a shear crack mode is mostly like to become an opening one than the contrary way (POOK, 1994; MILLER; BROWN; YATES, 1999; ALFREDSSON, 2000).

At the moment when the crack achieves the surface, the opposite extremity overcomes the critical intensity factor (K_{Ic}), defining the crack critical length. An uncontrolled crack growth is expected and it takes the crack to the branching effect labeled as the third stage in this mechanism (GLODEŽ; WINTER; STÜWE, 1997; ALFREDSSON, 2000; ABERŠEK; FLAŠKER, 2004). A fourth and final stage, which removes the material portion, takes place in a mechanism called as ligament collapse. Rather than crack propagation, it is formed by the collapse of material in the crack tip ligament regions (DING; GEAR, 2009). Previous cracks from the bifurcation of the third stage are still able to propagate under the opening crack mode. Their growth promotes further removal of material, gradually increasing the damage size in the direction of the pitch circle (left and right bottom images of the Figure 5.40).

With the understanding of the mechanism initiation, the cracks were characterized by means of the measurement of their depth. The same groups investigated for the damage evolution (G1P, GDT and G3P) are herein analyzed. For each group, teeth were observed in the microscope up to the point when there were identified ten cracks according to the explained mechanism. An image with some measurements, as well as a boxplot compiling the results, is displayed in the Figure 5.41. The criterion for defining the crack's depth is the region where a flat geometry, though short, is observed.

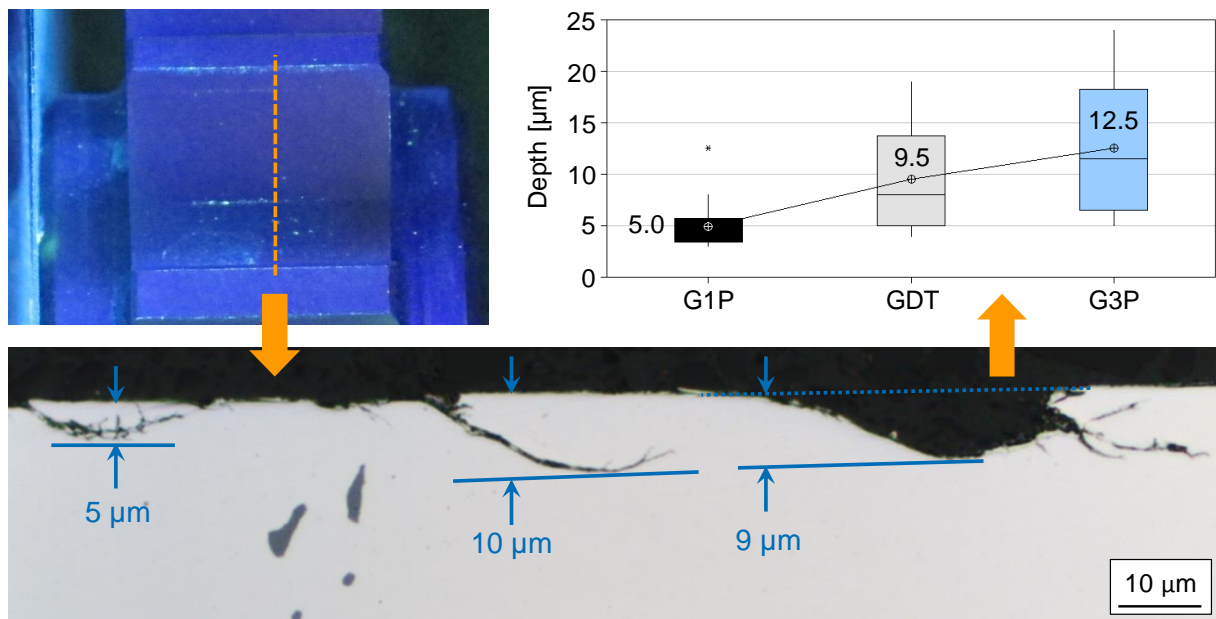


Figure 5.41 – The depth of the crack initiation is 10 μm in average.

A minor difference is observed, for which the group G1P produced the shallowest cracks, whereas the group G3P the deepest ones. Statistically, the only proved depth difference is between G1P and G3P (P-value = 0.009). As an overall result, the cracks can be most probably found around a depth of 10 μm from the surface.

The registered depth is slightly smaller than the ones published in previous articles. As an example, the study of Ding and Gear (2009) showed an initiation depth of 46 μm to the same *Hertzian* pressure contact here applied. For the mentioned publication, however, the failure took place around the pitch diameter, whereas the damages of this study are closer to the transition flank-root. In this region, the contribution of the rolling to the balance of forces is reduced, moving the depth of the maximum stresses outwards the surface. The reasons for the damage appearance on the observed region are not only related to the residual stress state. Among other factors, they depend on the material, the gear geometry and the applied load level, being beyond the scope of this thesis. The important statement from the metallographic analysis was to determine the crack initiation depth in this case. The information is a key-connection to the mapped residual stress states, which is to be explored at the forthcoming topic.

5.3.3 The Overall Phenomenological Interpretation

Along the first two parts of the chapter 5, the residual stress state was discussed in a macro and a micro level. Gears produced out of the investigated manufacturing treatments were submitted to fatigue tests, whose results were just presented. Up to this point, the only stated role of the processes interaction to the fatigue behavior is concerning the damage morphology. On the search for a more complete answer to the third research question, this topic recovers the residual stress results that support fulfilling the gap for the fatigue tests outcomes.

The first observation holds the discussion around the crack's depth, by bringing back to the spotlight the residual macrostress measured after the grinding process. This depth level covers both the crack initiation as well as its initial propagation stage, since it grows parallel to the surface. The postponement and the retardation at this stage potentially represent an improvement of the load capacity (MITSUBAYASHI; MIYATA; AIHARA, 1994; OLVER, 2005). The average crack depth result of 10 μm was then taken to highlight the residual macrostress intensity at this profile point (Figure 5.42).

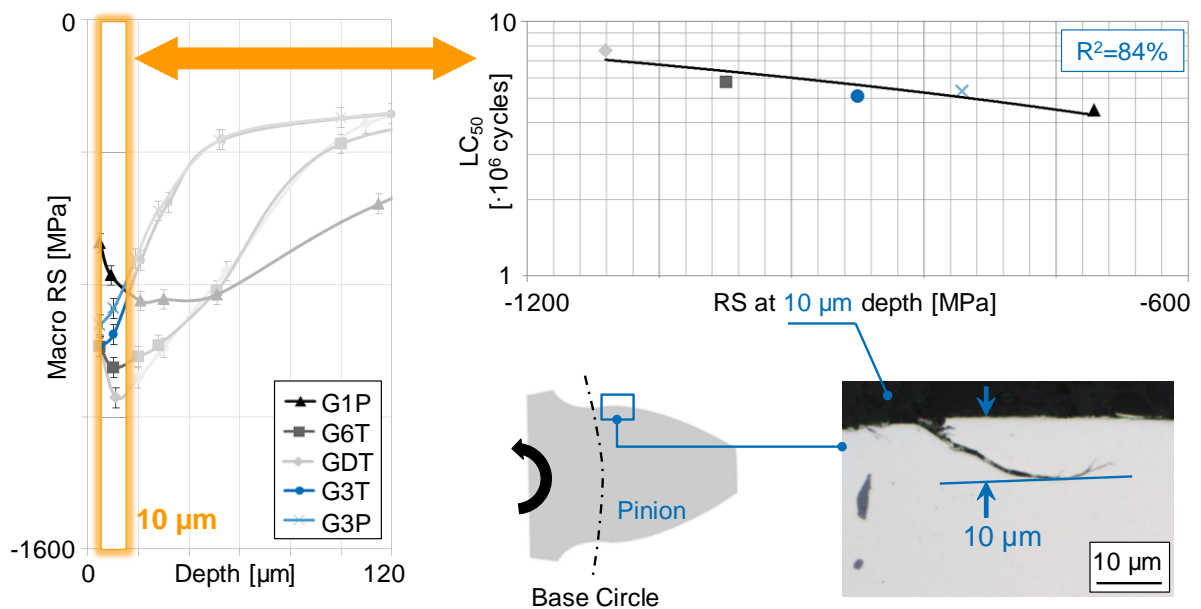


Figure 5.42 – A correlation is observed between the part lifetime and the residual stress intensity at the depth of the cracks' initiation.

With the concept that more compressive residual stresses induce a fatigue strength enhancement, the stress states show a good match to the lifetime results (LC_{50}) achieved. The two groups with the most compressive residual stresses bear respectively the longest lifetimes, whereas the worst performance is associated to the less compressive stress state. The sequence divergence appears only to the groups G3T and G3P. Nonetheless, they present very close results for both the stress state and the fatigue performance. In order to quantify the observed convergence, the tested lifetime was now plotted against the residual macrostress level measured at a depth of 10 μm (Figure 5.42). The goodness-of-fit, represented by a R^2 value of 84%, indicates a reasonable relationship.

In the context of this thesis, the correlation between the residual stress level and the fatigue performance is not yet the most important inference. It is actually the holistic comprehension that the lifetime is a direct outcome from a specific depth level, which was shown to be highly dependent on the shot peening residual stress state. In other words, the magnitude of the R^2 value characterizes the importance of the role of the residual stress interaction to the fatigue behavior.

Additionally, the result drives the analysis to a recurrent discussion within the gear industry: the demand for an optimal residual stress state. It is here important to verify that the most compressive residual stress intensity belongs to different groups along the depth profile. The fatigue assessment does not come from the groups' comparison on the outer surface, over the peak nor from the intensity at the final damage depth. The correlation is closely linked to the failure mechanism, which, in this case, was evaluated under only one torque level and one gear geometry condition. Consequently, the concept of unique optimal residual stress state is not attainable. The three mentioned factors must be combined, with the aid of the fracture mechanics theory, to provide a specific optimal residual stress state to each application.

The failure mechanism seems also to be influenced by the shape of the residual stress depth profile. This interpretation is an attempt to understand the crack depth difference previously observed between the groups. Onto this goal, the same residual stress chart is highlighted between the crack initiation depth and the following layers. It was also rotated in 90° to couple the visualization of the surface reference with the cracks' images (Figure 5.43).

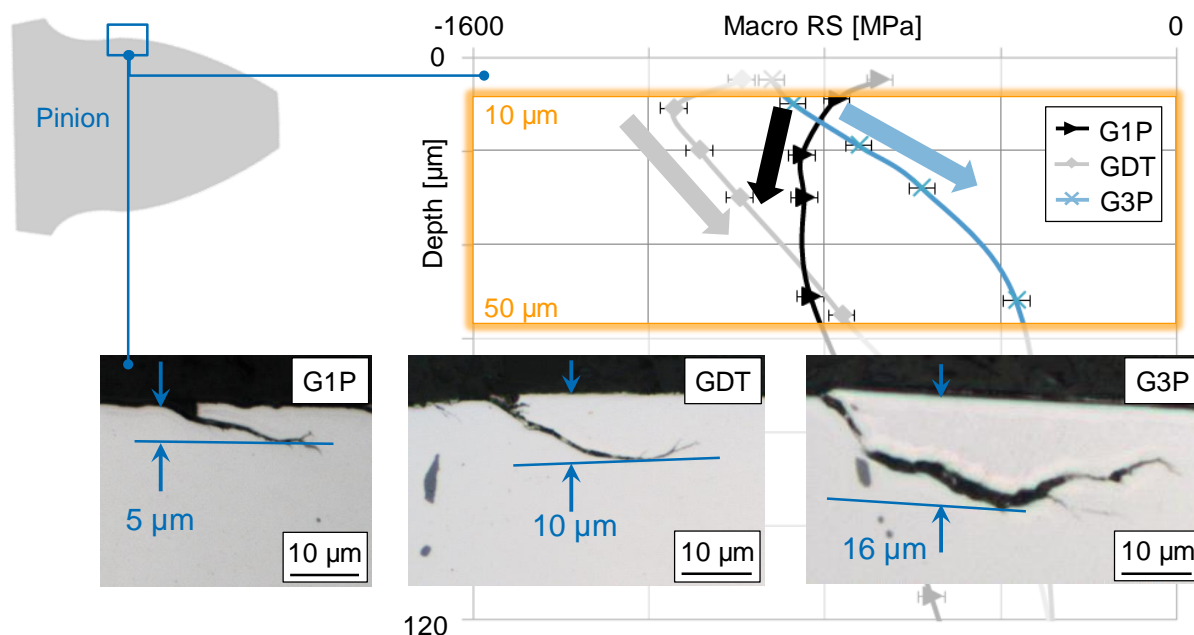


Figure 5.43 – The cracks' initiation depth is possibly influenced by the transition behavior of the residual stress along the depth.

Arrows were drawn over the chart to indicate the alteration rate of the stress intensity along the depth. By comparing it to the cracks depth boxplot of the Figure 5.41, it is possible to observe that the only group with an increasing rate (G1P) has also the shallowest mechanism initiation. Analogously, the other two groups present similar decreasing rates and similar cracks depth mean. It is even not too much to recognize that the group G3P joins the highest depth mean and the highest decreasing rate towards the core.

The statement goes in agreement with the thesis of Alfredsson (2000). Although studying surface-initiated cracks, it showed that compressive residual stresses lead to a reduction on the crack's propagation angle, concentrating it close to the surface. Brought to the present investigations, a higher decreasing rate can be understood as a favorable condition to initiate the crack deeper. Also, the rate is an indication of the inverted sequence of stress intensities at higher depth levels. At a depth of 50 μm, the group G1P is already the most compressive stress state, while the group G3P assumes the least compressive position. This difference sequence classification is yet reinforcing the statement of an optimal residual stress state to be closely connected to the failure mode.

The drawn conclusion of a reasonable match between the fatigue performance and the residual macrostress state brings the analysis back to the microstresses. It was already verified (topic 5.2.5) that the peening microstresses at the grinding stock depth may have some

influence on the ground values for the *Gauss* integral breadth. Moderately, however, once it required the peening groups to be organized in two classes. The open point, for the lifetime assessment, is then over the significance of the heterogeneity after grinding. In this case, the results do not show the same weight that the heterogeneity created on the fatigue results of the tests with the twin-discs run during the assessment validation (topic 5.2.3).

The comprehension of the difference between the tests with the gears and the discs demands their comparison, joining the intensity and the heterogeneity levels simultaneously (Figure 5.44). It is possible to observe that the *Gauss* integral breadth assumes similar values between both the samples, especially over the depth levels where both were approached. But the comparison shows also that the residual macrostress of the gears are notably higher than the ones of the discs. The same heterogeneity level for very different intensities highlights the dominance of the macrostress role to the fatigue behavior.

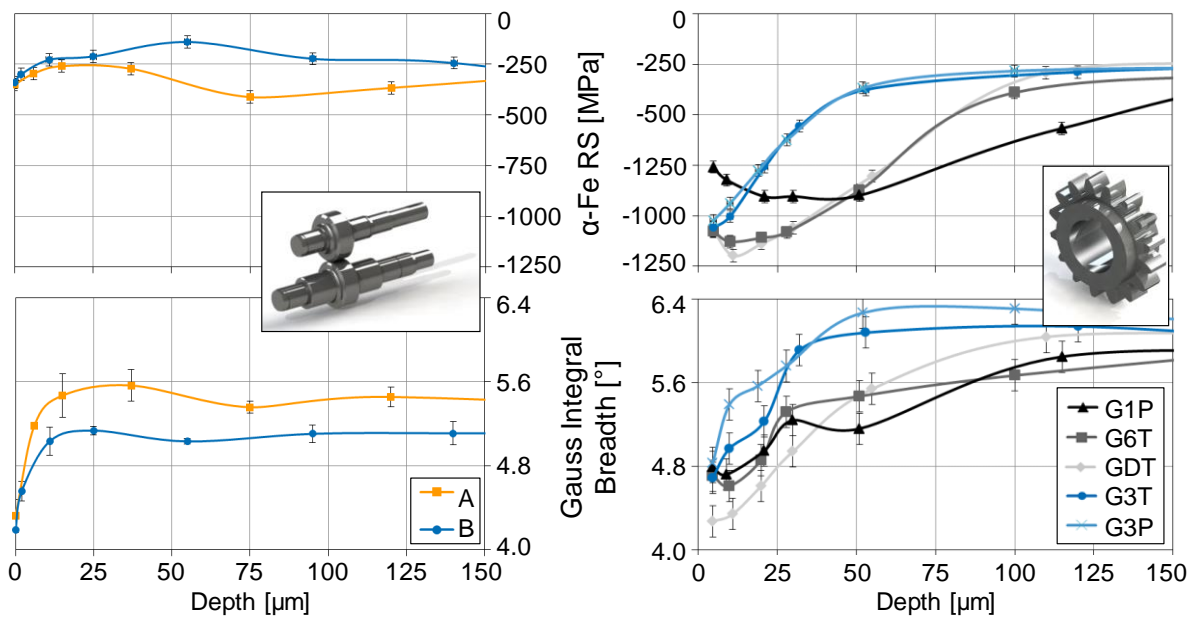


Figure 5.44 – The high intensity of residual macrostresses induced on the gears minimized the role of their microstresses to the fatigue performance.

These coupled observations support the conclusion of the microstress assessment method. The heterogeneity evaluation should not be taken as to overcome the importance of the intensity for the fatigue performance prediction. It is a tool for complementing the fatigue behavior comprehension under the perspective of residual stresses. The *Gauss* integral breadth is proportional to the intensity of the microstress, and thus to the macrostress

deviation. As for a generic statistical approach, the deviation has to be analyzed by considering its proportional magnitude to the mean value. In this comparison, the mean value of the gears is approximately the double of the discs. Had the intensity been lower and the heterogeneity the same, this deviation would be probably more effective on the gears' fatigue performance.

Overall, the process interaction shows to be definitely present to the fatigue tests' results. Without the residual stress state created by the shot peening, the failure mechanism would not be exactly the same. Distinct initiation and propagation conditions would finally lead to different lifetime results than the ones herein collected.

6 Conclusions and Outlook

The study was conducted to explore the mode how the manufacturing processes of a production chain interact to define final surface integrity of the gear. It was sought to identify whether the interaction effects have practical consequence to the gear functionality, represented by its load carrying capacity.

The focus of the literature on optimizing individual manufacturing processes can be considered excessive, when balanced the need of comprehending its previous integrity history. As direct consequences, the accuracy of the prediction models is lowered, the control on the production dispersion is jeopardized and the product design is not optimized.

The disclosed gap brought the opportunity of seeking the answer for scientific and technological improvements, by means of three questions. At a first instance, the several features of a residual stress depth profile demands the identification of which is the most relevant one to alter the final surface integrity. In the sequence, the discussion approaches the deviations and, therefore, which is the role of the residual stress heterogeneity on the processes interaction. Lastly, the analysis is forwarded to the understanding on how these two previous outcomes impact the gear fatigue behavior.

In spite of the full attention given by the literature to the final process, the hypothesis of not neglecting the influence of the previous processes to the final integrity state was confirmed. The empirical findings of this thesis reinforce the strength of describing the evolution of residual stresses by means of a model of springs. This should be actually read as the self-equilibrated potential energy theory. It was solely necessary to propose a derivative adaptation, which could handle with the areal impact of the interaction's disturbance. The proposal was defined as the Equivalent Layers Model. Sustained by this concept, the following statements are outlined:

The mode in which the energy is rearranged is a function of the disturbance source:

According to the potential energy approach, any change to the energy magnitude from one process to another is reflected either as a displacement or a stiffness modification. Accordingly, the loss of the system's stability will result in a geometric distortion or a change in the residual stress state. The surface disturbance can be represented by a mechanical, thermal or structural load. The grinding processes disturbs the system

through the material removal, which is the combination of mechanical and thermal loads. In the generic conception of removing material, the tool is constantly in touch with the surface, which partially restraints the displacement of the outer layers. In this case, the energy is favorably driven to change the residual stress state itself. Conversely, the residual stresses prior to the heat treatment are basically converted in geometric distortion. The thermal load, followed by the phase transformation, represents the disturbance. It takes place in the absence of any restraints of the surface degrees of freedom, and the energy is released as a distortion.

The magnitude of the system modification is proportional to the unstable area:

The disturbance source determines also the region up to where it exerts effects. For processes leading to a complete stress relaxation, the region was observed to extend from the surface to the position where the stress state sign is inverted. The region determination is different for the interaction process in which the disturbance does not promote the complete relief. In this last case, the end of the disturbance is taken as the point where the stress state is stable, with a much reduced increase/decrease rate. The two described regions were respectively represented by the machining and the shot peening, whereas the disturbance by the heat treatment and the grinding. The integral of the residual macrostress profile within the disturbed range was defined as the Unstable Area of Residual Stresses. It was proved to be the primary factor from the previous process to have influence on the final integrity state.

The application of the concept follows the approached domain size:

The balance of energy respects the extension to which the equilibrium must be restored. It requests a simultaneous approach of the intensity and the heterogeneity of the residual stress state. The macrostress interaction leads to large volumetric deviations and change on the residual macrostress itself. On the other hand, the microstresses evolution in-between the processes showed influence on the surface roughness, which can be considered as a local volumetric deviation. The analysis of microstresses also evidenced the actuation of microstructural inhomogeneities such as carbides, even when their effects were not noticed by the macrostress measurements.

The three statements compose a general answer to how the intensity and the heterogeneity of the residual stresses are present on the interaction in-between processes of

the gear manufacturing chain. They form the basis of the scientific original contribution of the thesis. For a practical transference of knowledge, the statements must be jointly interpreted in order to define the chain stage in which development efforts must be invested. Depending whether the focus is on the distortion or on the residual stresses, the prioritization of processes to be investigated lays on early or late stages of the chain, respectively.

The achievements enabled the study to forward these outcomes to the perspective of the gear functionality, by means of the fatigue behavior investigation. The support from the damage analysis was the linkage between the previously described findings and the fatigue investigation. The fatigue crack initiation is exactly at the depth level where the residual stress after the grinding is mostly influenced by the previous peening process. The residual stress level at this depth shows 84% correlation with the lifetime results of the contact fatigue tests. Even the damage morphology emphasizes the process interaction. The shape of the damaged zone is more similar to what is reported as a peened surface failure than to a ground one.

The fatigue results are brought in this context to emphasize the importance of the findings related to the residual stress interaction. In the present thesis, the validation considered specific gear geometry and applied load level. However, the main idea behind the observed correlation can be transferred to the tooth stress analysis of different geometries, load levels and fatigue failure modes. With this conception, the findings offer the following new concept to society:

Design for Residual Stress (DRS):

The search for the optimal residual stress is a usual discussion within the gear community. The gear design is a function of the applied load distribution for a certain geometry and material. The lowest safety factor out of the design defines the most susceptible criterion to fail. Only with an interactive approach between these requirements and the residual stresses, an optimal state can be defined. By comprehending the residual stress interaction effects, the manufacturing chain can be designed with the specific purpose of providing the so called optimal residual stress state. The oriented development of the manufacturing chain for a specific residual stress state is the basic concept of the herein defined Design for Residual Stress.

Inspired by the concepts of the Design for eXcellence (DfX) referred by Bralla (1996) and recently reviewed by Chiu and Kremer (2011), the DRS consists of a novel term. It is not the pioneering introduction of the expression that is here highlighted. It is the comprehension

of the evolutionary behavior of the surface integrity properties along the production chain that offers this conception possibility. In this study, the concept presents a focus on the design of the manufacturing chain, as a material branch of the Design for Manufacturing (DfM). In order to provide it a holistic characteristic, the DRS concept must now incorporate guidelines for the product design. The further development of the DRS grounding is an expected short-term outlook of this thesis.

With regard to the methodological aspect, a remark is here given to the assessment of the heterogeneity of the residual stress state. The correlation validation by means of the *Gauss* integral breadth parameter provides an additional tool to enhance the comprehension of the fatigue failure, and it consists of a new contribution of this study. Likewise the interaction effects, the conclusions were drawn based on the manufacturing processes and materials considered for the two approached case studies. Exploring other processes, and the response of different alloys, appears as a future research that can be derived from the present thesis. Also for this specific topic, a continuation is planned in the direction of enhancing the model robustness. Further mathematical developments can be implemented, such as the *Fourier-Space* procedure for the effects' deconvolution.

Target of extensive debates, another assessed point of the study deserves supplementary research efforts. The crack mechanism identification was correlated to the residual stress profile, based on the crack initial stages. But for rolling contact fatigue, the crack mechanism and its relationship with both the residual macro and microstresses is frequently contrasted by the researchers. The application of the fracture mechanics theory in order to strengthen the observed correlations is then suggested. It may not only grant more lucidity to the residual stress influence on the crack propagation phases. The interaction effect to the stress relaxation behavior along the load cycles can be also verified.

A final outlook is especially connected to the objective of this study. The most relevant factors of the previous residual stress state were sought and identified, providing an important upgrade to the state-of-the-art. It enables now that a straight continuation, based on a simulation model and probably by means of a numerical method, can concentrate the focus on the outlined aspects. As a quantified approach, different combinations of UARS values and disturbance sources can be simulated. As a volumetric approach, it will consider the residual stress gradients both along the depth and across the surface. The outcome can be the creation of a predictive model for the balance of the energy released in the form of displacement and change in the residual stress state. The combination of the proposed future researches, under

the DRS perspective, drives to a common goal of optimized product designs and manufacturing chains, enhancing the gear load carrying capacity.

7 Bibliography

ABERŠEK, B.; FLAŠKER, J. **How gears break**. Southampton: WIT Press, 2004.

ABUKHSHIM, N.A.; MATIVENGA, P.T.; SHEIKH, M.A. Heat generation and temperature prediction in metal cutting: A review and implications for high speed machining. **International Journal of Machine Tools and Manufacture** Vol. 46. Elsevier Science Ltd., 2006. p. 782-800.

AFAZOV, S. Modeling and simulation of manufacturing process chains. In: **CIRP Journal of Manufacturing Science and Technology** Vol. 6. Elsevier Science Ltd., 2013. p. 70-77.

ALBAN, L.E. Failure of Gears. In: **ASM Handbook** Vol. 11 "Failure Analysis and Prevention". Materials Park: ASM International, 2002. p. 2558-2603.

ALBAN, L.E. **Systematic Analysis of Gear Failures**. Metals Park: ASM International, 1993, 232p.

ALFREDSSON, B. **A Study on Contact Fatigue Mechanisms**. 2000. Doctorate Thesis - KTH School of Electrical Engineering, Stockholm.

ALMEN, J.O., BLACK, P.H. **Residual stresses and fatigue in metals**. Nova York: Mc Graw-Hill Book Company, 1963. 226p.

AMERICAN GEAR MANUFACTURERS ASSOCIATION. **ANSI/AGMA 1012-G05**: Gear Nomenclature, Definition of Terms with Symbols. Alexandria, 2011.

AMERICAN GEAR MANUFACTURERS ASSOCIATION. **ANSI/AGMA 2004-B89**: Gear Materials and Heat Treatment Manual. Alexandria, 2004.

AMINI, N., RÓSEN, B., WESTBERG, H. Optimization of Gear Tooth Surfaces. **International Journal of Machine Tools and Manufacture** Vol. 38. Elsevier Science Ltd., 1998. p. 425-435.

ANDERSON, T.L. **Fracture Mechanics**: Fundamentals and Applications. Boca Raton: CRC Press, 2005. 610p.

ANTOINE, F.; BESSON, J.M. Simplified Modellization of gear micropitting. **Proceedings of the Institution of Mechanical Engineers, Part G: Journal of Aerospace Engineering** Vol. 216. SAGE, 2002. p. 291-302.

ASHBY, M.; SHERCLIFF, H.; CEBON, D. **Materials: Engineering, Science, Processing and Design**. Jordan Hill: Butterworth-Heinemann, 2007, 514p.

ASI, O. Fatigue failure of helical gear in gearbox. **Engineering Failure Analysis** Vol. 13, 2006. p. 1116-1125.

ASLANTAŞ, K.; TASGERIREN, S. A study of spur gear pitting formation and life prediction. **Wear** Vol. 257. Elsevier Science Ltd., 2004. p. 1167-1175.

ASM INTERNATIONAL HANDBOOK COMMITTEE. Classification and designation of carbon and low-alloy. In: **ASM Handbook** Vol. 1 “Properties and selection: Iron steels and high performance alloys”. Materials Park: ASM International, 2002, p. 328-517.

ASPINWALL, D.K.; MANTLE, A.L.; CHAN, W.K.; HOOD, R.; SOO, S.L. Cutting temperatures when ball nose end milling γ -TiAl intermetallic alloys. **CIRP Annals - Manufacturing Technology** Vol. 62. Elsevier Science Ltd., 2013. p. 75-78.

AUTOMOTIVE INDUSTRY ACTION GROUP: **CQI-9**. Special Process: Heat Treat System Assessment, Version 3. Southfield, 2011.

BAGH, A.J. **Auslegung PVD-beschichteter Stirnräder**. Doctorate Thesis – Werkzeugmaschinenlabor, Rheinisch-Westfälische Technische Hochschule, 2015.

BAGHERIFARD, S.; GHELICHI, R.; GUAGLIANO, M. On the shot peening surface coverage and its assessment by means of finite element simulation: A critical review and some original developments. **Applied Surface Science** Vol. 259. Elsevier Science Ltd., 2012. p. 186-194.

BATISTA, A.C.; DIAS, A.M, LEBRUN, J.L.; LE FLOUR, J.C.; INGLEBERT, G. Contact fatigue of automotive gears evolution and effects of residual stresses introduced by surface treatments. **Fatigue & Fracture of Engineering Materials & Structures** Vol. 23. Wiley, 2000. p. 217-228.

BHADESHIA, H.K.D.H. Material Factors. In: TOTTEN, G.; HOWES, M.; INOUE, T. **Handbook of residual stress and steel deformation**. Materials Park: ASM, 2002. p. 3-10.

BARSOUM, Z.; BARSOUM, I. Residual stress effects on fatigue life of welded structures using LEFM. **Engineering Failure Analysis** Vol. 16. Elsevier Science Ltd., 2009. p. 449-467.

BEHNKEN, H. Some basic relations to the stress analysis using diffraction methods. In: HAUKE, V. **Structural and Residual Stress Analysis by Nondestructive Methods**. Amsterdam: Elsevier; 1997. Chapter 2.03, p. 39-65.

BELL, A.J. **Temperature in High Efficiency Deep Grinding**. Doctorate Thesis – School of Applied Sciences, Cranfield University, 2009.

BELSAK, A.; FLASKER, J. Method for detecting fatigue crack in gears. **Theoretical and Applied Fracture Mechanics** Vol. 46. Elsevier Science Ltd., 2006. p. 105-113.

BRALLA, J.G. **Design for Excellence**. New York: McGraw-Hill Education, 1996, 326 p.

BRAMFITT, B.L.; BENSCOTER, A.O. **Metallographer's Guide: Practice and Procedures for Irons and Steels**. Materials Park: ASM, 2002, 354p.

BRAMFITT, B.L.; HINGWE, A.K. Annealing of Steel. In: **ASM Handbook** Vol. 4 “Heat Treating”. Materials Park: ASM International, 2002. p. 102-134.

BRECHER, C.; BRUMM, M.; GRESCHERT, R. Auswirkung fertigungsbedingter Grenzschichten auf das Einsatzverhalten. In: ARBEITSTAGUNG „ZAHNRAD- UND GETRIEBETECHNIK“ DES WZL, 55., 2014, Aachen, Germany. **Zahnrad- und Getriebeuntersuchungen**. Aachen: WZL, 2014, p. 10–1-10–32.

BRECHER, C.; LÖPENHAUS, C.; REGO, R. Methodology for residual stress heterogeneity state analysis on gear manufacturing chain. In: ARBEITSTAGUNG „ZAHNRAD- UND GETRIEBETECHNIK“ DES WZL, 56., 2015, Aachen, Germany. **Zahnrad- und Getriebeuntersuchungen**. Aachen: WZL, 2015, p. 7–1-7–30.

BRINKSMEIER, E.; CAMMETT, J.T.; KÖNIG, W.; LESKOVAR, P.; PETERS, J.; TÖNSHOFF, J.K. Residual Stresses — Measurement and Causes in Machining Processes. **CIRP Annals - Manufacturing Technology** Vol. 31. Elsevier Science Ltd., 1982. p. 491-510.

BRINKSMEIER, E. GIWERZEW, A. Hard gear finishing viewed as a process of abrasive wear. **Wear** Vol. 258. Elsevier Science Ltd., 2005. p. 62-69.

BRINKSMEIER, E.; LÜBBEN, T.; FRITSCHING, U.; CUI, C.; RENTSCH, R.; SÖLTER, J. Distortion minimization of disks for gear manufacture. **International Journal of Machine Tools and Manufacture** Vol. 51. Elsevier Science Ltd., 2011. p. 331-338.

CAPELLO, E. Residual stresses in turning Part I: Influence of process parameters. **Journal of Materials Processing Technology** Vol. 160. Elsevier Science Ltd., 2005. p. 221-228.

CHEN, X; ROWE, W.B.; MCCORMACK, D.F. Analysis of the transitional temperature for tensile residual stress in grinding. **Journal of Materials Processing Technology** Vol. 107. Elsevier Science Ltd., 2000. p. 216-221.

CHIU, M.-C.; KREMER, G.E.O. Investigation of the applicability of Design for X tools during design concept evolution: a literature review. **International Journal of Product Development** Vol. 13. Inderscience Enterprises, 2011. p. 132-167.

CUI, X.; ZHAO, J.; JIA, C.; ZHOU, Y. Surface roughness and chip formation in high-speed face milling AISI H13 steel. **Journal of Advanced Manufacturing Technology** Vol. 61. Springer, 2012, p. 1-13.

CULLITY, B.D. **Elements of X-Ray Diffraction**. 2nd ed. Reading: Addison-Wesley Publishing Company; 1978. 514p.

DAVIS, J.R. **Gear Materials, Properties, and Manufacture**. Materials Park: ASM International, 2005, 339p.

DELHEZ, R.; DE KEIJSER, T.H., MITTEMEIJER, E.J. Role of x-ray diffraction analysis in surface engineering: investigation of microstructure of nitrided iron and steels. **Surface Engineering** Vol. 3. Maney, 1987. p. 331-342.

DENIS, S.; ARCHAMBAULT, P.; GAUTIER, E.; SIMON, A.; BECK, G. Prediction of residual stress and distortion of ferrous and non-ferrous metals: current status and future developments. **Journal of Materials Engineering and Performance** Vol. 11. ASM International, 2002. p. 92-102.

DEUTSCHES INSTITUT FÜR NORMUNG. **DIN EN ISO 3452-1**: Non-destructive testing—Penetrant testing – Part 1: General principles. Berlin, 2014.

DEUTSCHES INSTITUT FÜR NORMUNG. **DIN 3960**: Definitions on involute cylindrical gears and gear pairs; Classification of the equations. Berlin, 1980.

DEUTSCHES INSTITUT FÜR NORMUNG. **DIN 3961**: Accuracy of cylindrical gears: general bases. Berlin, 1978.

DEUTSCHES INSTITUT FÜR NORMUNG. **DIN 3962-1**: Accuracy of cylindrical gears: tolerances for individual errors. Berlin, 1978.

DEUTSCHES INSTITUT FÜR NORMUNG. **DIN 3962-2**: Accuracy of cylindrical gears: tolerances for alignment deviations. Berlin, 1978.

DEUTSCHES INSTITUT FÜR NORMUNG. **DIN EN ISO 4287:1998**. Geometrical Product Specifications (GPS) – Surface Texture: Profile method – Terms, definitions and surface texture parameters. Berlin, 2010.

DEUTSCHES INSTITUT FÜR NORMUNG. **DIN EN ISO 4288:1998**. Geometrical Product Specifications (GPS) – Surface Texture: Profile method - Rules and procedures for the assessment of surface texture. Berlin, 1998.

DEUTSCHES INSTITUT FÜR NORMUNG. **DIN ISO 14635-1**. Gears – FZG test procedures – Part 1: FZG test method A/8,3/90 for relative scuffing load-carrying capacity of oils. Berlin, 2006.

DEUTSCHES INSTITUT FÜR NORMUNG. **DIN EN ISO 6507-1**. Metallic materials – Vickers hardness test – Part 1: Test method. Berlin, 2006.

DEUTSCHES INSTITUT FÜR NORMUNG. **DIN EN ISO 10084:1998-06**. Case hardening steels – Technical delivery conditions. Berlin, 2008.

DING, Y.; GEAR, J.A. Spalling depth prediction model. **Wear** Vol. 267. Elsevier Science Ltd., 2009. p. 1181-1190.

DING, Y.; RIEGER, N.F. Spalling formation mechanism for gears. **Wear** Vol. 254. Elsevier Science Ltd., 2003. p. 1307-1317.

DONG, W.P.; SULLIVAN, P.J.; STOUT, K.J. Comprehensive study of parameters for characterizing three-dimensional surface topography I: Some inherent properties of parameter variation. **Wear** Vol. 159. Elsevier Science Ltd., 1992. p. 161-171.

DONG, W.P.; SULLIVAN, P.J.; STOUT, K.J. Comprehensive study of parameters for characterising three-dimensional surface topography III: Parameters for characterising

amplitude and some functional properties. **Wear** Vol. 118. Elsevier Science Ltd., 1994. p. 29-43.

EBERT, L.J. The role of residual stresses in the mechanical performance of case carburized steels. **Metallurgical and Materials Transactions A** Vol. 9. Springer Boston, 1978. p. 1537-1551.

ENDOY, R. **Gear Hobbing, Shaping and Shaving: A guide to Cycle Time Estimating and Process Planning**. Dearborn: SME, 1990, 181p.

EPP, J.; SURM, H.; HIRSCH, T.; HOFFMANN, F. Residual stress relaxation during heating of bearing rings produced in two different manufacturing chains. **Journal of Materials Processing Technology** Vol. 211. Elsevier Science Ltd., 2011. p. 637-643.

ERICSSON, T. The effect of Final Shaping Prior to Heat Treatment. In: TOTTEN, G.; HOWES, M.; INOUE, T. **Handbook of residual stress and steel deformation**. Materials Park: ASM, 2002. p. 150-158.

ERICSSON, T. Principles of Heat Treating of Steels. In: **ASM Handbook** Vol. 4 "Heat Treating". Materials Park: ASM International, 2002. p. 14-49.

FADJIGA, G.; GLODEŽ, S.; KRAMAR, J. Pitting formation due to surface and subsurface initiated fatigue crack growth in contacting mechanical elements. **Wear** Vol. 262. Elsevier Science Ltd., 2007. p. 1217-1224.

FUNATANI, K. Residual Stresses during Gear Manufacture. In: TOTTEN, G.; HOWES, M.; INOUE, T. **Handbook of residual stress and steel deformation**. Materials Park: ASM, 2002. p. 437-457.

GENEL, K. Estimation method for the fatigue limit of case hardened steels. **Surface & Coatings Technology** Vol. 194. Elsevier Science Ltd., 2005. p. 91-95.

GENZEL, C. Line Broadening by non-oriented micro RS. In: HAUKE, V. **Structural and Residual Stress Analysis by Nondestructive Methods**. Amsterdam: Elsevier; 1997. Chapter 2.17, p. 435-460.

GERTH, J.; WERNER, M.; LARSSON, M.; WIKLUND, U. Reproducing wear mechanisms in gear hobbing – Evaluation of a single insert milling test. **Wear** Vol. 267. Elsevier Science Ltd., 2009. p. 2257-2268.

GLODEŽ, S.; WINTER, H.; STÜWE, H.P. A fracture mechanics model for the wear of gear flanks by pitting. **Wear** Vol. 208. Elsevier Science Ltd., 1997. p. 177-183.

GOCH, G. Gear Metrology. **CIRP Annals - Manufacturing Technology** Vol. 52 (2). Elsevier Science Ltd., 2003. p. 659-695.

GOMES, J.O. **Fabricação de Superfícies de Forma Livre por Fresamento no Aço Temperado ABNT 420 e nas Ligas de Alumínio AMP800 e de Cobre-Berílio Cu-Be**. Doctorate Thesis – Centro Tecnológico, Universidade Federal de Santa Catarina, 2001.

GROSCH; J. Microstructure and properties of gas carburized steels. In: HASHMI, S. **Comprehensive Materials Processing**. Elsevier Science Ltd., 2014. Vol. 12, chapter 12-12, p. 379-411.

GRUM, J. Residual Stresses and Microstructural Modifications. In: DAVIM, J.P. **Surface Integrity in Machining**. London: Springer-Verlag, 2010. p. 67-126.

GUAGLIANO, M.; RIVA, E.; GUIDETTI, M. Contact fatigue failure analysis of shot-peened gears. **Engineering Failure Analysis** Vol. 9. Elsevier Science Ltd., 2002. p. 147-158.

GUAGLIANO, M.; VERGANI, L. An approach for prediction of fatigue strength of shot peened components. **Engineering Fracture Mechanics** Vol. 71. Elsevier Science Ltd., 2004. p. 501-512.

HARADA, Y.; MORI, K.-I.; MAKI, S. Lining of metal surface with hard-metal foil using shot peening. In: **Shot Peening**. Weinheim: Wiley-VCH, 2003. 570p.

HASSANI-GANGARAJ, S.M.; MORIDI, A.; GUAGLIANO, M.; GHIDINI, A.; BONIARDI, M. The effect of nitriding, severe shot peening and their combination on the fatigue behavior and micro-structure of a low-alloy steel. **International Journal of Fatigue** Vol. 62: Elsevier Science Ltd., 2014. p. 67-76.

HAUK, V. **Structural and Residual Stress Analysis by Nondestructive Methods**. Amsterdam: Elsevier; 1997. 640p.

HAUK, V.; NIKOLIN, H.J. The evaluation of the distribution of residual stresses of the I. kind (RS I) and of the II. kind (RS II) in textured materials. **Textures and Microstructures** Vol. 8&9. Hindawi, 1988. p. 693-716.

HEYN; E. Internal Strains in Cold Wrought Metals and Some Troubles Caused Thereby. **The Journal of the Institute of Metals** Vol. 12. The Institute of Metals, 1914, p. 3-37.

HÖHN, B.-R. **Influence of lubricant on the pitting capacity of case carburized gears in load-spectra and single-stage-investigations**. Frankfurt: FVA, 2010. 7 p. (Technical Report FVA-Research Project 2/IV).

HONG, T.; OOI, J.Y.; SHAW, B. A numerical simulation to relate the shot peening parameters to the induced residual stresses. **Engineering Failure Analysis** Vol. 15. Elsevier Science Ltd., 2008. p. 1097-1110.

HU, Y., GONG, C, YAO, Z.; HU, J. Investigation on the non-homogeneity of residual stress field induced by laser shock peening. **Surface and Coatings Technology** Vol. 203. Elsevier Science Ltd., 2009. p. 3503-3508.

HUA, J.; SHIVPURI, R.; CHENG, X.; BEDEKAR, V.; MATSUMOTO, Y.; HASIMOTO, F.; WATKINS, T. Effect of feed rate, workpiece hardness and cutting edge on subsurface residual stress in the hard turning of bearing steel using chamfer + hone cutting edge geometry. **Materials Science & Engineering A** Vol. 394. Elsevier Science Ltd., 2005. p. 238-248.

HUSSON, R., DANTAN, J-Y., BAUDOUIN, C., SILVANI, S., SCHEER, T., BIGOT, R. Evaluation of process causes and influences of residual stress on gear distortion. **CIRP Annals - Manufacturing Technology** Vol. 61. Elsevier Science Ltd., 2012. p. 551-554.

INOUE; T. Metallo-thermo-mechanical coupling in quenching. In: HASHMI, S. **Comprehensive Materials Processing**. Elsevier Science Ltd., 2014. Vol. 12, chapter 12-06, p. 177-251.

INTERNATIONAL ORGANIZATION FOR STANDARDIZATION. **ISO 1328-1:1995**: Cylindrical Gears – ISO system of accuracy – Part 1: Definitions and allowable values of deviations relevant to corresponding flanks of gear teeth. Geneve, 1995.

INTERNATIONAL ORGANIZATION FOR STANDARDIZATION. **ISO 13565-2:1996**: Geometrical Product Specifications (GPS) – Surface Texture: Profile Method; Surfaces Having Stratified Functional Properties – Part 2: Height Characterization using the Linear Material Ratio Curve. Geneve, 1996.

JACOBUS, K.; DEVOR, R.E.; KAPOOR, S.G. Machining-induced residual stress: Experimentation and Modeling. **Journal of Manufacturing Science and Engineering** Vol. 22. ASME, 2000. p. 20-31.

JANG, D.Y.; WATKINS, T.R.; KOZACZEK, K.J.; HUBBARD, C.R.; CAVIN, O.B. Surface residual stresses in machined austenitic stainless steel. **Wear** Vol. 194. . Elsevier Science Ltd., 1996. p. 168-173.

JOHNSON, R.A.; BHATTACHARYYA, G.K. **Statistics**: Principles and Methods 6th ed. Danvers, John Wiley & Sons, Inc., 2010, 686p.

KARABELCHTCHIKOVA, O.; RIVERO, V. Variability of residual stresses and superposition effect in multipass grinding of high-carbon high-chromium steel. **Journal of Materials Engineering and Performance** Vol. 14. ASM International, 2005. p. 50-60.

KARPUSCHEWSKI, B.; KNOCHE, H.-J.; HIPKE, M. Gear finishing by abrasive processes. **CIRP Annals – Manufacturing Technology** Vol. 57. Elsevier Science Ltd., 2008. p. 621-640.

KIM, J.C.; CHEONG, S.K.; NOGUCHI, H. Evolution of residual stress redistribution associated with localized surface microcracking in shot-peened medium-carbon steel during fatigue test. **International Journal of Fatigue** Vol. 55. Elsevier Science Ltd., 2013. p. 147-157.

KIM, S.-B.; SCHACKLETON, J.; PREUSS, M.; WITHERS, P.J.; EVANS, A.; BRUNO, G. Stress relaxation of shot-peened udimet 720li under solely elevated-temperature exposure and under isothermal fatigue. **Metallurgical and Materials Transactions A** Vol.36. Springer, 2005. p. 3041-3053.

KIRK, D. Coverage - Development, measurement, control and significance. **The Shot Peener** Vol. 16. Electronics Inc., 2002. p. 33-36.

KLEIN, M. EIFLER, D. Influences of the manufacturing process chain design on the near surface condition and the resulting fatigue behaviour of quenched and tempered SAE 4140. **Journal of Physics: Conference Series** Vol. 240. IOP Publishing, 2010, p. 1-4.

KLOCKE, F., BRECHER, E. BRUMM, M. **Zahrad- und Getriebetechnik**. Aachen: Apprimus Verlag, 2014, 323 p.

KLOCKE, F., BRINKSMEIER, E. WEINERT, K. Capability profile of hard cutting and grinding processes. **CIRP Annals - Manufacturing Technology** Vol. 54. Elsevier Science Ltd., 2005. p. 22-45.

KLOCKE, F.; GOMES, J.; LÖPENHAUS, C.; REGO, R. R. Assessing the heterogeneity of residual stress for complementing the fatigue performance comprehension. **Journal of Strain Analysis for Engineering Design** Vol. 51. Elsevier Science Ltd., 2016. p. 347-357.

KÖCHER, J. **Erhöhung der Zahnflankentragfähigkeit einsatzgehärteter Zylinderräder durch Kugelstrahlen**. Doctorate Thesis – Werkzeugmaschinenlabor, Rheinisch-Westfälische Technische Hochschule, 1996.

KOSTILNIK, T. Shot Peening. In: **ASM Handbook** Vol. 5 “Surface Engineering”. 10.ed. Materials Park: ASM International, 1994. p. 278-301

KOVAC, M. Residual stress measurements in bevel gear after different production phases. **Journal of Materials Engineering and Performance** Vol. 3. Springer, 1994, p. 61-64.

KRAUSS, G. Microstructures and properties of carburized steels. In: **ASM Handbook** Vol. 4 “Heat Treating”. Materials Park: ASM International, 2002. p. 827-854.

KRITZLER, J. WÜBBENHORST, W. Inducing compressive stresses through controlled shot peening. In: TOTTEN, G.; HOWES, M.; INOUE, T. **Handbook of residual stress and steel deformation**. Materials Park: ASM, 2002. p. 345-358.

LAMPMAN, S. Introduction to Surface Hardening of Steels. In: **ASM Handbook** Vol. 4 “Heat Treating”. Materials Park: ASM International, 2002. p. 607-624.

LANGFORD, J.I. A rapid method for analysing the breadths of diffraction and spectral lines using the Voigt function. **Journal of Applied Crystallography** Vol. 11. IUCr, 1978, p. 10-14.

LAW, M.; LUZIN, V. Effect of spatial variation of stress-free lattice spacings on measured residual stresses. **Journal of Strain Analysis for Engineering Design** Vol. 46. SAGE, 2011, p. 837-841.

LAZOGLU, I.; ULUTAN, D.; ALACA, B.E.; ENGIN, S.; KAFTANOGLU, B. n enhanced analytical model for residual stress prediction in machining. **CIRP Annals - Manufacturing Technology** Vol. 57. Elsevier Science Ltd., 2008. p. 81-84.

LECHNER, G.; NAUNHEIMER, H. **Automotive Transmissions: Fundamentals, Selection, Design and Application**. New York: Springer, 1999, 448p.

- LI, J.K.; MEI, Y.; DUO, W.; RENZHI, W. Mechanical approach to the residual stress field induced by shot peening. **Materials Science and Engineering A** Vol. 147, 1991. p. 167-173.
- LIN, S.; PENG, F.; WEN, J.; LIU, Y.; YAN, R. An investigation of workpiece temperature variation in end milling considering flank rubbing effect. In: **International Journal of Machine Tools and Manufacture** Vol. 73. Elsevier Science Ltd., 2013. p. 71-86.
- LINGAMANAIAK, S., CHEN, B. The effects of carburising and quenching process on the formation of residual stresses in automotive gears. **Computational Materials Science** Vol. 62. Elsevier Science Ltd., 2012. p. 99-104.
- LINK, H.; LACAVA, W.; VAN DAM, J.; MCNIFF, B.; SHENG, S.; WALLEN, R.; MCDADE, M.; LAMBERT, S.; BUTTERFIELD, S.; OYAGUE, F. **Gearbox Reliability Collaborative Project Report: Findings from Phase 1 and Phase 2 Testing**. Golden: NREL, June 2011. 85 p. (Technical Report NREL/TP-5000-51885).
- LIŠČIĆ, B. Steel heat treatment. In: TOTTEN, G. **Steel Heat Treatment** – Metallurgy and Technologies. Boca Raton: CRC Press, 2007. p. 277-414.
- LÖHE, D.; LANG, K.-H.; VÖHRINGER, O. Residual Stresses and Fatigue Behavior. In: TOTTEN, G.; HOWES, M.; INOUE, T. **Handbook of residual stress and steel deformation**. Materials Park: ASM, 2002. p. 27-53.
- LÖPENHAUS, C. **Untersuchung und Berechnung der Wälzfestigkeit im Scheiben- und Zahnflankenkontakt**. Doctorate Thesis – Werkzeugmaschinenlabor, Rheinisch-Westfälische Technische Hochschule, 2015.
- LU, J. Prestress engineering of structural material: A global design approach to the residual stress problem. In: TOTTEN, G.; HOWES, M.; INOUE, T. **Handbook of residual stress and steel deformation**. Materials Park: ASM, 2002. p. 11-26.
- LUNT, A.J.G.; BAIMPAS, N.; SALVATI, E.; et al. A. A state-of-the-art review of micronscale spatially resolved residual stress analysis by FIB-DIC ring-core milling and other techniques. **Journal of Strain Analysis for Engineering Design** Vol. 50. SAGE, 2015. p. 426-444.
- LV, Y.; LEI, L.; SUN, L. Effect of shot peening on the fatigue resistance of laser surface melted 20CrMnTi steel gear. **Materials Science & Engineering A** Vol. 629. Elsevier Science Ltd., 2015. p. 8-15.
- MACHERAUCH, E.; VÖHRINGER, O. Residual Stresses After Quenching. In: LIŠČIĆ, B.; TENSI, H.; LUTY, W. **Theory and Technology of Quenching**. New York: Springer, 1992. p. 117-181.
- MACHERAUCH, E.; WOHLFAHRT, H.; WOLFSTIEG, U. Zur zweckmäßigen Definition von Eigenspannungen. **Härterei-Tech. Mitt.** Vol. 28. 1973, p. 201-211.
- MALKIN, S.; GUO, C. Thermal Analysis of Grinding. **CIRP Annals – Manufacturing Technology**, Vol. 56. Elsevier Science Ltd., 2007. p. 760-782.

MAZZO, N. **Engrenagens Cilíndricas: da concepção à fabricação**. São Paulo: Blucher, 2013. 840p.

MATSUMOTO, Y.; HASHIMOTO, F.; LAHOTI, G. Surface Integrity Generated by Precision Hard Turning. **CIRP Annals - Manufacturing Technology** Vol. 48. Elsevier Science Ltd., 1999. p. 59-62.

MAUCH, H.; ZENNER, H. **Statistische Methoden zur Beurteilung von Bauteillebensdauer und Zuverlässigkeit und ihre beispielhafte Anwendung auf Zahnräder**. Frankfurt: FVA, 1999. 175 p. (Technical Report FVA-Research Project 304).

MCEVILY, A.J. **Metal Failures: mechanisms, analysis, prevention**. New York: John Wiley & Sons, Inc., 2002. 336p.

MILLER, K.J.; BROWN, M.W.; YATES, J.R. Some observations on mixed-mode fatigue behavior of polycrystalline metals. . In: MILLER, K.J.; MCDOWELL, D.L. **Mixed-Mode Crack Behavior**. West Conshohocken: ASTM, 1999. p. 229-257.

MITSUBAYASHI, M.; MIYATA, T.; AIHARA, H. Phenomenal analysis of shot peening: analysis of fatigue strength by fracture mechanics for shot peened steel. **JSAE Technical Papers** Vol. 15, 1994. p. 67-71.

MITTEMEIJER, E.J. Fatigue of case-hardened steels; role of residual macro- and microstresses. **Journal of Heat Treating** Vol. 3. Springer, 1983. p. 114-119.

MOLZEN, M.; HORNBACH, D. Evaluation of welding residual stress levels through shot peening and heat treating. **SAE Technical Papers**, 2000. Paper #2000-01-2564.

MURAKAMI, Y. **Metal Fatigue: Effects of small defects and nonmetallic inclusions**. Oxford: Elsevier Science Ltd., 2002. 369p.

MUSIAL, W., BUTTERFIELD, S., MCNIFF, B. Improving wind turbine gearbox reliability. In: 2007 EUROPEAN WIND ENERGY CONFERENCE, 2007, Milan. **NREL Conference Papers**, Springfield: U.S. Department of Commerce, 2007, p. 1-10.

NARAZAKI, M. Hardening by Reheating and Quenching. In: TOTTEN, G.; HOWES, M.; INOUE, T. **Handbook of residual stress and steel deformation**. Materials Park: ASM, 2002. p. 248-295.

NAVAS, V., GONZALO, O., QUINTANA, I., PIRLING, T. Residual stresses and structural changes generated at different steps of the manufacturing of gears: Effect of banded structures. **Materials Science & Engineering A** Vol. 528. Elsevier Science Ltd., 2011. p. 5146-5157.

NAVAS, V., GONZALO, O., BENGOTXEA, I. Effect of cutting parameters in the surface residual stresses generated by turning in AISI 4340 steel. **International Journal of Machine Tools & Manufacture** Vol. 61. Elsevier Science Ltd., 2012. p. 18-57.

NEDIN, R.; VATULYAN, A. Inverse problem of non-homogeneous residual stress identification in thin plates. **International Journal of Solids and Structures** Vol. Elsevier Science Ltd., 2013. p. 2107-2114.

NIKOLAOS, T.; ARISTOMENIS, A. CAD-Based Calculation of Cutting Force Components in Gear Hobbing. **Journal of Manufacturing Science and Engineering** Vol. 134. ASME, 2012.

NING, Y.; RHAMAN, M.; WONG, Y.S. Investigation of chip formation in high speed end milling. **Journal of Materials Processing Technology** Vol. 113. Elsevier Science Ltd., 2001. p. 360-367.

NOWAG, L.; SÖLTER, J.; BRINKSMEIER, E. Influence of turning parameters on distortion of bearing rings. **Production Engineering** Vol. 1. Springer, 2007. p. 135-139.

OLVER, A.V. The mechanism of rolling contact fatigue: an update. **Journal of Engineering Tribology** Vol. 219. SAGE, 2005. p. 313-330.

OLVER, A.V.; TIEW, L.K.; MEDINA, S.; CHOO, J.W. Direct observations of a micropit in an elastohydrodynamic contact. **Wear** Vol. 256. Elsevier Science Ltd., 2004. p. 168-175.

OUTEIRO, J.C.; UMBRELLO, D.; M'SAOUBI, R. Experimental and numerical modelling of the residual stresses induced in orthogonal cutting of AISI 316L steel. **International Journal of Machine Tools & Manufacture** Vol. 46. Elsevier Science Ltd., 2006. p. 1786-1794.

OYAGUE, F. **Gearbox Modeling and Load Simulation of a Baseline 750-kW Wind Turbine Using State-of-the-Art Simulation Codes**. Golden: NREL, February 2009. 81 p. (Technical Report NREL/TP-500-41160).

PANGBORN, R.N.; WEISSMAN, S.; KRAMER, I.R. Dislocation distribution and prediction of fatigue damage. **Metallurgical Transactions A** Vol. 12. Springer, 1981. p. 109-120.

PARRISH, G. **Carburizing: Microstructures and Properties**. Materials Park: ASM, 1999. 147p.

PARRISH, G.; HARPER, G.S. **Production gas Carburising**. Oxford: Pergamon Press Ltd., 1985. 280p.

PERLOVICH, Y.; ISAENKOVA, M.; FESENKO, V. Principles of microstress equilibrium in textured metal materials. In: DENVER X-RAY CONFERENCE (DXC) ON APPLICATIONS OF X-RAY ANALYSIS. **International Centre for Diffraction Data 2010**. Denver: ICDD, 2010. p. 125-140.

PITALLÀ, G.M.; MONNO, M. A new approach to the prediction of temperature of the workpiece of face milling operations of Ti-6Al-4V. **Applied Thermal Engineering** Vol. 31. Elsevier Science Ltd., 2011. p. 173-180.

POOK, L.P. Mixed mode fatigue crack propagation. In: CARPINTERI, A. **Handbook of fatigue crack propagation in metallic structures**. Newnes: Elsevier Science Ltd, 1994. p. 1027-1071.

PREVÉY, P.; JAYARAMAN, N. A design methodology to take credit for residual stresses in fatigue limited designs. **Journal of ASTM International** Vol. 2. ASTM, 2005, p. 69-84.

PRZYLECKA, M.; GĘSTWA, W.; CANALE, L.C.F.; YAO, X.; TOTTEN, G.E. Sources of Failures in Carburized and Carbonitrided Component. In: CANALE, L.C.F.; MESQUITA, R.A.; TOTTEN, G.E. **Failure Analysis of Heat Treated Steel Components**. Materials Park: ASM, 2008. p. 177-240.

RAJE; N. SADEGHI, F. A statistical damage mechanics model for subsurface initiated spalling in rolling contacts. **Journal of Tribology** Vol. 130. ASME, 2008.

RAKHIT, A.K. **Heat Treatment of Gears: A practical guide to engineers**. Materials Park: ASM International , 2000. 209p.

REGO, R.R. **Influência do uso de distribuição bimodal de classes de granalha no processo de shot peening sobre o perfil de tensões residuais de engrenagens**. 2011. 184p. Master Thesis – Faculdade de Tecnologia Senai-CIMATEC, Salvador, 2011.

REGO, R.R.; GOMES, J.O.; BARROS, A.M. The influence on gear surface properties using shot peening with a bimodal media size distribution. **Journal of Materials Processing Technology** Vol. 213. Elsevier Science Ltd., 2013. p. 2152-2162.

REIMANN, J. **Randzonenbeeinflussung beim kontinuierlichen Wälzschleifen von Stirnradverzahnungen**. 2014. Doctorate Thesis - Werkzeugmaschinenlabor, Rheinisch-Westfälische Technische Hochschule, 2014.

RÉTI, T. Residual stresses in carburized, carbonitrided, and case-hardened components. In: TOTTEN, G.; HOWES, M.; INOUE, T. **Handbook of residual stress and steel deformation**. Materials Park: ASM, 2002. p. 189-208.

RIBRANT, J. **Reliability performance and maintenance: A survey of failures in wind power systems**. 2006. Master Thesis - KTH School of Electrical Engineering, Stockholm.

RUUD, C. Measurement of residual stresses. In: TOTTEN, G.; HOWES, M.; INOUE, T. **Handbook of residual stress and steel deformation**. Materials Park: ASM, 2002. p. 99–117.

SADEGHI, F.; JALALAHMADI, B.; SLACK, T.; RAJE, N. A review on rolling contact fatigue. **Journal of Tribology** Vol. 131. ASME, 2009.

SAHA, D.C.; NAYAK, S.S.; BIRO, E.; GERLICH, A.P.; ZHOU, Y. Mechanism of secondary hardening in rapid tempering of dual-phase steel. **Metallurgical and Materials Transactions A** Vol. 45. Springer, 2014. p. 6153-6162.

SCHRÖDER, T. **Analyse der Werkzeugbelastungen beim Zahnradschaben**. Doctorate Thesis – Werkzeugmaschinenlabor, Rheinisch-Westfälische Technische Hochschule, 2007.

SCHUH, G.; POTENTE, T.; VARANDANI, R.; HAUSBERG, C.; FRÄNKEN, B. Collaboration moves productivity to the next level. **Procedia CIRP** Vol. 17. Elsevier Science Ltd., 2014. p. 3-8.

SCHWIENBACHER, S. **Einfluss von Schleifbrand auf die Flankentragfähigkeit einsatzgehärteter Zahnräder**. 2008. Doctorate Thesis - Fakultät für Maschinenwesen, Technischen Universität München.

SHAH, S.M.A. **Prediction of residual stresses due to grinding with phase transformation**. 2011. Doctorate Thesis – Ecole Doctorale des Sciences de l'Ingenieur de Lyon, Institut National des Sciences Appliquees de Lyon.

SHELL. **Shell Spirax ASX**: Technical data sheet. 2006.

SHENG, S., MCDADE, M., ERRICHELLO, R. Wind turbine gearbox failure modes – A brief. In: **ASME/STLE 2011 International Joint Tribology Conference**, 2011, Los Angeles.

SHI, K., LI, P., YIN, S., LIU, Z. Chromatic confocal microscopy using supercontinuum light. **Optics Express** Vol. 12. PubMed, 2004. p. 2096-2101.

SHIN, H.C.; HA, T.K.; CHANG, Y.W. Kinetics of deformation induced martensitic transformation in a 304 stainless steel. **Scripta Materialia** Vol. 45. Elsevier Science Ltd., 2001. p. 823-829.

SHIVPURI, R.; CHENG, X.; MAO, Y. Elasto-plastic pseudo-dynamic numerical model for the design of shot peening process parameters. **Materials and Design** Vol. 30. Elsevier Science Ltd., 2009. p. 3112-3120.

SOADY, K.A.; MELLOR, B.G.; WEST, G.D.; HARRISON, G.; MORRIS, A. REED, P.A.S. Evaluating surface deformation and near surface strain hardening resulting from shot peening a tempered martensitic steel and application to low cycle fatigue. **International Journal of Fatigue** Vol. 54. Elsevier Science Ltd., 2013. p. 106-117.

SOCIETY OF AUTOMOTIVE ENGINEERS. **Chemical Compositions of SAE Alloy Steels**: SAE J404, 4 ed. Warrendale: SAE Inc, 2000. 5p.

SOCIETY OF AUTOMOTIVE ENGINEERS. **Manual on Shot Peening**: SAE HS-84, 4 ed. Warrendale: SAE Inc, 2001. p. 5-51.

SOCIETY OF AUTOMOTIVE ENGINEERS. **Residual Stress Measurement by X-Ray Diffraction** - SAE J784a, 2 ed. New York: SAE Inc, 1971. 76p.

SONG, G.; LIU, X.; WANG, G.; XIANG, X. Numerical Simulation on Carburizing and Quenching of Gear Ring. **Journal of Iron and Steel Research, International** Vol. 14. Elsevier Science Ltd., 2007. p. 47-52.

SPIß, L.; TEICHERT, G.; SCHWARZER, R.; BEHNKEN, H. GENZEL, C. **Moderne Röntgebeugung**: Röntgendiffraktometrie für Materialwissenschaftler Physiker und Chemiker. 2.ed. Wiesbaden: Vieweg + Teubner, 2009. 564 p.

SVERDLIN, A.V.; NESS, A.R. The effects of alloying elements on the heat treatment of steel. In: TOTTEN, G.; HOWES, M. **Steel Heat Treatment Handbook**. New York: Marcel Dekker, Inc., 1997. p. 45-92.

TANG, Z.T.; LIU, Z.Q.; PAN, Y.Z.; WAN, Y.; AI, X. The influence of tool flank wear on residual stresses induced by milling aluminum alloy. **Journal of Materials Processing Technology** Vol. 209. Elsevier Science Ltd., 2009. p. 4502-4508.

THIELE, J.D.; MELKOTE, S.N.; PEASCOE, R.A.; WATKINS, T.R. Effect of cutting-edge geometry and workpiece hardness on surface residual stresses in finish hard turning of AISI 52100 steel. **Journal of Manufacturing Science and Engineering** Vol. 122. ASME, 2000. p. 642-649.

TIZIANI, H.J., WEGNER, M., STEUDLE, D. Confocal principle for macro and microscopic surface and defect analysis. **Optical Engineering** Vol. 39. SPIE, 2000. p. 32-39.

TOBIE, T.; MATT, P. **Empfehlungen zur Vereinheitlichung von Tragfähigkeitsversuchen an vergüteten und gehärteten Zylinderrädern**. Frankfurt: FVA, 2012. 26 p. (Technical Report FVA-Richtlinie 563-I).

TOH, C.K. Comparison of chip surface temperature between up and down milling orientations in high speed rough milling of hardened steel. **Journal of Materials Processing Technology** Vol. 167. Elsevier Science Ltd., 2005. p. 110-118.

TÖNSHOFF, H., FRIEMUTH, T., MARZENELL, C. Properties of Honed Gears During Lifetime. **CIRP Annals – Manufacturing Technology**, Vol. 49. Elsevier Science Ltd., 2000. p. 431-434.

TOUALBI, L.; KANOUTÉ, P.; KRUCH, S.; LONGUET, A.; SEROR, A.; GOULMY, J.P.; PUYDT, Q. Assessment of shot-peening on fatigue life prediction: microstructural effects. In: 12th INTERNATIONAL CONFERENCE ON THE MECHANICAL BEHAVIOR OF MATERIALS, 2015, Karlsruhe. **ICM12 Book of Abstracts**, 2015. p. 79-80.

UNITED STATES STEEL CORPORATION. **Atlas of isothermal transformation diagrams**. Pittsburgh: United States Steel, 1953. 143 p.

USTINOVSHCHIKOV, Y.I. Secondary hardening mechanism of alloy steels. **Metal Science**, Vol. 18. Maney, 1984. p. 337-344.

VALIORGUE, F.; RECH, J.; HAMDI, H.; GILLES, P.; BERGHEAU, J.M. 3D modelling of residual stresses induced in finish turning of an AISI304L stainless steel. **International Journal of Machine Tools and Manufacture** Vol. 53. Elsevier Science Ltd., 2012. p.77-90.

VIELMA, A.T.; LLANEZA, V.; BELZUNCE, F.J. Effect of coverage and double peening treatments on the fatigue life of a quenched and tempered structural steel. **Surface & Coatings Technology** Vol. 249. Elsevier Science Ltd., 2014. p.75-83.

WANG, Z.; GONG, B. Residual Stress in the Forming of Materials. In: TOTTEN, G.; HOWES, M.; INOUE, T. **Handbook of residual stress and steel deformation**. Materials Park: ASM, 2002. p. 141-149.

WIKRENT, T. **Can the U.S. achieve 20% wind energy by 2030?** Epluribus Media, 2008. Available in: <http://discuss.epluribusmedia.net/node/1584>. Access in 07 Feb. 2013.

WITHERS, P.J.; BADHESIA, H.K.D.H. Residual stress part I – Measurement techniques. **Materials Science and Technology** Vol. 17. Elsevier Science Ltd., 2001. p. 355-365.

WULPI, D.J. **Understanding how components fail**. 2.ed. Metals Park: ASM International, 2000.

XIE, L.; JIANG, C.H.; JI, V. Thermal relaxation of residual stresses in shot peened surface layer of (TiB + TiC)/Ti–6Al–4V composite at elevated temperatures. **Materials Science and Engineering A** Vol. 528. Elsevier Science Ltd., 2011. p. 6478-6483.

YAN, J.; ZHAO, H.; KURIYAGAWA, T. Effects of tool edge radius on ductile machining of silicon: an investigation by FEM. **Semiconductor Science and Technology** Vol. 24. IOP Publishing, 2009, p.1-11.

ZAFOŠNIK, B.; GLODEŽ, S.; ULBIN, M.; FLAŠKER, J. A fracture mechanics model for the analysis of micro-pitting in regard to lubricated rolling–sliding contact problems. **International Journal of Fatigue** Vol. 29. Elsevier Science Ltd., 2007. p. 1950-1958.

ZHAN, K.; JIANG, C.H.; JI, V. Uniformity of residual stress distribution on the surface of S30432 austenitic stainless steel by different shot peening processes. **Materials Letters** Vol. 99. Elsevier Science Ltd., 2013. p. 61-64.

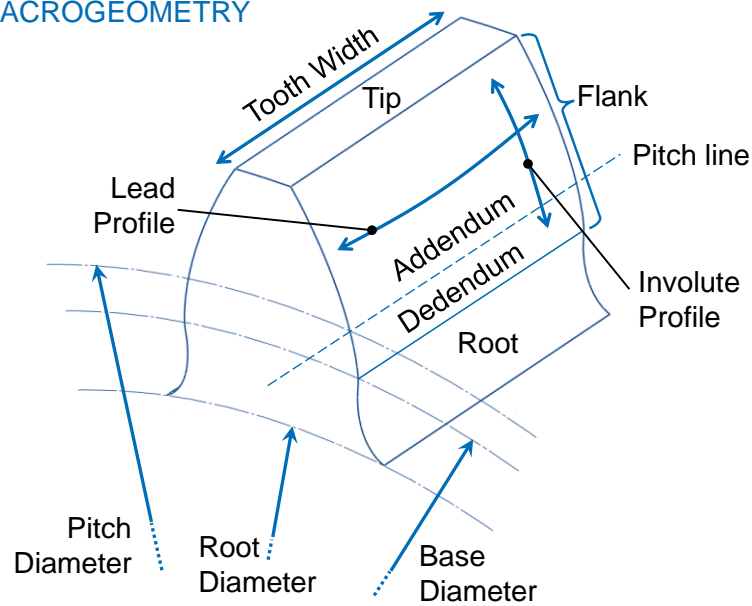
ZHANG, S., DING, T., LI, J. Determination of surface and in-depth residual stress distributions induced by hard milling of H13 steel. **Production Engineering** Vol. 6. Springer, 2012, p. 375-383.

Appendix A – Terminology

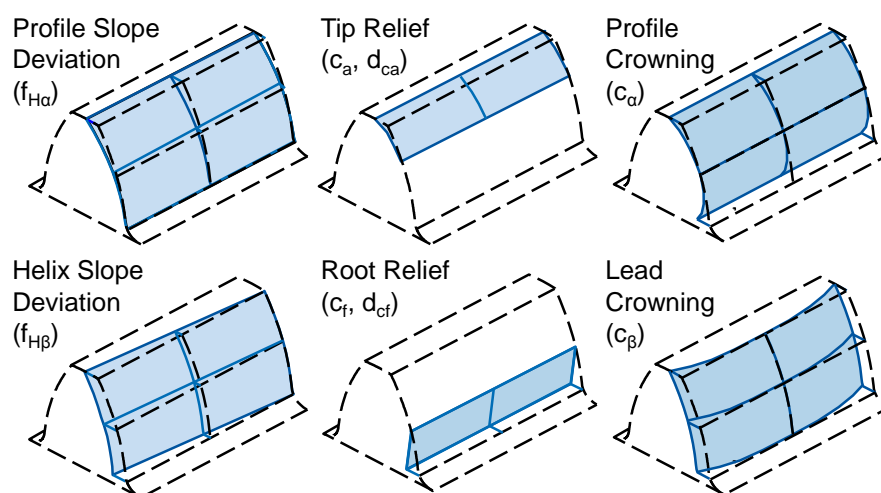
A.1 Gear Nomenclature for Macro and Micro-Geometry

Dimensions in mm

MACROGEOMETRY



MICROGEOMETRY

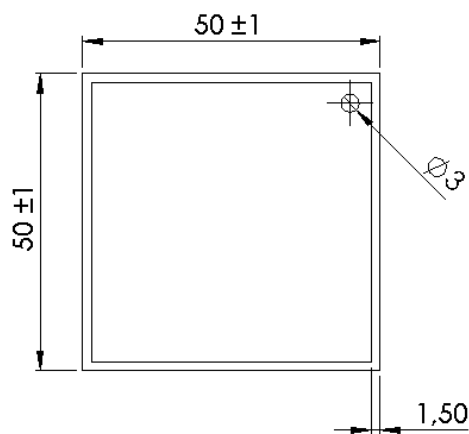


Ref: DIN, 1978; AGMA, 2011; MAZZO, 2013; KLOCKE; BRECHER; BRUMM, 2014

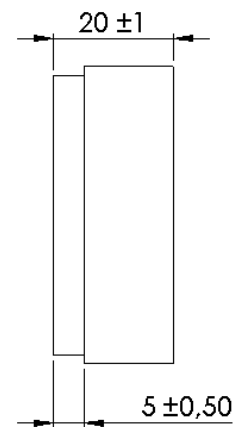
Appendix B – Specimens Geometry

B.1 Blocks for Sample Groups BFH and BFL

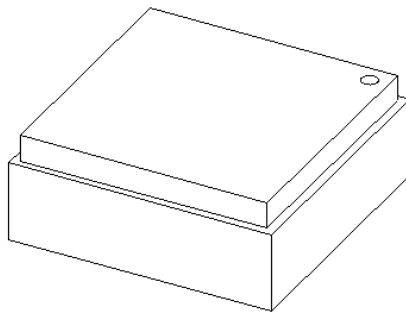
Dimensions in mm



Top view



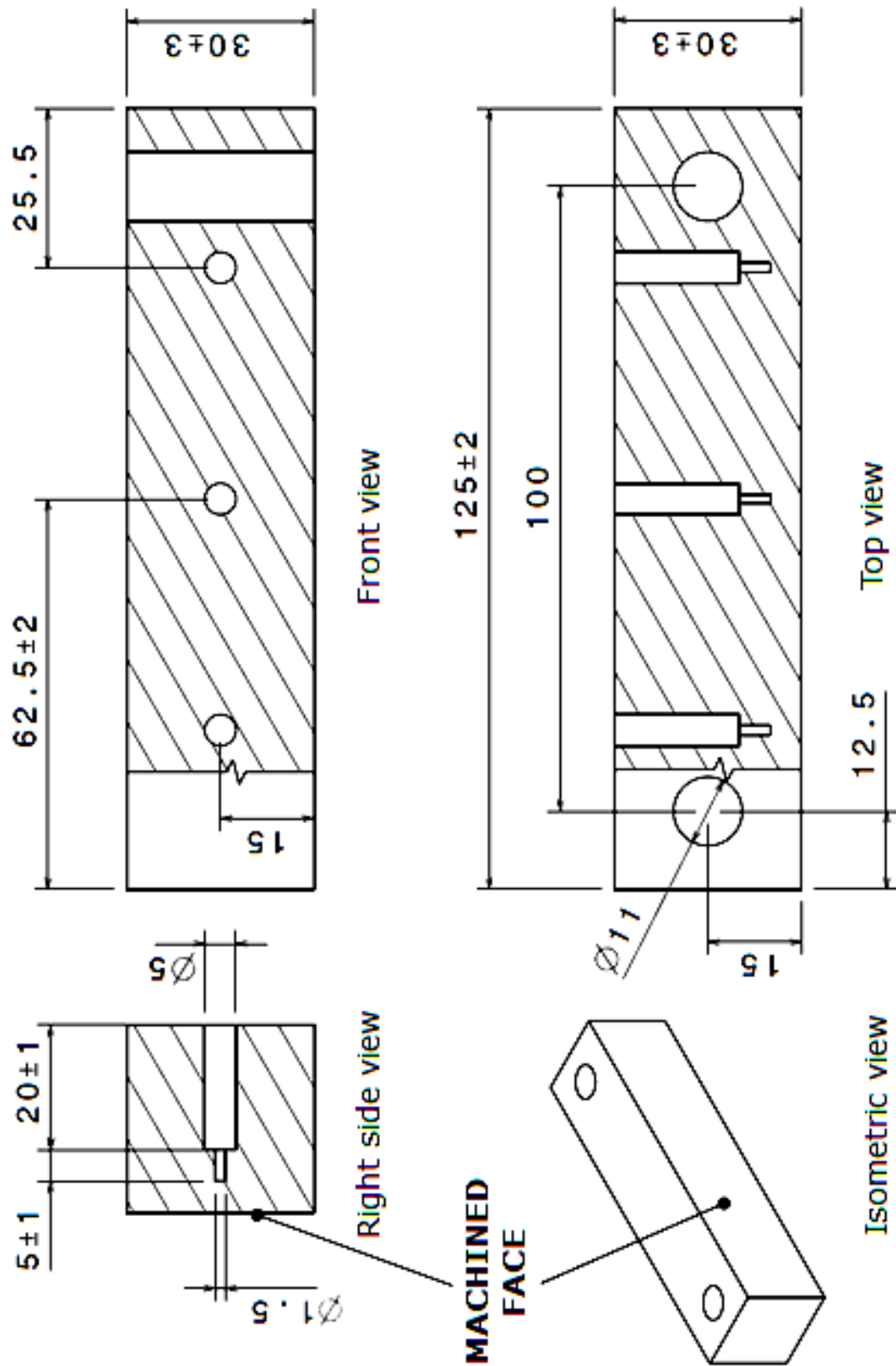
Side view



Isometric view

B.2 Blocks for Sample Groups BRH, BRM1, BRM2 and BRL

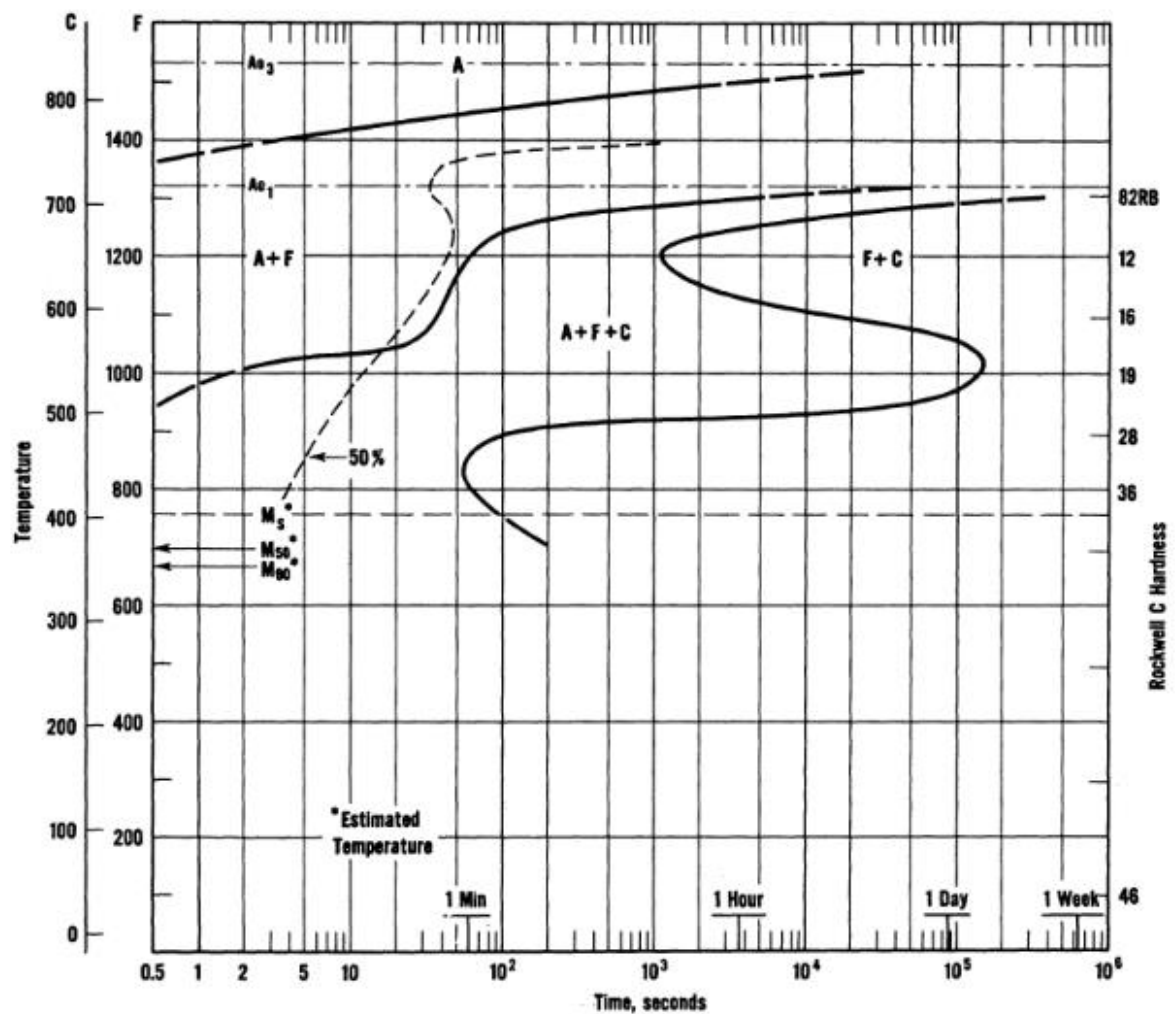
Dimensions in mm



Attachment C – Specimens Material

C.1 Blocks, SAE 8620

Element	C	Mn	P	S	Si	Ni	Cr	Mo	V
Specification [%]	0.18-0.23	0.70-0.90	≤ 0.03	≤ 0.04	0.15-0.35	0.40-0.70	0.40-0.60	0.15-0.25	-
Samples [%]	0.21	0.79	0.02	0.02	0.27	0.43	0.50	0.18	0.00



Sources: UNITED STATES STEEL CORPORATION; 1953, SAE, 2000; ASM, 2002

Attachment D – Testing Specification

D.1 Testing Oil Specification (*Shell Spirax ASX 75W90*)



Technical Data Sheet

Shell Spirax ASX

High performance, fuel economy, synthetic transmission and axle oil

Spirax ASX is a unique fuel-efficient, long life transmission and axle oil, designed to provide ultimate protection to the latest heavy duty manual transmissions and axles. Specially formulated with synthetic base oils and additive technology unique for Shell, gives improved lubrication of the drive train, lowers the operating temperature and helps promote longer life for the equipment. Spirax ASX is also extended oil drain capable and is approved by several OEMs for their extended drain specifications.

Available in SAE 75W-90 and 75W-140 grades.

Typical Physical Characteristics

Spirax ASX		75W-90	75W-140
SAE Viscosity Grade	SAE J 306	75W-90	75W-140
Kinematic Viscosity			
@ 40°C mm ² /s	ISO 3104	115.0	172.4
@ 100°C mm ² /s		15.2	24.5
Dynamic Viscosity			
@ -40°C mPa s	ISO 9262	135,000	135,000
Shear Stability			
Viscosity after shearing	CEC L-45_A-99	14.5	24.3
@ 100°C mm ² /s	ISO 3104		
Viscosity Index	ISO 2909	138	174
Density @ 15°C kg/m ³	ISO 12185	878	869
Flash Point COC °C	ISO 2592	210	210
Pour Point °C	ISO 3016	-42	-45

These characteristics are typical of current production. Whilst future production will conform to Shell's specification, variations in these characteristics may occur.

Source: SHELL, 2006

FOLHA DE REGISTRO DO DOCUMENTO			
1. CLASSIFICAÇÃO/TIPO TD	2. DATA 12 de Julho de 2016	3. REGISTRO N° DCTA/ITA/TD-019/2016	4. N° DE PÁGINAS 196
5. TÍTULO E SUBTÍTULO: Residual Stress Interaction In-Between Processes Of The Gear Manufacturing Chain			
6. AUTOR(ES): Ronnie Rodrigo Rego			
7. INSTITUIÇÃO(ÕES)/ÓRGÃO(S) INTERNO(S)/DIVISÃO(ÕES): Instituto Tecnológico de Aeronáutica - ITA			
8. PALAVRAS-CHAVE SUGERIDAS PELO AUTOR: 1. Residual stress. 2. Gear. 3. Manufacturing chain.			
9. PALAVRAS-CHAVE RESULTANTES DE INDEXAÇÃO: Engrenagens; Processos de fabricação; Tensão residual; Usinagem; Tratamento térmico; Engenharia mecânica.			
10. APRESENTAÇÃO: X Nacional Internacional			
ITA, São José dos Campos. Curso de Mestrado. Programa de Pós-Graduação em Engenharia Aeronáutica e Mecânica. Área de Materiais e Processos de Fabricação. Orientador: Jefferson de Oliveira Gomes; co-orientador: Fritz Klocke. Defesa em 06/07/2016. Publicada em 2016.			
11. RESUMO: Several sources of residual stresses characterize the entire gear manufacturing chain. In-between processes, their redistribution has to be the condition to satisfy the equilibrium principle. Nevertheless, the state-of-the-art reveals an excessive concern on optimizing the processes individually. As direct consequences, the accuracy of the prediction models is lowered, the control on the production dispersion is jeopardized and the product design is not optimized. The hypothesis herein stated is that the residual stress intensity and heterogeneity induced by previous processes are significant to the surface integrity of a subsequent process. Consequently, the objective is the identification of the residual stress factors induced along the gear manufacturing chain with relevant influence on the final surface integrity. An experimental investigation was conducted on the interaction between soft machining and heat treatment, and between shot peening and grinding. This study originally proposed to structure the investigation into a convergent approach. Whereas every parameter modification is to be done at the first process, the second process is kept the same. The ground gears were submitted to contact fatigue tests, to identify the relevance of the interaction effects to the part lifetime. The results proved that the previous process can exert a noteworthy influence on the final integrity state. The interaction is understood by a model of springs, into a self-equilibrated potential energy concept. The primary factor from the previous process is the hereafter named unstable area of residual stresses (UARS). It proportionally drives the modifications induced to the surface after the next process. They happen either as distortion or as change in the stress state itself, depending on the equilibrium disturbance mode that the manufacturing process represents. The effect follows the domain size under analysis. Residual microstresses carry and reflect microstructural inhomogeneity and roughness patterns between neighboring processes. The correlation was enabled due to a novel assessment method of the residual stress heterogeneity state, through the Gauss integral breadth parameter. The interaction showed also to be present to the gear fatigue behavior. Both the failure mode and the lifetime correspond to the region where the interaction effects were mostly observed. The comprehension of the residual stress interaction effects derives the newly introduced concept of Design for Residual Stress (DRS). The manufacturing chain can be designed with the purpose of providing an optimal residual stress state, with a consequent potential for enhancing the gear load carrying capacity.			
12. GRAU DE SIGILO: (X) OSTENSIVO () RESERVADO () SECRETO			